LATE PLEISTOCENE TO HOLOCENE SEA-LEVEL CHANGES IN NEW JERSEY: CAUSES AND PALEOENVIRONMENTAL IMPLICATIONS

By

CHRISTOPHER STEPHEN JOHNSON

A dissertation submitted to the

School of Graduate Studies

Rutgers, The State University of New Jersey

In partial fulfillment of the requirements

For the degree of

Doctor of Philosophy

Graduate Program in Geological Sciences

Written under the direction of

Kenneth G. Miller

And approved by

_____

_____

_____

_____

_____

New Brunswick, New Jersey

October 2019

ABSTRACT OF THE DISSERTATION

LATE PLEISTOCENE TO HOLOCENE SEA LEVEL IN NEW JERSEY: CAUSES AND PALEOENVIRONMENTAL IMPLICATIONS

by CHRISTOPHER STEPHEN JOHNSON

Dissertation Director:

Kenneth G. Miller

With locations such as Norfolk, VA, Atlantic City, NJ, and Sandy Hook, NJ experiencing ≥4 mm/yr of relative sea-level (RSL) rise over the 20th century, sea-level rise is an issue facing many coastal communities. As such, it is important to understand the factors controlling the rate of RSL rise and to be able to quantify their contributions. RSL rise is a combination of global mean sea-level change, vertical land motion (VLM), changes in Earth gravity, Earth rotation, and viscoelastic solid-Earth Deformation (GRD), and sterodynamic effects. VLM can include thermal subsidence of the lithosphere, Glacial Isostatic Adjustment (GIA), sea-level change due to Mantle Dynamic Topography (MDT), and sediment compaction (both autocompaction and groundwater induced). Sterodynamic changes involve thermosteric sea-level change, gravitational effects of changing ice-volume, dynamic topography, and changes in tidal regime. In this thesis, I attempt to quantify the local sources of VLM at Sandy Hook, NJ, and improve our understanding of the regional sources of VLM along the New Jersey margin. At Sandy Hook, the tide gauge measurements detected a twentieth century mean rate of RSL rise of 4.0±0.4 mm/yr, whereas 26 km north at The Battery, NY, the rate of RSL rise was 3.0±0.3 mm/yr for the twentieth century. The proximity of these two stations rules out most sterodynamic changes and many of the larger scale processes driving VLM as the

primary driver of the diference. The major cause of the 0.9±0.5 mm/yr difference between these two points is the underlying geology. The Battery lies directly on crystalline bedrock, while Sandy Hook rests atop >226 m of compressible Cretaceous to Holocene coastal plain sediments overlying bedrock. In 2014, three coreholes, drilled at Sandy Hook, revealed a thick (84+ m) Quaternary section underlying the tide gauge. As such, we hypothesized that natural compaction of this relatively young (<13,350 cal yrs bp) package of sediment was the source of the "excess" subsidence detected at this location. We tested this hypothesis in Chapter 2 (Johnson et al., 2018) by creating a numerical model that simulated autocompaction through time and resulted in a 20th century average compaction rate of 0.16 mm/yr (90% Confidence Interval; C.I. 0.06-0.32 mm/yr). We then hypothesized that the remaining 0.7 mm/yr (90% C.I. 0.3-1.2 mm/yr) was due to groundwater extraction. Chapter 3 tested this hypothesis by building a groundwater model that evaluated the subsidence caused by drawdown of the groundwater under Sandy Hook and the resulting compaction. We found that groundwater extraction was responsible for 20th century average of 0.3±0.2 mm/yr of subsidence at Sandy Hook. For the duration of the tide gauge record during the 20th century the average was 0.4 mm/yr, and the current rate of groundwater related subsidence is ~0.7 mm/yr. We then compared our results to the vertical land motion measured by continually operating reference station global positioning systems, and there was generally a good qualitative agreement. The magnitudes of vertical land motion were consistent with the total of our estimates of the GIA, autocompaction, and groundwater related subsidence components of RSL at Sandy Hook. Chapter 4 examined Quaternary paleochannels on the inner continental shelf of New Jersey and their responses to GIA.

We measured the incision depths of several channel systems looking for a pattern that would suggest a record of differential uplift of the region due to GIA, but the spatial coverage was insufficient to see such large-scale features. We also identified two sets of paleochannels on the inner shelf, the first older than 30 ka and trending north-south, while the younger (<30 ka) set trended northwest-southeast. This suggests that GIA caused a shift in channel orientations ~30 ka and is consistent with previous work and estimates of the distribution of GIA-related tilting in the region at the time.

ACKNOWLEDGEMENTS

I would first like to thank my advisor, Dr. Kenneth Miller, without whom none of this would have been possible. He gave me the freedom and encouragement to explore my interests and follow the research wherever it took me. I would like to thank my committee members; Dr. Ying Fan who devoted countless hours to helping me wade into the world of groundwater modeling, Dr. Gregory Mountain who always had time for a quick chat on the seismic stratigraphy of the New Jersey Margin or to play catch and gave me the opportunity to go to sea, an experience I will always treasure, Dr. Robert Kopp who helped me in my pursuit to understand and quantify my uncertainty, and to Dr. Scott Stanford who always had time to talk about my crazy questions and hypotheses for the deglacial history of New Jersey. I would also like to thank Drs. Gail Ashley and James Browning for numerous discussions on sedimentology and help learning the ropes of sedimentological analyses. Additionally, thank you everyone at EPS, the faculty, staff, my fellow graduates students, and all of the undergraduates for making me a part of the family and making the last five years so great. I would like to thank my friends and family who were always supportive. A specially thank you to my parents and sister who were always available to talk and give encouragement. Finally, I would like to thank my fiancée Kim Baldwin whose love, support, and encouragement throughout this process meant more to me than I can ever put into words.

Chapter 2 was previously published in Quaternary Science Reviews.

Johnson, C. S., Miller, K. G., Browning, J. V., Kopp, R. E., Khan, N. S., Fan, Y., Stanford, S. D., and Horton, B. P., 2018, The role of sediment compaction and groundwater withdrawal in local sea-level rise, Sandy Hook, New Jersey, USA: Quaternary Science Reviews, v. 181, p. 30-42.

TABLE OF CONTENTS OF THE DISSERTATION

LATE PLEISTOCENE TO HOLOCENE SEA LEVEL IN NEW JERSEY: CAUSES AND PALEOENVIRONMENTAL IMPLICATIONS

LIST OF TABLES OF THE DISSERTATION

LATE PLEISTOCENE TO HOLOCENE SEA LEVEL IN NEW JERSEY: CAUSES AND PALEOENVIRONMENTAL IMPLICATIONS

LIST OF ILLUSTRATRATIONS OF THE DISSERTATION

LATE PLEISTOCENE TO HOLOCENE SEA LEVEL IN NEW JERSEY: CAUSES AND PALEOENVIRONMENTAL IMPLICATIONS

CHAPTER 1: Introduction

The New Jersey continental margin (coastal plain to continental shelf) provides an opportunity to study both the sources of relative sea-level (RSL) change and the effects they have on the region. RSL is the height of the sea surface over the solid earth (See Gregory et al., 2019 for sea-level definitions). The New Jersey margin has experienced and recorded numerous RSL cycles from the Mesozoic to the present (Miller et al., 2005). Instrumental records only cover the last ~100 years of that history, but that record shows that sea-level change can vary significantly (>1mm/yr) over short distances (<26 km) (e.g., Miller et al., 2013). These variations in the rate of RSL change can be caused by a number of factors including Glacial Isostatic Adjustment (GIA; e.g., Clark et al., 1978), mantle dynamic topography (MDT; e.g., Gurnis, 1990; Moucha et al., 2008), changes in Earth gravity, Earth rotation, and viscoelastic solid-earth deformation (GRD) (e.g. Mitrovica et al., 2001), and changes in ocean circulation (e.g., Yin et al., 2009). Over very short distances (<100 km) these differences are often caused by local factors including autocompaction of organic material or inorganic fine-grained sediments (Törnqvist et al., 2008) and groundwater extraction induced compaction (Sneed and Galloway, 2000). The causes of RSL change can be broadly separated into three categories, geoid changes, dynamic changes, and vertical land motion (VLM). The goal of this study is to identify and quantify regional and local sources of RSL rise that affect the New Jersey Coastal Plain. Each of the next three chapters will focus on a different VLM component of relative sea-level rise.

Global mean sea level, the average RSL over the whole ocean (Gregory et al., 2019), rose at a rate of 1.4±0.2mm/yr for the 20th century (Hay et al., 2015) and 3.1±0.3 mm/yr since

1993 (The WCRP Sea Level Budget Group, 2018). In New Jersey, the 20th century rate of RSL rise varied geographically between 3 and 4 mm/yr (Kopp, 2013), significantly higher than the global mean. Chapters 2 and 3 examine Sandy Hook, NJ, where the 20th century rate of RSL rise was 4.0±0.5 mm/yr, with 0.9±0.5 mm/yr due to local processes (Kopp, 2013), to test methods for quantifying the contributions to subsidence from natural and anthropogenic processes. Coring, tide gauge records, continually operating reference station global positioning systems (CORS GPS), and historical records at Sandy Hook provide an opportunity to examine the compositions, ages, and physical properties of the underlying sediments, use models to quantify the sources of RSL rise, and test our results against the tide gauge records and CORS GPS records.

Chapter 2 focuses on quantifying the natural sources of local subsidence at Sandy Hook. To this end, we performed sedimentological studies including measurements of grain size, porosity, and percent organic matter on the sediments collected in a transect of cores that sampled the latest Pleistocene to Holocene section at Sandy Hook. We used the organic content to semi-quantitatively evaluate the potential for compaction of organic rich sediments. The results of the other analyses were then used to develop a numerical model to quantify natural compaction of the Quaternary section underlying Sandy Hook. We concluded that natural compaction of Quaternary strata account for ~0.2 mm/yr of modern subsidence. The results were published as Johnson et al. (2018).

Chapter 3 quantifies the local anthropogenic sources of subsidence and RSL rise at Sandy Hook. Historical records for Gateway National Recreation Area and the now decommissioned Fort Hancock showed the potential for subsidence due to groundwater extraction at Sandy Hook. Evidence pointed toward groundwater extraction as a major

contributor to the rate of RSL rise. Based on the unexplained ~0.7 mm/yr difference between the rates of RSL rise between Sandy Hook and The Battery, Johnson et al., 2018 hypothesized that >0.5 mm/yr out of 4.0 ±0.5 mm/yr at Sandy Hook was due to compaction caused by groundwater extraction. Therefore, a groundwater model for the northern half of the New Jersey coastal plain was built to quantify the potential groundwater related subsidence at Sandy Hook. The model was designed to determine the rate of subsidence through time and the relative contributions of regional and local pumping to the rate of RSL at Sandy Hook. We conclude that groundwater extraction is responsible for an average of 0.3±0.2 mm/yr of subsidence for the 20th century, and 0.4±0.2 mm/yr for the duration of the tide gauge record at Sandy Hook during the 20th century. The modern rate of subsidence due to groundwater withdrawal is ~0.7 mm/yr. Local and regional pumping have contributed ~equal amounts of total subsidence with local pumping as the primary contributor prior to the 1960s and regional pumping is the major cause from the 1960s to 2015. This chapter is intended for publication in Environmental Research Letters.

Chapter 4 is an offshore study of the effects of GIA on paleochannels across New Jersey's Inner Continental Shelf. There were two main sets of objectives for this project. First, we sought to evaluate the impact of GIA related uplift on the incision depths of paleochannels, determine if channel profiles reflected differential uplift and subsidence of the landscape, and assess the viability of the paleochannel record to test GIA models. Towards this goal, we attempted to measure the channel incision depths from several paleochannel systems imaged in a recently acquired 3D seismic volume, MGL1510, The second goal was to determine if GIA was responsible for the diversion of paleochannels

on the exposed inner continental shelf around 30 ka as proposed by Knebel et al. (1979) and later modeled by Pico et al. (2018). To do this, we mapped all visible drainage systems in the MGL1510 survey grid and applied relative dating techniques to determine if regional drainage orientations were reorganized at any point during the last 125 ka. We conclude that the effects of GIA on the incision depths of thalwegs must be studied on a larger spatial scale to capture the large (100s of km) wavelength signal of GIA. Further, tilting of the landscape at ~30 ka resulted in the reorientation of the regional drainage from a north-south orientation to a northwest–southeast orientation.

References

Clark, J.A., Farrell, W.E., and Peltier, W.R., 1978. Global changes in postglacial sea level: a numerical calculation: Quaternary Research v. 9, n. 3, p. 265-287.

Gurnis, M., 1990. Bounds on global dynamic topography from Phanerozoic flooding of continental platforms. Nature v. 344, n. 6268, p. 754.

Gregory, J.M., Griffies, S.M., Hughes, C.W., et al., 2019. Concepts and terminology for sea level: mean, variability and change, both local and global. Surveys in Geophysics https://doi.org/10.1007/s10712-019-09525-z.

Hay, C.C., Morrow, E., Kopp, R.E., and Mitrovica, J.X., 2015, Probabilistic reanalysis of twentieth-century sea-level rise. Nature v. 517, n. 7535, p. 481-484.

Knebel, H.J., Wood, S.A., and Spiker, E.C., 1979. Hudson River: evidence for extensive migration on the exposed continental shelf during Pleistocene time. Geology v. 7, n. 5, p. 254-258.

Kopp, R.E., 2013, Does the mid-Atlantic United States sea-level acceleration hot spot reflect ocean dynamic variability? Geophysical Research Letters v. 40, p. 3981-3985.

Johnson, C.S., Miller, K.G., Browning, J.V., Kopp, R.E., Khan, N.S., Fan, Y., Stanford, S.D., and Horton, B.P., 2018. The role of sediment compaction and groundwater withdrawal in local sea-level rise, Sandy Hook, New Jersey, USA. Quaternary Science Reviews v. 181, p. 30-42.

Miller, K.G., Kominz, M.A., Browning, J.V., Wright, J.D., Mountain, G.S., Katz, M.E., Sugarman, P.J., Cramer, B.S., Christie-Blick, N., and Pekar, S.F., 2005. The Phanerozoic record of global sea-level change. Science v. 310, n. 5752, p. 1293-1298.

Miller, K.G., Kopp, R.E., Horton, B.P., Browning, J.V., and Kemp, A.C., 2013. A geological perspective on sea-level rise and its impacts along the US mid-Atlantic coast. Earth's Future v. 1, n. 1, p. 3-18.

Mitrovica, J.X., Tamisiea, M.E., Davis, J.L., and Milne, G.A., 2001. Recent mass balance of polar ice sheets inferred from patterns of global sea-level change. Nature v. 409, p. 1026-1029. doi: 10.1111/j.1365-246X.1976.tb01252.x.

Moucha, R., Forte, A.M., Mitrovica, J.X., Rowley, D.B., Quéré, S., Simmons, N.A., and Grand, S.P., 2008. Dynamic topography and long-term sea-level variations: There is no such thing as a stable continental platform. Earth and Planetary Science Letters, v. 271, n. 1, p. 101-108.

Pico, T., Mitrovica, J., Braun, J., and Ferrier, K., 2018. Glacial isostatic adjustment deflects the path of the ancestral Hudson River. Geology v. 46, n. 7, p. 591-594.

Sneed, M., and Galloway, D., 2000. Aquifer-system compaction: analyses and simulations the Holly site. Edwards Air Force Base, Antelope Valley, California. US Geological Survey Water-Resources Investigations Report 00-4015.

Törnqvist, T.E., Wallace, D.J., Storms, J.E., Wallinga, J., Van Dam, R.L., Blaauw, M., Derksen, M.S., Klerks, C.J., Meijneken, C., and Snijders, E.M., 2008. Mississippi Delta subsidence primarily caused by compaction of Holocene strata. Nature Geoscience v. 1, n. 3, p. 173.

WCRP Global Sea Level Budget Group, 2018. Global sea-level budget 1993–present, Earth System Science Data v. 10, p. 1551-1590. https://doi.org/10.5194/essd-10-1551-2018.

Yin, J., Schlesinger, M.E., and Stouffer, R.J., 2009. Model projections of rapid sea-level rise on the northeast coast of the United States: Nature Geoscience v. 2, n. 4, p. 262.

CHAPTER 2: The Role of Sediment Compaction and Groundwater Withdrawal in Local Sea-Level Rise, Sandy Hook, New Jersey, USA*

Christopher S. Johnson,[a,b*] Kenneth G. Miller,[a,b] James V. Browning,[a,b] Robert E. Kopp,[a,b,c] Nicole S. Khan,[d,e,f] Ying Fan,[a,b] Scott D. Stanford,[g] and Benjamin P. Horton[b,d,e,f]

[a]*Department of Earth and Planetary Sciences, Rutgers University, 610 Taylor Road, Piscataway, New Jersey 08854, USA; *Corresponding author, E-mail: c.s.johnson@rutgers.edu*

[b]*Institute of Earth, Ocean and Atmospheric Sciences, Rutgers University, 71 Dudley Road, New Brunswick, New Jersey 08901, USA*

[c]*Rutgers Energy Institute, Rutgers University, 71 Dudley Road, New Brunswick, New Jersey 08901, USA*

[d,]*Sea Level Research, Department of Marine and Coastal Sciences, Rutgers University, 71 Dudley Road, New Brunswick, New Jersey 08901, USA*

[e]*Earth Observatory of Singapore, Nanyang Technological University, 50 Nanyang Avenue, Singapore 639798, Singapore*

[f]*Asian School of the Environment, Nanyang Technological University, 50 Nanyang Avenue, Singapore 639798, Singapore*

[g]*New Jersey Geological and Water Survey, P.O. Box 420, Trenton, New Jersey 08625-0420, USA*

[*]Published as Johnson, C. S., Miller, K. G., Browning, J. V., Kopp, R. E., Khan, N. S., Fan, Y., Stanford, S. D., and Horton, B. P., 2018, The role of sediment compaction and groundwater withdrawal in local sea-level rise, Sandy Hook, New Jersey, USA: Quaternary Science Reviews, v. 181, p. 30-42.

Key Words

Quaternary, Sea-level Change, North America, Sedimentology, Marginal Marine, Numerical Modeling

Highlights

- We quantify subsidence at Sandy Hook to determine the effects of natural and anthropogenic sources causing high local rates of sea-level rise.
- We develop a single decompaction equation describing porosity as a function of grain size, burial depth, and age applicable to other regions.
- Compaction of Quaternary organic material has a negligible contribution, whereas compaction of fine-grained siliciclastic sediments is causing 0.16 mm/yr (90% C.I., 0.6-0.32 mm/yr) of local sea-level rise.
- Anthropogenic groundwater withdrawal likely contributes the remaining 0.7 mm/yr (90% C. I. 0.3-1.2 mm/yr) of local sea-level rise.

Abstract

The rate of relative sea-level (RSL) rise at Sandy Hook, NJ (4.0±0.5 mm/yr) was higher than The Battery, NY (3.0±0.3 mm/yr) from 1900-2012 despite being separated by just 26 km. The difference cannot be explained by differential glacial isostatic adjustment (GIA; 1.4±0.4 and 1.3±0.4 mm/yr RSL rise, respectively) alone. We estimate the contribution of sediment compaction to subsidence at Sandy Hook using high-resolution grain size, percent organic matter, and porosity data from three late Quaternary (≤13,350 cal yr) cores. The organic matter content (< 2%) is too low to contribute to local subsidence. However, numerical modeling of the grain size-depth-age-porosity

relationship indicates that compaction of deglacial silts likely reduced the column thickness by 10-20% over the past 13,350 cal yrs. While compaction rates were high immediately after the main silt deposition (13,350-13,150 cal yrs BP), rates decreased exponentially after deposition to an average 20th century rate of 0.16 mm/yr (90% Confidence Interval (C.I.), 0.06-0.32 mm/yr). The remaining ~0.7 mm/yr (90% C.I. 0.3-1.2 mm/yr) difference in subsidence between Sandy Hook and The Battery is likely due to anthropogenic groundwater withdrawal. Historical data from Fort Hancock (2 km to the southeast of the Sandy Hook tide gauge) and previous regional work show that local and regional water extraction lowered the water levels in the aquifers underlying Sandy Hook. We suggest that the modern order of contribution to subsidence (highest to lowest) appears to be GIA, local/regional groundwater extraction, and compaction of thick Quaternary silts.

2.1 Introduction

Global, regional, and local processes cause changes in relative sea level (RSL). Global mean sea-level (GMSL) change describes changes in sea surface height averaged over the whole ocean (e.g., Kopp et al., 2015). Due primarily to thermal expansion and shrinking of land ice, GMSL rose at a rate of about 1.4±0.2 mm/yr during the 20th century (Hay et al., 2015; Dangendorf et al., 2017), which is significantly lower than previously published estimates of 1.5-1.9 mm/yr (e.g., Jevrejeva et al., 2008; Church and White, 2011). GMSL has been rising at a rate of about 3 mm/yr from 1993-2014 (Chen et al., 2017). RSL is the vertical distance between sea-surface height and the solid-Earth surface at a specific location (Kopp et al., 2015). RSL may be falling or rising at a different rate from GMSL and can be used to describe sea-level trends for areas on regional (~100

km^2) and local (single location; ~10 km^2) scales. Comparison of RSL rise at Sandy Hook, which lies on thick compressible sediments, and the nearby (26 km) Battery, NY, which lies on incompressible bedrock, provides a natural experiment evaluating the natural and anthropogenic effects on compaction.

The increasing availability of tide-gauge records and geologically based reconstructions of past RSL has made it possible to analyze RSL change with finer spatial resolution (e.g. Kopp, 2013; Kemp et al., 2011; Horton and Shennan, 2009). These analyses have shown it is possible, if not common, to have large variations in rates of RSL change over relatively small (a few kilometers) distances. For example, spatio-temporal statistical analysis of tide-gauge records estimated the rate of RSL rise at Sandy Hook between 1900 and 2012 to be 4.0±0.5 mm/yr (Fig. 2.2). This rate is significantly higher than the 3.0±0.3 mm/yr observed over the same period at The Battery tide gauge, located just 26 km to the northwest (Kopp, 2013).

RSL change can be influenced by many factors, including glacial isostatic adjustment (GIA; Clark et al., 1978), mantle dynamic topography (e.g., Gurnis, 1990), ocean dynamics (Yin et al., 2009), and local processes including active tectonics (Simms et al., 2016), sediment loading, and compaction (Törnqvist et al., 2008; Brian et al., 2015). Both Sandy Hook and The Battery show 20^{th} century rates greater than the 1.4±0.2 mm/yr of GMSL rise (Hay et al., 2015, Kopp et al., 2016). The excess RSL rise above GMSL rise at these two locations is mainly due to GIA (Clark et al., 1978). Kopp (2013) estimated the GIA effect to be 1.3±0.4 mm/yr at The Battery and 1.4±0.4 mm/yr at Sandy Hook.

Accounting for the difference in GIA between Sandy Hook and The Battery leaves a 0.9 ± 0.5 mm/yr difference in RSL change (Kopp, 2013). This difference cannot be attributed to regional processes, but must be due to unquantified local processes. Moucha et al. (2008) showed that there is little or no difference (≤0.003 mm/yr) in mantle dynamic topography driven RSL change between Sandy Hook and The Battery. Furthermore, changes in ocean dynamics occur over spatial scales too large to affect Sandy Hook and The Battery differently (Yin et al., 2009). Similarly, spatial variation arising from the static-equilibrium (gravitational, rotational, and deformational) effects of shifting mass from land ice to or from the ocean occurs over distances greater than the 26 km between Sandy Hook and The Battery (Kopp et al., 2015). Based on models of long-term thermal subsidence and compaction of pre-Quaternary strata (Kominz et al., 2008), these effects are too low (<0.1 mm/yr difference between sites) to explain the difference (Miller et al., 2013). Thus the 0.9±0.5 mm/yr difference is likely due to sediment compaction.

Here we seek to quantify the sources of local subsidence to account for the high rate of local RSL rise at Sandy Hook. Potential contributors include compaction of organic-rich strata and/or siliciclastic sediments due to natural effects (e.g., Törnqvist et al., 2008) and compaction induced by anthropogenic groundwater withdrawal (e.g., Pope and Burbey, 2004). Locations with high rates of RSL rise (≥~4.0 mm/yr) (e.g. Norfolk, VA and Atlantic City, NJ) are typically affected by high rates of compaction due to groundwater withdrawal (Pope and Burbey, 2004; Cronin, 2012; Miller et al., 2013). In this study, we assess the RSL contributions from compaction of Quaternary organic material and siliciclastic sediments at Sandy Hook. We conduct sedimentological studies

(percent organic matter, grain size, and porosity) on a transect of three cores drilled on Sandy Hook (Fig. 2.1). We use these data to model the contributions of compaction in young unconsolidated siliciclastic silts to local RSL changes and compare the residual to rates of groundwater withdrawal. Our approach to quantify RSL budgets is applicable to other regions.

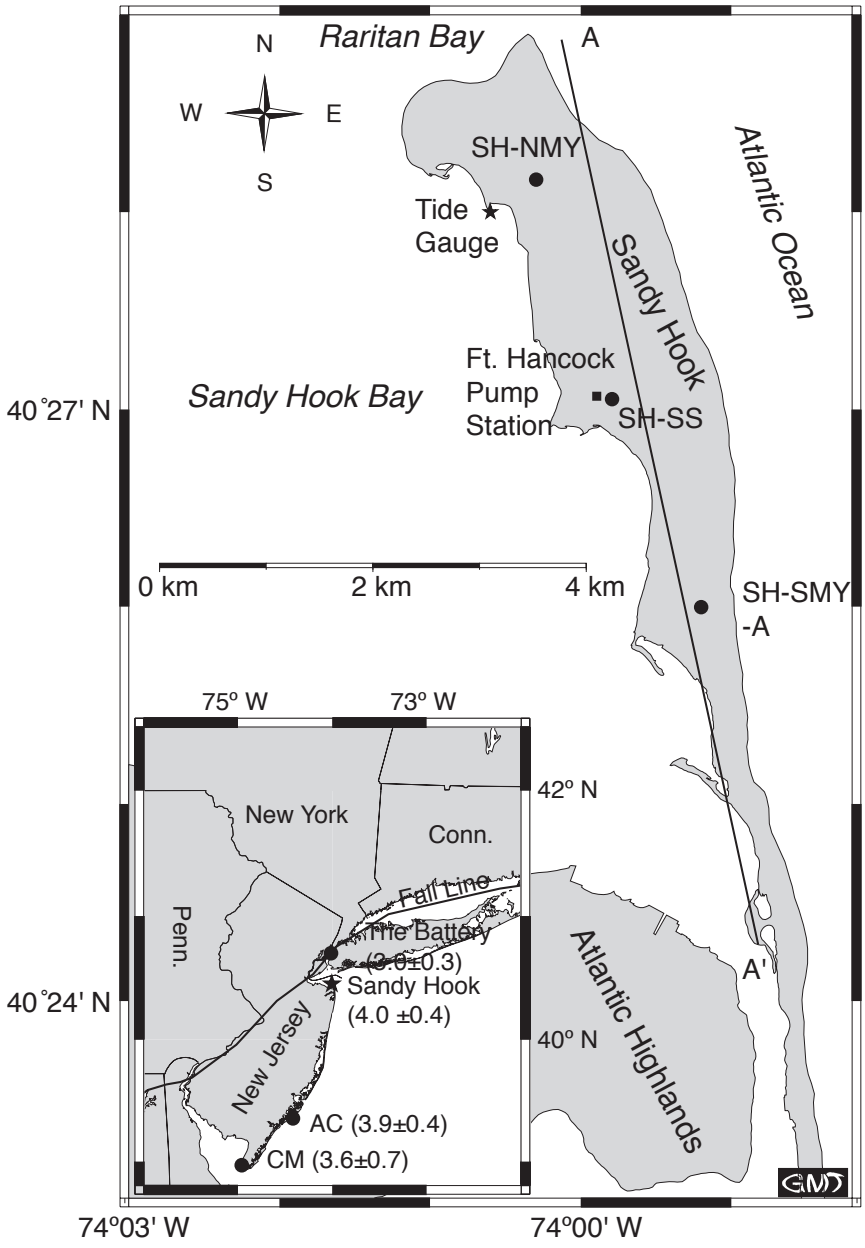

Figure. 2.1: Sandy Hook Location Map. SH-NMY Sandy Hook North Maintenance Yard Corehole, SH-SS Sandy Hook Salt Shed Corehole, SH-SMY-A Sandy Hook South Maintenance Yard Corehole A.Inset map shows the Fall Line, B = The Battery Tide Gauge, AC = Atlantic City Tide Gauge, CM = Cape May Tide Gauge, and 1900-2012

average rates of sea-level rise at each of those locations including Sandy Hook (Miller et al., 2013). A-A' is the location of the cross-section in Fig. 2.3.

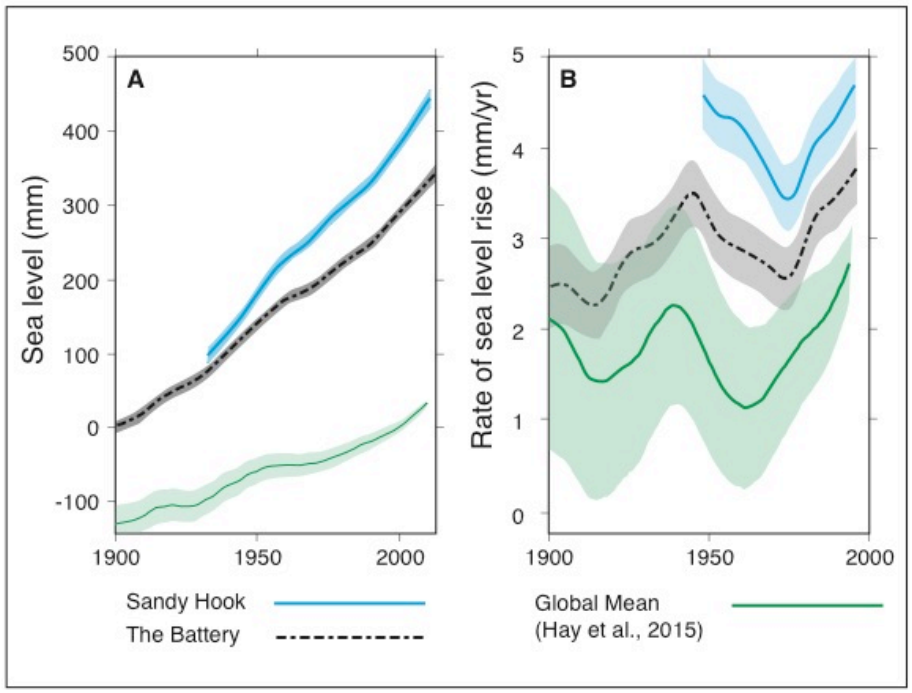

Figure 2.2: A: Sea level from tide gauges at Sandy Hook, NJ (cyan) and The Battery, NY (black dashed) compared to the global sea-level curve of Hay et al. (2015) (green). B: 31-year averaged rate of sea-level rise at Sandy Hook (black) and The Battery (blue) compared to global (green; based on data from Hay et al., 2015). Shaded areas are 2σ uncertainty (Modified from Miller et al., 2013).

2.2 Study Area

Sandy Hook is a sand spit extending 8 km north into Sandy Hook and Raritan Bays between New York and New Jersey, USA (Fig. 2.1). The spit has been growing northward into Raritan Bay at an average rate of ~8 m/yr over the past two centuries (see supplementary material for calculation). The Sandy Hook tide gauge is located near the NW end of the spit, 26 km southeast of The Battery tide gauge in New York, NY. Sandy

Hook and The Battery are in different geologic settings. The Battery is underlain by Paleozoic and Proterozoic crystalline metamorphic bedrock (Lyttle and Epstein, 1987), whereas Sandy Hook is in the New Jersey coastal plain underlain by ~300 m of unconsolidated Cretaceous to recent marine, near shore, and terrestrial sediments that onlap the bedrock seaward of the fall line (Owens et al., 1998). The fall line, demarcated by a linear series of waterfalls along rivers traversing the line, marks the transition between unconsolidated sediments and more resistant bedrock to the west (e.g., Owens et al., 1998; Fig. 2.1).

Miller et al. (2013) used tide gauge records to show that the 20th century regional rate of sea-level rise along the fall line and to the west in the Piedmont is ~3.0 mm/yr. Major cities including New York (3.0±0.3 mm/yr), Philadelphia (3.1±0.3 mm/yr), Baltimore (3.1±0.3 mm/yr), and Washington D.C. (3.0±0.5 mm/yr) are located in this region. These rates closely match the sum of GMSL rise and GIA-driven RSL change. Tide gauges located east of the fall line in the coastal plain typically exhibit rates of rise of at least 3.5 mm/yr and can reach rates as high as 3.9 and 4.0 mm/yr in locations such as Atlantic City, NJ and Sandy Hook, NJ, respectively (Miller et al., 2013) and higher in Virginia (Pope and Burbey, 2004). While the coastal plain sea-level signal includes GMSL rise and GIA similar to the bedrock sites, most coastal plain sites experience an additional 0.5-1.5 mm/yr RSL rise.

2.3 Methods

2.3.1 Drilling

In order to study the effects of the underlying geology and quantify the contribution of different processes on the local rate of sea-level rise at Sandy Hook, a

transect of three continuously cored and logged holes were obtained on a N-S transect (1.6 km apart) on the spit (Miller et al., 2018) (Figs. 2.1, 2.3, and S1.1) in 2014 as part of the ongoing Coastal Plain Drilling Project. The three core holes (Figs. 2.4, 2.5, and S1.2) were designated Sandy Hook North Maintenance Yard (NMY) at 40°28.165' N, 74°00.297' W, Sandy Hook Salt Shed (SS) at 40°27.052' N, 73°59.793' W, and Sandy Hook South Maintenance Yard A (SMY-A) at 40° 25.998’ N, 73° 59.202’ W (Miller et al., 2018). Basic sediment and stratigraphic descriptions of the cores were done onsite and subsequently along with preliminary interpretations of the depositional environments (Stanford, 2015; Miller et al., 2018). Here we provide interpretations along with our new sedimentological data. More detail is provided in the results and discussion.

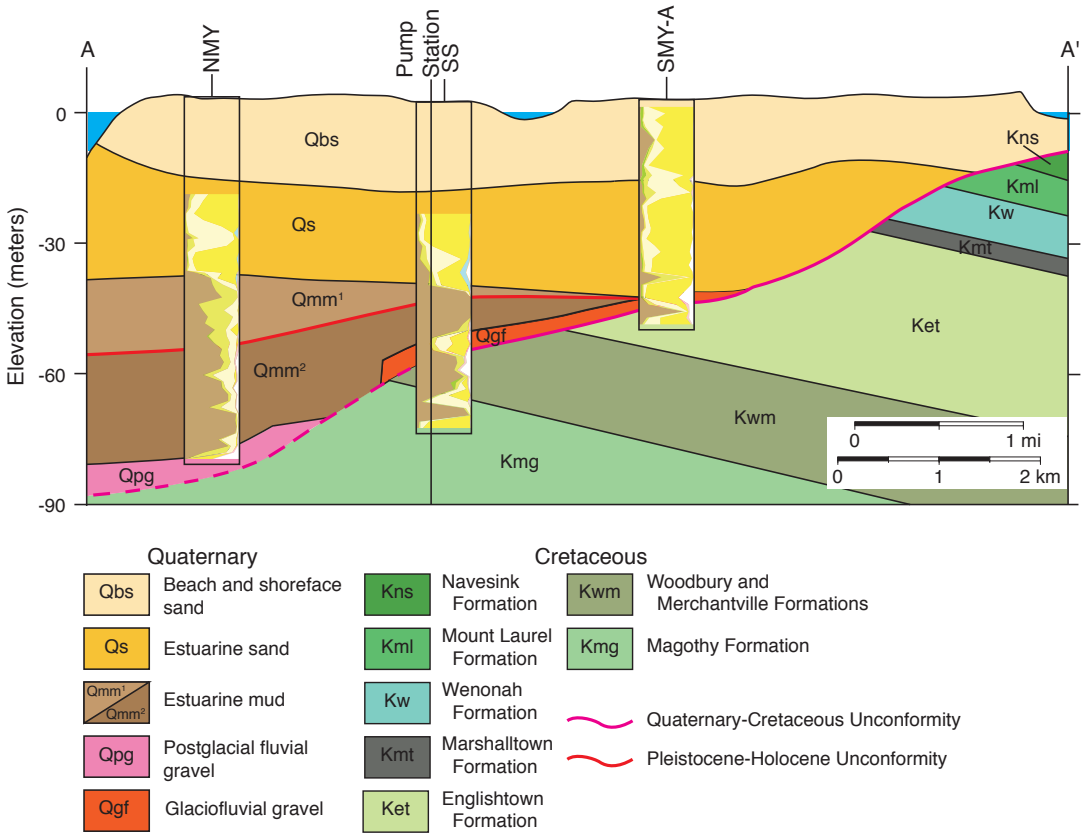

Figure 2.3: Schematic cross section of Sandy Hook. Cretaceous sediments are shades of green and Quaternary sediments are shades of yellow. The basal Quaternary postglacial outwash gravel deposit is shown in magenta. Unconformities are marked in red and the inferred glacial incised valley outline is magenta. The correlation between the gravels at the NMY and SS is based on elevation, provenance, and fluvial grade to outcropping terminal moraines in Staten Island, NY (Miller et al., 2018). We follow the nomenclatures of Stanford et al. (2015), and Minard (1969). Modified from Stanford et al. (2015). Cross-section location in Fig. 2.1. Inserts are cumulative percent plots from each of the cores, see Fig. 2.4 for explanation.

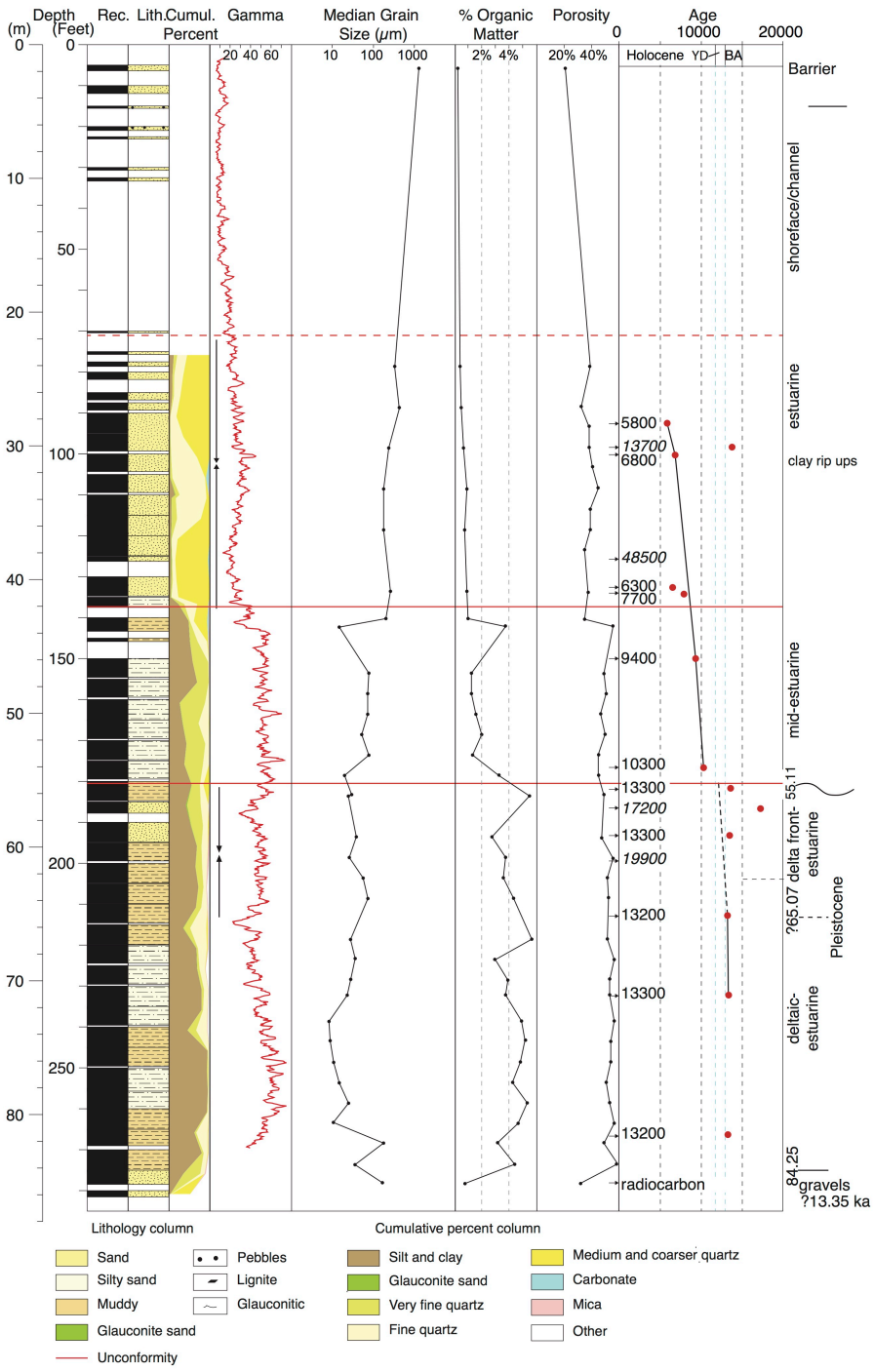

Figure 2.4: North Maintenance Yard (NMY) core properties including: recovery, blank spaces indicate unrecovered intervals; lithology; cumulative percent (see key); downhole gamma log; grain size (μm); percent organic matter; porosity; radiocarbon ages in cal years, errors for radiocarbon ages are smaller than data points.

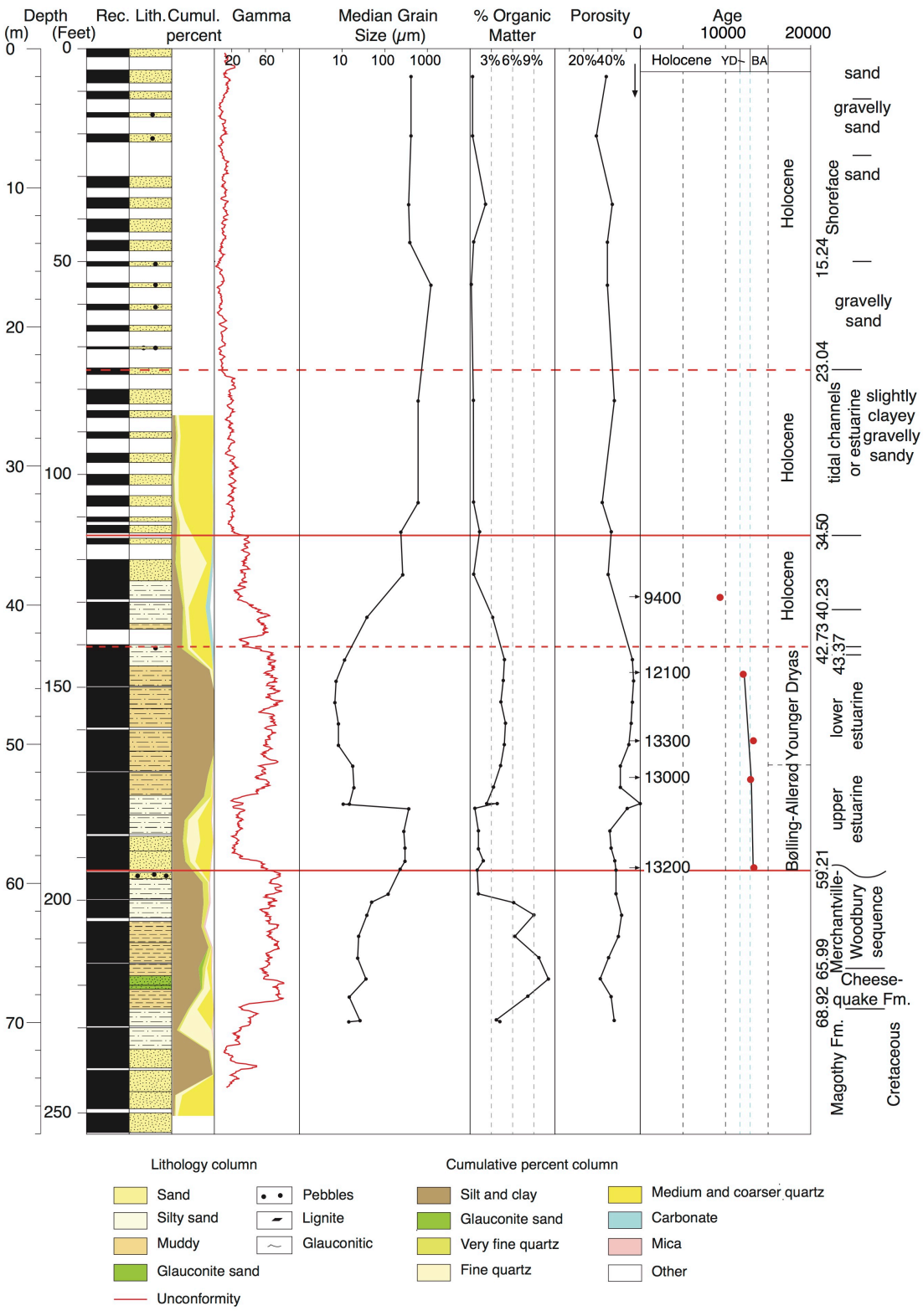

Figure 2.5: Salt Shed (SS) core properties including gamma, grain size, %OM, porosity, and age model. See caption for Fig. 2.4 for details.

2.3.2 Sedimentological Analyses

We measured percent organic matter (%OM), grain size, radiocarbon ages, and porosity. The lithologic descriptions were synthesized into general lithology columns (Miller et al., 2018). We also added quantitative and semi-quantitative lithology data. We quantitatively measured weight percent mud (<63 mm), fine sand (63-125 mm), and medium-coarse sand (>125 mm) in washed samples at ~1.5 m intervals. We semi-quantitatively estimated the abundance of glauconite, shells, and mica in the sand fraction (>63 mm) by splitting samples into aliquots and visually estimating percentages on a picking tray. The semi-quantitative and quantitative percent data were combined and presented as "Cumulative lithology" (Figs. 2.4, 2.5, and S1.1); these clearly show distinct trends in grain size and mineralogy and are particularly useful in showing fining upward and coarsening upward trends not readily observable in the descriptive lithology (e.g., Fig. 2.4). Where available, samples were taken at ~1.5 m intervals in all silts and ~3 m intervals in the sands, with a higher sample density in zones of rapid sedimentological changes (Table ST1.1). Percentage organic matter (OM) was measured using loss on ignition, following the method of Heiri et al. (2001), at the Benthic Ecology Lab at Rutgers Department of Marine and Coastal Sciences. The equivalent percent total organic carbon is ~1/2 %OM (Vereş, 2002). Grain size analysis was performed on the <3 mm size fraction using a Malvern Mastersizer 3000 at the Sea Level Research Lab at Rutgers Department of Marine and Coastal Sciences. Radiocarbon dates were acquired using mollusk shells and plant material. Porosity was measured volumetrically, using the mass of pore water to estimate pore volume and the volume of grains to estimate matrix

volume. More detailed methods for determining grain size, %OM, and porosity are available in the supplementary material.

2.3.3 Radiocarbon Ages and Age Models

The Quaternary chronology at Sandy Hook was established using radiocarbon dating, and an age model is developed and presented here in the Methods. The material dated was primarily plant matter, supplemented by shell fragments (Table 2.1). The shell fragments were mainly *Mercenaria mercenaria*, *Crassostrea virginica*, and indeterminate species. The plant material included wood fragments, peats, and roots; we picked fragile or fresh-looking organic matter that could not have been transported a long distance. All of the dated materials are from facies interpreted as estuarine and equivalent to the modern back bay environments (Raritan and Sandy Hook Bays). Although movement of material in these environments is possible, it does not suffer from the reworking issues of modern and Quaternary shelf and nearshore environments because of rapid deposition at the NMY. The samples were removed from the bulk substrate and adhered detrital material was removed from the sample under a microscope prior to radiocarbon dating.

Table 2.1: Radiocarbon Results. NM=Not Measured

Lab Number	Sample Depth (m)	Type	^{13}C (‰)	^{14}C Age	Median age (cal yr BP)	Midpoint (cal yr BP)	2 sigma error (from midpoint)	ΔR	ΔR Error	Material Dated
North Maintenance Yard:										
OS-115212	28.22	Plant/ Wood	-17.42	5020±25	5771	5775.5	115.5			Leaf and wood fragments
OS-115277	29.98	Plant/ Wood	-24.44	11900±30	13728	13683	100			Leaf and wood fragments
OS-115213	30.6	Plant/ Wood	-25.51	5990±25	6829	6820.5	71.5			Wood fragments
OS-115278	38.27	Plant/ Wood	-29.27	45200±800	48508	48475	1525			Wood fragment
OS-121907	40.44	Mollusk	NM	6050±20	6337	6338.5	132.5	130	60	Shell fragment (indeterminate)
OS-121999	40.9	Plant/ Wood	NM	6920±30	7744	7752.5	72.5			Wood fragment
OS-115450	45.74	Mollusk	-0.83	8830±40	9365	9347	164	130	60	Articulated *Mercenaria mercenaria* in shell bed
OS-115453	53.84	Mollusk	-0.87	9580±25	10302	10323.5	152.5	130	60	*Crassostrea virginica* shell
OS-121909	55.41	Plant/ Wood	NM	11500±50	13349	13354	102			Small piece of decayed organic matter
OS-115279	56.88	Plant/ Wood	-26.65	14150±35	17228	17242.5	182.5			Leaf, wood and charcoal fragments from thin peat unit
OS-121969	58.92	Plant/ Wood	NM	11500±65	13347	13335.5	130.5			Small piece of decayed organic matter
OS-121906	60.81	Plant/ Wood	NM	16500±95	19902	19886.5	270.5			Fragile detrital organic material
OS-115280	64.9	Plant/ Wood	-27.39	11350±30	13194	13196	85			Fragile detrital organic material
OS-115281	70.81	Plant/ Wood	-27.33	11450±30	13295	13297	89			Fragile detrital organic material
OS-121908	81.27	Plant/ Wood	NM	11300±50	13152	13165.5	96.5			Fragile detrital organic material
OS-115282	84.63	Plant/ Wood	-22.8	> 48000±3500						Wood fragments

Lab Number	Sample Depth (m)	Type	^{13}C (‰)	^{14}C Age	Median age (cal yr BP)	Midpoint (cal yr BP)	2 sigma error (from midpoint)	ΔR	ΔR Error	Material Dated
South Maintenance Yard:										
OS-121910	20.3	Mollusk	NM	4220±15	4136	4146.5	194.5	130	60	Articulated (indeterminate) mollusk in shell bed
OS-121911	23	Mollusk	NM	5450±20	5685	5712	141	130	60	Fragmented (indeterminate) mollusk in shell bed
Lab Number	Sample Depth (m)	Type	^{13}C (‰)	^{14}C Age	Median age (cal yr BP)	Midpoint (cal yr BP)	2 sigma error (from midpoint)	ΔR	ΔR Error	Material Dated
OS-115287	23.17	Plant/ Wood	-28.05	> 48000±0						Bulk peat
OS-115288	23.22	Plant/ Wood	-27.26	> 48000±2700						Bulk peat
Salt Shed:										
OS-115283	39.26	Plant/ Wood	NM	8350±25	9378	9376.5	77.5			Wood and plant debris
OS-115284	44.7	Plant/ Wood	NM	10300±30	12076	12161.5	213.5			Plant fragments and charcoal
OS-115285	52.23	Plant/ Wood	-27.24	11100±30	12991	12957.5	114.5			Wood and charcoal fragments
OS-115286	58.61	Plant/ Wood	-28.9	11400±30	13241	13228.5	78.5			Fragile detrital organic material
OS-122000	49.59	Plant/ Wood	NM	11450±55	13296	13290	133			Fragile detrital organic material

Samples were analyzed at the National Ocean Science Accelerator Mass Spectrometry (NOSAMS) Lab at Woods Hole Oceanographic Institute and the resulting radiocarbon ages calibrated to calendar years using IntCal13 or Marine13 for terrestrial and marine samples respectively (Reimer et al., 2013). A ΔR value of 130 ± 60 was applied to samples determined to form in the marine realm (i.e., marine mollusk and shell fragments) to account for local marine reservoir effects. This ΔR value was obtained from the closest known location available in Shark River, NJ (McNeely et al., 2006).

Age models for the NMY and SS sites were developed using radiocarbon dates and detailed core examination. From 55.11-84.25 m at the NMY, where radiocarbon dates were indistinguishable, we assumed constant deposition across the interval and used the earliest and latest dates (13,347 and 13,152 cal yrs BP) to establish our age model. These dates correlate the silts from 55.11-84.25 m with the Lake Iroquois outburst floods into the Hudson River Valley at 13,350 cal yr BP (Rayburn et al., 2005; Donnelly et al., 2005; Thieler et al., 2007; see discussion). We thus anchor the age model at 13,350 cal yr BP. Above this, we applied linear trend lines to the radiocarbon dates. At points of major (order-of-magnitude) change in deposition rates, we compared the depths of those changes to the depths of potential unconformities in the cores. Where there appeared to be an unconformity, we evaluated the age of the surface of discontinuity from above and below and compared the two ages. The process was repeated for the SS. Error bars were generated using Bacon Version 2.2 (Blaauw and Christen, 2011). More details of the method and the errors are provided in the supplementary material and Figs. S1.3-S1.4.

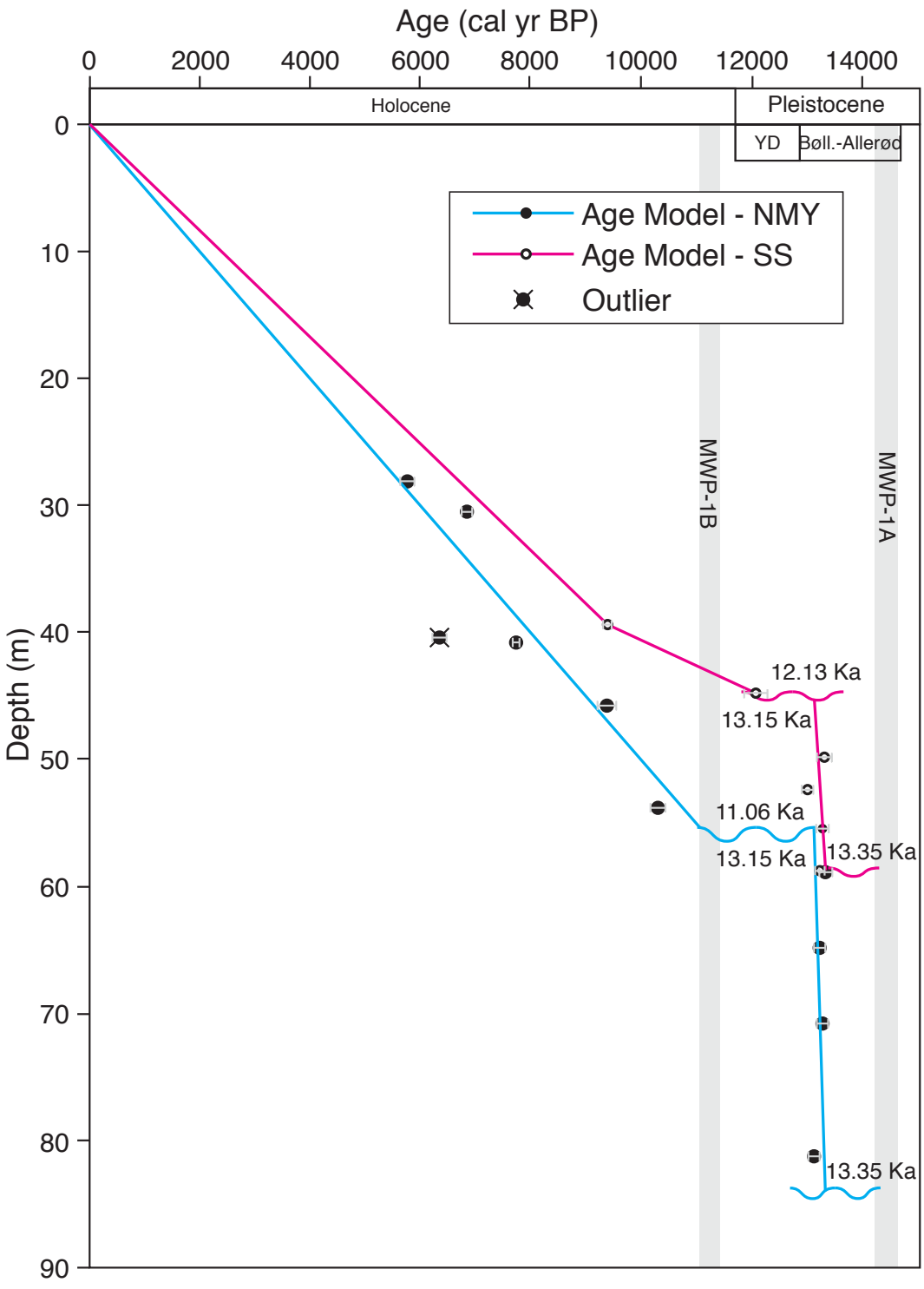

Figure 2.6: Age models for NMY and SS sites. Gray bars indicate 2σ uncertainties in the calibrated ages. Dates for events and time periods are from Rasmussen et al., 2006, Deschamps et al., 2012, and Abdul et al., 2016.

2.3.4 Numerical Modeling

Numerical modeling was employed to quantify the contribution from compaction of siliciclastic sediments to the rate of RSL rise. We sought to decompact the sediment column in discrete time steps. We derived an equation for porosity and used it to model changes in porosity through time and across changes in burial depth.

We tested multiple equations for porosity, changing both the variables of grain size, age, and burial depth controlling porosity and the form of the equation itself. Previously, Kominz et al. (2011) identified strong relationships between grain size and porosity, burial depth and porosity, and age and porosity. We used trends visible in our data set (porosity vs. grain size and porosity vs. depth/age) to design our equations.

Porosity data show a strong logarithmic dependency on median grain size (Fig. SF1.5). Porosities of sands are typically 40%. Quaternary sediments composed primarily of silts had a porosity of ~50-55%. This agrees with the divisions used by Kominz et al. (2011) when describing porosity as a function of depth or age. Even within the silt category (4-63μm), there was a strong dependency of porosity on grain size, with coarser sediments silts having a relatively lower porosity (Figs. 2.4-2.5). This may have been, in part, be partly an artifact of dewatering of coarse sections of the core before sampling. Dewatering was clearly visible in the coarsest sediments (coarse sands and gravels). There is also a trend of decreasing porosity in the silts with increasing burial depth/age (Fig. SF1.6), similar to the trend shown by Kominz et al. (2011). This is particularly evident when the Quaternary silts are compared to similar silts in the Cretaceous section underlying the deglacial sediments at the SS. The Cretaceous silts have a porosity of

~40% and are assumed to have been fully compacted. Unlike the results of Kominz et al. (2011), at Sandy Hook, porosity in sands (> 63 μm) did not exhibit a strong relationship with depth or age.

Kominz et al. (2011) also showed that there is greater potential for compaction in finer grained sediments, with young silts having a porosity of ~75% decreasing to a minimum of ~30%. Alternatively, sands start between 45-55% porosity and only decrease to 30% (Kominz et al., 2011). In the coarser Sandy Hook samples, there was very little change in porosity related to changes in burial depth or age that could not be attributed purely to changes in grain size. As such, we assumed that for the time scales seen on Sandy Hook, anything with a median grain size ≥63 μm was relatively incompressible.

Previously, Kominz et al. (2011) employed multiple equations to describe changes in porosity. They separated samples based on grain size into the categories clay, silt, and sand, with separate equations for each. Within each category, they derived two equations, one as a function of depth and another as a function of age. We sought to arrive at a single equation that described porosity (*por*) as a function of grain size in μm (ϕ), burial depth in meters (z), and age in years (a). Using the available data from all three drill sites, Equation 2.1 was created by regressing the natural logs of median grain size, burial depth, and age against the porosity values (r^2=0.672, Akaike Information Criterion (AIC; an estimator of the relative quality of models for a given set of data)=-115.8796);

$$\mathrm{por} = -0.0158\ln(\phi) - 0.0034\ln(z) - 0.0138\ln(a) + 0.7132 \quad (2.1)$$

To check our results, we performed a second regression that described porosity as a function of only median grain size and burial depth (Equation 2.2; r^2=0.348, AIC= -93.8796):

$$\mathrm{por} = -0.0315\ln(\phi) - 0.0350\ln(z) + 0.7385 \quad (2.2)$$

The inputs used to constrain these equations are available in the supplementary material (Table ST1.3). A data point taken from the modern upper Hudson River Estuary, with the approximated values of 70% porosity, 10 cm burial depth, and a median grain size of 33.5 μm, was used in the regression to constrain the younger, shallowly buried portion of the curve (Woodruff et al., 2001). Properties of the Cretaceous sediments at the SS site were used to constrain porosities in the older, more deeply buried layers. Due to erosion of overlying sediments, the maximum burial depths for the Cretaceous sediments are unknown and we estimated the values at ~100 m below their current burial depth. The equations do not take sorting into account. This is a potential source of error, as it likely influences the compressibility of the sediments. The average spread of grain sizes (10^{th} percentile to 90^{th} percentile) is ~130 μm at the NMY. The finer sediments tended to have a positive skewness in grain size.

Equations 2.1 and 2.2 were used in two separate versions of the numerical model to decompact Sandy Hook at the NMY. The models divide the sediment column into discrete layers and remove them sequentially from the top down, peeling away sediment and time. As each layer is removed, the underlying layers are each decompacted. This is accomplished by calculating the porosity of each layer before removing the top layer and then recalculating the porosity for each layer after the top layer is removed (changing both the burial depth and age of each underlying layer). The change in porosity is then

used to calculate a change in thickness for each layer. This process is repeated one layer at a time from the top down in order to account for changes in the thickness of the overlying sediments when calculating the new porosity of each

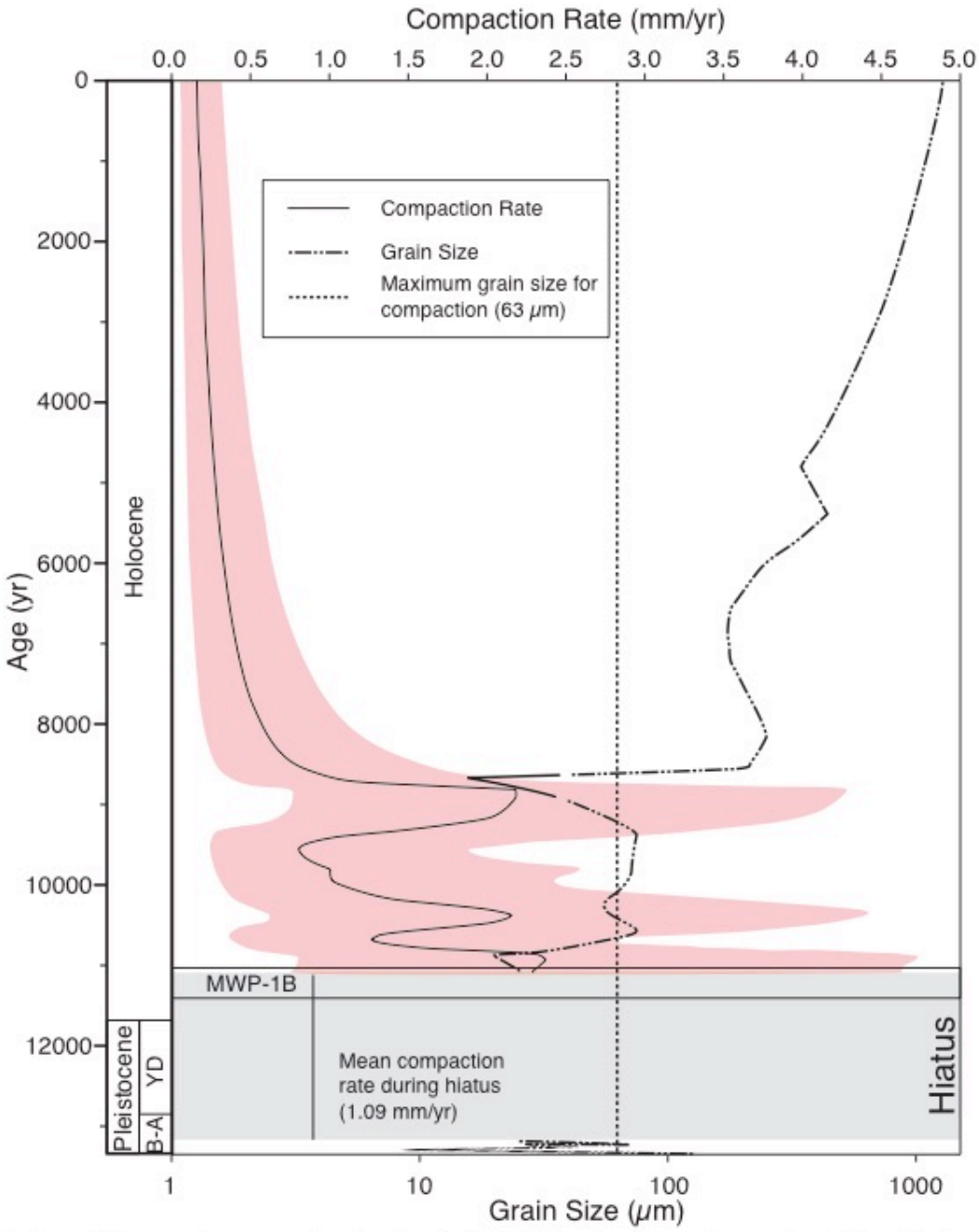

Figure 2.7: Modeled compaction rate at NMY through time, calculated using a porosity model (Equation 2.1) that is a function of median grain size, burial depth, and age at the NMY through time (solid red line) with 2σ error (red shaded area). Compaction rate at any given time is strongly influenced by the grain size of the sediments being deposited at that time (intermittent dashed line). Sediments with grain size above 63 μm (vertical dashed line) were assumed to be incompressible. B-A = Bølling-Allerød; YD = Younger Dryas. Dates for events and time periods are from Rasmussen et al., 2006, Deschamps et al., 2012, and Abdul et al., 2016.

underlying layer. In this way, each layer is able to respond to the removal of the top layer and thickness changes in each layer remaining above it. Because sands and larger particles are assumed to be relatively incompressible on the time scales and depths found in the NMY section, the model did not calculate porosity changes for sediments >63 μm (illustrated by the vertical line in Fig. 2.7). This layer-by-layer method makes it possible to see how the rate of compaction varies through time and provides a more realistic estimate of the modern contribution of compaction to the relative rate of sea-level rise at the Sandy Hook tide gauge. The model scripts are available in the supplementary material.

2.4 Results

2.4.1 Drilling Results

The cores were drilled to 86.9, 77.7, and 53.3 m at the NMY, SS, and SMY-A sites respectively (Figs. 2.4, 2.5, S1.1, and S1.2). At the NMY, adjacent to the tide gauge, we recovered 84+ m of Quaternary sands and silts overlying the inferred

Quaternary/Cretaceous contact. At the base, there was a thin (3+ m) layer of upper Pleistocene basal gravels interpreted as a post- glacial fluvial deposit (Figs, 2.3, 2.4; Stanford et al., 2015; Miller et al., 2018) overlain by thick (25 m) moderately organic-rich (up to 1.9%) sandy clayey silts. These sediments are a mix of thinly laminated planar, cross-laminated, and massive layers and were deposited in deltaic/estuarine environments (Figs. 2.3, 2.4; Stanford et al., 2015; Miller et al., 2018). This unit is separated from the overlying strata by a surface at 55.1 m marked by sediment disturbance and possibly erosion. The surface is overlain by 13 m of lower Holocene silty sands and sandy silts. At ~43.7 m, benthic foraminiferal (*Elphidium*, *Guttulina)*, diatoms, and sponge spicules have all been identified leading to the interpretation that these sediments were deposited in estuarine environments (Stanford et al., 2015; Miller et al., 2018). Above these silty sands are 20 m of middle Holocene medium to well-sorted sands containing frequent large wood fragments, lignite, and lithic fragments suggesting a strong riverine influence, supporting the interpretation of an estuarine deposit (Miller et al., 2018). Thick (18 m) upper Holocene gravelly sands overlie these sands. The coarse nature of the sediments indicates a higher energy environment supporting an upper shoreface interpretation for the environment of deposition (Stanford et al., 2015; Miller et al., 2018). The uppermost 5 m consists of moderately well-sorted medium to coarse sands (past 1000 years, Fig. 2.6) deposited contiguous with the modern prograding shoreface. Recovery was very poor in the uppermost ~24 m.

A similar succession of sediments occurs at the SS (Fig. 2.5) with the Cretaceous/Quaternary contact at 59.2 m. Here, more competent compacted glauconite silts of the Merchantville Formation and silty clays of the overlying Woodbury Formation

are overlain by ~4 m of unconsolidated uppermost Pleistocene sands and gravels interpreted as a glaciofluvial deposit covered by 16.5 m of alternating laminated and massive silts deposited in estuarine environments (Stanford et al., 2015; Miller et al., 2018). Above this are 8.2 m of Holocene medium to fine silty sands. This unit is overlain by 11.5 m of slightly clayey gravelly sands deposited in tidal channel or estuarine environments (Stanford et al., 2015; Miller et al., 2018). The uppermost 23 m consists of gravelly sands with some gravel concentrated into distinct layers representing deposition in shoreface environments contiguous with the modern spit. Recovery was limited though this interval.

At the SMY-A (Fig. SF1.2), the Quaternary/Cretaceous contact was at 47.1 m. It is overlain by 1.9 m of glaciofluvial gravel. The gravel is overlain by 22.2 m of slightly silty sands that are in turn overlain by 3.7 m of slightly silty fine sand deposited in estuarine environments overlain by 19.3 m of slightly silty medium to coarse sand deposited in tidal channel and shoreface environments.

2.4.2 Grain Sizes

Grain sizes across all three cores generally fine upward in the lower section of Quaternary sediments and coarsen upward in the upper section (Table ST1.5). At the NMY (Fig. 2.4), sediments generally fine upward from 84 to 72.5 m, with median grain sizes transitioning from gravels at the base to ~8 μm fine silt. Above 72.5 m, the sediments coarsen upward to ~70 μm (median grain size) at 63.5 m. Grain sizes then decrease to ~20 μm silts at 54.5 m. Above 54.5 m, the sediments coarsen upward to coarse sand (1.2 mm) and gravels in the uppermost 20 m. There is a fine grained (~15 μm) bed at 43.3 m. The SS (Fig. 2.5) shows similar trends in the Quaternary section with

a coarse basal section of ~300 μm sands fining upward to ~7 μm at 45 m. The section then coarsens to coarse sands (~600 μm) and gravels around 33 m. The uppermost 30 m at the SS is composed primarily of medium (350-400 μm) sands. The entire Quaternary section at the SMY-A (Fig. SF1.2) consists of medium sands with median values between 250 and 450 μm, with a thin interval of coarse silts and fine sands (48-141 μm) from 19.2-23 m.

2.4.3 Percent Organic Matter

Organic matter content in the Quaternary sections (Figs. 2.4-2.5, S1.2, Table ST1.6) is low, with values of ~0.4-1.5% and an average of ~1% for most sands and ~1-6% with an average of ~4% in the silts. As grain size decreases, the %OM typically increases. Aside from thin (< ~1 mm) laminae, the organic material is typically suspended in a siliciclastic matrix. At the NMY, %OM decreases upsection from peak values of ~5% in the upper Pleistocene and lower Holocene silts. The %OM reaches 1.2-1.9% between 53-43 m before decreasing to values of ~0.9-0.2% in the uppermost 43 m. At the SS site, the basal Quaternary section from 59.21 to 54.40 m consists of between 0.6 and 1.7 % OM. Above 54.40 m, the %OM increases to 4.9% at 48.31 m before decreasing to 0.5 % at 32.46 m. The uppermost 32.46 m have %OM values generally ≤0.5% with intervals of 1.3 and 2.2 % at 34.56 and 11.12 m, respectively. Similar to grain size, the SMY-A shows much less variability with samples throughout the section generally containing between 0.3 and 0.5 % organic carbon.

2.4.4 Radiocarbon Ages and Age Models

Radiocarbon age estimates (Table 2.1) indicate high mean sedimentation rates of 400-500 cm/kyr during the Holocene (Fig. 2.6). At the base of the NMY there are 30 m

of sediment with 5 radiocarbon ages that range from 13,350-13,150 cal yrs BP. The best estimate is that these silts were deposited in < 200 years with a mean sedimentation rate of 15,000 cm/kyr and are associated with the Lake Iroquois outburst floods (Rayburn et al., 2005; Donnelly et al., 2005; Thieler et al., 2007). We interpret the previously described surface at 55.1 m, directly above these rapidly emplaced sediments to be an unconformity. Based on our age model, this surface represents a hiatus from 13,150-11,060 cal yrs BP. Above the unconformity, the sedimentation rate decreases to 500 cm/kyr.

At the SS, there is a similar section of sediments at the base of the Quaternary with radiocarbon ages between 13,300 and 13,000 cal yrs BP, that we interpret to be the same time interval represented by the 30 m package of sediments at the base of the NMY. This results in a mean sedimentation rate of 7,200 cm/kyr. Above this unit, while there is no obvious surface visible in the lithology as seen at the NMY, we infer an unconformity at 44.8 m, which, based on our age model, marks a hiatus from 13,150 to 12,130 cal yrs. This is supported by the rapid shift in mean sedimentation rates from 7,200 cm/kyr below to 200 cm/kyr from 39.3 to 44.8 m and then 420 cm/kyr in the uppermost 39.3 m. Whereas age resolution increases with depth at the NMY and SS, poor organic preservation limits age control on the SMY-A core precluding any further analysis.

2.4.5 Porosity

At the NMY site, porosity generally tracks grain size (Fig. 2.4, Table ST1.7) increasing from 31.2% at the base to between 50 and 60% from 83.37 to 60.55 m. Porosity decreases to between 34.9 and 38.6% from 60.55 to 34.61 m before increasing to 44.6% at 33.09 m. Values then decrease to 20.2% by 1.75 m.

At the SS site (Fig. 2.5), porosities are generally lower with a basal porosity of 41.9% at 58.79 m in the upper Pleistocene. Values then increase to 59.0% at 54.05 m before decreasing to 45.9% at 51.37 m. Porosity then increases to 55.1% at 45.27 m, then porosity decreases to between ~20 and ~30% for the uppermost 45.27 m.

Porosities at the SMY-A (Fig. SF1.2) show little variability with values between 46.5 and 31.1% for the entire section. There are no strong trends, rather the porosity seems fairly steady between 36 and 38% with several excursions.

The error associated with the porosity measurements is generally low ≤4%. Error increases with grain size. In coarser samples (>63 μm median grain size) the average error (1$\boldsymbol{\sigma}$) is ~4% with a maximum of ~8% in some of the coarsest samples. For finer samples (<63μm) the average error (1$\boldsymbol{\sigma}$) is closer to 1%. The error is sampled in the numerical model to define the error in the model results.

2.5 Discussion

Local processes must be invoked to explain the 0.9±0.5 mm/yr additional, non-GIA-related RSL rise at Sandy Hook relative to The Battery. The potential contributors to the locally high relative rate of sea-level rise include compaction of organic material or peats, compaction of inorganic silts and clays, and anthropogenic compaction resulting from groundwater removal. This study revealed that compaction of Quaternary silts and clays and groundwater removal are the two primary factors controlling the localized sea-level change at Sandy Hook. While organic material has a negligible impact on the rate of RSL rise at Sandy Hook, compaction of inorganic Quaternary sediments is a contributor, and there is evidence that groundwater extraction may also be a key factor.

2.5.1 Depositional Environments

The majority of the non-anthropogenic compaction at Sandy Hook is derived from the relatively young (<13,350 cal yr BP) sediments (Fig. 2.3). We base the following history primarily upon results from the NMY site, though the general trends are similar at the SS site. The Quaternary sediments lie above an unconformity separating Cretaceous and uppermost Pleistocene strata. The most striking feature of the sedimentary record under Sandy Hook is the thin (+3 m) layer of gravels. Above the gravels there is ~25 m of sediment deposited rapidly between 13,350-13,150 cal yrs BP. The thick, rapidly deposited sediment unit drives the compaction (Fig. 2.7) and our interpretation of the deglacial history. Based on the radiocarbon evidence from the overlying 25 m of silts, and the timing of the incision of the Raritan and Hudson shelf valleys, which border Sandy Hook (Stanford, 2010), we interpret the 3+ m of basal gravels to be post-glacial fluvial deposits. The ~25 m of overlying postglacial silts (Qmm^2, Fig. 2.3) were then deposited rapidly (13,350-13,150 cal yrs BP). Given the close match of radiocarbon ages, we suggest that the silts are the result of multiple floods that discharged from Glacial Lake Iroquois and down the Hudson Valley at that time (Rayburn et al., 2005; Donnelly et al., 2005; Thieler et al., 2007). Based on the presence of occasional cross laminations and wavy bedding, the sediments were deposited in an estuarine or deltaic environment. As the sediment saturated waters of the Hudson River reached the mid to lower estuarine environment near modern day Sandy Hook, there was likely rapid deposition as seen in the modern Hudson Estuary (Traykovski et al., 2004). Above these postglacial silts, is an unconformity that, based on our age model, marks a hiatus from 13,150-11,060 cal yrs. Overlying the unconformity are 13 m (11,060-8,600

cal yrs) of mid-estuarine silty sands. Above this, 20 m (8,600-4,600 cal yrs) of estuarine sediments coarsen upward from silty sands to sands. This unit is overlain by 18 m (4,600-1,000 cal yrs) of sands interpreted to be shoreface and channel sands. The uppermost 5 m is composed of coarse sand deposits of the modern (1,000 cal yr BP-present) barrier island.

2.5.2 Minimal Organic Compaction

Previous studies of organic-rich Quaternary nearshore deposits in England and the U.S. Gulf of Mexico (Horton and Shennan, 2009; Törnqvist et al., 2008) have shown that compaction of organic rich layers could make a significant contribution to local subsidence. During and after drilling, the cores were examined for thick peats, deposits that could contribute significantly to the subsidence at Sandy Hook. While there are thin, millimeter thick organic-rich laminae, there are no evident organic zones and the OM values are relatively low (< 2%). The error on the measurements (<3%) is negligible (see supplement for uncertainty estimation). Even at the high end of the error at the NMY, there is insufficient organic material for the sediments to be classified as carbonaceous. Furthermore, the dispersed nature of the organics and lack of thick, concentrated bands of peats suggest that the compaction of the organic material would be dependent on the compaction of the siliciclastic matrix. The %OM values measured in this study (0.4-1.9%), are within the range measured in modern estuaries (~1-10%; Thornton and McManus, 1994; Andrews et al., 1998). This suggests that the organic material is not undergoing decomposition. Based on this, we conclude that there is insufficient organic material present and it is not concentrated enough to be a significant contributor to the subsidence at Sandy Hook.

2.5.3 Siliciclastic Compaction

Compaction of siliciclastic sediment is another potential contributor to Sandy Hook's subsidence history. Sandy Hook, particularly near the tide gauge, is underlain by a thick (85+ m) Quaternary section, the lower ~40 m of which is dominantly silts with the potential to compact nearly 50% due to porosity loss through time and burial (Kominz et al., 2011).

Our regression models indicate that the rate at which a unit of silt compacts decays exponentially through time as the unit approaches its minimum porosity (~40% based on the Cretaceous section at the SS site). Without the addition of new silts, the rate of compaction in the entire sediment column would eventually reach ~0 mm/yr. Note that this has been the case at the NMY since ~8,500 cal yr BP, when the deposition of mud ceased; our forward model indicates that the rate of compaction has decayed since this time to the modern rate (Fig. 2.7). Due to the thick Quaternary section, the numerical model of porosity as a function of grain size, burial depth, and age (Equation 2.1) yields an average 20th century compaction rate of 0.16 mm/yr (90% C.I. 0.06-0.32) that can be attributed to the natural compaction of the siliciclastic sediments underlying the northern portion of Sandy Hook. When porosity is modeled only as a function of grain size and burial depth (Equation 2.2), the rate is 0.19 mm/yr (90% C.I. 0.03-0.39; Fig. SF1.7). Based on the lower AIC and higher r^2 values of Equation 2.1 indicate that the Equation 2.1 model is preferred. The 90% C.I. of 0.06 to 0.32 mm/yr from Equation 2.1 ranges from nearly zero impact to ~1/3 of the local rate of sea-level rise at Sandy Hook. When the rate of compaction is subtracted from the local rate of sea-level rise, the remaining

rate is 0.7 mm/yr (90% C.I. 0.3-1.2). This suggests that there is still a significant source of local sea-level rise that is unaccounted for.

During deposition following the glacial outburst, rates of compaction were on the order of 10s of mm/yr, peaking between ~40 and ~80 mm/yr. Compaction during this period was high due to rapid (15,000 cm/kyr) deposition supplying a large amount of highly compressible silts (Fig. 2.7). In addition to supplying silts, the high sedimentation rate also means that the sediments were rapidly buried. The rate is further augmented by the ability of deposited silts to quickly lose porosity after deposition (Woodruff et al., 2001).

The modeled rates of compaction include natural compaction and compaction due to groundwater pumping from the Quaternary units we sampled. Historical records show that groundwater extraction from the Quaternary sediments at Sandy Hook began in the 1890s. Any drawdown in the groundwater levels resulting from that pumping would have induced compaction and affect our porosity measurements. However, our model shows that the majority of natural compaction occurred during the early Holocene and has decayed exponentially to present (Fig. 2.7). This concentrates any model uncertainty due to porosity uncertainties in the early portion of the record, resulting in a minimal influence on the modeled 20th century rate. Also, most groundwater pumping effects would be expected from the much more heavily pumped Cretaceous aquifers (see Section 5.4 below). While groundwater effects may influence the modeled ~0.16 mm/yr Quaternary compaction, the dominant effect controlling the modeled 20th century compaction rate is the compaction of the deglacial silts (Fig. 2.7).

Poor recovery in the uppermost ~24 m at the NMY adds some uncertainty to the numerical model, particularly in the recent portion of the model. However, poor recovery is associated with coarse sands as indicated by the gamma log (Fig. 2.4), less cohesive sediments that would be excluded from the model. Also, the log signatures in the unrecovered intervals indicate coarse sediments and shows that there are no significant lithologic changes that would have been missed in the unrecovered intervals, lending additional support that the unrecovered intervals likely had a negligible impact on the rate of compaction at Sandy Hook.

2.5.4 Groundwater Withdrawal

With a 20th century natural compaction rate of 0.16 mm/yr (90% C.I. 0.06-0.32) for siliciclastic sediments, there is 0.7 mm/yr (90% C.I. 0.3-1.2 mm/yr) of subsidence at Sandy Hook that is unaccounted for. We hypothesize that groundwater withdrawal is potentially a leading cause of this subsidence, making it the dominant local contributor after GIA. Land subsidence due to groundwater pumping in confined aquifers is a well-documented phenomenon of the 20th century (see review in Galloway et al. 1999; Sun et al., 1999; Galloway and Burby, 2011; Galloway and Sneed, 2013). Pertaining to Sandy Hook, historical records of local groundwater depletion and previous regional groundwater models support this hypothesis, suggesting significant drawdown of the groundwater level underlying Sandy Hook (dePaul et al., 2008).

Regarding local effects, the Sandy Hook tide gauge is located ~2 km from the Ft. Hancock Pumping Station, adjacent to the SS site (Fig. 2.1). The pumping station is the sole water source for facilities located on Sandy Hook. It has also been the site of many wells servicing Fort Hancock over the years. Construction of Fort Hancock began in 1896

at which time 36 artesian wells were installed to supply 150,000 gallons of water per day (Bearss, 1981). During installation of one well point, the drillers encountered a pocket of pressurized gas at ~45 m (~151 ft) that they described as carbonic acid. The resulting ~15 m (50 ft) geyser of sand and water lasted for more than 5 hours. Once the artesian wells were established, they began to show signs of depletion by 1905 and most were exhausted by 1907 (Bearss, 1981). This evidence shows that even before the base reached its largest population during World War II (Fig. 2.8), Fort Hancock caused a significant drawdown of the local groundwater level.

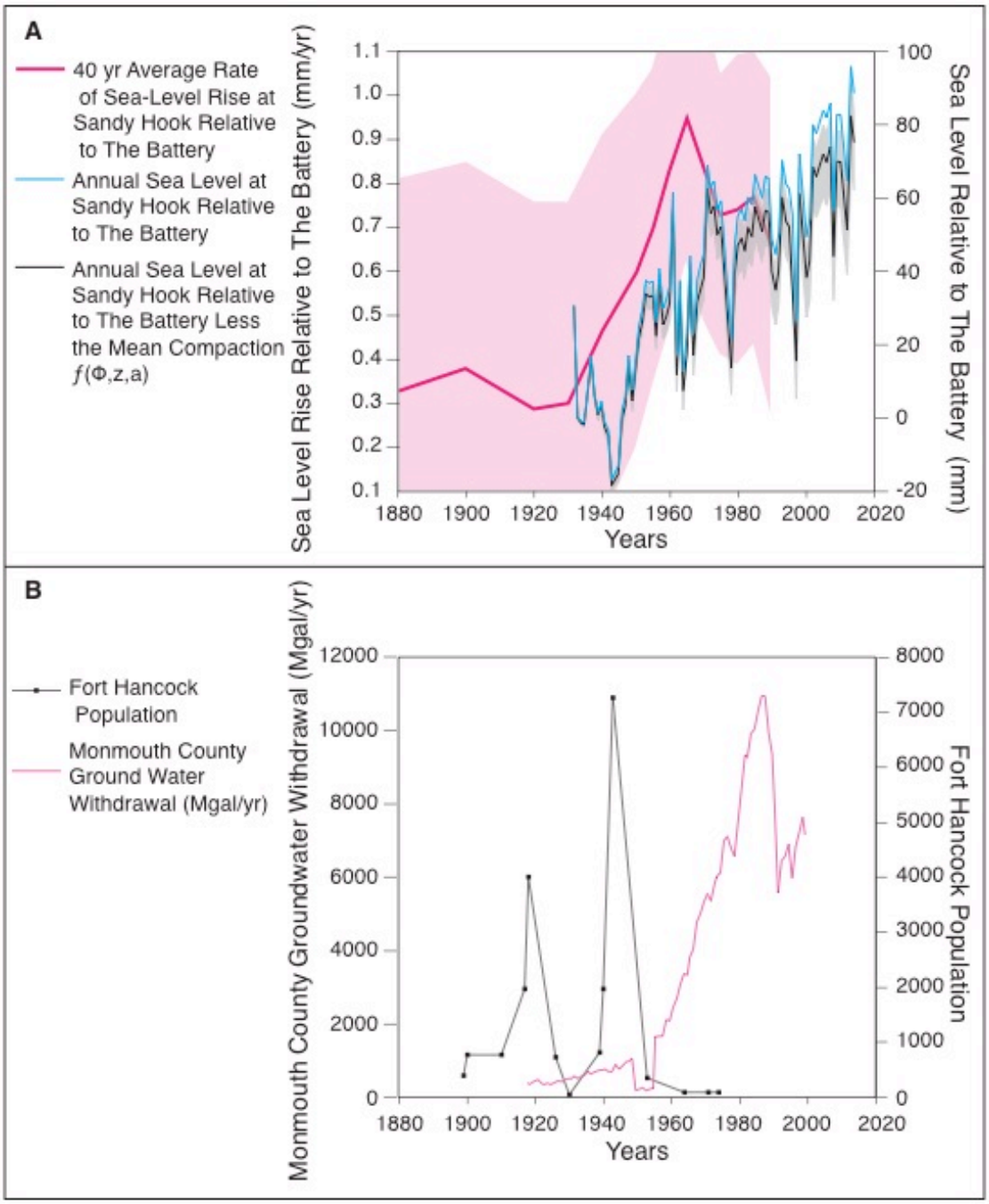

Figure 2.8: Sea Level vs. Groundwater Withdrawal. A: Modeled 40 yr average rate of sea-level rise at Sandy Hook minus the rate at The Battery with 2σ uncertainty (pink; see supplementary section S1.9 for method), Annual sea level at Sandy Hook minus The Battery (cyan) and the sea level at Sandy Hook minus The Battery and modeled compaction with 2σ uncertainty (black). B: The rate of regional groundwater withdrawal

for Monmouth County (magenta) and the local population of Ft. Hancock (black), a proxy for groundwater withdrawal (Bearss, 1981; T. Hoffman personal communication; Hoffman, T., An Old Army Town; Holgate et al., 2013; Permanent Service for Mean Sea Level, 2016; J. Shourds, personal communication). The population of Fort Hancock, a proxy for the local groundwater withdrawal, is shown with the regional groundwater pumpage from Monmouth County southwest of Sandy Hook (Fig. 2.8). From the onset of significant withdrawal on the mainland in the early 20th century to 1980 aquifers underlying the northern portion of Sandy Hook experienced a cumulative ~9-18 m (30-60 ft) decrease in water level (Fig. 2.9) (dePaul et al., 2008).

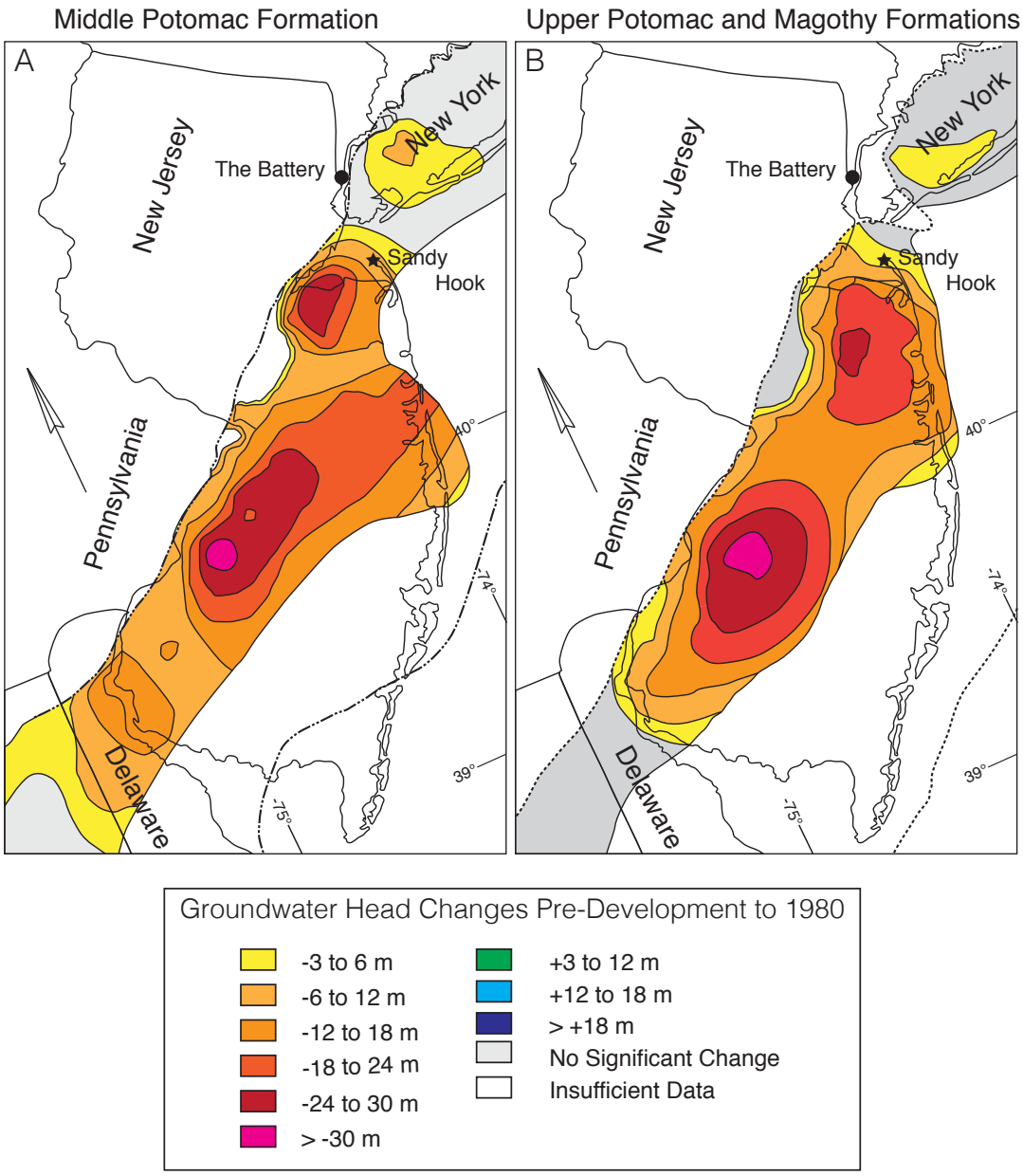

Figure 2.9: Estimated groundwater level changes pre-development to 1980. A: The Middle Potomac Formation, B: The Upper Potomac and Magothy Formations. Modified from dePaul et al. (2008).

The period between 1980-2000 saw no significant change in the water levels in the underlying aquifers, because withdrawals were curtailed beginning in 1990 to prevent saltwater intrusion (dePaul et al., 2008). The overlapping local and regional drawdowns

are likely sufficient to reduce pore fluid pressure in the underlying strata, thereby allowing compaction and subsidence (Holzer and Galloway, 2005). While there does appear to be a link between the timing of changes in the local rate of RSL rise at Sandy Hook and the events in the history of groundwater withdrawal (Fig. 2.8), it is not straightforward. The disconnect may be due to a lag between the drawdown of groundwater and the compaction of fine grained sediments in the confining units above and below the aquifers as documented by Sneed and Galloway (2000). Furthermore, the 40 year average for the rate of sea-level rise at Sandy Hook relative to the Battery (Fig. 2.8A) also introduces a lag. Future groundwater modeling will attempt to test this hypothesis and provide insight into the relative contributions of local and regional groundwater withdrawal to the subsidence at Sandy Hook.

Our quantification of contributions from global mean, regional (especially GIA), and local (compaction due to natural and anthropogenic change) effects can be applied to other regions using the principles and compaction model developed here. Whereas the greatest uncertainty in planning for regional and local projections is the global response of thermal expansion and continental ice sheets (Kopp et al., 2014, 2017), we show that not only can we quantify the regional GIA response (Kopp, 2013; Miller et al., 2013; Kopp et al., 2016), we can also quantify contributions from natural compaction and attribute the remainder to compaction induced by groundwater withdrawal. For example, our approach can be applied used to make predictions for the entire Mid-Atlantic U.S. region based on the local Quaternary geology and local/regional groundwater withdrawal rates. By considering cones of depression (e.g., Fig. 2.9; DePaul et al., 2008) and considering groundwater extraction rates, we predict that lower rates of local subsidence

would be experienced from Cape May, NJ south through much of the Delmarva peninsula.

2.6 Conclusion

After accounting for GIA, tide gauge records from Sandy Hook, NJ and The Battery, NY, show a 0.9±0.5 mm/yr difference in the 20th century rates of sea-level rise experienced at two locations within 26 km of each other. Based on the low organic matter in our corehole transect, we eliminate compaction of organic material as a significant contributor at Sandy Hook. Based on our porosity, grain size, and age constraints, we model natural subsidence due to compaction as 0.16 mm/yr (90% C.I. 0.06-0.32 mm/yr). The remaining 0.7 mm/yr (90% C.I. 0.3-1.2 mm/yr) is likely due to anthropogenic groundwater withdrawal. Future work will attempt to constrain the relative contributions of both regional and local groundwater withdrawal to Sandy Hook's subsidence history.

2.7 Acknowledgements

We thank G. Ashley for numerous insightful discussions and the use of her lab for sample processing, I. Hong and T. Dura for their help and instruction when running the Malvern Mastersizer 3000, C. Fuller and G. Taghon at the Benthic Ecology Lab for their assistance with LOI measurements, M. Kominz for insights into modeling decompaction and changes in porosity, J. Shourds at the U.S. Geological Survey for enlightening insights and information on groundwater usage in the New Jersey Coastal Plain, A. Fiore at the U.S. Geological Survey for insightful discussions and information on historical wells at Ft. Hancock, and T. Hoffman at the National Park Service for help when researching historic groundwater extraction and base population at Ft. Hancock. We would like to acknowledge three anonymous reviewers and the editorial oversight of I.

Hendy whose contributions helped to improve the paper. Drilling was supported by the New Jersey Geological and Water Survey and NSF Grants OCE14-63759 and OCE-1154379 (Miller). This publication is the result of research sponsored by the New Jersey Sea Grant Consortium (NJSGC) with funds from the National Oceanographic and Atmospheric Administration (NOAA) Office of Sea Grant, U.S. Department of Commerce, under NOAA grant number NA14OAR4170085. It was also supported by the Nation Science Foundation (OCE-1458904 to Horton and Kopp). The statements, findings, conclusions, and recommendations are those of the authors and do not necessarily reflect the views of the funding agencies. NJSGC Publication Number: NJSG-17-927 and Earth Observatory of Singapore Contribution 171.

2.8 References

Abdul, N.A., Mortlock, R.A., Wright, J.D., and Fairbanks, R.G., 2016. Younger Dryas sea level and meltwater pulse 1B recorded in Barbados reef crest coral *Acropora palmata*. Paleoceanography v. 31, is. 2, p. 330-344.

Andrews, J.E., Greenaway, A.M., and Dennis, P.F., 1998. Combined carbon isotope and C/N ratios as indicators of source and fate of organic matter in a poorly flushed tropical estuary: Hunts Bay, Kingston Harbor, Jamaica. Estuarine, Coastal and Shelf Science v. 46, n. 5, p. 743-756.

Bearss, E.C., 1981. Historic resource study Fort Hancock 1895-1948: Gateway National Recreation Center New York/New Jersey. National Park Service, Denver, Colorado.

Blaauw, M., Christen, J.A., 2011. Flexible paleoclimate age-depth models using an autoregressive gamma process. Bayesian Analysis v. 6, p. 457-474.

Brian, M.J., Kemp, A.C., Horton, B.P., Culver, S.J., Parnell, A.C., Cahill, N., 2015. Quantifying the contribution of sediment compaction to late Holocene salt-marsh sea-level reconstructions, North Carolina, USA. Quaternary Research v. 83, n. 1, p. 41-51.

Chen, X., Zhang, X., Church, J.A., Watson, C.S., King, M.A., Monselesan, D., Legresy, B., and Harig, C., 2017. The increasing rate of global mean sea-level rise during 1993-2014. Nature Climate Change v. 7, n. 7, p. 492-495.

Church, J.A., and White., N.J., 2011. Sea-level rise from the late 19th to the early 21st century. Surveys in Geophysics v. 32, n.4-5, p. 585-602.

Clark J.A., Farrell, W.E., and Peltier, W.R., 1978. Global changes in postglacial sea level: A numerical calculation. Quaternary Research v. 9, p. 265-287.

Cronin, T.M., 2012. Rapid sea-level rise. Quaternary Science Reviews, v. 56, p. 11-30.

Dangendorf, S., Marco, M., Wöppelmann, G., Conrad, C. P., Frederikse, T., and Riva, R., 2017. Reassessment of 20th century global mean sea level rise. PNAS v. 114, n. 23, p. 5946-5951.

dePaul, V.T., Rice, D.E., and Zapecza, O.S., 2008. Water-level changes in aquifers of the Atlantic Coastal Plain, predevelopment to 2000. U.S. Geological Survey Scientific Investigations Report 2007-5247, p 1-88.

Deschamps, P., Durand, N., Bard, E., Hamelin, B., Camoin, G., Thomas, A.L., Henderson, G.M., Okuno, J., and Yokoyama, Y., 2012. Ice-sheet collapse and sea-level rise at the Bølling warming 14,600 years ago. Nature v. 483, p. 559-564.

Donnelly, J.P., Driscoll, N.W., Uchupi, E., Keigwin, L.D., Schwab, W.C., Thieler, E.R., and Swift, S.A., 2005. Catastrophic meltwater discharge down the Hudson Valley: a potential trigger for the Intra-Allerød cold period. Geology v. 33, no. 2, p. 89-92.

Galloway D., D.R. Jones, and S.E. Ingebritsen, 1999. Land Subsidence in the United States. U.S. Geological Survey Circular 1182. https://pubs.usgs.gov/circ/circ1182/

Galloway D., and J. Burbey, 2011. Review: Regional land subsidence accompanying groundwater extraction. Hydrogeology Journal v.19, p. 1459–1486.

Galloway D., and M. Sneed, 2013. Analysis and simulation of regional subsidence accompanying groundwater abstraction and compaction of susceptible aquifer systems in the USA. Boletín de la Sociedad Geológica Mexicana v. 65, n. 1, p. 123-136.

Gurnis, M., 1990. Bounds on global dynamic topography from Phanerozoic flooding of continental platforms. Nature v. 344, p. 754-756.

Hay, C.C., Morrow, E., Kopp, R.E., and Mitrovica, J.X., 2015. Probabilistic reanalysis of twentieth-century sea-level rise. Nature v. 517, p. 481-484.

Heiri, O., Lotter A.F., and Lemcke, G., 2001. Loss on ignition as a method for estimating organic and carbonate content in sediments: reproducibility and comparability of results. Journal of Paleolimnology v. 25, p. 101-110.

Hoffman, T.J.. An old army town. https://www.nps.gov/gate/learn/historyculture/upload/old_army_town.pdf [17 May, 2016]

Holgate, S.J., Matthes, A., Woodworth, P.L., Rickards, L.J., Tamisiea, M.E., Bradshaw, E., Foden, P.R., Gordon, K.M., Juvrejeva, S., Pugh, J., 2013. New data systems and products at the permanent service for mean sea level. Journal of Coastal Research v. 29, n. 3, p. 493-504.

Holzer, T.L. and Galloway, D.L., 2005. Impacts of land subsidence caused by withdrawal of underground fluids in the United States. in Ehlen, J., Haneberg, W.C., and Larson, R.A., eds., Humans as Geologic Agents: Boulder, Colorado, Geological Society of America Reviews in Engineering Geology *16*, 87-99. doi:10.1130/2005.4016(08)

Horton, B.P., and Shennan, I., 2009. Compaction of Holocene strata and the implications for relative sea-level change on the east coast of England. Geology v. 37, n. 12, p. 1083-1086.

Jevrejeva, S., Moore, J.C., Grinsted, A., and Woodworth, P.L., 2008. Recent global sea level acceleration started over 200 years ago? Geophysical Research Letters v. 35, n. 8.

Kemp, A.C., Horton, B.P., Donnelly, J.P., Mann, M.E., Vermeer, Martin, and Rahmstorf, S., 2011. Climate related sea-level variations over the past two millennia. Proceedings of the National Academy of Sciences v. 108, n. 27, p. 11017-11022.

Kominz, M.A., Browning, J.V., Miller, K.G., Sugarman, P. J., Mizintseva, S., and Scotese, C.R., 2008. Late Cretaceous to Miocene sea‐level estimates from the New Jersey and Delaware coastal plain coreholes: An error analysis. Basin Research v. 20, n. 2, p. 211-226.

Kominz, M. A., Paterson, K., and Odette, D., 2011. Lithology dependence of porosity in slope and deep marine sediments. Journal of Sedimentary Research v. 81, p. 730-742.

Kopp, R.E., 2013. Does the mid-Atlantic United States sea-level acceleration hot spot reflect ocean dynamic variability? Geophysical Research Letters v. 40, p. 3981-3985.

Kopp, R.E., Hay, C.C., Little, C.M., and Mitrovica, J.X., 2015. Geographic variability of sea-level change. Current Climate Change Reports v. 1, p. 192-204.

Kopp R.E., Kemp, A.C., Bittermann, K., Horton, B.P., Donnelly, J.P., Gehrels, W.R., Hay, C.C., Mitrovica, J.X., Morrow, E.D., and Rahmstorf, 2016. Temperature-driven global sea-level variability in the common era. Proceedings of the National Academy of Sciences v. 113, n. 11, E1434-E1441.

Kopp, R.E., Deconto, R.M., Bader, D.A., Horton, R.M., Hay, C.C., Kulp, S., Oppenheimer, M., Pllard, D., and Strauss, B.H., 2017. Implications of Antarctic ice-cliff collapse and ice-shelf hydrofracturing mechanisms for sea-level projections. ArXiv e-prints. eprint: 1704.05597.

Lyttle, P.T., and Epstein, J.B., 1987. Geologic map of the Newark 1°x2° quadrangle, New Jersey, Pennsylvania, and New York. U.S. Geological Survey Miscellaneous Investigations Series 1-1715.

McNeely R., Dyke A. S., and Southon J. R., 2006. Canadian marine reservoir ages, preliminary data assessment. Geological Survey Canada Open File 5049, pp. 3.

Miller K.G., Kopp, R.E., Horton, B.P., Browning, J.V., and Kemp, A.C., 2013. A geological perspective on sea-level rise and its impacts along the U.S. Mid-Atlantic Coast. Earth's Future v. 1, n. 1, p. 3-18.

Minard, J. P., 1969. Geology of the Sandy Hook quadrangle in Monmouth County, New Jersey. U. S. Geological Survey Bulletin 1276, p. 43.

Moucha, R., Forte, A.M., Mitrovica, J.X., Rowley, D.B., Quéré, S., Simmons, N.A., and Grand, S.P., 2008. Dynamic topography and long-term sea-level variations: There is no such thing as a stable continental platform. Earth and Planetary Science Letters v. 271, n. 1, p. 101-108.

Owens, J.P., Sugarman, P.J., Sohl, N.F., Parker, R.A., Houghton, H.F., Volkert, R.A., Drake, A.A., and Orndorff, R.C., 1998. Geologic map of Central and Southern New Jersey. U.S. Geological Survey Miscellaneous Investigation Series Map I-2540-B.

Permanent Service for Mean Sea Level (PSMSL), 2016. Tide Gauge Data. http://www.psmsl.org/obtaining/ [17 July, 2016]

Pope, J.P., and Burbey, T.J., 2004. Multiple-aquifer characterization from single borehole extensometer records. Ground Water v. 42, n. 1, p. 45-54.

Rasmussen, S.O., Andersen, K.K., Svensson, A.M., Steffensen, J.P., Vinther, B.M., Clausen, H.B., Siggard-Andersen, M.-L., Johnson, S.J., Larsen, L.B., Dahl-Jensen, D., Bigler, M., Röthlisberger, R., Fischer, H., Goto-Azuma, K., Hansson, M.E., and Ruth, U., 2006. A new Greenland ice core chronology for the last glacial termination. Journal of Geophysical Research v. 111, is. D6, p. 1-16.

Rayburn, J.A., Knuepfer, P.L., and Franzi, D.A., 2005. A series of large, Late Wisconsinan meltwater floods through the Champlain and Hudson Valleys, New York State, USA. Quaternary Science Reviews v. 24, n. 22, p. 2410-2419.

Reimer, P.J., Bard, E., Bayliss, A., Beck, J.W., et al., 2013. INTCAL13 and Marine13 radiocarbon age calibration curves 0-50,000 years cal BP. Radiocarbon v. 55, n. 4, p. 1869-1887.

Simms, A., Reynolds, L.C., Bentz, M., Roman, A., Rockwell, T., and Peters, R., 2016. Tectonic subsidence of California estuaries and coasts. Estuaries and Coasts v. 39, p. 1571-1581.

Sneed, M. and Galloway, D.L., 2000. Aquifer-system compaction: analyses and simulations–the Holly site. Edwards Air Force Base, Anetelope Valley, California. U.S. Geological Survey Water-Resources Investirgations Report 00-4015.

Stanford, S.D., 2010. Onshore record of Hudson River drainage to the continental shelf from the late Miocene through the late Wisconsinan deglaciation, USA: synthesis and revision. Boreas v. 39, n. 1, p. 1-17.

Stanford, S.D., Miller, K.G., and Browning, J.V., 2015. Coreholes reveal glacial and postglacial history at Sandy Hook. Unearthing New Jersey v. 11, n. 1, p. 1-6.

Sun, H., Grandstaff, D., and Shagam, R., 1999. Land subsidence due to groundwater withdrawal; potential damage of subsidence and sea-level rise in southern New Jersey, USA. Environmental Geology v. 37, n. 4, p. 290-296.

Thieler, E.R., Butman, B., Schwab, W.C., Allison, M.A., Driscoll, N.W., Donnelly, J.P., and Uchupi, E., 2007. A catastrophic meltwater flood event and the formation of the Hudson Shelf Valley. Paleogeography, Paleoclimatology, Paleoecology v. 246, p. 120-136.

Thornton, S.F. and McManus, J., 1994. Application of organic carbon and nitrogen stable isotope and C/N ratios as source indicators of organic matter provenance in estuarine systems: evidence from the Tay Estuary, Scotland. Estuarine, Coastal and Shelf Science v. 38, i. 3, p. 219-233.

Törnqvist, T.E., Wallace, D.J., Storms, J.E.A., Wallinga, J., Van Dam, R.L., Blaauw, M., Derksen, M.S., Klerks, C.J.W., Meijneken, C., and Snijders, E.M.A., 2008. Mississippi Delta subsidence primarily caused by compaction of Holocene strata. Nature Geoscience v. 1, p. 173-176.

Traykovski, P., Geyer, R., and Sommerfield, C., 2004. Rapid sediment deposition and fine-scale strata formation in the Hudson estuary. Journal of Geophysical Research v. 109, i. F2, p. 1-20.

Vereş, D.Ş., 2002. A comparative study between loss on ignition and total carbon analysis on minerogenic sediments. Studia UBB v. 47, n. 1, p. 171-182.

Woodruff, J.D., Rockwell Geyer, W., Sommerfield, C.K., and Driscoll, N.W., 2001. Seasonal variation of sediment deposition in the Hudson River estuary. Marine Geology v. 179, p. 105-119.

Yin, J., Schlesinger, M.E., and Stouffer, R.J., 2009. Model projections of rapid sea-level rise on the northeast coast of the United States. Nature Geoscience Letters v. 2, p. 262-266.

CHAPTER 3: Groundwater Extraction and Land Subsidence at Sandy Hook, NJ USA: A Groundwater Modeling Approach to Estimate Potential Contributions of Aquifer Compaction to Relative Sea-Level Rise

Christopher S. Johnson,[a,b*] Ying Fan,[a,b] Kenneth G. Miller[a,b]

[a]*Department of Earth and Planetary Sciences, Rutgers University, 610 Taylor Road, Piscataway, New Jersey 08854, USA*

[b]*Institute of Earth, Ocean and Atmospheric Sciences, Rutgers University, 71 Dudley Road, New Brunswick, New Jersey 08901, USA*

Abstract

The tide gauge at Sandy Hook, NJ, a spit of sand extending 8 km into Sandy Hook and Raritan Bays, recorded a 20th century rate of relative sea-level (RSL) rise of 4.0±0.5 mm/yr, significantly higher than both the 1.4±0.2 mm/yr rate of global mean sea-level (GMSL) rise and the 3.0±0.3 mm/yr recorded at The Battery, NY tide gauge 26 km to the north. The Battery tide gauge is located atop crystalline bedrock and reflects the regional processes and GMSL rise. After global and regional effects are removed from the rate of RSL rise at Sandy Hook, the remaining 0.9±0.5 mm/yr must be attributed to processes in the unconsolidated Cretaceous to Holocene sediments underlying Sandy Hook. Previous studies showed that 0.13 mm/yr (90% CI 0.16- 0.32 mm/yr) is due to autocompaction of the young (≤13,350 cal yrs BP), highly compressible, Quaternary sediments underlying Sandy Hook. The remaining 0.7 mm/yr (90% CI 0.3-1.2 mm/yr) is hypothesized to be due to regional and local groundwater extraction. This study employs a simulation modeling approach to test this hypothesis. Using the U.S. Geological Survey's MODFLOW 2005 in concert with the Subsidence Aquifer and Compaction (SUB) Package, we created a groundwater model for the northern half of the New Jersey Coastal Plain that simulates drawdown of the hydraulic heads throughout the region and calculates the resulting subsidence. The model shows that groundwater withdrawal is responsible for ~42 mm of total subsidence between 1885 and 2015 at the Sandy Hook tide gauge and a rate of 0.3±0.2 mm/yr for the 20th century, 0.4 ±0.2 mm/yr for the duration of the Sandy Hook tide gauge record during the 20th century. The model shows that the modern (2015) rate of subsidence is ~0.7 mm/yr, more than twice the 20th century average. We simulated the effects of local and regional pumping by running three

versions of the model, one with all of local and regional wells, one with only the wells on Sandy Hook pumping, and one with all regional wells pumping, but no pumping on Sandy Hook. We found that the contributions from each to the total amount of subsidence are roughly equal, but the rate of subsidence from each through time changes. Local pumping for Fort Hancock is the primary driver of subsidence up to 1965, while after 1965 regional pumping becomes the primary driver of subsidence.

3.1 Introduction

Relative sea level (RSL) is the measured difference in height between the solid earth surface and the sea surface, typically measured by tide gauges (Kopp et al., 2015; see Gregory et al., 2019 for sea level definitions). RSL change is highly variable around the world with twentieth century rates along the central east coast of North America ranging from 4.3 ± 0.5 mm/yr at Portsmouth, VA to 2.7 ± 0.6 mm/yr at Willets Point, NY (Miller et al., 2013). To the south and north, RSL rise is as low as 0.8 ±0.9 mm/yr in Daytona Beach, FL and 1.7 ± 0.4 mm/yr in Portland, ME (Kopp, 2013). 20^{th} century sea-level rise can vary by >1 mm/yr along the ~200 km of New Jersey coastline (Kopp, 2013). These variations in RSL change can be caused by geographically variable rates of vertical land motion due to Glacial Isostatic Adjustment (GIA) (Clark et al., 1978), tectonics (Simms et al., 2016), mantle dynamic topography (Gurnis, 1990), autocompaction (Johnson et al., 2018), and groundwater withdrawal (e.g. Sun et al., 1999; Erban et al., 2014). Sterodynamic changes including thermosteric sea-level change (Church et al., 2011), and changes in ocean circulation (e.g. Cronin et al., 2014; Goddard et al., 2015) can also play a role.

Sandy Hook is a spit of sand that extends north from New Jersey into Raritan and Sandy Hook Bays of New Jersey and New York (Fig. 3.1). Due to the abundance of data at and around Sandy Hook, including tide gauges (Kopp, 2013), Continually Operating Reference Station (CORS) Global Positioning Systems (GPS) (Blewitt et al., 2016), marine seismic reflection data, and 3 sediment cores (Miller et al., 2018), the site provides an opportunity to study sea-level rise on a relatively small (a few square kilometers) spatial scale. Furthermore, the available data make it possible to quantify the various regional and local sources of sea-level rise at Sandy Hook (e.g. Johnson et al., 2018) and test these results.

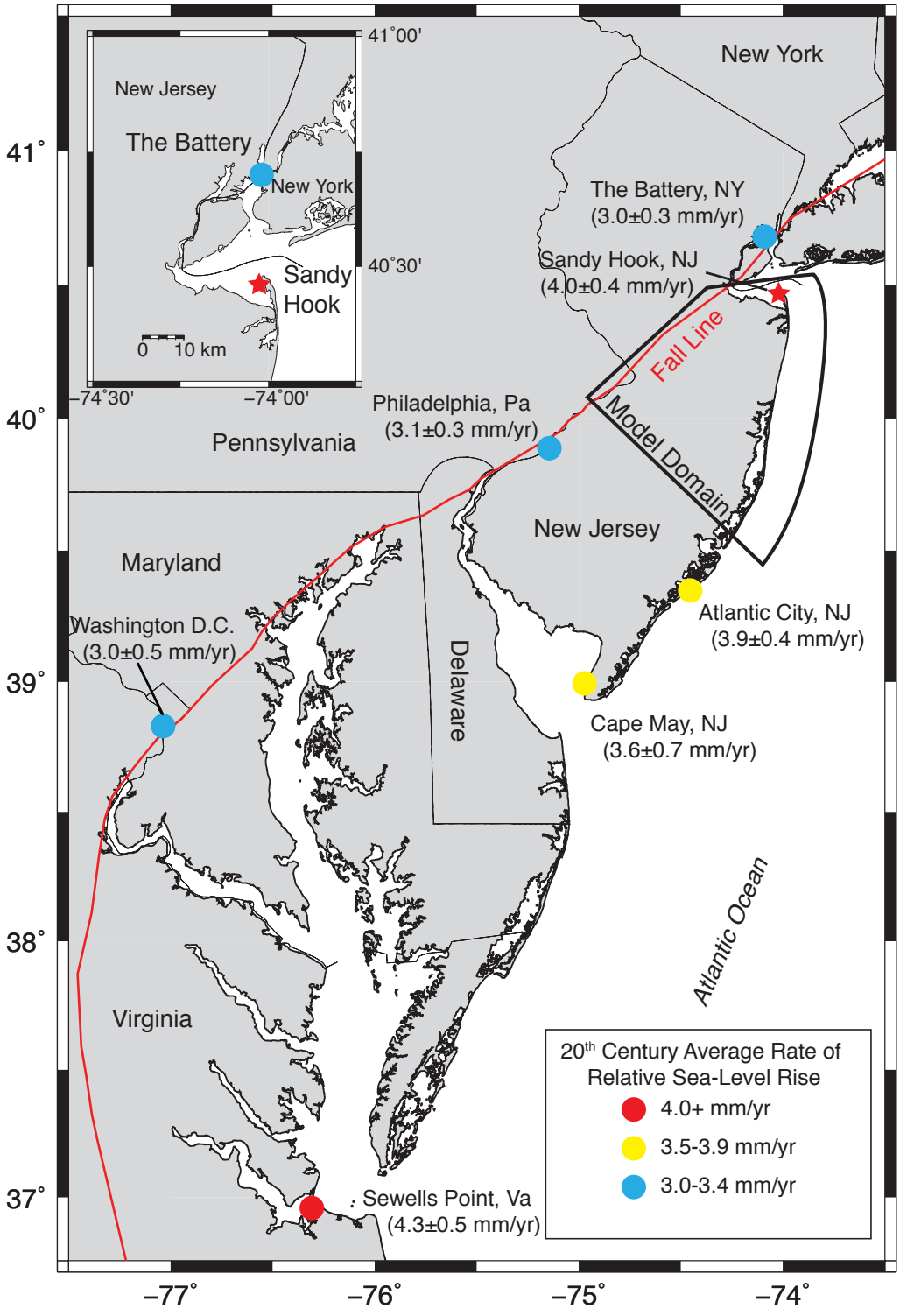

Figure 3.1: Location map with 20th century average rates of RSL rise measured at tide gauges along the Atlantic coast of North America. The red line indicates the fall line,

dividing the Piedmont in west from the coastal plain in the east. The bold black box indicates the approximate boundary of the model domain. Figure modified after Miller et al., 2013.

Tide gauge records show that Sandy Hook experienced an average of 4.0±0.5 mm/yr of sea-level rise over the 20th century while The Battery, NY experienced 3.0±0.3 mm/yr just 26 km to the NW (Fig. 3.1) (Kopp, 2013). Both of these rates are significantly higher than the 1.4±0.2 mm/yr rate of global mean sea-level GMSL rise (Hay et al., 2015, Kopp et al., 2016; Dangendorf et al., 2017). By comparing two relatively closely spaced records, we are able to eliminate processes that operate on larger spatial scales from the list of processes that cause the difference in rate of RSL rise between the two sites (Johnson et al., 2018). This includes thermal subsidence of the lithosphere, mantle dynamic topography, and most sterodynamic effects. While these processes may play a role at both Sandy Hook and The Battery, the contribution at both sites is the same (Johnson et al., 2018). Part of the difference between the two sites may be the result of the 0.1±0.8 mm/yr difference in GIA between the two sites (Kopp, 2013). Johnson et al. (2018) showed that, of the remaining 0.9 ± 0.5 mm/yr difference in sea level rise, 0.16 mm/ yr (90% Confidence Interval (C.I.) 0.06-0.32 mm/yr) is due to compaction of the thick (84+ m), relatively young (<13,300 cal yr BP) uppermost Pleistocene and Holocene section underlying Sandy Hook. Compaction of the older, Cretaceous section is assumed to be too slow to significantly contribute to the rates of RSL rise at Sandy Hook (Johnson et al., 2018). In this paper we use a groundwater model to test their hypothesis that the remaining 0.7 mm/yr (90% C.I. 0.3-1.2 mm/yr) of Johnson et al., (2018) is due to anthropogenic groundwater withdrawal.

Groundwater withdrawal causes subsidence by reducing the pore fluid pressure within water bearing strata. As the fluid pressure decreases and overburden pressure remains the same from above, the differential stresses cause the sediment to compact vertically (Sun et al., 1999). Changes in hydraulic head are a measure of changes in pore fluid pressure. Groundwater withdrawal has been found to be a major contributor to subsidence and subsequently the rate of RSL rise in places such as Norfolk, VA and Atlantic City, NJ (Miller et al., 2013). In fact, the majority of southern New Jersey has been found to have undergone 2-3 cm of subsidence due to groundwater withdrawal (Sun et al., 1999). At Sandy Hook, historical records show that groundwater extraction for Fort Hancock, a former military base located at the northern part of the spit, began lowering the hydraulic heads under Sandy Hook as early as the late 1800s. Construction first began at Ft. Hancock in 1896 with the installation of 36 artesian wells that were meant to supply 150,000 gallons per day. Those wells were exhausted by 1907 and replaced by deeper and deeper wells roughly every 20 years (Bearss, 1981). Also, the population stationed on the base correlates to the divergence between the rates of RSL rise at Sandy Hook and The Battery (Fig. 2.8B, Johnson et al., 2018). This suggests that local groundwater withdrawal has likely been a significant cause of local subsidence.

Additional subsidence was likely caused by regional groundwater withdrawal from surrounding Monmouth County. dePaul et al. (2008) showed a regional cone of depression in several aquifers underlying Sandy Hook that extends from central Monmouth County offshore north of Sandy Hook (Fig. 2.9). This qualitatively shows that regional groundwater extraction is likely adding to natural subsidence at Sandy Hook. In this paper we use a groundwater model to show that groundwater withdrawal has the

potential to produce modern rates of subsidence of ~0.7 mm/yr. This is the first groundwater model developed to study groundwater-related subsidence in New Jersey. We show that, while local and regional groundwater extraction have each produced approximately equal amounts of subsidence, regional extraction is the dominant driver since 1965.

3.2 Background and Previous Studies

3.2.1 Previous Models of the Northern New Jersey Coastal Plain

The groundwater systems of the New Jersey coastal plain have been the focus of a number of numerical models since the early 1980s. Luzier (1980) created a single-layer finite-difference model to study the head changes in the Potomac-Raritan-Magothy (PRM) aquifer system of the New Jersey coastal plain between 1956 and 1973. It was the first groundwater model examining the potential effects of overuse on the groundwater resources in New Jersey. He found that, in 1973, the cones of depression were nearly in equilibrium, and that, should pumping continue at its current rate, the drawdown would not increase significantly. However, he warned that the steep gradients induced by pumping would likely accelerate saltwater intrusion.

Pucci et al. (1994) used a 3-dimensional finite difference model to study the effects of development on the groundwater systems Potomac-Raritan-Magothy (PRM) aquifer system in the northern coastal plain of New Jersey including Monmouth, Middlesex, and parts of Mercer Counties, NJ. They found that with increased pumping (69 Mgal/day in the upper PRM and 37 Mgal in the lower PRM) from 1986-2019 cones of depression could be as much as 100 ft below sea level. If pumping was restricted to

42.5 Mgal/day in the upper PRM and 15 Mgal/d in the middle PRM the hydraulic heads would recover to well above sea level throughout the region.

Martin (1998) published the most recent comprehensive groundwater model of the New Jersey Coastal Plain. As such, we will often compare and contrast the model presented in this paper to Martin's. Martin's model was a multilayer finite difference model that simulated prepumping conditions and transient conditions from 1896-1980 to aid water resource management. Of particular interest was the potential for saltwater intrusion, flow of contaminants, and reorganization of regional flow. Martin's model included 19 lithologic units of alternating confining units and aquifers. Under prepumping conditions, water entered the model via recharge at the updip outcrops of the strata and flowed downdip in the aquifers before being discharged to the Atlantic Ocean and other large surface water bodies. In the transient run from 1896-1980, Martin (1998) found that, by 1980, conditions near pumping centers had nearly stabilized, but that areas away from pumping wells, particularly downdip, would likely experience as much as 8 m of further head reduction should pumping continue at 1980 rates until the groundwater system reached equilibrium. Martin also found that in the nearly steady state conditions by 1980, the primary way the system compensated for the withdrawals by pumping was by decreasing discharge to rivers and streams, rather than by further lowing hydraulic heads, suggesting that the majority of water reduction in the aquifers was complete at that time.

More recently Cauller et al. (2016) created a 3 dimensional finite difference model to study the impacts of groundwater withdrawal in Ocean County, NJ. Since their interest was on saltwater intrusion and freshwater discharge to estuaries, their model focused on

the relatively shallow aquifers. They found at pumping at years 2000-2003 rates could significantly reduce the freshwater discharge of river systems into estuaries when compared to pre-pumping conditions.

3.2.2 History of Groundwater Related Subsidence

Subsidence due to fluid extraction was first hypothesized in the early 1900s (Fuller, 1908) and the first reports followed from Texas oil fields in the 1920s (Minor, 1925). By the middle of the twentieth century, subsidence due to groundwater extraction had been identified and documented across the globe (e.g. Wilson and Grace, 1942; Poland, 1960). See Poland and Davis (1969) and Galloway and Burbey (2011) for thorough reviews. Rapid groundwater depletion can cause steep rates of subsidence, much faster than the rate of excess sea-level rise at Sandy Hook. For example, in the San Joaquin Valley of California, groundwater extraction caused as much as 9 m of subsidence between 1925 and 1977 (~173 mm/yr) (Galloway and Sneed, 2013).

Subsidence takes place when groundwater withdrawal causes hydraulic head declines. With a static total pressure (σ_t) generated by the weight of the overburden, a decrease in pore fluid pressure (σ_p) increases the effective stress (σ_e) on the strata.

$$\boldsymbol{\sigma_e = \sigma_t - \sigma_p} \qquad \text{Equation 3.1}$$

In response, the sediments compact until the pore fluid pressure increases to reach equilibrium and the effective stress is reduced (Sun et al., 1999; Galloway and Sneed, 2013). This process can be either elastic or inelastic. Pope and Burbey (2004) showed that there can be slight (typically <1 mm) elastic recoveries when groundwater levels recover, for instance in a wet season.

While most subsidence due to groundwater withdrawal is associated with relatively arid regions with significant agricultural water requirements or population centers (e.g. San Joaquin Valley, Mexico City (Poland and Davis, 1969)), groundwater related subsidence has been documented on the east coast as well. Pope and Burbey (2004) used extensometers, semi-permanent wire line tools installed in observation wells, to measure the change in subsidence on the coastal plain of Virginia, USA over a 15 year period between ~1980 and 1995. They found rates of 1.5 and 3.7 mm/yr of subsidence at Franklin and Suffolk, Virginia respectively. This is significantly less than the rates observed in more arid settings, but still significant, particularly in coastal regions where it adds to the rate of RSL rise. Pope and Burbey (2004) also created a 1-D compaction model that uses the transient vertical effective stress, a result of the water level and the hydraulic properties, to simulate the rate of compaction as a whole and in individual layers. This method showed good agreement for the model period that overlapped the extensometer measurements. Sun et al. (1999) used the relationship between elastic and inelastic compaction to estimate the response of confining units to the drawdown of aquifers in the southern New Jersey Coastal Plain. They found that ~10 m of drawdown over 22 years (1972-1994) resulted in 2-3 cm of compaction (~1 mm/yr). However, these methods are limited to the specific locations simulated and to locations where sufficient data are available, including measured hydraulic heads, aquifer properties, and stratigraphic thicknesses. At Sandy Hook, while there are stratigraphic data at several locations (SH-NMY and the pumping station) proximal to the tide gauge, there are limited hydraulic and water level data near to the tide gauge (Fig. 3.1).

Modeling provides an opportunity to evaluate compaction in non-ideal situations with limited data and over relatively large regions. The U.S. Geological Survey's MODFLOW software provides a good platform for testing groundwater compaction hypotheses in areas with limited data sets and where the spatial distribution of compaction is of interest. MODFLOW is a modular finite difference groundwater flow model that simulates 3 dimensional fluid flow through a porous medium. It was first developed in 1984 (Harbaugh, 2005). In the 2000 release of MODFLOW, a subsidence package was added to simulate compaction within aquifers (Hoffmann et al., 2003). We use this package in this study with the MODEMUSE graphical user interface (Winston, 2009).

More recent compaction studies have focused on applications of satellite technology including gravity measurements, global positioning systems (GPS), and inferometric synthetic aperture radar (InSAR) to address the problem. Gravity data from the Gravity Recovery and Climate Experiment (GRACE) has been used to remotely measure aquifer properties including water storage change in time (e.g. Yeh et al., 2006). InSAR is capable of measuring changes in the Earth's surface on the millimeter to centimeter scale. Galloway et al. (1998) used InSAR to measure subsidence in the aquifer system of the Antelope Valley of California with only a ~2 year record. GPS records on the east coast of North America have only recently become long enough to provide reliable time series. Karegar et al. (2016) used Continually Operating Reference Station (CORS) GPS records from eastern North America in conjunction with Holocene sea-level indicators to estimate subsidence. These technologies provide large, readily

available data sets for testing modeling results. This study uses CORS GPS records from distinct geologic provinces to evaluate the subsidence rate at stations on the coastal plain.

3.3 Geologic Setting

The difference between rates of RSL rise experienced at Sandy Hook and The Battery is due to the difference in the lithologic properties of the underlying strata. Sandy Hook is situated on the coastal plain of New Jersey. The coastal plain is characterized by unconsolidated Cretaceous to Holocene sediments deposited in environments that range from marine to terrestrial (Owens et al., 1999). The strata dip gently to the southeast and continue offshore. The coastal plain sediments alternate between coarse grained near-shore sediments (aquifers like the Magothy) deposited during sea-level lows and fine grained, marine sediments deposited during sea-level highs (Miller et al., 2004) (Table 3.1). The unconsolidated nature of the Coastal Plain sediments make them particularly susceptible to both autocompaction and groundwater pumping induced compaction (Domenico and Mifflin, 1965). At depth, the coastal plain sediments overlie crystalline bedrock of the Piedmont exposed to the west (Owens et al., 1998). The western border of the coastal plain is marked by the fall line (Fig. 3.1), defined as the transition from unconsolidated sediments of the coastal plain in the east to the Proterozoic and Paleozoic metamorphic terranes and Mesozoic rift basins of the Piedmont are to the west. The fall line typically coincides with a series of waterfalls or rapids. The Battery, NY is located on these relatively incompressible Proterozoic and Paleozoic metamorphic rocks (Lyttle and Epstein, 1987). Tide gauges in the Piedmont, including The Battery, typically record

rates of RSL rise of ~3 mm/yr, whereas those in the coastal plain record rates of 3.5-4.5 mm/yr (Miller et al., 2013).

Table 3.1: Regional stratigraphy used in the model. Modified after Martin, 1998.

System	Series	Geologic Formation	Hydrologic Unit	Model Units (Martin, 1998)		Model Units (This Study)
				Up Dip	Down Dip	Sandy Hook, NJ
Quaternary	Holocene	Alluvial Deposits	Undifferen-tiated	Upper Kirkwood Cohansey Aquifer (A9)		Latest Pleistocene-Holocene Sands Aquifer
		Beach Sand and Gravel			Holly Beach Aquifer (A10)	
	Pleistocene	Cape May Formation	K-C aq. sys.		Cape May Confining Unit (C9)	Quaternary Muds Confining Unit
					Upper Kirkwood-Cohansey Aquifer (A9)	
Tertiary	Miocene	Pensauken Formation	Kirkwood-Cohansey Aquifer System	Upper Kirkwood-Cohansey Aquifer (A9)		Kirkwood Cohansey Aquifer
		Bridgeton Formation				
		Beacon Hill Gravel				
		Cohansey Sand		Lower Kirkwood-Cohansey Aquifer (A8)		
		Kirkwood Formation	Confining Unit		Confining Unit Overlying the Rio Grande Water Bearing Zone (C8)	
			Rio Grande Confining Unit		Confined Kirkwood Aquifer (A8)	
			Atlantic City 800-foot sand			
				Basal Kirkwood Confining Unit (C7)		
	Eocene	Piney Point Formation	Composite Confining Bed: Piney Point Aquifer	Piney Point Aquifer (A7)		Confining Unit 1
		Shark River Formation	Composite Confining Bed	Vincentown-Manasquan Confining Unit (C6)		
		Manasquan Formation				
	Paleocene	Vincentown Formation	Vincentown Aquifer	Vincentown Aquifer (A6)		
		Hornerstown Sandy	Composite Confining Bed			
Cretaceous	Upper Cretaceous	Tinton Sand	Red Bank Sand	Navesink-Hornerstown Confining Unit (C5)		
		Red Bank Sand				
		Navesink Formation				
		Mount Laurel Sand	Wenonah-Mount Laurel Aquifer	Wenonah-Mount Laurel Aquifer (A5)		Mount Laurel Aquifer
		Wenonah Formation	Marshalltown-Wenonah Confining Unit	Marshalltown-Wenonah Confining Unit (C4)		Confining Unit 2
		Marshalltown Formation				
		Englishtown Formation	Englishtown aquifer system	Englishtown Aquifer(A4)		Upper Englishtown Aquifer
		Woodbury Clay	Merchantville-Woodbury Confining Unit	Merchantivlle-Woodbury Confining Unit (C3)		Confining Unit 3
		Merchantville Formation				
		Magothy Formation	Potomac-Raritan-Magothy Aquifer System: Upper Aquifer	Upper Potomac-Raritan-Magothy Aquifer (A3)		Magothy Aquifer
			Conf. Un.	Confining Unit Between the Middle and Upper Potomac-Raritan-Magothy Aquifers (C2)		Confining Unit 4
		Raritan Formation	Middle Aquifer	Middle Potomac-Raritan-Magothy Aquifer (A2)		Potomac III Aquifer
			Conf. Un.	Confining Unit Between the Lower and Middle Potomac-Raritan-Magothy Aquifers (C2)		Confining Unit 5
	Lower Cretaceous	Potomac Group	Lower Aquifer	Lower Potomac-Raritan-Magothy Aquifer (A1)		Potomac II Aquifer
Pre-Cretaceous		Basement	Bedrock confining unit			Basement Confining Units

3.4 Methods

3.4.1 Conceptual Model

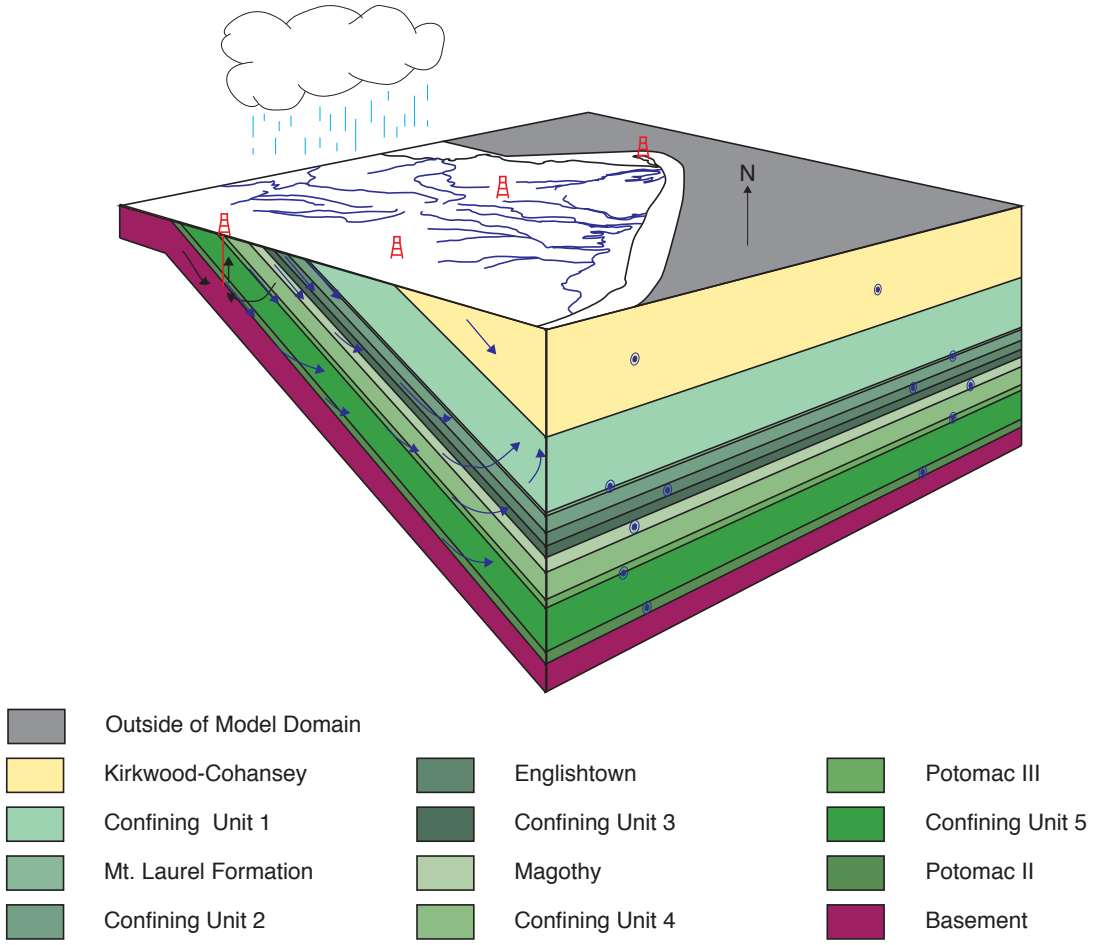

Figure 3.2: Conceptual Model. The Cretaceous to Miocene stratigraphy of the northern New Jersey Coastal Plain is shown with a gentle east-southeast dip. The confining units are composite confining units, each comprising 2 or more low permeability lithologic units. Blue arrows indicate idealized regional flow and bullseyes indicate flow out of the model across that boundary. The blue lines in map view indicate rivers, simulated by a mix of constant head and drain features. Recharge comes from precipitation while water

is removed from the model by pumping wells and by flow of water out of model along the ocean boundary to the east and southeast.

The hydrologic system of the New Jersey Coastal Plain consists of interactions between the underlying geology and various sources and sinks of groundwater. The New Jersey Coastal Plain stratigraphy consists of Cretaceous to Holocene sediments dipping to the southeast (Fig. 3.2). The strata are exposed at the surface updip to the west, near the fall line. The strata include numerous lithologic units, which, for the most part, alternate between aquifers and confining units (Sugarman et al., 2013). In our model, we simplify that stratigraphy to the primary aquifers and composite confining units in between (Table 3.1) Water enters the system as recharge in locations where the strata intersect the land surface. Flow is typically parallel to dip with a smaller component of vertical (up-section) flow (Fig. 3.2). Consistent with Martin (1998), water is removed from the system through three main sinks including the rivers, the coastal boundary to the east and north, and pumping wells.

3.4.2 Model Domain and Grid

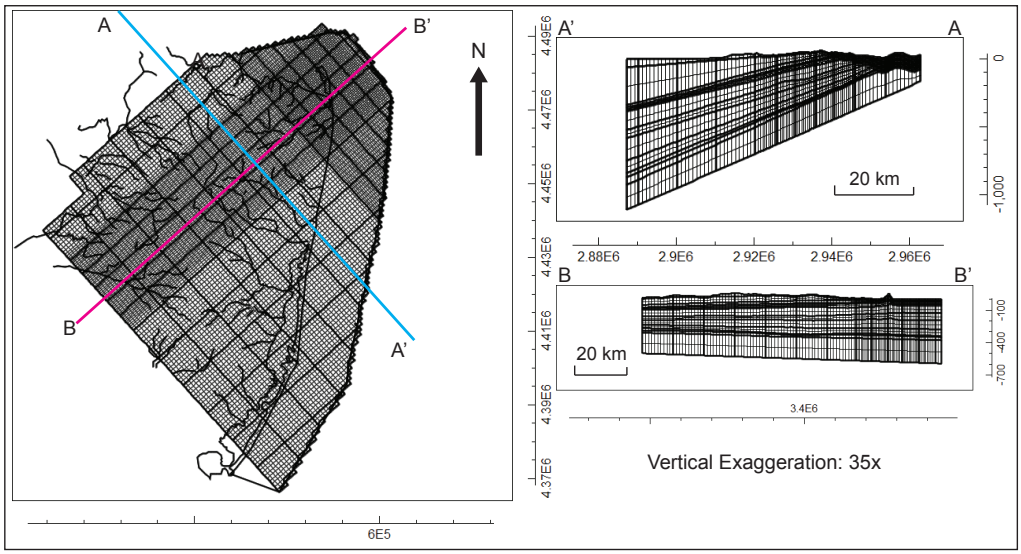

Figure 3.3: Model Grid. The grid is 1 km x 1 km for the majority of the model domain with 500 m x 500 m grid spacing around Sandy Hook for higher resolution.

The model domain encompasses the northern half of the New Jersey Coastal Plain, an area of approximately 7,000 km^2. The model domain is divided into a grid of 1 km by 1 km for the majority of the model (Fig. 3.3). In the area of interest around Sandy Hook, the model is divided into 0.5 km by 0.5 km cells for better resolution. The model contains 129 rows and 123 columns, significantly more than the <30 of each that Martin (1998) had in her model that encompassed the entire New Jersey coastal plain. The grid is rotated 42° to align the grid cells of the model with regional dip, such that the main flow direction is parallel to the rows. The model is divided vertically into 19 layers. The vertical grid spacing was set using the elevation of the land surface and geologic formations included in the model with a minimum cell thickness of 5 m. The surface elevation was taken from the NJDEP 100m Digital Elevation Grid for New Jersey (2002).

The geometry for the model layers, excluding the latest Pleistocene to Holocene stratigraphy near Sandy Hook, was created using formation tops from Sugarman et al. (2013), outcrop extents from Herman et al. (1998), and drilling results from ODP 174AX (Miller et al., 2018). The geometry of the surface marking the base of the uppermost Pleistocene to Holocene strata underlying Sandy Hook (Fig. 3.4) is based on sparse data points from ODP 174AX (Miller et al., 2018), boomer subbottom data (NJGWS, unpublished), and interpretation based on the drilling results and the regional deglacial history (e.g. Stanford et al., 2002; Stanford, 2010; Stanford et al., 2016; Miller et al., 2018; Johnson et al., 2018). This was not included in the model grid, but instead used to set the hydraulic properties of the grid cells located above this surface. Borings suggest

that the thalweg may be farther north into Raritan Bay than the geometry used in the model (MacClintock and Richards, 1936). This would mean that the model may include less of the compressible Quaternary material than is actually present under Raritan bay making the model slightly conservative.

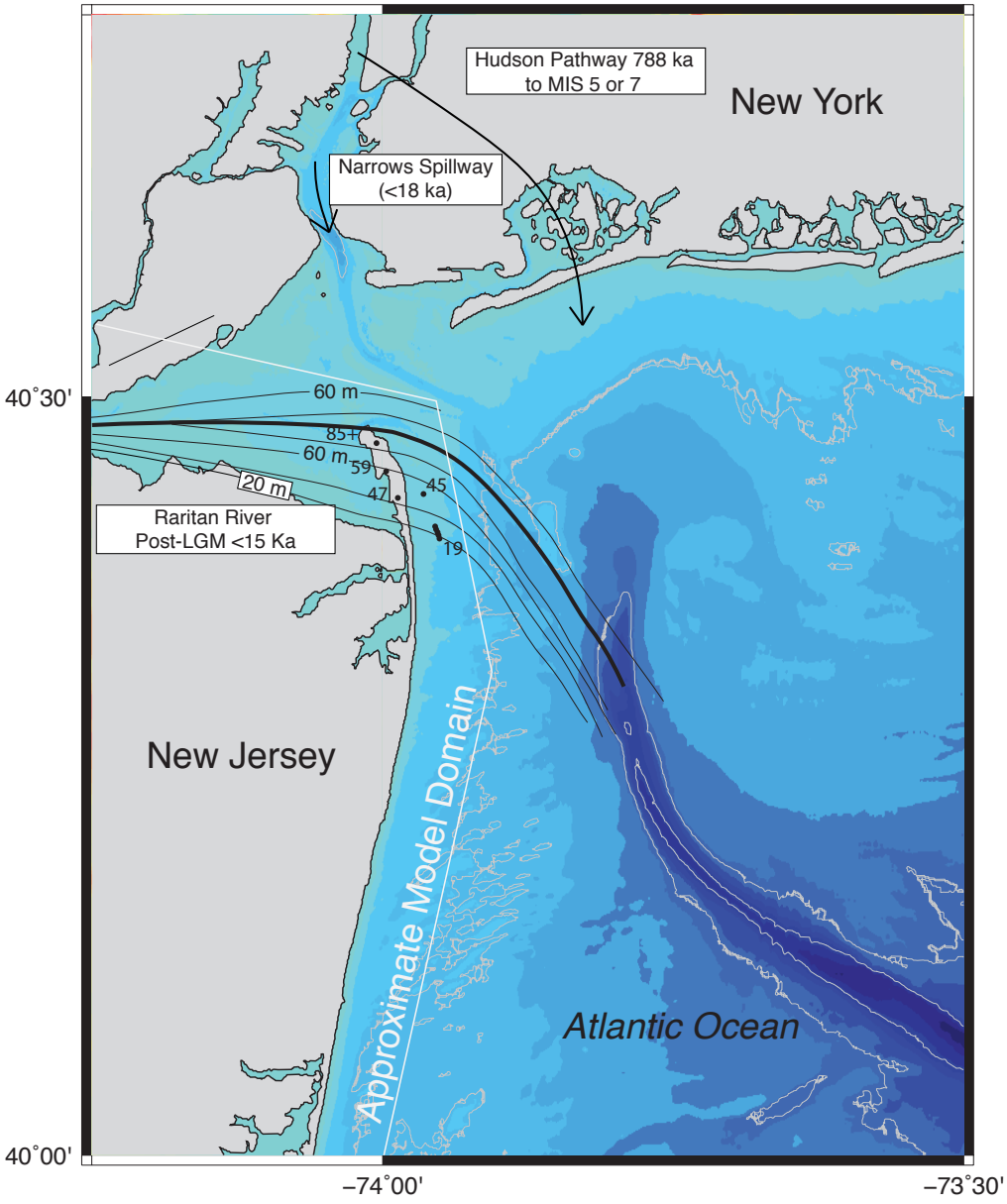

Figure 3.4: Contour map of the base of the uppermost Pleistocene to Holocene section at Sandy Hook. Black lines are 20 m contours in meters below sea level. Black dots indicate

data points from (Miller et al., 2018), boomer subbottom data (NJGWS, unpublished), and interpretation based on the drilling results and the regional deglacial history (e.g. Stanford et al., 2002; Stanford, 2010; Stanford et al., 2016; Miller et al., 2018; Johnson et al., 2018).

3.4.3 Model Boundary Constraints

The model has 6 boundaries, their placement and type were chosen based on logical divides in the hydrogeology of New Jersey. The western edge of the model is defined as a constant flux boundary with no flow. We use this hydraulic boundary since we assume that the water in the system is supplied by surficial recharge with little input from the crystalline rocks of the Piedmont. This assumption is justified because the boundary is relatively distant from the area of interest at Sandy Hook (minimum of ~40 km). The coastal boundary of the model, which comprises the entire eastern edge of the model and a large portion of the northern edge, is set as a constant head at 0 m that extends from the model top to the bottom. This simulates a sea level hydraulic head or hydro-static condition (no vertical gradient) for the units under the ocean. Unlike a no-flow boundary, this allows for some head driven flow across the boundary. We know that this takes place, since studies have shown saltwater intrusion in the northern coastal plain (Pucci et al., 1994). However, this makes the assumption that salt-water intrusion does not significantly affect the compaction results of the model. The remainder of the northern boundary and the southern boundaries are set as constant flux boundaries with no flow. The northern boundary is approximately equidistant between the pumping epicenters in Monmouth County and Long Island to the north. The southern boundary is located at the midway point between the cone of depression for Monmouth/Ocean

Counties and Atlantic City to the south (dePaul et al., 2008). The top of the model is set as a constant flux boundary (i.e. water table recharge from precipitation) using the recharge package. The bottom of the model is set as a constant flux boundary with no flow below a thin layer group representing the top crystalline bedrock. This allows the model some interaction with the relatively impermeable basement while providing a barrier at the base of the model. The no flow boundary is justified because the crystalline bedrock is relatively impermeable (Mennel and Canace, 2012). With the exception of the coastal constant head boundary, these boundaries are consistent with those used by the Martin (1998) model. In her model, Martin used a no flow boundary for the coast, which can overestimate drawdown since no water can come in. We chose to use a constant head boundary because water can be sourced from the offshore, though it may be saline as shown by Cauller et al. (2016).

3.4.4 Model Hydrogeologic Zones and Lithologic Properties

The coastal plain stratigraphy is relatively complex, with numerous formations and members. For the purposes of the model we simplified the stratigraphy and focused on the main aquifers and confining units underlying Sandy Hook (Table 3.1, Figs. 3.2, 3.5). This reduced the number of aquifers to 7. The uppermost aquifer included is the combined Kirkwood-Cohansey ("Pine Barren") and the lowermost is the Cretaceous Potomac II Formation. Between each of the aquifers there are often several confining units. For simplicity, these have been consolidated into single composite "Confining Units" similar to Martin (1998). For instance, between the Magothy Formation and the Englishtown there are typically 3 units including the Cheesequake, Merchantville, and Woodbury Formations. In our model, these units are consolidated into 1 unit called

Confining Unit 3. In the model, “basement” is located beneath the Potomac II. The composition of the basement is unknown under Sandy Hook, but it is assumed to have properties similar to that of a confining unit (Mennel and Canace, 2012). The geometries of the various lithologic units used in the model were generated using gamma logs at numerous wells throughout the region.

The x, y, and z, coordinates of the top and bottom of each aquifer included in the model were taken from Sugarman et al. (2013). Generic Mapping Tools (GMT; https://www.soest.hawaii.edu/gmt/) was used to interpolate between wells with a continuous curvature spline and create a grid of data that could be input into MODFLOW. The hydraulic conductivities, or the rate at which a fluid can flow through a medium (Freeze and Cherry, 1979), for each of the included aquifers were initially estimated from NJDEP (2012) and Martin (1998) and then calibrated. The final calibrated conductivities are included in Table 3.2. We used a single value for conductivity in each of the confining units. The bedrock hydraulic conductivity was assumed to be very low and as such was set to the same as the confining units. A similar process was used to set the specific storage for each of the units (See section 3.4.10 for more details). We used a single specific storage for all of the aquifers and another for all confining units.

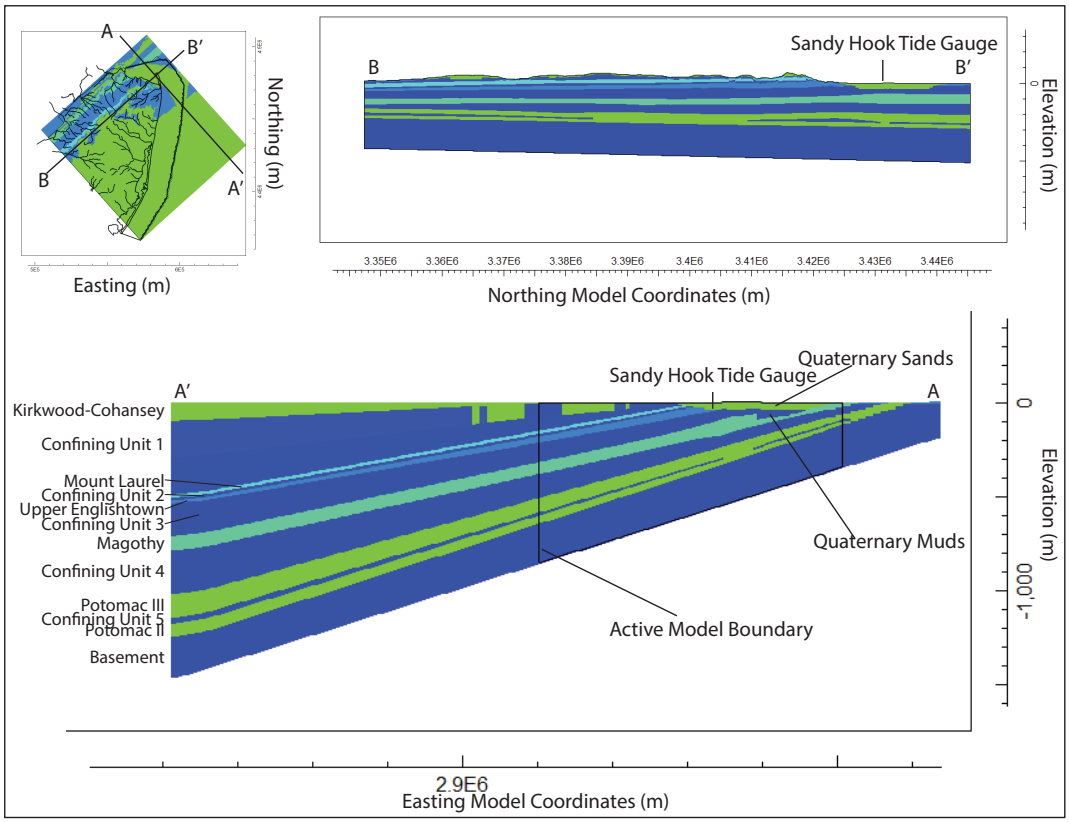

Figure 3.5: Cross sections of the hydrologic units at Sandy Hook. Note that blocks of Kirkwood Cohansey extending down into the underlying Confining Unit 1 are artifacts caused by the relatively coarse gridding of the layers causing the properties of the Kirkwood Cohansey to be applied to layer 2 in a few places.

Table 3.2: Hydrologic properties from literature for the aquifers and confining units used in the model. Bold data are the calibrated values for each of the units in the final version of the model. Modified after Martin (1998).

Unit	Sub-Unit	Hydraulic Conductivity Kx/Ky (m/d)	Hydraulic Conductivity Kz (m/d)	Specific Storage (1/m)	Location	Data Type	Original Source
Quaternary Sands		**30**	**3**	**$1.00E^{-6}$**		**Model Calibration**	**This Study**
Quaternary Muds		**0.005**	**$6.00*10^{-05}$**	**0.0064**			**This Study**
Kirkwood Cohansey	Lower KwC	12.8-14.6		$1.2*10^{-4}$ to $2*10^{-4}$	Atlantic City, Atlantic County	Aquifer Test	USGS Unpub in Martin, 1998
		36.6-45.7		$2.3*10^{-4}$ to $2.8*10^{-4}$	Pleasantville, Atlantic County	Aquifer Test	Gill, 1962
		32.9-36.6		$2.6*10^{-4}$ to $2.7*10^{-4}$	Pleasantville, Atlantic County	Aquifer Test	Gill, 1962
				$6.00*10^{-4}$	Ocean Gate, Ocean County	Aquifer Test	Anderson and Appel, 1969
		39.6			Batsto, Burlington County	Aquifer Test	Rhodehamel, 1974
	Upper KwC	36.6			Lebanon State Forest, Burlington County	Aquifer Test	Rhodehamel, 1975
		42.7			Toms River, Ocean County	Aquifer Test	Rhodehamel, 1982
	Kirkwood Formation	17.4 to 46.9				Aquifer Test	NJDEP, 2012
	Kirkwood Shilo Marl Member	10.1 to 37.7				Aquifer Test	NJDEP, 2012
	Kirkwood Formation - Wildwood Member	24.4 to 111.3				Aquifer Test	NJDEP, 2012
	Kirkwood Formation - Belleplain Member	58.2				Aquifer Test	NJDEP, 2012
	Kirkwood Formation - Lower member (sand Facies)	6.7 to 86.9				Aquifer Test	NJDEP, 2012
	Undifferentiated Kirkwood Cohansey	**30**	**3**			**Model Calibration**	**This Study**

Unit	Sub-Unit	Hydraulic Conductivity Kx/Ky (m/d)	Hydraulic Conductivity Kz (m/d)	Specific Storage (1/m)	Location	Data Type	Original Source
Mount Laurel	Mount Laurel	5.18		**7.0 10^{-5} to 2.1*10^{-4}**	Bradley Beach, Monmouth County	Aquifer Test	Jablonski, 1959
	Mount Laurel	3.96 to 5.79		1.5*10^{-5} to 3.5*10^{-4}	Monmouth, Ocean and Northeastern Burlington Counties	Model Results	Nemickas et al., 1976
	Mount Laurel Formation	6.71 to 12.50				Aquifer Test	NJDEP, 2012
	Mount Laurel and Wenonah Formation	1.52 to 9.22				Aquifer Test	NJDEP, 2012
	Mount Laurel	**15**	**1.5**			**Model Calibration**	**This Study**
Englishtown Formation	Englishtown Formation	3.66		7.60*10^{-5}	Allenwood, Monmouth County	Aquifer Test	Nichols, 1977a
		4.57			Lakewood, Ocean County	Aquifer Test	Nichols, 1977a
		3.13 to 12.8			Monmouth, Ocean and Northeastern Burlington Counties	Model Results	Nichols, 1977a
						Aquifer Test	
		5	**0.05**			**Model Calibration**	**This Study**
Upper Potomac-Raritan-Magothy/ Magothy Formation	Upper PRM			5.8*10^{-4} to 2.4*10^{-3}	Old Bridge, Middlesex County	Aquifer Test	Barksdale et al., 1958
	Upper PRM			8*10^{-5} to 8*10^{-3}	New Jersey Coastal Plain	Model Results	Luzier, 1980
	Magothy	0 to 95.7				Aquifer Test	NJDEP, 2012
	Magothy Formation - Old Bridge Sand Member	19.4 to 60.0				Aquifer Test	NJDEP, 2012
	Magothy Formation	**20**	**2**	**1.00*10^{-6}**		**Model Calibration**	**This Study**

Unit	Sub-Unit	Hydraulic Conductivity Kx/Ky (m/d)	Hydraulic Conductivity Kz (m/d)	Specific Storage (1/m)	Location	Data Type	Original Source
Middle Potomac-Raritan-Magothy (P3-Ferrington)	Middle Potomac-Raritan-Magothy (P3-Ferrington)	39.6 to 82.3		$2.00*10^{-4}$	Burlington Township, Burlington	Aquifer Test	Rush, 1968
		60.96		$6.00*10^{-2}$	Burlington, Burlington County	Aquifer Test	Rush, 1968
				$1.1*10^{-4}$ to $5.8*10^{-4}$	Palmyra, Burlington County	Aquifer Test	Rush, 1968
		66.1-88.4		$1.0*10^{-4}$ to $2.4*10^{-4}$	Beverly, Burlington County	Aquifer Test	Rush, 1968
		60.96		$1.50*10^{-4}$	Riverton, Burlington County	Aquifer Test	Barksdale et al., 1958
		609.5		$1.50*10^{-3}$	Parlin, Middlesex County	Aquifer Test	Barksdale et al., 1958
		24.1 to 36.3		$3.7*10^{-5}$ to $8.6*10^{-5}$	Parlin, Middlesex County	Aquifer Test	Barksdale et al., 1958
		9.75 to 26.8		$4.0*10^{-5}$ to $8.1*10^{-2}$	Barber, Middlesex County	Aquifer Test	Barksdale et al., 1958
				$5.8*10^{-4}$ to $2.4*10^{-3}$	Old Bridge, Middlesex County	Aquifer Test	Barksdale et al., 1958
		32		$1.60*10^{-4}$	Southeaster Mercer, Middlesex, Monmouth, and northern Ocean Counties	Model Results	Farlekas, 1979
				$8.0*10^{-5}$ to $8.0*10^{-3}$	New Jersey Coastal Plain	Model Results	Luzier et al., 1980
		28.8 to 87.8				Aquifer Test	NJDEP, 2012
	Potomac III	**30**	**3**	**$1.00*10^{-6}$**		**Model Calibration**	**This Study**
Lower Potomac-Raritan-Magothy	Lower Potomac-Raritan-Magothy			$8*10^{-5}$ to $8*10^{-3}$	New Jersey Coastal Plain	Model Results	Luzier, 1980
	Potomac Formation Unit II	7.32				Aquifer Test	NJDEP, 2012
	Potomac II	30	3	$1.00*10^{-6}$		Model Calibtration	This Study

Unit	Sub-Unit	Hydraulic Conductivity Kx/Ky (m/d)	Hydraulic Conductivity Kz (m/d)	Specific Storage (1/m)	Location	Data Type	Original Source
Confining Unit	**All Confining Units**	**0.005**	**$6.00*10^{-5}$**	**0.0064**		**Model Calibration**	**This Study**
	Woodbridge Clay Member of Raritan Formation		$2.62*10^{-6}$ to $1.1*10^{-2}$		Southeastern Middlesex County to Northern Monmouth County	Model Results	Farlekas, 1979
			$2.60*10^{-2}$		South Brunswick Twp. Middlesex County	Aquifer Test and Model Results	Farlekas, 1979
	Merchantivelle Formation and Woodbury Clay		$1.13*10^{-6}$ to $1.83*10^{-5}$		Fort Dix, Burlington County	Laboratory Tests	Nichols, 1977a
	Merchantivelle Formation and Woodbury Clay		$1.1*10^{-6}$ to $4.3*10^{-6}$		Lakewood, Ocean County	Laboratory Tests	Nichols, 1977a
	Merchantivelle Formation and Woodbury Clay		$1.31*10^{-6}$		Northern Coasal Plain, New Jersey	Model Results	Nichols, 1977a
	Merchantivelle Formation and Woodbury Clay		$2.6*10^{-7}$ to $5.2*10^{-4}$		New Jersey Coastal Plain	Model Results	Luzier, 1980
	Englishtown Formation, clayey silt lithofacies		$5.80*10^{-7}$		Lakewood, Ocean County	Laboratory Tests	Nichols, 1977a
	Marshalltown Formation		$2.60*10^{-4}$		Fort Dix, Burlington County	Laboratory Test	Nichols, 1977a
	Marshalltown Formation		$4.90*10^{-4}$		Lakewood, Ocean County	Laboratory Test	Nichols, 1977a
	Marshalltown Formation and Wenonah Formation		$5.7*10^{-6}$ to $2.4*10^{-5}$		Brick Township, Ocean County	Laboratory Test	Nichols, 1977b
	Marshalltown Formation and Wenonah Formation		$1.50*10^{-5}$		Northern Coastal Plain, New Jersey	Model Results	Nichols, 1977a
	Navesink Formation		2		Arneytown, Burlington County	Laboratory Tests	Rush, 1968
	RedBank Sand		$1.30*10^{-1}$		Arneytown, Burlington County	Laboratory Test	Rush, 1968
	Hornerstown Sandy		$3.0*10^{-3}$ to $2.0*10^{-2}$		Arneytown, Burlington County	Laboratory Test	Rush, 1968

3.4.5 Raritan Bay uppermost Pleistocene to Holocene Geology

In order to constrain the geometry of the Quaternary section, data were compiled from the coreholes located on Sandy Hook (Johnson et al., 2018; Miller et al., 2018), shallow seismic surveys offshore Sandy Hook collected by the New Jersey Geological and Water Survey (NJGWS; Unpublished), and surficial geologic maps (Stanford, 1992, 1995, 1999, 2009; Stanford et al., 1998). Unlike most of the New Jersey Coastal Plain, the stratigraphy beneath Sandy Hook includes a complex and unusually thick (84+ m at the northern end), young (<13,350 cal yr BP) Quaternary section (Johnson et al., 2018). Much of the interpretation of this unit is derived from drilling at Sandy Hook and the deglacial history of the region. At the North Maintenance Yard on Sandy Hook (Fig. 2.1), the Cretaceous sediments are overlain by 3 m of basal gravel interpreted as postglacial outwash gravels. Though no radiometric dates constrain this unit, it is thought to have been deposited <20 ka. These gravels are overlain by a rapidly deposited section of silts. The 25 m of silts were deposited between 13,350 and 13,150 cal yr BP, and are interpreted to be estuarine.

Based on the Quaternary stratigraphy at Sandy Hook (Miller et al., 2018, Johnson et al., 2018), the model assumes that for elevations <40 mbsl the Quaternary unit is confining for the Quaternary section under Raritan Bay. Above 40 mbsl, the model assumes that the Quaternary sediments are an aquifer. Based on borings landward in Raritan Bay (MacClintock and Richards, 1936; Stanford, 1992; Stanford, 1995; Stanford, 1999; Stanfrod; 2009; Stanford et al., 1998), this may overestimate the presence of coarse-grained material under Raritan Bay. The sands may be limited to the immediate vicinity of Sandy Hook, which would result in an underestimate of the amount of highly

compressible material around Sandy Hook and thus an underestimate of the potential subsidence.

3.4.6 Recharge Package

Recharge from precipitation is the source for the groundwater system. The recharge package (Harbaugh, 2005) was used because in New Jersey the rate of recharge is positive (precipitation > evapotranspiration). Several publications have given estimates of the rate of recharge for various regions of New Jersey. Pucci et al. (1994) show ~114 cm of annual rainfall. The authors suggest that approximately half is lost to evapotranspiration. The NJGWS has published maps of groundwater recharge for each of the counties in the state. In Monmouth County, nearest the area of interest, the recharge rate ranges from 0 to 46 cm/yr, for the majority of the county the range is 30 to 41 cm/yr range (French, 2004a). In Ocean County, French (2004b), reported a rate of 38 to 41 cm/yr in the southwest portion of the county and 30 to 36 cm/yr in the northeast. Through calibration of the model (discussed in section 3.4.10), we determined that a recharge rate of 26 cm/yr over aquifers and 8.7 cm/yr over the exposed confining units made the model best fit the well observations.

3.4.7 Fluvial Systems – Constant Heads and Drain Packages

The model includes 31 fluvial systems, which act as sinks, removing water from the groundwater system. The locations for the rivers were taken from the NJDEP State Rivers for New Jersey (Third order or Higher) (1993) and their elevations at various points along their paths were estimated from Google Earth (2019; https://www.google.com/earth/).

The rivers were simulated using a mixture of constant head and drain features in MODFLOW (Harbaugh, 2005). Ideally, all of the river systems in New Jersey would be simulated using the Constant-Head Package (Harbaugh, 2005). This is because it requires fewer input parameters that are difficult to obtain. However, the downside is that the Constant-Head Package can result in rivers acting as sources, while in New Jersey rivers should act as sinks because the water table is generally higher than the stream bed (Martin, 1998).

To ensure that the rivers were only acting as sinks, we used the ZoneBudget tool (Harbaugh, 2005) within MODFLOW to determine the flux of water entering and exiting the model through each of the fluvial systems. We found at least two scenarios where rivers tended to act as sources. The first were cases where there was a large amount of localized pumping near the river and the second was for rivers at relatively high elevations near their headwaters.

When our analysis using ZoneBudget revealed a river segment that was acting as a source, we first reevaluated the elevations of the constant head nodes of that river using Google Earth and made certain that they were at the lowest reasonable elevation. We often lowered the elevation of the river node as much as 5 m below the elevation reported by Google Earth at forested locations. This was justified by testing the elevation of the forest against adjacent open spaces.

If, after lowering the constant-head elevations of the river segment, it was still acting as a source, we converted segments of the river to a drain using the MODFLOW Drain Package (Harbaugh, 2005). While the Drain Package only allows water to be removed from the model, it requires the user to input the river length, width, bed

thickness, and bed conductivity for each river segment in order to calculate the flux of water through the riverbed. While this introduced more uncertainty, it was necessary to ensure unidirectional flow of water out of the model through the river systems. Using the ZoneBudget Tool we calibrated the conductivity of the converted river segments such that the amount of water being removed from the model by the drain was roughly equal to the net amount of water being removed from the model by the river segment as a constant head before it was converted. We found that Equation 3.2 did the best job at approximating the conductance of the river segments in each cell and kept things simple by having one universal equation for all drains.

$$\text{Conductivity} = 2 * K_z * \text{ObjectIntersectLength} \qquad \text{Equation 3.2}$$

In equation 3.2, the constant "2" is a combined term that represents both the river width and the bed thickness (each in m), Kz is the vertical hydraulic conductivity (m/d) in each grid cell and ObjectIntersectLength is the length (m) of the river segment in that grid cell. This equation was used in each model cell with a river segment simulated by the drain package to set the drain conductance. By following this process of lowering and, if necessary, converting river segments from constant heads to drains, we ensured that no more than 1% of the flux from each river segment was into the model.

3.4.8 Observation Wells

Data from observation wells were used to constrain the model**.** Monthly historical head observations for wells throughout the model domain were downloaded from the U.S. Geological Survey's Groundwater Historical Instantaneous Database for the Nation (USGS, 2019). Within Middlesex, Monmouth, and Ocean counties there were 3332 observation wells with a total of 44750 observations. The database contained some wells

with reference points in elevation sea level while others were referenced to land surface. For those the latter, we extracted their approximate surface elevations from the NJDEP 100m Digital Elevation Grid for New Jersey (2002) and corrected each so that it was referenced to elevation above mean sea level. The monthly data were then converted into annual averages for the transient model and a 10-year average from 2006-2015 for a steady state calibration version of the model. The data were then gridded with Matlab to match the model grid, taking the averages of multiple observations in the same model grid cell over the same time period. This prevented large variations in observations within a single grid cell. This was particularly necessary for parts of the model with coarse (1 km^2) grid cells. The full MATLAB script is available in the supplement.

For the 10-year average there were 4222 observations prior to gridding. After gridding the data, there were 521 cells with an observation in each. For the annual data set, there were a total of 26,169 observations prior to gridding. Once gridded, this resulted in a total of 8,011 observations. Observations in the model grid began in 1916, with sporadic observations until the 1920s. By 1962 there were observations in at least 50 of the model grid cells and after 1978 there were at least 75 model cells with observations in them for the remainder of the modeled period with some years reaching over 400.

3.4.9 Pumping Wells

Pumping wells were incorporated into the model as one of the primary means for removal of water from the model. All available annual pumping records for the model domain, between 1880 and 2015, were provided by the New Jersey Department of Environmental Protection. Similar to the observation wells, there was a mix of reference formats, and the same process was used to convert all data to be elevation above mean

sea level. Two data sets were created: the first was a 10 year average of pumping between 2006 and 2015 for the steady state calibration model, and the second was an annual pumping data set for the transient model. There were records from 2,041 pumping wells in Monmouth, Ocean, and Middlesex Counties with a total of 34,191 annual rates. The earliest recorded pumping was from 1918. Starting in 1960, recorded pumping began to increase rapidly from <100,000 m^3/yr to ~650,000 m^3/yr by 2015.

The pumping wells at Sandy Hook were not included in the data set provided by the NJDEP. We used historical records and driller's logs to estimate the pumping rates and locations between 1906 and 2015. From historical records and drilling reports, we determined that there have been a total of 5 wells or sets of wells at Sandy Hook servicing Fort Hancock and now Gateway National Recreation Area. We designate them SHK1-SHK5. The first "well" included in the model represents a set of 36 artesian wells drilled to a depth of ~ 108 mbsl (Bearss, 1981). These wells were active from 1896 to 1910 when they went dry and were replaced. The second well (SHK2) was drilled in 1907 to a depth of ~225 mbsl. The third well (SHK3) was drilled in 1911 to 243 mbsl (Kasabach and Scudder, 1961) to replace the failing artesian wells from 1896 (Bearss, 1981). There is no record of the exact date that SHK2 and SHK3 went offline, but we assume that it was when SHK4 came online in 1941. SHK4 was drilled to a depth 150 mbsl (Kasabach and Scudder, 1961). SHK5 was drilled in 1971 and we assume that it replaced the 1941 well. It was drilled to 256 mbsl and is still active today (unpublished, on file at the NJGWS).

For the first portion of the pumping history, while Fort Hancock was still in operation between 1896 and 1974, we were able to determine the population on the base

(Fig. 2.8B) at various times throughout its history from historical records (e.g. Bearss, 1981; Johnson et al., 2018). Occasionally we were able to tie the base's population to records of its water requirements and from this we could begin to estimate the water usage per person. When the base was first build it had a population of 400 people and used 568 m^3/d (150,000 gal/d), resulting in water consumption of 1.4 m^3/d per person (375 gal/d per person) (Bearss, 1981). By 1910, the population had doubled to 800 full time residents and the water usage had increased to 757 m^3/d (200,000 gal/d) (Bearss, 1981). This resulted in 0.94 m^3/d per person (250 gal/d per person). We chose to use the latter as an estimate of the per person pumping rate for approximating Fort Hancock's pumping rate records. This may seem like a lot of water, but the base not only provided water for the individuals but it also had to provide water for boilers, steam locomotives, and even thousands of gallons per minute for watering the firing range before testing munitions (Bearss, 1981). For time periods when two wells were active, we split the estimated pumping rate evenly between the two.

We also estimated the rate of withdrawal for Gateway National Recreation Area, which opened after Fort Hancock was decommissioned in 1971. Similar to the estimate for the military base, we used the annual number of visitors per year and an approximation of the amount of water that each person would likely use per day visiting the park. This number must attempt to include use of the showers, restrooms, and other facilities at Sandy Hook by the daily visitors as well as the permanent population of Sandy Hook that includes a U.S. Coast Guard Station, a small school, several small offices, a ranger station, and the facilities management for the park. In light of this we used a rate of 0.1893 m^3/d per person (50 gal/d per person). Due to the uncertainty for

both civilian use during the post Fort Hancock years and the military use during the Fort's operation we ran sensitivity analyses to determine how responsive the subsidence at Sandy Hook was to our choice of pumping rates.

3.4.10 Calibration

In order to improve the model's ability to simulate the real world, some of the hydrologic properties in the model were calibrated in two sets of calibration runs. For the first set, the model was set up as a steady state model. The steady state model simulated the average conditions between 2006 and 2015. It uses the 10-year average of the pumping rates from each of the wells and tests the resulting simulated heads against the gridded 10-year averages of the observation wells. In the 1980s, as people became aware of the need to manage and conserve water resources, there was a shift in pumping from an emphasis on pumping from the deep aquifers to pumping in the more easily recharged shallow aquifers (dePaul et al., 2008). The 2006-2015 time period was chosen to avoid residual draw down from pre-1980 overuse of the deeper aquifers. When calibrating the model, we compared the observed head to the simulated head. With this comparison we could use several metrics to gauge model improvement. These included the mean residual (residual is the difference between the simulated and observed head value), the root mean squared residual, the relative root mean squared residual, and graphs illustrating these metrics against formation, depth, and location. Figure 3.6 is an example of one such graph illustrating the observed head vs. the simulated head and color coded by formation for our fully calibrated transient model.

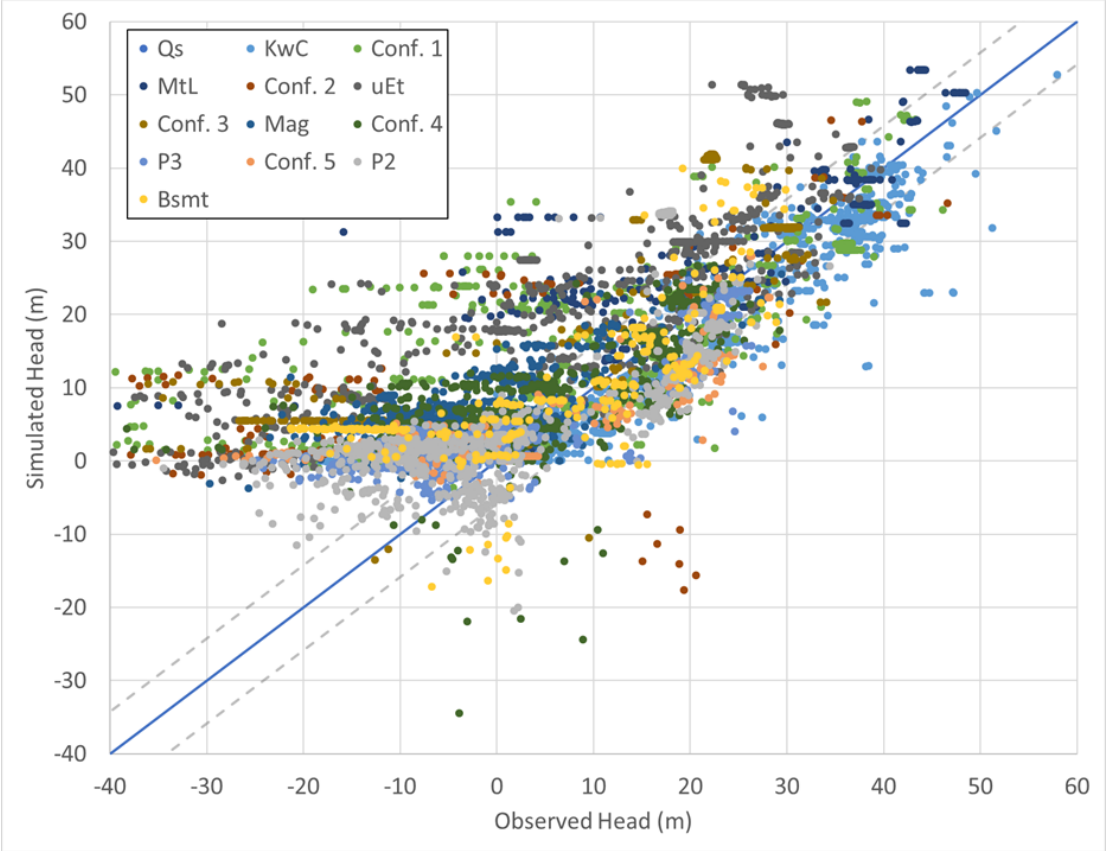

Figure 3.6: Graph of simulated head vs. observed from calibration in the steady state . The data points are colored by formation. The blue line indicates the target 1:1 line where the simulated results match the observed heads. This model run is the final transient model with all of the hydrologic parameters calibrated. The dashed lines are ±5m from the 1:1 line.

The steady state version of the model was used to calibrate the recharge values and the hydraulic conductivities. Recharge was calibrated first, followed by hydraulic conductivities. These properties were calibrated by beginning with published values from Martin (1998) and then adjusting them up and down incrementally. After each model run we evaluated the results and, if the change improved the model results as compared to the head observations, we continued to the next increment. If not we started moving the

values of the property back the other direction in smaller increments until we reached the best possible result. We also stopped if we reached the limits of what was reasonable. We determined what was reasonable based on the range of published values for each property.

Once the recharge rates were calibrated, we began to calibrate the hydraulic conductivities. Initially we assumed that all aquifers and all confining units had the same conductivity values. We assumed a 1:10 anisotropy ratio for the aquifers and a roughly 1:100 anisotropy ratio in the confining units. We began by adjusting the conductivity value assigned to all of the confining units. Once we achieved the best possible result, we began to adjust the conductivity value assigned to all of the aquifers. After reaching the best possible result we began to calibrate each of the aquifers individually beginning at the surface, working down section.

When the steady state parameters were all calibrated, we converted the model from steady state to transient for the second set of calibration runs in order to calibrate the storage parameter values. For the transient model we used the annual pumping records and the gridded annual observations with the conductivity and recharge values calibrated in the steady state version of the model. The first time step (1885), with no wells pumping, was set as a steady state time step and used to set initial conditions for hydraulic head throughout the model. The transient model had 1-year stress periods broken up into 1-day time steps with a multiplier of 4, such that for each stress period there were 5 time steps when calibrating using the transient version of the model, we compared the observed head to the simulated head at each time step. Similar to the hydraulic conductivities, we used one value for all of the confining units and one value

for all of the aquifers. Once these values were calibrated we activated the MODFLOW SUB Package to begin calculating the regional subsidence.

3.4.11 MODFLOW Subsidence and Aquifer-System Compaction (SUB) Package

We used the MODFLOW Subsidence and Aquifer-System Compaction (SUB) Package (Hoffmann et al., 2003) to simulate aquifer and confining unit compaction. The SUB Package is designed to calculate the change in thickness of each model layer in response to changes in effective stress (hydraulic head as a result of changing fluid pressure). The package essentially solves Equation 3.3 for each cell at each time step where Δb is the change in thickness, S_k is the skeletal storage coefficient, and Δh is the change in hydraulic head.

$$\Delta b = S_k * \Delta h \qquad \text{Equation 3.3}$$

It then sums these values to calculate the total vertical subsidence for each time step. The package requires that the user input a starting compaction, an initial stress (initial head), a skeletal elastic storage coefficient (S_{ske}), and a skeletal inelastic storage coefficient (S_{skv}) (Hoffmann et al., 2003). For the starting compaction, we assume that no compaction occurred prior to the start of the model (1885) and thus assign a value of 0. For the initial stress we chose to use the head values from the pre-pumping steady state model run. The SUB package can simulate both inelastic (unrecoverable) compaction and elastic (recoverable) compaction/expansion of each layer. The skeletal elastic storage coefficient is used when the head increases or decreases but is still above the minimum head for the duration of the model run (Hoffmann et al., 2003). The skeletal inelastic storage coefficient is used when the hydraulic head decreases. For the confining units we used the calibrated specific storage value times the layer thickness to assign a skeletal inelastic

specific storage. Following the examples given in Hoffmann et al. (2003), we set the elastic component of specific storage to 1/100th of the inelastic component for the confining units. For the aquifers, we did not apply an inelastic specific storage value and used the calibrated specific storage times the cell thickness to assign the skeletal elastic specific storage coefficient. While this likely underestimates the total compaction, it avoids making estimates of the thickness and composition of clay interbeds within the sands throughout the model domain. When defining the lithologic units, we limited the aquifers to only the cleanest sands based on interpretation from gamma logs to minimize the potential for fine grained, compressible interbeds.

3.4.12 Manual Calculation of Subsidence

As an independent check on the subsidence package we decided to also calculate the subsidence without using the MODFLOW SUB package. We used Equation 3.3 to calculate the total subsidence between pre-pumping conditions in 1885 and the end of the model duration in 2015. Using the total drawdown for each grid cell and the specific storage assigned to that cell we were able to calculate the total compaction between 1885 and 2015 and compare this value to the value generated by the SUB package.

3.5 Results

3.5.1 Subsidence at Sandy Hook, NJ

The model was run once with our calibrated estimates for all values, 16 times as part of a sensitivity analysis, and twice to evaluate the relative contributions of regional and local groundwater withdrawal to the rate of subsidence at Sandy Hook. Based on our best-calibrated parameters, the model shows that the pumping at Sandy

Hook and from the surrounding region is capable of producing a total subsidence of 42.4 mm (Fig. 3.7) between 1885 and 2015, most of which was between 1940 and 2015 (Fig. 3.8). The rate of subsidence may have exceeded 1.4 mm/yr between 1941 and 1944. After that the rate fell to between 0.1 and 0.2 mm/yr until the 1970s when the rate increased again to between 0.6 and 0.8 mm/yr and remained at that level for the rest of the modeled time period.

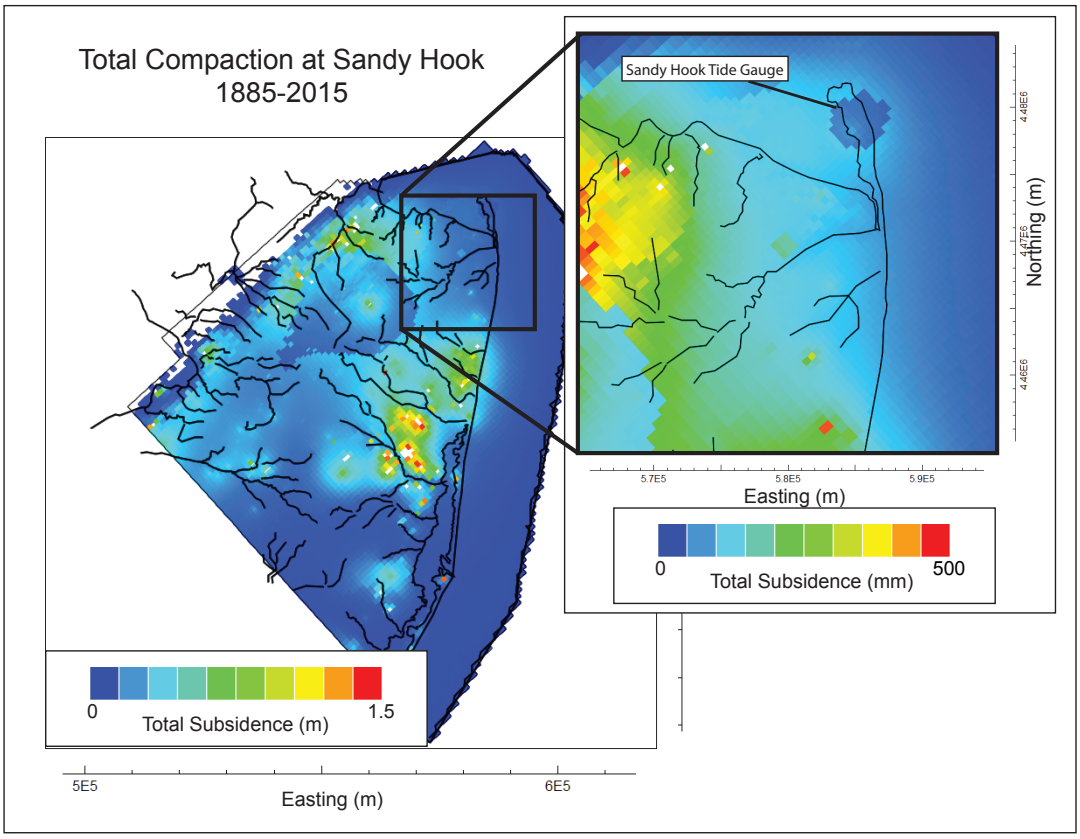

Figure 3.7: Map of modeled groundwater related subsidence. Note the different scale for total subsidence in the inset. The ring of low subsidence around Sandy Hook is likely due to the absence of Confining Unit 5 at Sandy Hook.

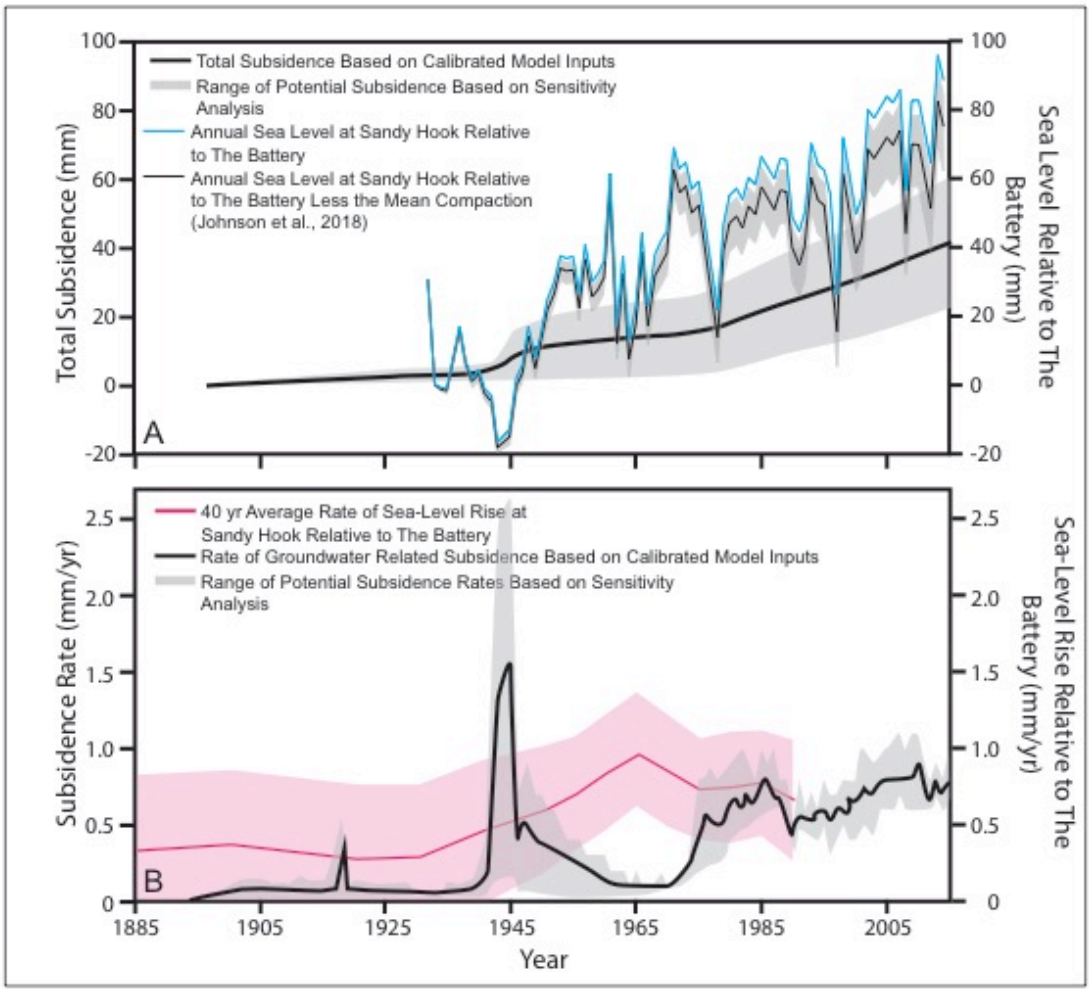

Figure 3.8: Groundwater related subsidence and sea-level rise at the Sandy Hook tide gauge. A is the total subsidence due to groundwater extraction (in mm) at the Sandy Hook tide gauge (black) with gray range from sensitivity analysis. This is plotted against sea level at Sandy Hook minus The Battery (blue) and sea level at Sandy Hook minus The Battery less the amount of autocompaction (thin black). B is the rate of subsidence at the Sandy Hook gauge due to groundwater extraction in mm/yr (black). The magenta shows the 40-year average difference in the rates of RSL rise at Sandy Hook and The Battery. Modified after Johnson et al., 2018.

3.5.2 Manual Calculation of the Total Compaction at Sandy Hook

To check the model results we chose to manually calculate the subsidence at Sandy Hook using only equation 3.3. To make this calculation we recorded the total drawdown in each of the model cells underlying the tide gauge, measured their thicknesses, and their storage parameters (Table 3.3). The result was a total of ~97 mm of total subsidence at the tide gauge, significantly higher than the SUB package results. Potential causes for the difference between the manual calculation and the results of the SUB package are discussed in 3.6.2.

Table 3.3: Manual calculation of subsidence at Sandy Hook tide gauge based on changes in head and the calibrated storage parameters. Calculation uses Equation 3.3.

Layer	Unit	Change in Head (ΔH, m)	Specific Storage Ss (/m)	Layer Thickness b (m)	Change in Layer Thickness Δb (mm)
1	Quaternary Sand	N/A			
2		0.000	0.000	5.000	0.00
3		0.000	0.000	5.000	0.00
4		0.000	0.000	10.000	0.00
5		0.000	0.000	10.000	0.00
6	Quaternary Muds	0.019	0.006	5.000	0.60
7		0.061	0.006	5.000	1.95
8		0.144	0.006	9.957	9.17
9		0.408	0.006	9.957	25.99
10	Magothy	0.724	0.000	32.840	0.02
11		0.724	0.000	32.840	0.02
12	Confining Unit 4	0.170	0.006	31.030	33.80
13		0.131	0.006	31.030	26.09
14	Potomac III	0.887	0.000	28.150	0.02
15		0.887	0.000	28.150	0.02
16	Potomac II	0.887	0.000	10.000	0.01
17		0.887	0.000	22.620	0.02
18	Basement	N/A			
19					

Total Subsidence (mm)	
Manual Calculation	Model Results
97.74	42

3.5.3 Sensitivity Analysis

Sensitivity analysis shows that the subsidence results are relatively insensitive to changes in specific storage and skeletal specific storage for both the confining units and aquifers (Figs. 3.9 and 3.10 respectively). Even with range of one order of magnitude difference from our calibrated storage values for the confining units the range of resulting

total compaction was 25.8 to 42.6 mm. The model was more sensitive to decreases in confining unit storage than it was to increases (Fig. 3.9). We explored a range of 4 orders of magnitude for the storage values in the aquifer units (Fig. 3.10) and found that the range of potential total subsidence was between 26 and 42 mm. However, the results suggest that only Ss values between 5E-7 and 1E-5 m^{-1} are viable, values >1E-5 m^{-1} can cause >2 mm/yr of expansion and values <1E-5 m^{-1} show very little variability in total compaction.

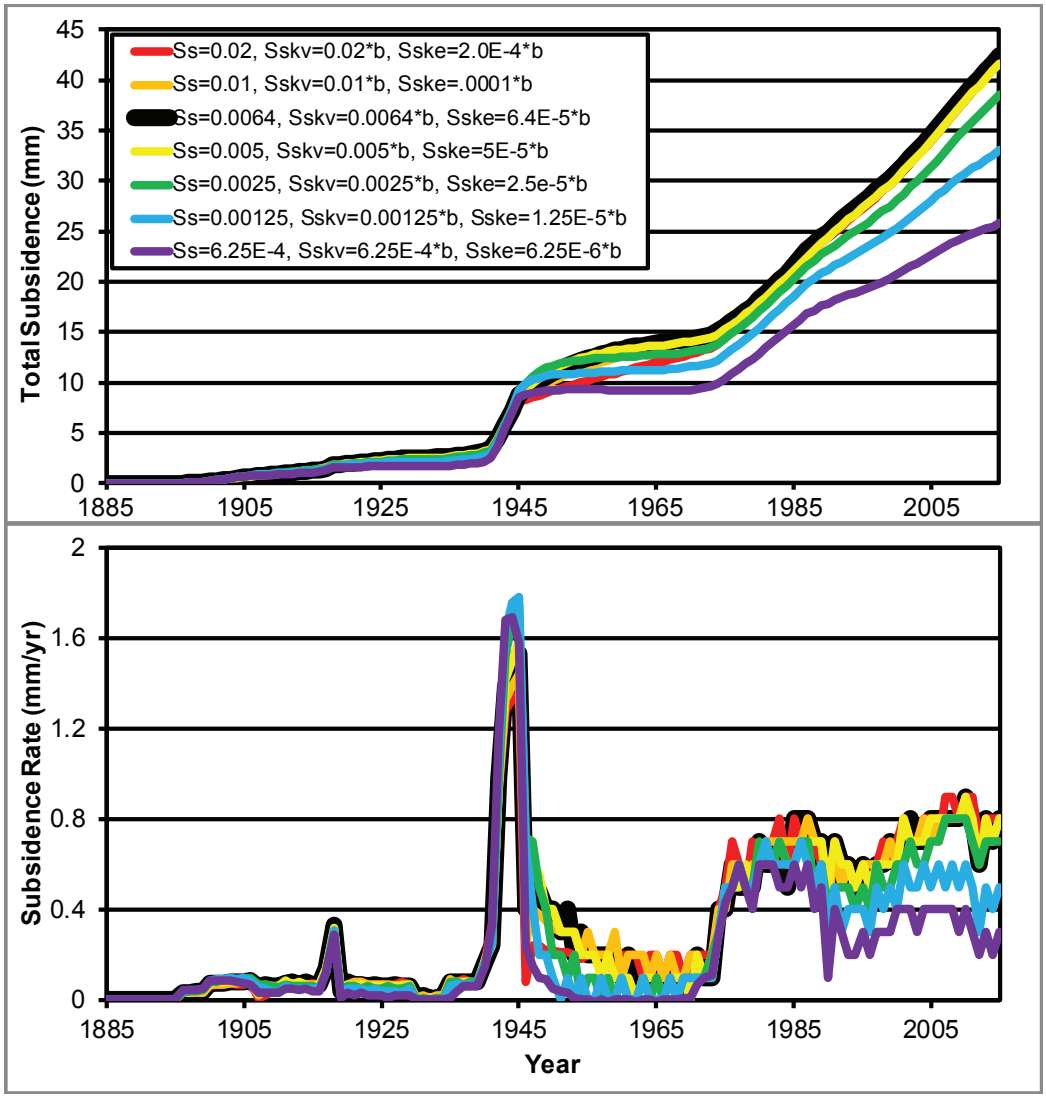

Figure 3.9: Model Sensitivity to changes in confining unit storage parameters. The top panel illustrates the total subsidence at each times step of the model in mm. The lower panel shows the yearly rate of subsidence in mm/yr.

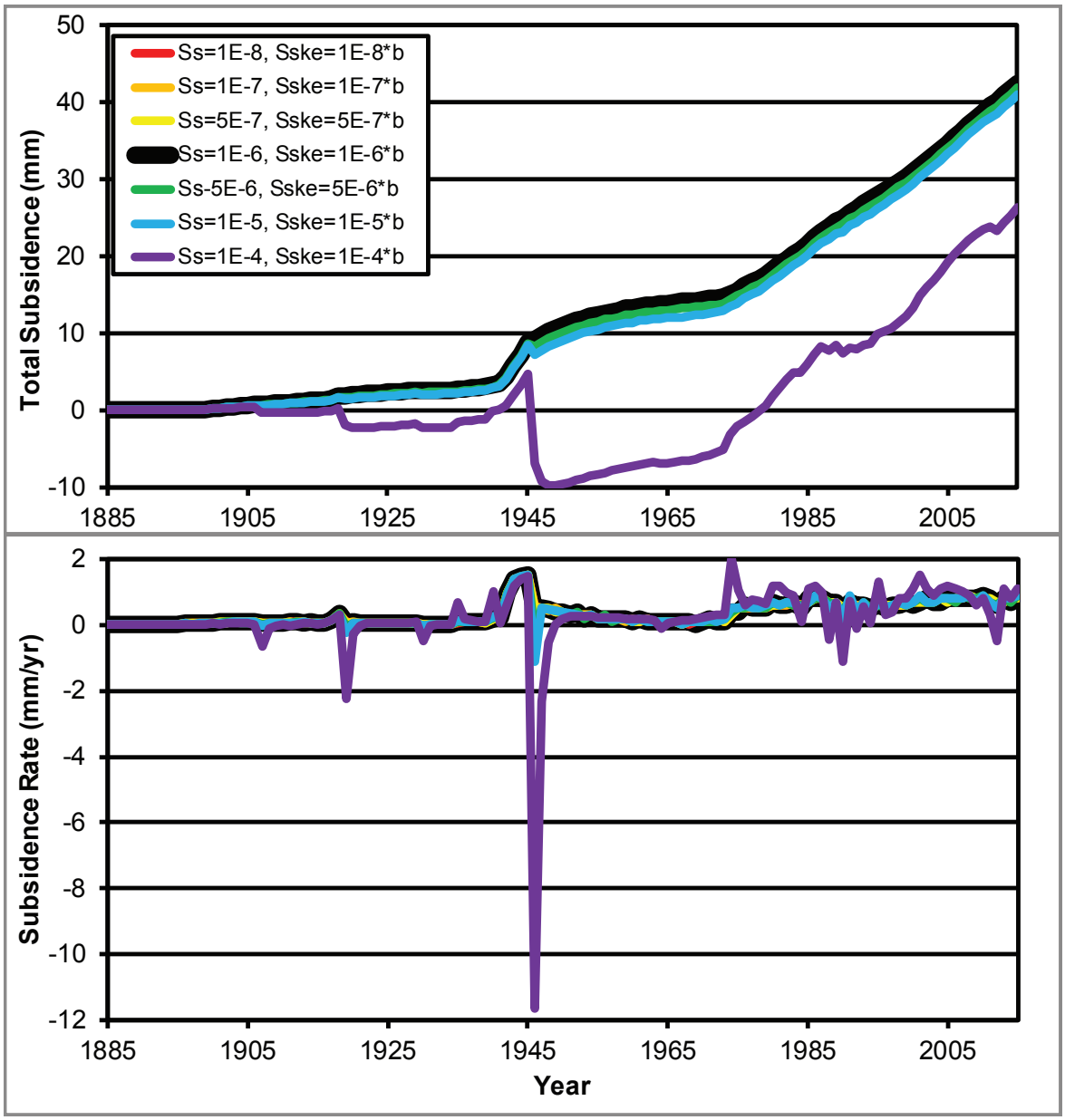

Figure 3.10: Model sensitivity to changes in aquifer unit storage parameters. The top panel illustrates the total subsidence at each times step of the model in mm. The lower panel shows the yearly rate of subsidence in mm/yr.

The model showed the most sensitivity to the pumping rate at Sandy Hook through time. Increasing the pumping rate to nearly double our initial estimate resulted in

61.5 mm of compaction, and decreasing the rate by 90% resulted in a total of 22.6 mm, a range of nearly 40 mm (Fig. 3.11).

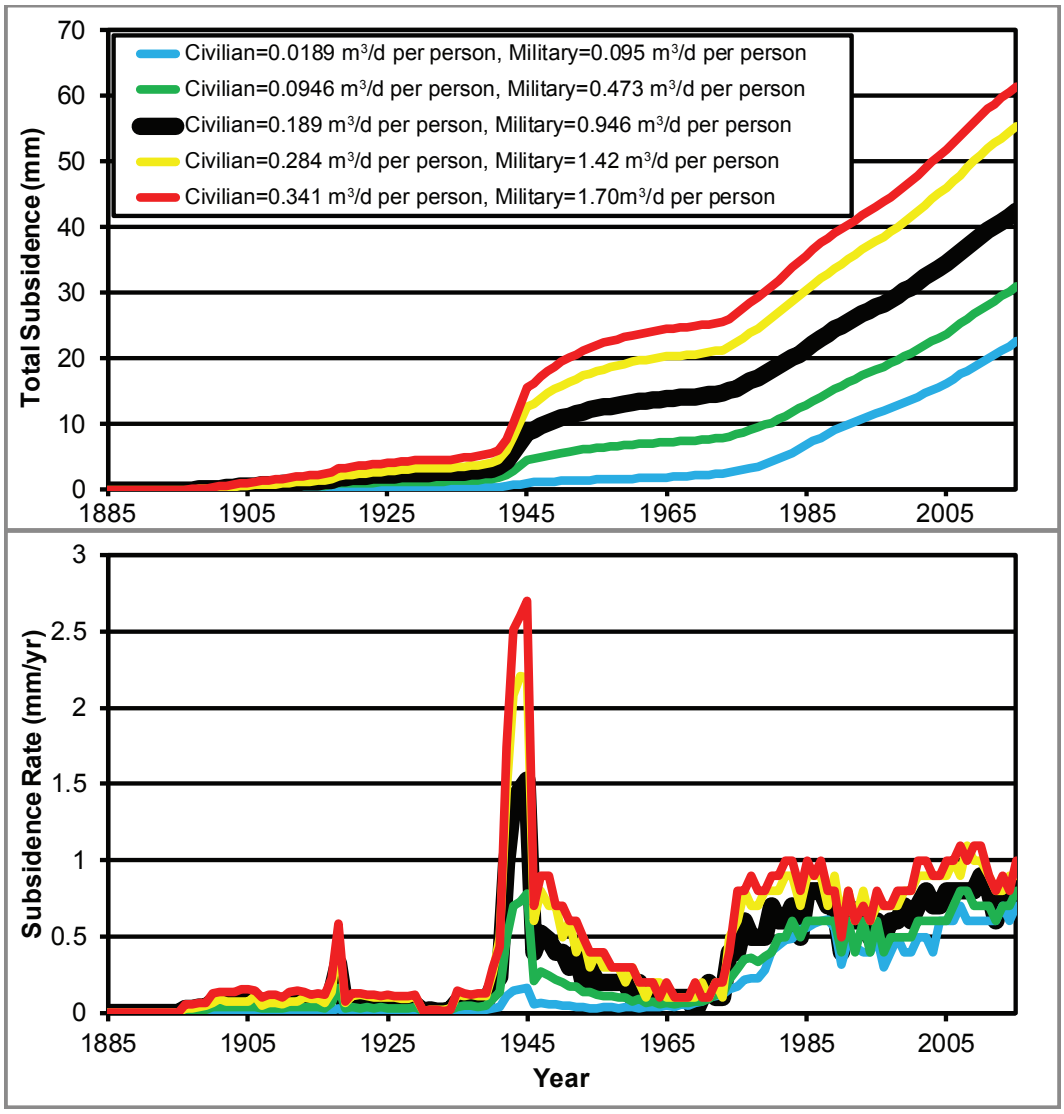

Figure 3.11: Model Sensitivity to pumping rate at Sandy Hook through time. The top panel illustrates the total subsidence at each times step of the model in mm. The lower panel shows the yearly rate of subsidence in mm/yr.

3.5.4 Contributions of Regional and Local Pumping to the Rate of Subsidence at the Sandy Hook Tide Gauge

We also tested the relative contributions of regional and local withdrawals by running three versions of the model. The first, labeled regional in Figs 3.12 and 3.13, does not use wells on Sandy Hook but leaves all other wells active. The second model run labeled local in Figs 3.12 and 3.13, disabled all wells outside of Sandy Hook and left the Sandy Hook wells active. Finally, the third run included all wells, both regional and local. Based on our calibrated model parameters with our middle estimate of pumping, the total subsidence from regional pumping alone is ~21 mm, while the total from local pumping is ~19 mm. The rate of subsidence from the local wells is significantly higher earlier in the study period. In the 1940s, subsidence rates reached 1.2 mm/yr before decreasing during the 1950s and 1960s. Regional pumping takes over as the dominant source of subsidence around 1965. Subsidence from regional and local pumping stabilized at ~0.5 mm/yr and ~0.2 mm/yr respectively from 1970-2015.

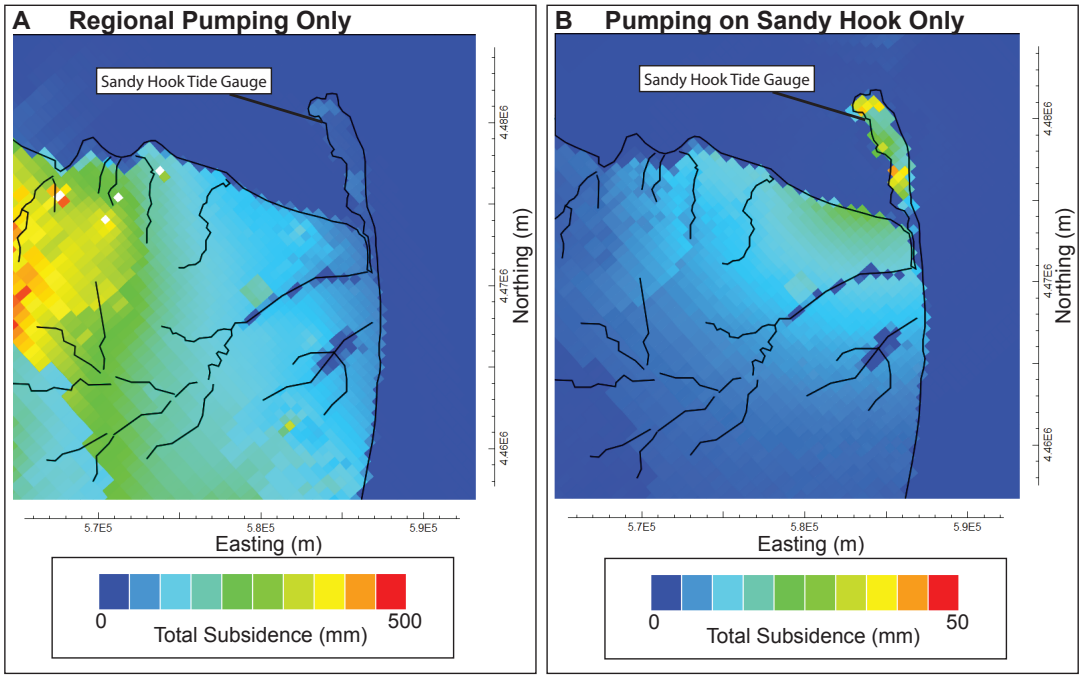

Figure 3.12: Maps of regional and local pumping related subsidence at Sandy Hook, NJ. A: Regional pumping model results for subsidence with all of the wells on Sandy Hook turned off. B: Local pumping model results with only the wells on Sandy Hook pumping. Note the difference in scales for total subsidence between the two maps.

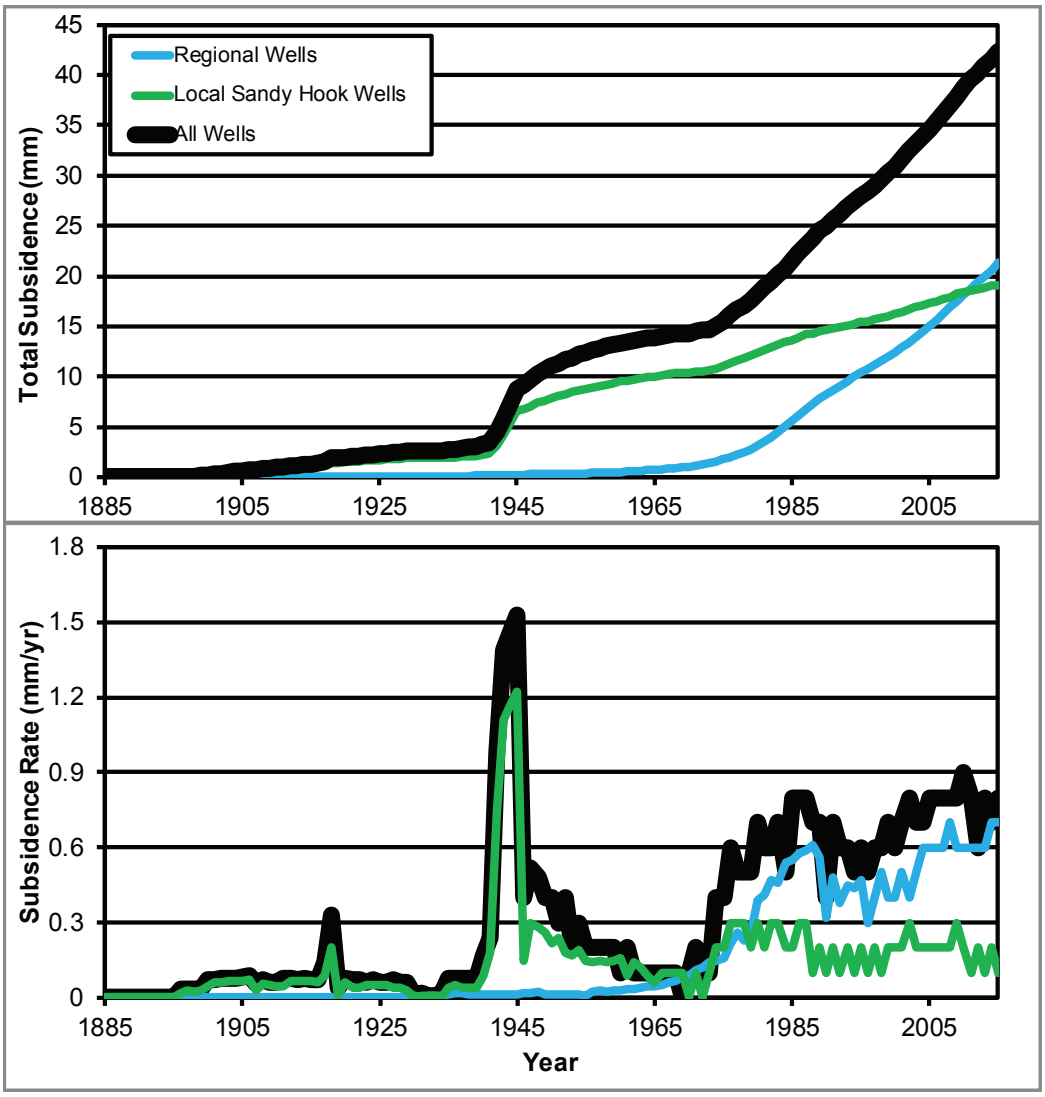

Figure 3.13: Contributions of regional and local groundwater extraction to subsidence at Sandy Hook. The top panel illustrates the total subsidence at each time step of the model in mm. The lower panel shows the yearly rate of subsidence in mm/yr.

3.6 Discussion

Previous studies have shown that the local processes, related to the underlying unconsolidated sediments at Sandy Hook must be responsible for the relatively the high rate of RSL rise measured at the tide gauge located there. There is a ~1 mm/yr difference in the rate of RSL rise between Sandy Hook and The Battery (26 km NW) and previous

work has identified GIA and autocompaction of sediments as two of the driving forces and quantified their contributions as ~0.1 and ~0.2 mm/yr of that difference respectively (Kopp, 2013; Johnson, 2018). Johnson et al. (2018) hypothesized that the remaining difference (~0.7 mm/yr) was caused by a combination of regional and local pumping resulting in a relatively high rate of subsidence at Sandy Hook. Our groundwater modeling approach to shows that this is likely the case and provides a reasonable range for the rate of groundwater related subsidence. Both regional and local groundwater extraction have played a significant role in causing subsidence at Sandy Hook between 1905 and 2015.

3.6.1 Groundwater Extraction, Subsidence and Sea-Level Rise at Sandy Hook, New Jersey

Sandy Hook is underlain by 400+ m of alternating aquifers and composite confining units of the New Jersey coastal plain (Sugarman et al., 2013; Johnson et al., 2018; Miller et al., 2018). Pope and Burbey (2004) showed that similar sediments of the Virginia coastal plain are susceptible to compaction when the aquifers are overtaxed. As the underlying sediments compact the land surface above subsides. In many places, such as the Great Valley of California, this results in aquifer degradation, including reduced porosity and permeability, and infrastructure damage due to surface deformation of the land surface (Galloway et al., 1998). When this occurs along a shoreline, as is the case at Sandy Hook, the rate of land subsidence adds to the rate of RSL rise. Our model shows that, at the Sandy Hook tide gauge, the 20th century average rate of groundwater related subsidence is 0.3±0.2 mm/yr (Fig. 3.8), 0.4±0.2 mm/yr for the duration of the tide gauge

record at Sandy Hook during the 20th century, and accelerating significantly to 0.7 mm/yr between 1960 and 2015.

Table 3.4: Sea level budget

Sandy Hook Relative Sea Level Budget

	20th Century		1993-2015	
	Rate	Source	Rate	Source
Sandy Hook Tide Gauge	4.0±0.5 mm/yr	Kopp, 2013	5.0 mm/yr	Linear Trend of Annual Data from PSMSL, 2019
The Battery Tide Gauge	3.0±0.3 mm/yr	Kopp, 2013	3.2 mm/yr	Linear Trend of Annual Data from PSMSL, 2019
GIA Difference Between Sandy Hook and The Battery	0.1±0.8 mm/yr	Kopp et al., 2013; Peltier et al., 2004	0.1±0.8 mm/yr	Kopp et al., 2013; Peltier et al., 2004
Sandy Hook - The Battery Less Difference in GIA	0.9±0.5 mm/yr (Kopp, 2013)	Johnson et al., 2018	1.7 mm/yr	

	Contributing Components at Sandy Hook			
GMSL Rise	1.4±0.2 mm/yr	Hay et al., 2015	~3	Chen et al. 2017 (1993-2014)
GIA (ICE-5G)	1.4 mm/yr	Kopp, 2013; Peltier, 2004	1.4 mm/yr	Kopp, 2013; Peltier, 2004
Autocompaction	0.16 mm/yr (90% C.I. 0.06-0.32 mm/yr)	Johnson et al., 2018	0.16 mm/yr (90% C.I. 0.06-0.32 mm/yr)	Johnson et al., 2018
Groundwater Induced Subsidence	0.3±0.2 mm/yr	This Study	0.7±0.1 mm/yr	This Study
Total of Components	3.3 mm/yr		5.4 mm/yr	

Based on our sensitivity analysis, where we ran multiple versions of the model in which we varied the model parameters that had the most uncertainty to the extent of their reasonable ranges we determined that the minimum average rate of subsidence of the 20th century is ~0.1 mm/yr and the maximum reasonable average rate was ~0.5 mm/yr. Through sensitivity analysis we determined that the model is relatively insensitive to changes in the storage parameters for both the confining units and the aquifers. Changing the storage parameters could result in a range of 22 mm of total subsidence, but, to do so, it took one or more orders of magnitude of difference in those parameters to significantly change the results. The results also show that changes in storage parameters cannot significantly increase the rate of subsidence beyond the modeled rate using the calibrated parameters. Not surprisingly, the model is very sensitive to the pumping rate at Sandy Hook. Unfortunately, this is one of the model parameters with the most uncertainty, due to lack of records. A single order of magnitude change in pumping rate above or below our estimate of 0.189 m^3/d per person for civilian and 0.946 m^3/d per person for military water use can result in total subsidence values between 22 and 62 mm. However, more than an order of magnitude is likely unreasonable since that would require the average water usage for visitors to Gateway National Recreation Area to use <0.019 m^3/d per person (<5 gal/d per person) or >0.341 m^3/d per person (>90 gal/d per person) and military usage of <0.095 m^3/d per person (<25 gal/d per person) or >1.70 m^3/d per person (>450 gal/d per person). These sensitivity tests provide a reasonable bracket for the minimum and maximum amounts and rates of subsidence at Sandy Hook that could be caused by groundwater extraction.

The previously estimated rate of subsidence at Sandy Hook due to groundwater extraction was 0.7 mm/yr (90% C.I. 0.3-1.2 mm/yr) based on the remaining difference between rates of RSL rise at Sandy Hook and The Battery after other components had been accounted for (Johnson et al., 2018). This model shows that the 20th century average rate of groundwater related subsidence is only 0.3 ±0.2 mm/yr. For the duration of the tide gauge record during the 20th century the subsidence was 0.4 ±0.2 mm/yr. The modern (2015) rate was ~0.7 mm/yr. Given the error bars in all of the estimates and models involved, this potentially closes the 20th century budget. However, it is possible that there is another local process at work at Sandy Hook that would close the remaining ~0.4 mm gap in the budget. One potential cause is changes in river discharge down the Hudson and East Rivers versus the Navesink (e.g. Piechuch et al., 2018a). However, looking at the modeled total subsidence through time at Sandy Hook in comparison to the sea-level curve at Sandy Hook minus The Battery (Fig 3.8A), the two records have very similar trends. This is particularly true for the period from 1945 to 2015. By subtracting the sea-level at The Battery from the sea-level rise at Sandy Hook, we isolate total contribution from local processes that only affect Sandy Hook. We also compare the record for the rate of RSL at Sandy Hook minus the rate at The Battery to the modeled rate of subsidence at Sandy Hook (Fig. 3.8B). While the rates do not match well, they have similar trends aside from prior to the 1940s and the 1960s. This could mean that there is an issue with the extrapolation of the tide gauge record prior to the installation of the gauge at Sandy Hook in the late 1930s. It could also be a function of the 40-year smooth on the data, which could make it appear that sea-level rise accelerated earlier than it did. After 1970 the two records begin to align well with similar rates of sea-level rise

and similar trends for sea-level and the total subsidence. This suggests, that at present, the model is a reasonable representation of the current processes taking place at Sandy Hook.

The groundwater model is likely a conservative estimate. The model uses a single hydraulic conductivity value for each lithologic unit across the whole model area. Martin (1998) used a variable hydraulic conductivity in her model. Kulpecz et al., (2008) showed that the sedimentary facies become finer grained and the depositional environment becomes deeper marine the farther east you go in the Cretaceous sediments of the coastal plain. Since the model uses an average of the conductivity value for each of the units across the entire model domain, the conductivity of the units under Sandy Hook is likely an overestimate. Similarly, the storage coefficients likely increase offshore as the sediments fine. Both of these factors could result in an underestimation of the total compaction. The model assumes no compaction in the aquifers and that there are no fine-grained interbeds within them. Addition of either of these features could add to the rate of compaction. Also, there is a lot of uncertainty in the records for the rate of groundwater extraction, particularly during the earlier part of the model run. There is likely unreported and/or underreported pumping that may explain this difference.

3.6.2 Comparison of Manual Calculation to SUB Package

The manual calculation of total subsidence resulted in ~97 mm between 1885 and 2015. This was more than double the 42 mm estimated by the SUB package in MODFLOW. This could be a result of several factors. When using the SUB package, the model assumes no compaction in the aquifers, while it was included in the manual calculation. While there was very little compaction in the aquifers in the manual calculation, it does contributed to the difference. Further, the manual calculation does not account for any

elastic expansion of the layers in response to recovery of hydraulic heads. This could reduce the total compaction significantly.

3.6.3 Comparison to CORS GPS Data

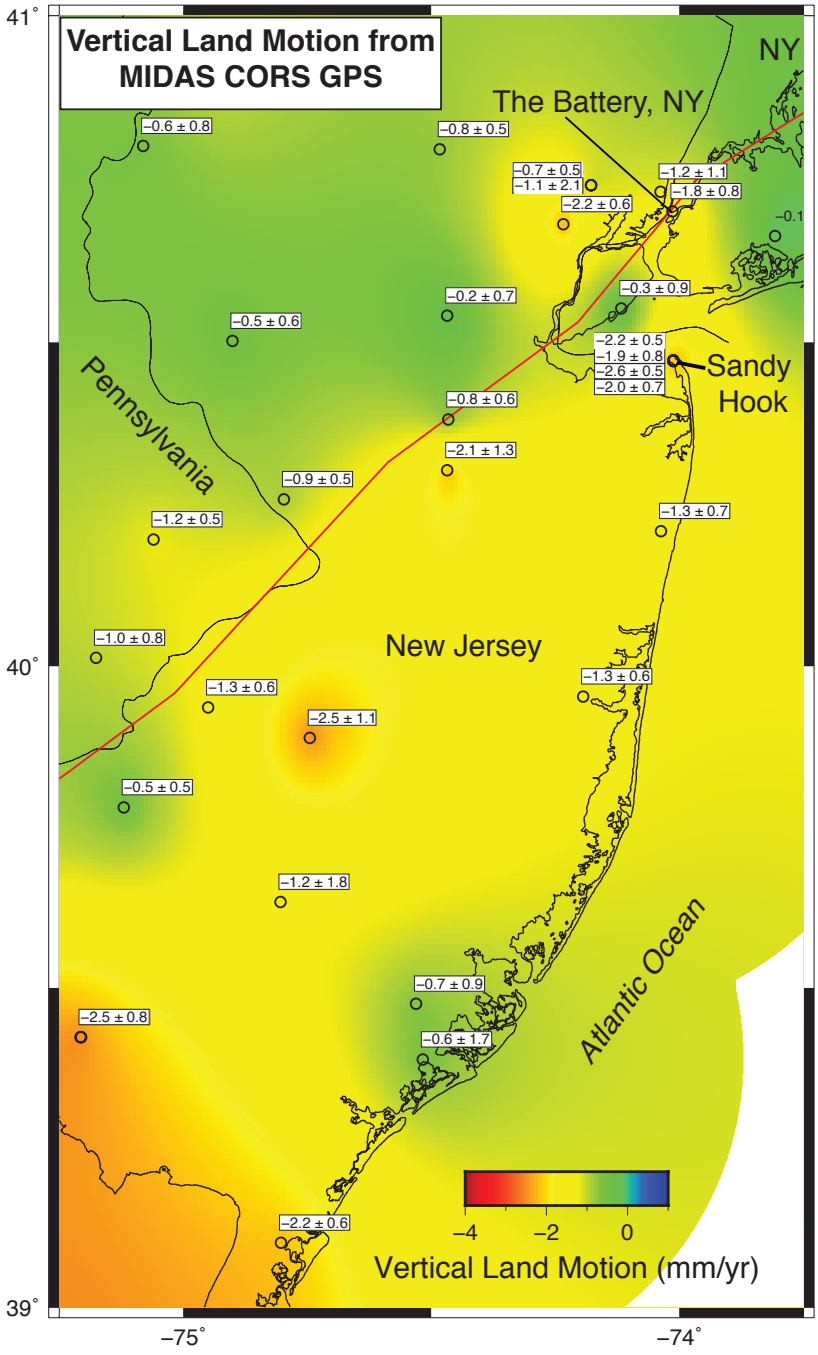

Figure 3.14: MIDAS CORS GPS measurements of vertical land motion. Circles indicate CORS GPS Stations. Those with multiple records display the rate calculated from each. Data are from Blewitt et al. (2016).

Tide gauge records provide a good measure of vertical land motion in locations, like Sandy Hook, where the signals from other processes can be isolated and removed. However, they are limited to coastal regions. While they have a relatively short record, CORS GPS stations provide a direct measurement of vertical land motion and can be used to test the results of this model. Figure 3.14 is a map of the vertical component of motion as measured by CORS GPS stations throughout New Jersey and the surrounding states published by Blewitt et al. (2016). We use it to qualitatively assess the spatial distribution of subsidence centers (Fig. 3.7) predicted by the model against areas of rapid subsidence shown by the GPS data (Fig. 3.14). The GPS data do not appear to show significant hot spots for subsidence. However, it is important to keep in mind that most of the GPS stations are co-located with population centers such as Toms River and Brick, NJ, areas that the model predicts would have higher rates of subsidence. As such the GPS map may be biased towards higher rates of subsidence across the whole region. Semi-quantitatively, the modern ~2.2 mm/yr rate of subsidence estimated from the 4 GPS stations at Sandy Hook is consistent with the budget that is established here and previously. Of the 1.9 to 2.6 mm/yr of recent subsidence recorded by the stations, 0.6-0.8 mm/yr is due to groundwater extraction between 2000 and 2015 as shown in this study, 0.1-0.2 mm/yr is due to sediment autocomapction (Johnson et al., 2018), and ~1.7 mm/yr is due to GIA based on the ICE-6G estimates of Peltier et al. (2015) (See Table 3.4 for summary of components). As such the GPS stations appear to be consistent with the model results, at least for Sandy Hook. Perhaps with more coverage the GPS measurements in the future CORS GPS could better assess the results of this model.

3.6.4 Regional Pumping vs. Local Pumping, Which has a Larger Impact?

One of the major questions raised by Johnson et al., 2018 was this: is regional pumping or local pumping the leading cause for subsidence at Sandy Hook? To answer that question we ran three versions of the model, one with all regional pumping but no pumping wells at Sandy Hook, one with only the pumping wells at Sandy Hook, and another with all of the pumping wells active. This produced a surprising result. In terms of total compaction, the two sources, regional and local pumping, have both contributed similar amounts of subsidence with 21 and 19 mm respectively. While they produced similar totals of subsidence, they both operated over different time periods and at different rates (Figs. 3.12 and 3.13). Local pumping began causing subsidence as early as 1920 and peaked in the early 1940s during World War II. After World War II, the rate of subsidence due to local pumping dropped significantly before increasing in early 1970s with the opening of Gateway National Recreation Area, and stabilizing at ~0.1-0.3 mm/yr for the rest of the model run. Regional pumping did not begin to affect the tide gauge at Sandy Hook until 1965 and increased to contributing 0.6-0.8 mm/yr by 1985 and continued for the remainder of the model. It is worth noting the total subsidence is greater than the sum of its parts. With 21 and 19 mm of total compaction from regional and local withdrawals respectively, this only sums up to 40 mm. That is short of the total of 42 mm when all the pumps are running. This suggests that there may be some interplay between the local and regional pumping that results in increased subsidence.

3.6.5 Model Limitations and Uncertainties

This model has a number of limitations. These include the coastal boundary condition near Sandy Hook, the rate of pumping at Sandy Hook and throughout the

region, and the subsidence package itself. The coastal constant head boundary presents an issue for this study because it is so close to our area of interest at Sandy Hook. This introduces the potential for boundary edge effects reaching Sandy Hook and affecting our results. We attempted to mitigate this by moving the boundary far enough offshore that there was no visible evidence of interference. For instance we tried to ensure that the cone of depression from Sandy Hook did not reach the coastal boundary. The boundary does act as a source along parts of the model, but this is consistent with the results of other studies that have shown that water is being brought towards the coast from offshore, resulting in saltwater intrusion in parts of Monmouth and Ocean Counties (Pucci et al., 1994).

We have already discussed some of the uncertainty in the pumping rates at Sandy Hook, but there are also uncertainties in the records for pumping throughout the region. During the calibration stages, we noticed early on, an inability for the model to simulate some of the lowest head observations in the model domain (Fig. 3.6). In some cases there are head observations as low as 20-40 mbsl and with reasonable parameters the model is unable to simulate these heads with the pumping records available. We attempted a model run with all of the wells pumping at the permitted capacity year round and this was still inadequate to reduce the simulated heads well below sea level. The well observations below sea level tend to be prior to the last decade. It may be that some wells, particularly historical wells, were not reported or their records were not kept over the years. Also, the pumping from wells could be under reported. As such this model may be underestimating the rate of subsidence at various points of the model run. Alternatively, the large grid cell size could be averaging out what would normally be steep local cones of depression.

Also, by using the NJ 100 m DEM to determine surface elevations for a number of the well observations and pumping wells, it could mean that in some cases we are using the 100 m average elevation which could be significantly different from the correct value in areas with steep topographic changes.

The relatively coarse nature of the model grid (1 km x1 km to 500 m x 500 m) in conjunction with the SUB package is another limitation of the model. While it is significantly less coarse than Martin (1998), who had <30 rows and columns, tour coarse gridding resulted in a number of observation wells and pumping wells being located in confining units. In reality these wells are likely all in aquifers. While most of the large pumping wells were manually moved from confining units to their appropriate aquifers in the model, there are still some small wells that are likely in confining unit cells or in cells surrounded on most sides by confining units. These resulted in isolated points of very high subsidence. Elsewhere the model resulted in 5 m of compaction in some cells with high rates of pumping. Similarly the subsidence package appears to have a difficult time simulating subsidence during peak pumping as illustrated by the pumping at Sandy Hook during World War II, where the rate of subsidence spiked to >1.5 mm/yr. While this can cause anomalous results for a single cell, the surrounding cells appear to be fine suggesting that while single cells with very large amounts of subsidence may be unrealistic and should be discarded; the regional signals are not significantly impacted.

Another important limitation of our model is that it does not account for compaction in aquifers or the presence of compressible interbeds within the aquifers. This keeps the model simple and avoids assumptions about the thickness, properties, and lateral extent of the interbeds. However, this makes the model estimate of the total

compaction and compaction rate a conservative one in that it likely underestimates the values.

3.7 Conclusions

There was a 1 mm/yr difference in the average rates of RSL rise between Sandy Hook, NJ and The Battery, NY for the 20th century. GIA and sediment autocompaction were responsible for ~0.3 mm/yr of that difference, leaving a 0.7 mm/yr (90% C.I. 0.3-1.2 mm/yr) gap between the two that was hypothesized to be the result of groundwater pumping (Johnson et al., 2018). This model shows that ~0.3±0.2 mm/yr are due to groundwater extraction. While this may indicate other local processes at work at Sandy Hook, it is within the error for the estimates and it could fill the budget. Further, results of this study align well with rates of sea-level rise for the latter half of the 20th century, which suggests that the mismatch may be due to an issue with either the model or the estimates of sea-level rise early in the 20th century record. Model results suggest that the total subsidence at Sandy Hook is a result of similar contributions from regional and local groundwater withdrawal. Up to 1965, primarily local pumping that drove the rate of subsidence; after 1965, regional withdrawals become the dominant source.

3.8 References

Anderson, H. R., and Appel, C. A., 1969, Geology and ground-water resources of Ocean County, New Jersey. New Jersey Department of Conservation and Economic Development, Division of Water Policy and Supply Special Report 29, p. 93.

Barksdale, H.C., Greenman, D.W., Lang, S.M., Hilton, G.S., and Outlaw, D.E., 1958. Ground-water resources in the tri-state region adjacent to the lower Delaware River. State of New Jersey Department of Convservation and Economic Development Special Report 13, p. 190.

Bearss, E.C., 1981. Historic resource study Fort Hancock 1895-1948: Gateway National Recreation Center New York/New Jersey, Denver, CO, National Park Service.

Blewitt, G., Kreemer, C., Hammond, W. C., and Gazeaux, J., 2016. MIDAS robust trend estimator for accurate GPS station velocities without step detection. Journal of Geophysical Research v. 121, n. 3, p. 2054-2068.

Cauller, S.J., Voronin, L.M., and Chepiga, M.M., 2016. Simulated effects of groundwater withdrawals from aquifers in Ocean County and vicinity, New Jersey: US Geological Survey, Scientific Investigations Report 2016-5045, p. 2328-0328.

Chen, X., Zhang, X., Church, J.A., Watson, C.S., King, M.A., Monselesan, D., Legresy, B., and Harig, C., 2017. The increasing rate of global mean sea-level rise during 1993-2014. Nature Climate Change v. 7, n. 7, p. 492-495.

Church, J.A., White, N.J., Konikow, L.F., Domingues, C.M., Cogley, J.G., Rignot, E., Gregory, J.M., van den Broeke, M.R., Monaghan, A.J., and Velicogna, I., 2011. Revisiting the Earth's sea-level and energy budgets from 1961 to 2008. Geophysical Research Letters v. 38, n. 18, p. 585-602.

Clark, J.A., Farrell, W.E., and Peltier, W.R., 1978. Global changes in postglacial sea level: a numerical calculation. Quaternary Research v. 9, no. 3, p. 265-287.

Cronin, T.M., Farmer, J., Marzen, R.E., Thomas, E., and Varekamp, J.C., 2014. Late Holocene sea level variability and Atlantic Meridional Overturning Circulation. Paleoceanography v. 29, p. 765-777, doi:10.1002/2014PA002632

Dangendorf, S., Marcos, M., Wöppelmann, G., Conrad, C.P., Frederikse, T., and Riva, R., 2017. Reassessment of 20th century global mean sea level rise. Proceedings of the National Academy of Sciences v. 114, n. 23, p. 5946-5951.

dePaul, V.T., Rice, D.E., and Zapeczam, O.S., 2008. Water-level changes in aquifers of the Atlantic Coastal Plain, predevelopment to 2000. U.S. Geological Survey Scientific Investigations Report v. 2007-5247, p. 1-88.

Domenico, P., and Mifflin, M., 1965. Water from low-permeability sediments and land subsidence. Water Resources Research v. 1, n. 4, p. 563-576.

Erban, L.E., Gorelick, S.M., and Zebker, H.A., 2014. Groundwater extraction, land subsidence, and sea-level rise in the Mekong Delta, Vietnam. Environmental Research Letters v. 9, n. 8, p. 1-6.

Farlekas, G.M., 1979. Geohydrology and digital-simulation model of the Farrington aquifer in the northern coastal plain of New Jersey: US Geological Survey Water-Resources Investigations Report 79-106, p. 1-55.

French, M., 2004a. Ground-Water Recharge for Monmouth County, NJ. Groundwater Recharge Series. New Jersey Geological Survey.

French, M, 2004b. Ground-Water Recharge for Ocean County, NJ. Groundwater Recharge Series. New Jersey Geological Survey.

Freeze, R.A., and Cherry, J. A., 1979. Groundwater. Prentice-Hall Inc., Englewood Cliffs, NJ.

Fuller M.L., 1908. Summary of the controlling factors of artesian flows. U.S. Geological Survey Bulletin v. 319, p. 1-44.

Galloway, D.L., and Burbey, T.J., 2011. Regional land subsidence accompanying groundwater extraction. Hydrogeology Journal v. 19, n. 8, p. 1459-1486.

Galloway, D.L., Hudnut, K.W., Ingebritsen, S., Phillips, S.P., Peltzer, G., Rogez, F., and Rosen, P., 1998. Detection of aquifer system compaction and land subsidence using interferometric synthetic aperture radar, Antelope Valley, Mojave Desert, California. Water Resources Research v. 34, n. 10, p. 2573-2585.

Galloway, D.L., and Sneed, M., 2013. Analysis and simulation of regional subsidence accompanying groundwater abstraction and compaction of susceptible aquifer systems in the USA. Boletín de la Sociedad Geológica Mexicana v. 65, n. 1, p. 123-136.

Gill, H.E., 1962, Ground-water Resources of Cape May County, New Jersey. , salt-water invasion of priciple aquifers. New Jersey Departmet of Conservation and Economic Development, Special Report 18, p. 1-171.

Goddard, P.B., Yin, J., Griffies, S.M., and Zhang, S., 2015. An extreme event of sea-level rise along the Northeast coast of North America in 2009–2010. Nature Communications v. 6, p. 6346.

Google LLC., 2019. Google Earth Pro V. 7.3.2.5776. <https://www.google.com/earth/versions/#download-pro>. Accessed March 5, 2019.

Gregory, J.M., Griffies, S.M., Hughes, C.W., et al., 2019. Concepts and terminology for sea level: mean, variability and change, both local and global. Surveys in Geophysics https://doi.org/10.1007/s10712-019-09525-z.

Gurnis, M., 1990. Bounds on global dynamic topography from Phanerozoic flooding of continental platforms. Nature v. 344, n. 6268, p. 754-756.

Harbaugh, A.W., 2005. MODFLOW-2005, the US Geological Survey modular ground-water model: the ground-water flow process. U.S. Geological Survey Techniques and Methods 6-A16.

Hay, C.C., Morrow, E., Kopp, R.E., and Mitrovica, J.X., 2015. Probabilistic reanalysis of twentieth-century sea-level rise. Nature v. 517, n. 7535, p. 481-484.

Herman, G.C., Canace, R.J., Stanford, S.D., Pristas, R.S., Sugarman, P.J., French, M.A., Hoffman, J.L., Serfes, M.S., and Mennel, W.J., 1998. Aquifers of New Jersey. Department of Environmental Protection Division of Science & Research, New Jersey Geological Survey, Open-File Map OFM-24, scale 1:500,000.

Hoffmann, J., Leake, S.A., Galloway, D.L., and Wilson, A.M., 2003. MODFLOW-2000 ground-water model--User guide to the subsidence and aquifer-system compaction (SUB) package. U.S. Geological Survey Open-File Report 03-233, p. 1-46.

Jablonski, L., 1959. Records of wells and ground-water quality in Monmouth County, New Jersey. New Jersey Department of Conservation and Economic Development, Water Resources Circular 2, p. 1-47.

Johnson, C.S., Miller, K.G., Browning, J.V., Kopp, R.E., Khan, N.S., Fan, Y., Stanford, S.D., and Horton, B.P., 2018. The role of sediment compaction and groundwater withdrawal in local sea-level rise, Sandy Hook, New Jersey, USA. Quaternary Science Reviews v. 181, p. 30-42.

Karegar, M.A., Dixon, T.H., and Engelhart, S.E., 2016. Subsidence along the Atlantic Coast of North America: Insights from GPS and late Holocene relative sea level data. Geophysical Research Letters v. 43, n. 7, p. 3126-3133.

Kasabach, H.F., and Scudder, R.J., 1961 Deep Wells of the New Jersey Coastal Plain. New Jersey Geological Survey,Department of Conservation and Economic Development, Geologic Resport Series 3, p. 1-62.

Kopp, R.E., 2013. Does the mid-Atlantic United States sea-level acceleration hot spot reflect ocean dynamic variability? Geophysical Research Letters v. 40, p. 3981-3985.

Kopp, R.E., Hay, C.C., Little, C.M., and Mitrovica, J.X., 2015. Geographic variability of sea-level change. Current Climate Change Reports v. 1, n. 3, p. 192-204.

Kopp, R.E., Kemp, A.C., Bittermann, K., Horton, B.P., Donnelly, J.P., Gehrels, W.R., Hay, C.C., Mitrovica, J.X., Morrow, E.D., and Rahmstorf, S., 2016. Temperature-driven global sea-level variability in the Common Era. Proceedings of the National Academy of Sciences v. 113, n. 11, p. E1434-E1441.

Kulpecz, A.A., Miller, K.G., Sugarman, P.J., and Browning, J.V., 2008. Response of Late Cretaceous migrating deltaic systems to sea level, tectonics, and sediment supply changes, New Jersey Coastal Plain, USA. Journal of Sedimentary Research v. 78, p. 112-129.

Luzier, J.E., 1980. Digital-simulation and projection of head changes in the Potomac-Raritan-Magothy aquifer system, Coastal Plain, New Jersey. U.S. Geological Survey Water-Resources Investigations 80-11, p. 1-72.

Lyttle, P.T., and Epstein, J.B., 1987. Geologic map of the Newark 1°x2° quadrangle, New Jersey, Pennsylvania, and New York. U.S. Geological Survey Miscellaneous Investigation Series I-1715, scale 1-250,000.

MacClintock, P., & Richards, H.G., 1936. Correlation of late Pleistocene marine and glacial deposits of New Jersey and New York. Bulletin of the Geological Society of America v. 47, n. 3, p. 289-338.

Martin, M., 1998. Ground-water flow in the New Jersey coastal plain. U.S. Geological Survey Professional Paper 1404-H, p. H1-H146.

Mennel, W.J. and Canace, R., 2012. New Jersey Geological Survey Hydro Database. Department of Environmental Protection (NJDEP), Division of Land Use Management, New Jersey Geological Survey, https://www.state.nj.us/dep/njgs/geodata/dgs02-1.htm. Accessed December 6, 2017.

Miller, K.G., Sugarman, P.J., Browning, J.V., Kominz, M.A., Olsson, R.K., Feigenson, M.D., and Hernández, J.C., 2004. Upper Cretaceous sequences and sea-level history, New Jersey coastal plain. Geological Society of America Bulletin v. 116, n. 3-4, p. 368-393.

Miller, K.G., Kopp, R.E., Horton, B.P., Browning, J.V., and Kemp, A.C., 2013. A geological perspective on sea-level rise and its impacts along the US mid-Atlantic coast. Earth's Future v. 1, n. 1, p. 3-18.

Miller, K.G., Sugarman, P.J., Stanford, S., Browning, J.V., Baldwin, K., Buttari, B., Dunham, B., Farazaneh, M., Filo, R., Gagliano, M.P., Horton, B., Gallegos, G., Graham, S., Johnson, C., Khan, N., Kulhanek, D.K., Lombardi, C.J., McKoy, K., McLaughlin, P.P., Monteverde, Jr., D.H., Stanley, J.N., Woodard, S., and Malerba, N., 2018. Sandy Hook site report, in Miller, K.G., Sugarman, P.J., Browning, J.V., et al., eds., Proceedings of the Ocean Drilling Program, Initial reports, Volume 174AX (Suppl.): College Station, TX, Ocean Drilling Program.

Minor, H.E., 1925. Goose Creek oil field, Harris Count, Texas. American Association of Petroleum Geologists Bulletin v. 9, n. 2, p. 286-297.

Nemickas, B., Carswell, L.D., and Trenton, N., 1976. Stratigraphic and hydrologic relationship of the Piney Point aquifer and the Alloway Clay Member of the Kirkwood Formation in New Jersey. U.S. Geological Survey Journal of Research v. 4, n. 1, p. 1-7.

Nichols, W. D., 1977a. Digital computer simulation model of the Englishtown aquifer in the northern coastal plain of New Jersey US Geological Survey Open-File Report 77-73, p. 1-101.

Nichols, W. D., 1977b. Geohydrology of the Englishtown Formation in the Northern Coastal Plain of New Jersey. U.S. Geological Survey Water-Resources Investigations Report 76-123, p. 1-62.

NJDEP, 2002. NJDEP Digital Elevation Grid for New Jersey (100 meter). NJ Department of Environmental Protection (NJDEP), Office of Information Resources Management (OIRM), Bureau of Geographic Information and Analysis (BGIA). https://nj.gov/dep/gis/digidownload/metadata/statewide/nj100mlat.htm Accessed January 16, 2018.

NJDEP, 1993. NJDEP State Rivers for New Jersey (Third Order or Higher). The New Jersey Depratment of Environmental Protection (NJDEP), Bureau of Geographic Information and Analysis (BGIA). https://www.state.nj.us/dep/gis/digidownload/metadata/statewide/stateriv.htm Accessed January 30, 2019.

NJGWS, Unpublished, Sandy Hook Seismic. New Jersey Geological Survey.

Owens, J.P., Sugarman, P.J., Sohl, N.F., Parker, R.A., Houghton, H.F., Volkert, R.A., Drake Jr, A.A., Orndorff, R.C., Bybell, L., and Andrews, G., 1999. Bedrock geologic map of central and southern New Jersey. U.S. Geological Survey IMAP 2540-B, scale: 1:100,000.

Peltier , W.R., Argus, D.F., and Drummond, R., 2015. Space geodesy constrains ice age terminal deglaciation. The global ICE-6G_C (VM5a) model. Journal of Geophysical Research. Solid Earth v. 120, p. 450-487. doi: 10.2003/3025JB011176.

Peltier, W., 2004. Global glacial isostasy and the surface of the ice-age Earth: the ICE-5G (VM2) model and GRACE. Annual Review of Earth and Planetary Sciences v. 32, p. 111-149.

Permanent Service for Mean Sea Level (PSMSL), 2019. Tide Gauge Data. http://www.psmsl.org/obtaining/ [20 July, 2019]

Piechuch, C.G., Bittermann, K., Kemp, A.C., Ponte, R.M., Little, C.M., Engelhart, S.E., and Lentz, S.J., 2018. River-discharge effects on United States Atlantic and Gulf coast sea-level changes. Proceedings of the National Academy of Science v. 115, n. 30, p. 7729-7734.

Poland, J., 1960, Land subsidence in the San Joaquin Valley, California, and its effect on estimates of ground-water resources. International Association of Scientific Hydrology Commission of Subterranean Waters Publication 52, p. 324-335.

Poland, J.F., and Davis, G.H., 1969. Land subsidence due to withdrawal of fluids. Reviews of Engineering Geology v. 2, p. 187-269.

Pope, J.P., and Burbey, T.J., 2004. Multiple Aquifer Characterization from Single Borehole Extensometer Records: Groundwater v. 42, n. 1, p. 45-58.

Pucci Jr, A.A., Pope, D.A., and Gronberg, J.M., 1994. Hydrogeology, simulation of regional ground-water flow, and saltwater intrusion, Potomac-Raritan-Magothy aquifer system, northern coastal plain of New Jersey. New Jersey Geological Survey, Geological Survey Report (GSR) 36, p. 1-209.

Rhodehamel, E.C., 1970. A hydrologic analysis of the New Jersey Pine Barrens region. New Jersey Department of Environmental Protection, Water Resources Circular 22, p. 1-35.

Rush, F.E., 1968. Geology and ground-water resources of Burlington County, New Jersey. New Jersey Department of Conservation and Economic Development, Division of WAter Policy and Supply, Special Report 26, p. 1-65.

Simms, A., Reynolds, L.C., Bentz, M., Roman, A., Rockwell, T., and Peters, R., 2016. Tectonic Subsidence of California Estuaries Increases Forecasts of Relative Sea-Level Rise. Estuaries and Coasts v. 39, p. 1571-1581.

Stanford, S.D., Witte, R. W., Braun, D.D., and Ridge, J.C., 2016. Quaternary fluvial history of the Delaware River, New Jersey and Pennsylvania, USA: The effects of glaciation, glacioisostasy, and eustasy on a proglacial river system. Geomorphology v. 264, p. 12-28.

Stanford, S.D., 2010. Onshore record of Hudson River drainage to the continental shelf from the late Miocene through the late Wisconsinan deglaciation, USA: synthesis and revision. Boreas v. 39, no. 1, p. 1-17.

Stanford, S.D., 2009. Surfical Geology of the Plainfield Quadrangle, Middlesex, Union, and Somerset Counties, New Jersey. New Jersey Geological and Water Survey, Open File Map 77. Scale 1:24000.

Stanford, S.D., Ashley, G.M., Russell, E.W.B., and Brenner, G.J., 2002. Rates and patterns of late Cenozoic denudation in the northernmost Atlantic Coastal Plain and Piedmont. Geological Society of America Buletin v. 114, n. 11, p. 1422-1437.

Stanford, S. D., 1999. Surficial Geology of the Perth Amboy and Arthur Kill Quadrangles, Middlesex and Union Counties, New Jersey. New Jersey Geological and Water Survey Open File Map 28, Scale 1:24000.

Stanford, S.D., Monteverde, D.H., Volkert, R.A., Sugarman, P.J., and Brenner, G.J., 1998. Geology of the New Brunswick Quadrangle, Middlesex and Somerset Counties, New Jersey. New Jersey Geological and Water Survey Open File Map 23, Scale 1:24000.

Stanford, S.D., 1995. Surficial Geology of the South Amboy Quadrangle, Middlesec and Monmouth Counties, New Jersey. New Jersey Geological and Water Survey Open File Map 19, Scale 1:24000.

Stanford, S.D., 1992. Surficial Geology of the Bound Brook Quadrangle, Somerset and Middlesex Counties. New Jersey. New Jersey Geological and Water Survey Open File Map 4, scale 1:24,000.

Sugarman, P.J., Monteverde, D.H., Boyle, J.T., and Domber, S.E., 2013. Aquifer correlation map of Monmouth and Ocean Counties, New Jersey. New Jersey Geologic and Water Survey. Geologic Map Series 13-1. Scale 1:150,000.

Sun, H., Grandstaff, D., and Shagam, R., 1999. Land subsidence due to groundwater withdrawal: potential damage of subsidence and sea level rise in southern New Jersey, USA. Environmental Geology v. 37, n. 4, p. 290-296.

USGS, 2019, USGS Groundwater Historical Instantaneous Data for the Nation: https://waterdata.usgs.gov/nwis/uv, U.S. Geological Survey. Accessed January 8, 2019.

Wilson, G., and Grace, H., 1942. The Settlement of London due to Underdrainage of the London Clay. Journal of the Institution of Civil Engineers v. 19, n. 2, p. 100-127.

Winston, R.B., 2009. ModelMuse: a graphical user interface for MODFLOW-2005 and PHAST. U.S. Geological Survey Techniques and Methods 6-A29, p. 1-52.

Yeh, P.J.F., Swenson, S., Famiglietti, J., and Rodell, M., 2006. Remote sensing of groundwater storage changes in Illinois using the Gravity Recovery and Climate Experiment (GRACE): Water Resources Research v. 42, no. 12, p. 1-7.

CHAPTER 4: Impacts of Late Pleistocene to Holocene Glacial Isostatic Adjustment on Paleochannels of the New Jersey Margin

Christopher S. Johnson[a,b], Gregory S. Mountain [a,b], Kenneth G. Miller [a,b]

[a]*Department of Earth and Planetary Sciences, Rutgers University, 610 Taylor Road, Piscataway, New Jersey 08854, USA;*

[b]*Institute of Earth, Ocean and Atmospheric Sciences, Rutgers University, 71 Dudley Road, New Brunswick, New Jersey 08901, USA*

Abstract

Previous studies have shown that the New Jersey Margin contains a record of Late Pleistocene to Holocene sea-level variations. Today, studies are focused on quantifying the relative contributions of processes including sediment compaction, groundwater related subsidence, and Glacial Isostatic Adjustment (GIA) to relative sea-level (RSL) rise. In New Jersey, GIA is thought to contribute ~1/3 of the average rate of 20th century RSL rise. However, GIA is primarily constrained by onshore records and modeling. To better understand the spatial and temporal variability of GIA, it is important that we consider all possible records. The inner continental shelf of New Jersey has experienced GIA related uplift and subsidence with each glaciation particularly for the large quasi 100 kyr advances of the last 800 kyr. This includes formation of a forebulge during times of ice sheet advance and retreat and subsidence as ice sheets withdrew. In

this paper, we examine the effects of the forebulge, on paleochannels of the New Jersey Margin. Previous studies have shown that paleochannels may record GIA in their orientations and incision depths. We integrate existing drillcore data from IODP Expedition 313 and high resolution acoustic sub-bottom profiles from *R/V Endeavor* cruise 370 with new 3D seismic data collected by *R/V Marcus G. Langseth* cruise 1510 (MGL1510) to assess if GIA has affected incision depth and orientations of channels formed between Marine Isotope Stages (MIS) 5 and 1 (125 ka to present). We compare channel orientations to ice sheet positions and estimated GIA fields during MISs 2, 4, and 5b to estimate the spatial effects of GIA during those times. We identify two distinct sets of paleochannels in the MGL1510 survey grid. Based on superposition and the work of Pico et al., (2018), we interpret the first be between 125 and 30 ka, and the second to be ≤30 ka. Incision depths from channels between 125 and 30 ka (40-60 meters below modern sea level) suggest these channels were too small and too far from the paleoshoreline to incise to base level. Thus, this set of paleochannels may indicate local paleotopography rather than GIA.. The channels in the MGL1510 survey area and those reported in the literature show a regional shift in channel orientations on the New Jersey margin as predicted by Knebel et al. (1979) and modeled by Pico et al. (2018). The channels between 125 ka and 30 ka have a north-south orientation, while channels <30 ka have a northeast-southwest orientation. This is consistent with a shift from an ~east-west trending forebulge during glaciations prior to 30 ka to a southeast-northwest trending forebulge during MIS2 that could have caused the landscape to dip southeast rerouting the drainage pattern.

4.1 Introduction

Quaternary sedimentation on the New Jersey continental shelf was not only strongly influenced by very large (up to 130 m) and rapid (>40 mm/yr) global mean sea-level changes, but also by large (10s m), rapid (with rates up to 10+ mm/yr) glacial isostatic adjustments (GIA). Relative sea-level is defined as sea surface height relative to the solid earth surface (Gregory et al., 2019). During RSL falls, when the shelf was subaerially exposed, widespread erosion and non-deposition resulted in regional unconformities (Ashley et al., 1991). During transgressive periods of RSL rise, highstand sediments were deposited, though it is often spatially and temporally discontinuous due to limited accommodation space. Relative sea-level changes on the New Jersey margin are a combination of global and regional effects.

Global mean sea level (GMSL) is the average RSL over the whole ocean (Kopp et al., 2015; See Gregory et al., 2019 for sea-level definitions). GMSL change is a product of tectonic changes to the ocean basin (Pitman and Golovchenko, 1983), ocean density changes(Church et al., 1991), and changes in ocean mass (Shackleton, 1987). Because the global sea-level variations over the last ~30 Myr have been driven primarily by glacial interglacial cycles, the oxygen isotope record in marine carbonates reflect these changes. Based on their signals in the isotopic record, periods of sea-level highs and lows during the Pleistocene and Holocene have been designated Marine Isotope Stages (MIS) with the most recent, the current interglacial, being MIS 1 (Emiliani, 1966).

RSL is an important factor controlling the depositional history of the New Jersey Margin. When studying a specific region it becomes necessary to examine sea level in terms of RSL, which is the height of the water column above the solid-Earth surface at a

single location (Kopp et al., 2015). RSL is influenced by a combination of the global processes discussed above and regional to local processes. These regional processes include mantle dynamic topography (MDT; Gurnis, 1990), ocean dynamics (Yin et al., 2009), and local processes including active tectonism (Simms et al., 2016), sediment loading, compaction (e.g. Törnqvist et al., 2008; Brian et al., 2015), GIA (Clark et al., 1978), and changes in Earth gravity, Earth rotation, and viscoelastic solid earth deformation (GRD) (Mitrovica et al., 2001).

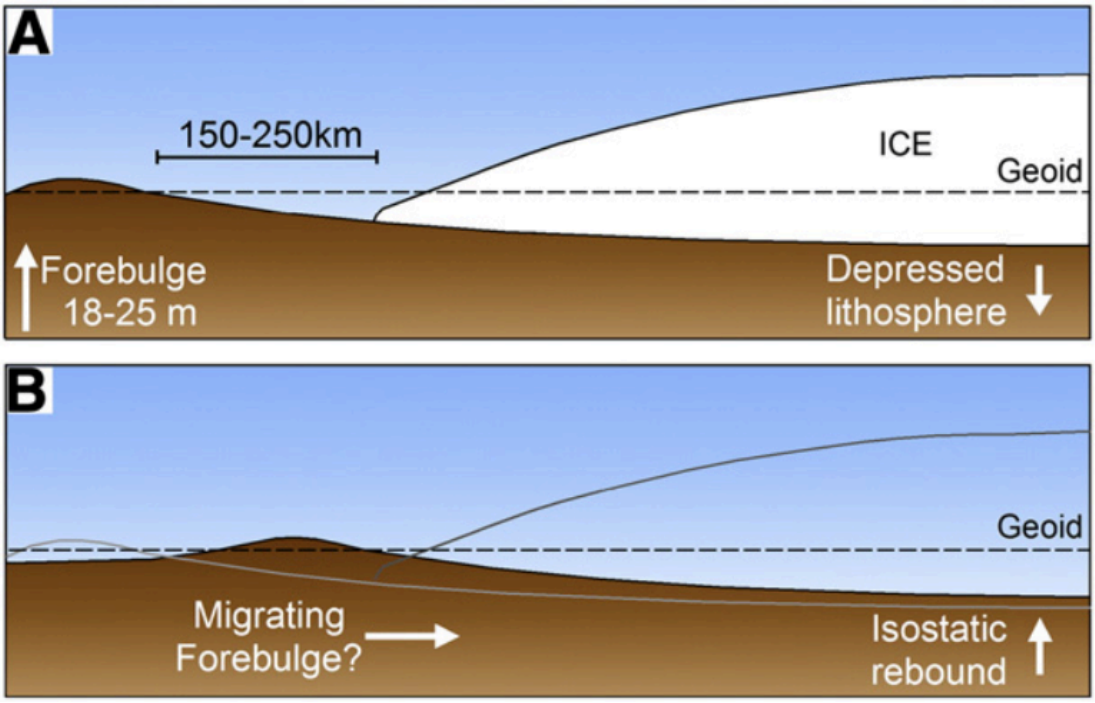

Figure 4.1: GIA Diagram. While the ice sheet is growing, the lithosphere is depressed underneath the mass of the growing ice sheet. Outboard of the ice sheet a bulge develops as the lithosphere flexes in response to the loading. As the ice sheet retreats (Panel B) the depressed lithosphere rebounds and the forebulge collapses or migrates back along the path of glacial retreat. Figure from Oakley and Boothroyd (2012)

Glacial Isostatic Adjustment (GIA) is the deformation of the Earth's lithosphere and geoid in response to loading of continents by large, kilometers thick, ice sheets (Farrell and Clark, 1970). The amount of deformation and vertical direction is dependent on the proximity to the ice sheet. Directly beneath the ice sheet, the crust is depressed during the glacial advance. Outboard of the ice, the crust is uplifted in what is called the glacial forebulge (Fig. 4.1). The proximity of the forebulge to the glacial front is a function of mantle viscosity and crustal flexure (Roy and Peltier, 2015). When the ice sheet retreats the forebulge subsides and migrates with the retreating ice sheet maintaining its position relative to the glacial front. The rate of GIA and its spatial distribution as the lithosphere relaxes after the retreat of the Laurentide Ice Sheet has been the focus of many studies (e.g. Roy and Peltier, 2015; Stanford, 2010). Regions that were uplifted as part of the forebulge are now undergoing increased sea-level rise as the forebulge continues to collapse.

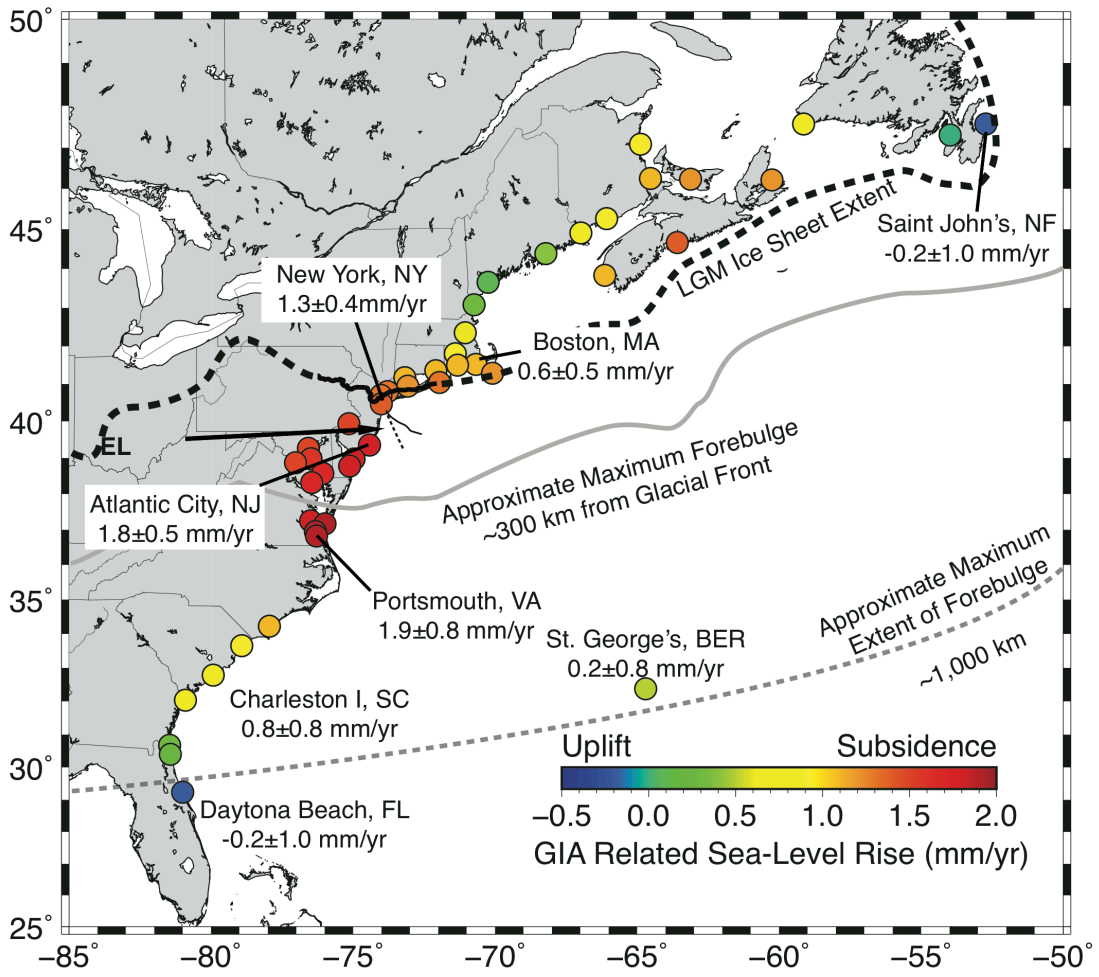

Figure 4.2: GIA Variability from Tide Gauge Records: Map of the linear regional component of the sea-level curve as measured by tide gauges. The primary component of the linear regional signal is GIA. Plotted data are archived by the Permanent Service for Mean Sea Level (http://www.psmsl.org/) compiled and modeled by Kopp (2013). The higher (red) values indicate the most rapid rate of subsidence associated with forebulge collapse. The black line indicates the maximum glacial extent at the last glacial maximum (LGM). The solid black line locates data points from Corbett et al. (2017) and while the dashed black line is from Dyke et al. (2003). The gray line indicates the approximate peak of the LGM forebulge based on the maximum rates of subsidence associated with its

collapse (Approximated from Peltier et al. (2015). It is ~300 km outboard of the terminal glacial extent. The dashed gray line indicates the limit of the forebulge, approximately ~1,000 km from the terminal moraine (Peltier et al., 2015). The likely zone of maximum uplift is between 200 and 300 km from the terminal moraine. EL is the Erie Lobe.

Today, GIA associated with the retreat of the Laurentide ice sheet is responsible for 1.3±0.4 mm/yr of subsidence in the vicinity of New York City while other locations such as Atlantic City are experiencing 1.8±0.5 mm/yr (Fig. 4.2, Kopp, 2013), at least 1.4 mm/yr of which is due to GIA based on the ICE-5G model of Peltier (2004). In New York this constitutes ~1/3 of the 3.0 ±0.3 mm/yr of the 20th century rate of relative sea-level (RSL) rise. New York City was within the limits of the Laurentide ice sheet during the LGM (Stanford, 2010) but was uplifted on the forebulge and as such is subsiding today (Peltier et al., 2015). As more studies try to quantify local rates of RSL rise and their sources in this region (e.g. Miller et al., 2013; Kopp et al., 2013; Johnson et al., 2018; Piechuch et al., 2018b; Johnson et al., in prep.), it is important to understand the rate and spatial variability of GIA. While direct observations of the crustal deformation during the last glacial maximum are impossible, modern GIA has been studied through a combination of observations of paleotopographic indicators (e.g. Oakley and Boothroyd, 2012), Holocene sea-level reconstructions (e.g. Engelhart et al., 2011), modern Continuously Operating Reference Station Global Positioning System (CORS GPS) records (e.g. Argus et al., 2014), and numerical models (e.g. Davis and Mitrovica, 1996; Peltier, 2004). The models are constrained by estimates of ice extent and thickness based on ice sheet terminations, radiometric dating of periglacial features, local tide gauge records, and global mean sea-level (GMSL) estimates (Peltier and Andrews, 1976). More

recently models have been constrained by Holocene sea-level, satellite gravity measurements, and Global Positioning System (GPS) records (e.g. Peltier , 2004; Engelhart et al., 2011; Argus et al., 2014). However, most of these observations have been primarily limited to land based records. This paper assesses the influence of GIA on the formation of paleochannels on the New Jersey continental shelf.

This study integrates past studies of the Pleistocene section on the New Jersey continental shelf with new 3D seismic and legacy sub-bottom data to assess the response of paleochannels, formed as fluvial systems on the subaerially exposed New Jersey margin, to changes in topography associated with GIA (e.g., Wickert et al., 2019). Based on the sea-level curves, periods of low sea level such as MISs 2, 4, and 5b would have all exposed the portion of the shelf covered in the MGL1510 survey area which is in ~40 m of modern water depth (Fig. SF3.2, Miller et al., Per. Comm.). As such we interpret the channels to be fluvial incisions on the exposed continental shelf. Rivers erode down to base level. The global base level is sea level, typically only reached at the river mouth. Along the river profile the local base level is sea level plus the fluvial gradient (Leopold and Bull, 1979). In a relatively stable fluvial system, the gradient should be concave up in an equilibrium profile where the slope decreases down stream. Perturbations in paleo-river profiles may reflect GIA related differential uplift of the landscape. However, the smaller drainage systems imaged by the 3D volume and those studied by Nordfjord et al. (2009), were likely unable to erode fast enough to keep pace with major changes in base level. Thus, the elevations across these drainage networks may instead indicate paleotopography and not differential rates of GIA across the study area. Greater

geographic coverage of paleochannels will provide an especially valuable means for evaluating GIA models in the future.

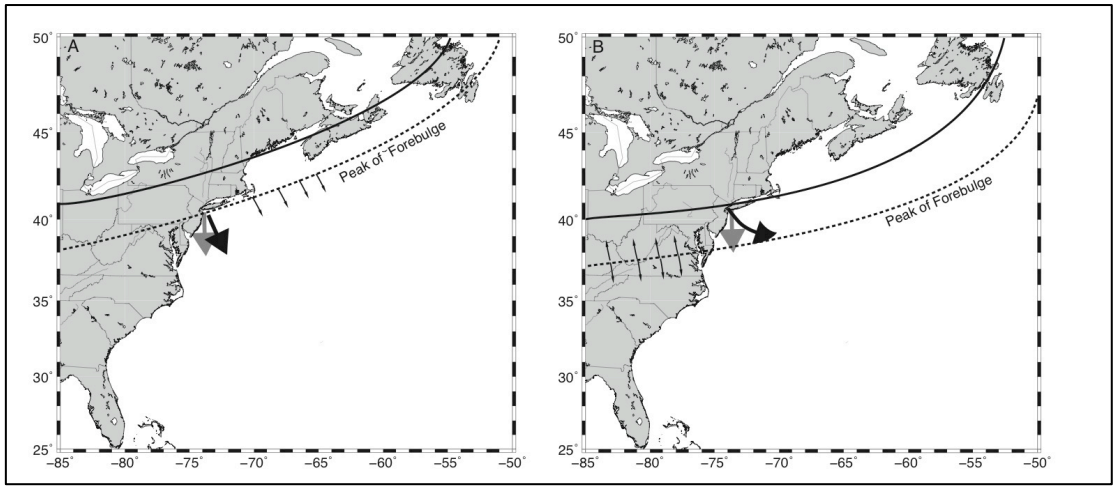

Figure 4.3: Cartoon of potential GIA mechanisms for diversion of the drainage on the New Jersey Continental Shelf. In scenario A, the forebulge is landward of the shelf and trends southeast-northwest. In scenario B, the forebulge is seaward of the shelf. The solid black lines indicate hypothetical ice sheet limits and the dashed lines indicate hypothetical forebulge peaks. The small arrows indicate the tilting of the landscape perpendicular to the forebulge peak. The large gray arrow indicates the previous drainage orientation and the large black arrow indicates the potential drainage response to the emplacement of the forebulge in each scenario.

Knebel et al. (1979) identified a possible paleo-Hudson river channel that trended ~160º across the now submerged shelf rather than the ~120º trend of the modern Hudson Shelf Valley (HSV). Knebel et al. (1979) and Carey et al. (2005) have hypothesized that differential tilting of the landscape by GIA could have redirected the paleo-Hudson to its modern orientation. Figure 4.3 shows a cartoon of two hypothetical scenarios for diversion of drainage on the New Jersey Continental Shelf. In Figure 4.3A, the drainage

is diverted as a southwest-northeast trending forebulge advances into the region causing the landscape on the shelf to tilt southeast. Figure 4.3B illustrates an alternate scenario where the forebulge peak is southeast of the shelf causing the landscape to tilt northwest diverting the channels east. In scenario B, the orientation of the forebulge peak is likely less important than in A.

Pico et al. (2018) used numerical modeling to show that hypothetical fluvial systems on the exposed New Jersey continental shelf could be affected by the forebulge advancing and retreating during the glacial-interglacial cycles leading up to the last glacial maximum (LGM). Their model shows that a rapid, late MIS 3 growth of the south-eastern Laurentide Ice Sheet (LIS), particularly the Erie Lobe (Fig. 4.2), could have induced a west to east tipping of the landscape thereby producing the shift interpreted by Knebel et al. (1979). Pico et al. (2018) note that the main peripheral forebulge signal for the LIS would be oriented parallel to the bulk of the ice sheet, resulting in north-south tipping of the landscape that would be unlikely to cause channels to shift. Instead they attribute the shift to emplacement of the Erie Lobe (Fig. 4.2; Dyke et al., 2002), which would have caused a smaller signal of west to east tipping causing the channels to shift to the east (Figs. 4.3 and 4.4). The Erie Lobe was an ice sheet that advanced into the Erie Valley near the end of MIS 3 (Pico et al., 2018). Alternatively, a north dipping forebulge signal on the New Jersey Margin could also generate the channel shift.

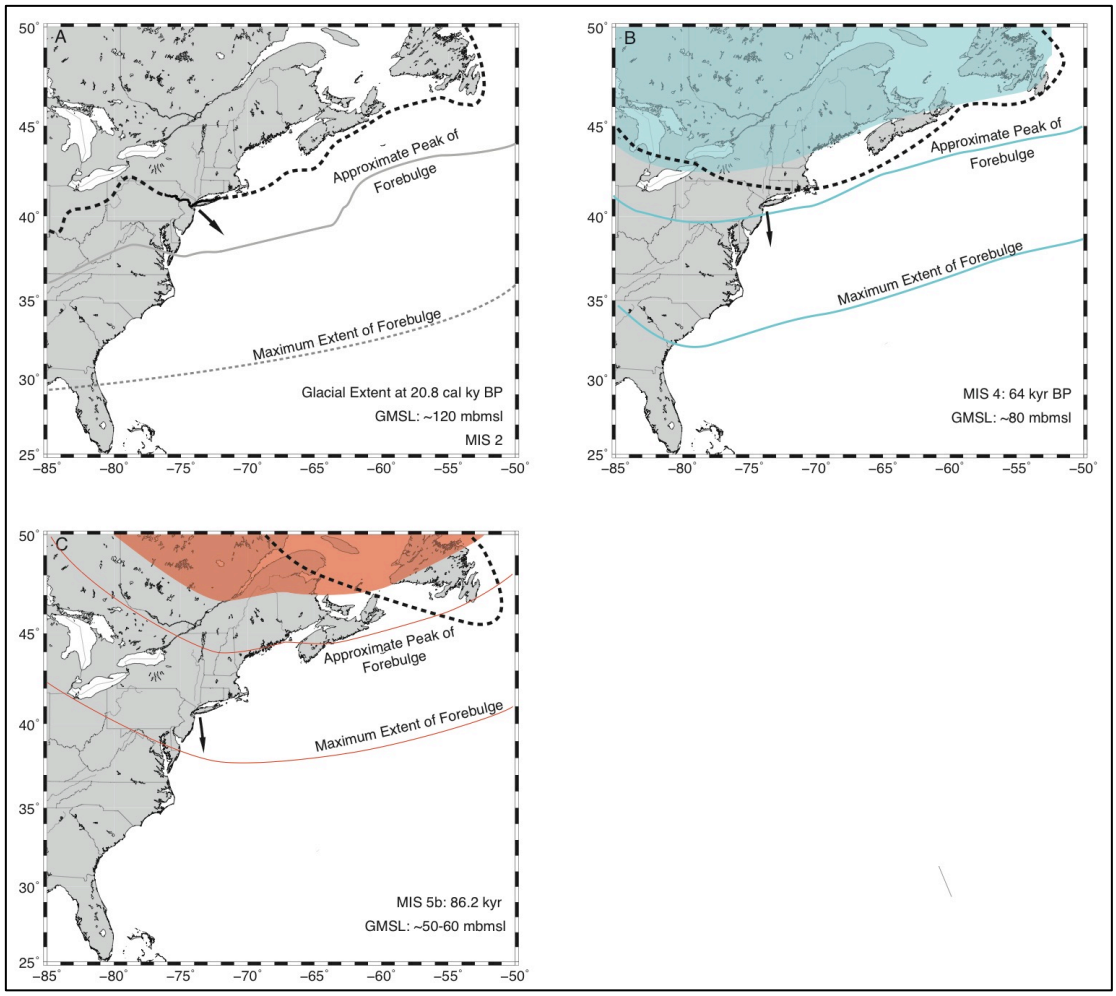

Figure 4.4: Estimates of GIA field for past glaciations published ice sheet extents from MISs 2, 4, and 5b along with the approximate distance to the forebulge from ICE-5g (Peltier, 2004). A: GIA field at ~25 cal ka during MIS 2. B: GIA field at 64 cal ka during MIS 4. C: GIA field at 86.2 ka that approximates MIS 5b. For A, dashed black line is the LGM ice sheet extent from Corbett et al. (2017) for the New Jersey, Pennsylvania, New York, and New England and approximated from deglacial maps of Dyke et al. (2003) for the remainder of the mapped region. The forebulge peak and limit are from Peltier et al. (2015). For B and C, the dashed black lines indicate the limits of geologic evidence for ice sheet extent during those times and the shaded areas indicate the modeled ice sheet

extent. MIS 4 and 5b glacial extents are approximated from the maps of Kleman et al. (2013). The distance to the forebulge peak and limit area estimated for MISs 4 and 5b based on the MIS 2 simulations by Peltier et al. (2015). The arrows indicate drainage orientations at that time.

By mapping the incised valleys all paleochannels <120 ka, measuring their incision depths, correlating them to previously dated sites, and comparing them to GIA fields at MIS 2, 4, and 5b, this study tests the hypothesis that incision depths of paleochannels across the region are controlled by relative sea-level, primarily due to GIA and provides evidence that the shift identified by Knebel et al., (1979) was a regional realignment of drainage systems consistent with the modeling results of Pico et al. (2018).

4.2 Background

The New Jersey continental shelf can be divided into 3 bathymetric zones: the inner, middle, and outer continental shelf. Swift (1974) provided a basis for this division based on identified scarps (Fig. 4.5). The scarps include the Fortune and Tiger Shoreline and Franklin Shoreline. There have been a number of interpretations for each of the scarps. Dillon and Oldale (1978) interpreted them to be paleoshorelines. Uchupi et al. (2001) proposed that the Fortune Scarp could be a sediment lobe deposited during a glacial outburst. Goff et al. (2013) interpreted the Franklin Shoreline as a paleoshelf edge. In this paper, when not using a formal name, we refer to them as scarps and do not imply a formational process. Here we define the beginning of the outer shelf at the shelf slope break, it then continues landward to approximately the Franklin Shoreline at ~120 meters water depth (Fig. 4.5). The middle continental shelf extends from the Franklin Shoreline

to Fortune Shoreline at ~50 mbsl, and the inner shelf extends from there to the coast. Studies of the New Jersey continental shelf are often limited to a single zone. The discontinuous nature of Pleistocene deposits on the shelf and the relatively limited number of data sets that bridge these zones make correlation between them difficult, and as such they tend to each be discussed individually.

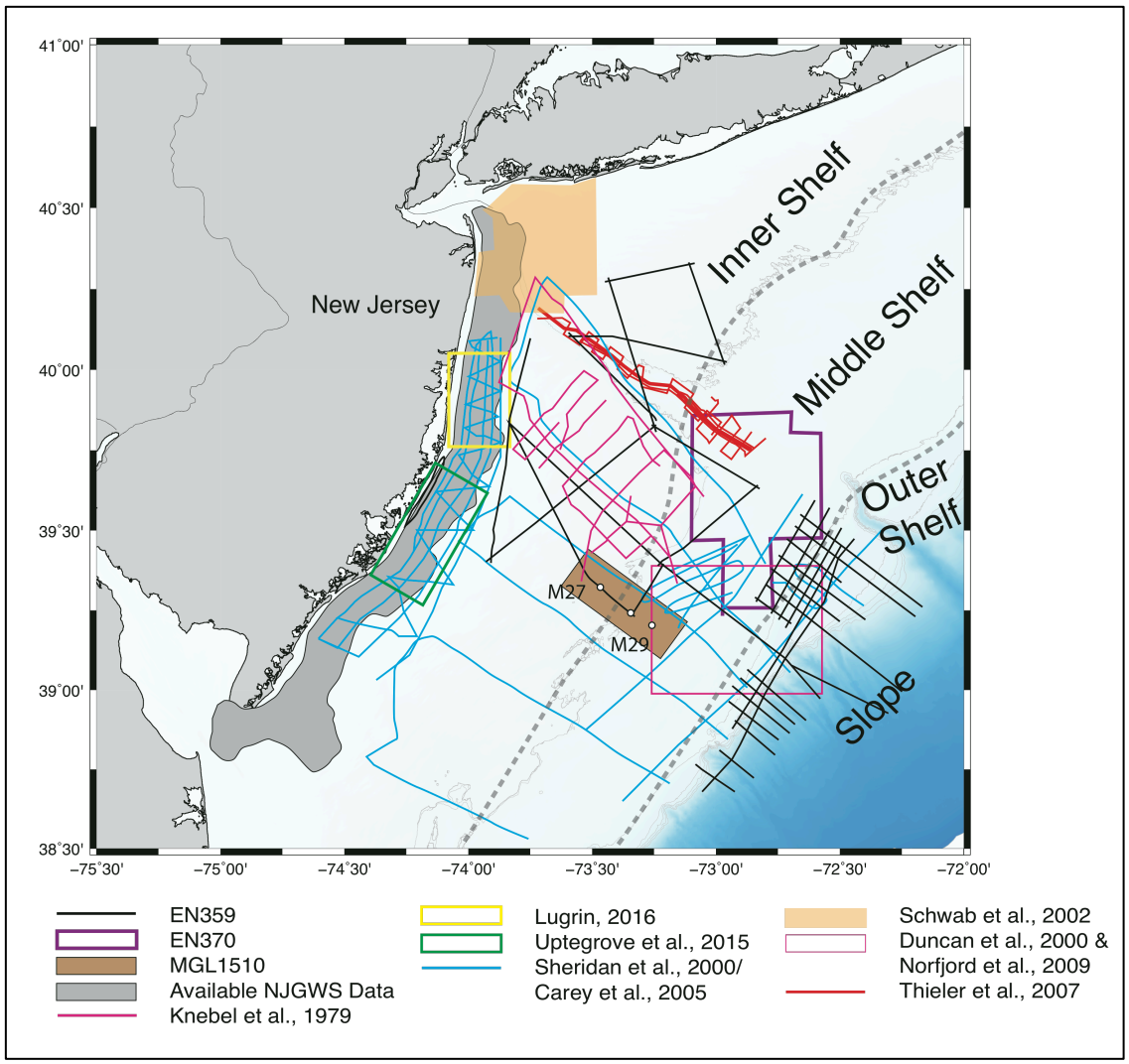

Figure 4.5: Map of available high-resolution subsurface data: This map includes available high frequency data sets targeted for the Pleistocene section offshore. These data sets include Chirp, Boomer, and Sparker sources. Also shown in the MGL1510 3D seismic

volume. Dashed lines indicate the approximate divisions between the inner, middle, and outer shelf. Knebel et al. (1979) data was unavailable, only the published images and interpretations.

McHugh et al. (2010) provided a good overview of the Pleistocene stratigraphy and paleoenvironments of the outer continental shelf of New York and New Jersey. There have been a number of vibracores collected on the outer continental shelf and deep core holes drilled by the Deep Sea Drilling Program (DSDP), Ocean Drilling Program (ODP), and International Ocean Discovery Program (IODP). The DSDP drilled Legs 11, 93, and 95 on the upper continental rise (Ewing and Hollister, 1972; Poag, 1985; van Hinte et al., 1987). The ODP drilled Legs 150 and 174A on the outer shelf, slope, and upper rise (Mountain et al., 1994; Austin et al., 1998). The IODP drilled Expedition 313 on the Middle shelf. McHugh et al. (2010) used all these data, except Expedition 313, in addition to hi-resolution sub-bottom data to identify sequences D, C, B, B', and A. Sequence D is thought to be equivalent to sequence Blue that was identified at ODP site 1073 (Mountain and Monteverde, 2000; McHugh and Olson, 2002; Mountain et al., 2007) on the upper continental slope (McHugh et al., 2010). Sequence Blue was assigned to MIS 8 based on correlation of oxygen isotopes to SPECMAP, the global oxygen isotope curve, at site 1073 (Montain and Monteverde, 2000; Mountain et al., 2007). Unit C is correlated to either MIS 3 or MIS 5 and is equivalent to Sequence Purple on the slope. Unit A is interpreted to be latest Pleistocene to Holocene. This stratigraphy has not been correlated to the inner continental shelf. As such we will be following the stratigraphy of Miller et al. (2012), discussed later in this report.

Previous studies have shown that the stratigraphy of the New Jersey inner to middle continental shelf contains a record of Pleistocene changes in GMSL (Ashley et al., 1991; Sheridan et al., 2000; Carey et al., 2005; Wright et al., 2009; Miller et al 2012) and regional effects including GIA and MDT (e.g. Peltier, 1998; Moucha et al., 2008; Pico et al., 2018). Marine Isotope Stages (MIS) 1-5 have been tentatively identified through a combination of isotope stratigraphy, biostratigraphy, and seismic stratigraphy. Between MISs, RSL on the New Jersey margin has been interpreted to rise and fall up to ~125 m (Wright et al., 2009). During times of falling sea level, at the transition from interglacial to glacial stages, the margin was dominated by fluvial systems with significant erosional features. During times of rising sea level, leading up to interglacial sea-level highstands, the coast was dominated by estuaries and barrier islands (Ashley et al., 1991). The interplay between these two regimes and the glacial history of eastern North America is reflected in the sedimentation of the New Jersey margin. However, the Late Pleistocene record is poorly preserved on the New Jersey margin due to a lack of accommodation space, limited sediment accumulation, and restricted chronologic resolution (Sheridan et al., 2000; Wright et al., 2009). Most published studies of Pleistocene stratigraphy on the inner continental shelf of New Jersey focus on Barnegat Inlet and south (Knebel et al., 1979; Ashley et al., 1991, Sheridan et al., 2000; Wright et al., 2009). Carey et al. (2005) and Lugrin (2016) extended the correlations north to Sea Girt, NJ (Fig. 4.5). Some studies extend north to the modern HSV, but with limited seismic data and no near shore data (e.g. McHugh et al., 2010; Schwab et al., 2002). Lugrin (2016) and Uptegrove et al. (2015) used high resolution sand resources surveys to do detailed mapping of the near-shore from Sea Girt to Brigantine, NJ.

Miller et al. (2012) identified 4 sequences; uP1, uP2, uP3, and uP4 in subbottom profiles, 2D seismic, and cores at sites M27 and M29 of IODP Expedition 313. Expedition 313 was a northwest-southeast transect of three cores drilled on the New Jersey inner continental shelf in 2010 (Mountain et al., 2010). Based on their correlations Miller et al. (2012) assigned sequence uP1 to MIS 7, uP2 to MIS 5c, uP3 to MIS5a, and using superposition and proximity to the seafloor they interpreted their uP4 sequences to be MIS 2. The discontinuous nature of the sediments and the limited data overlaps result in many disparate and generally poorly dated seismic data sets exist. Here, we attempt to integrate these datasets with new 3D data to better understand the Pleistocene history of the inner to middle continental shelf of New Jersey.

4.3 Methods and Data

4.3.1 Seismic

4.3.1.1 EN370 Sub-bottom Profiles

Sub-bottom data for the New Jersey inner to outer continental shelf were collected between May 23 and May 29 of 2002 on cruise 370 aboard the *RV Endeavor* (EN370)using an Edgetech 512I towfish sub-bottom profiler customized and operated by Steve Schock from Florida Atlantic University. McHugh et al. (2010) provide a summary of collection methods. We converted the data from native Edgetech .jsf format to segy using the jsf2segy software package (T. O'Brian, Woods Hole Oceanographic Institution, 2004; written comm.). The data were then processed for display using SeismicUnix. This included applying a varying depth correction based on the depth of the towfish, and stacking the envelope traces from the same shot point to convert from envelope to

standard SEG-Y. The complete script is available in the supplement. The data were then loaded into Petrel for interpretation.

4.3.1.2 MGL1510 3D Seismic

550 km^2 of 3D seismic data were collected by the *R/V Marcus G. Langseth* cruise 1510 (MGL1510) in June and July of 2015 (Mountain et al., 2015). The sound source was an array of 4 airguns totaling to 700 cu. in. of 2,000 psi of compressed air. The receivers were an array of twenty 8-channel GeoEel PCables towed on a bridal between two paravains deployed behind the Langseth (see Fig. SF3.1 for a diagram of the collection schematics). The array of 4 airguns hung from a single harness towed along the ship's centerline proved problematic during processing. For a single long streamer the series of airguns acted as a single point source and resulted in a consistent source waveform. However, 24 100-m PCables were towed 12 m apart from a 287 m athwartship cable 58 m aft of the center of the airgun array. This resulted in source waveforms at each of the 192 streamer hydrophones that varied due to individual positions; those in streamers astern of the source array effectively 'saw' the 4 airguns in a line while those in the far outboard streamers 'saw' them from the side of the linear array. Correcting for this angle-dependent source character required customized processing that caused 1-3 msec errors in arrival times of shallow (< 100 msec) reflections across a 24-PCable crossline display. Furthermore, the athwartship cable bowed more than anticipated, making it difficult to assign accurate source-receiver offsets to every trace. These issues resulted in artifacts in the seismic displays visible in time slices along each of the track lines and inadequate imaging in crossline display (perpendicular to direction of data collection) relative to the inlines, which are parallel to the direction of data

collection. Time slices are map view images of the seismic volume at specific two-way travel times (twtts). The time slices often show that what appears to be incoherent noise in an inline or crossline to be part of a larger feature that stands out better in map view in the time slices. The data were processed by DECA under contract from NCS Subsea to correct for this variability. The 3D volume has a record length of 1.5 seconds and a sample rate of 1 ms. The PCable traces were stacked in bins measuring 6.25 m in the inline direction and 3.125 m in the crossline direction. This resulted in a 2 traces in each bin. The delivered seismic volume was then loaded into Petrel for interpretation.

4.3.2 Seismic Interpretation

Seismic horizons were chosen based on lateral continuity, the presence of terminations that suggested they may be sequence boundaries, and their presence at International Ocean Drilling Project (IODP) sites M27 and M29 so that they could be correlated to previous studies with some age control (Miller et al., 2012) . Reflector terminations were used to identify key Pleistocene sequence boundaries previously published by Miller et al. (2012). While picking surfaces in the MGL1510 data sets, we preferentially used inlines (NW-SE; parallel to the direction of data collection) for their superior resolution when compared to crosslines (NE-SW). Arbitrary lines, combinations of inline and crossline data, were also used to help fill in gaps and avoid relying too heavily on crossline correlations.

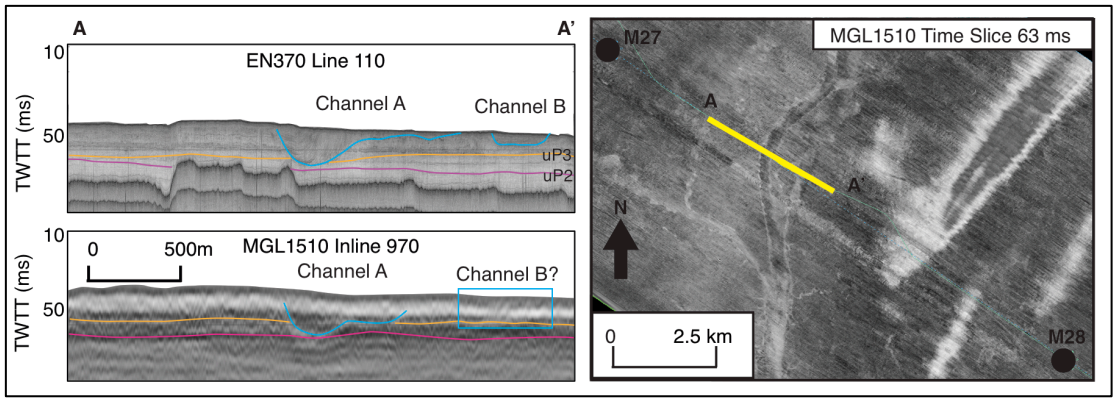

Figure 4.6: Examples of channel imaging in sub-bottom, 3D inline, and 3D time slice. The channels, interpreted as uP4 by Miller et al. (2012), are well imaged in Chirp sub-bottom profiles while only the largest channels are imaged reliably in the inlines and crosslines of the MGL1510 3D seismic volume. This is compensated for by the ability of the 3D seismic volume to image the channels in time slices. uP2 and uP3 of Miller et al. (2012) are shown in magenta and orange respectively.

Where possible, paleochannels were mapped in 2D inlines and crosslines of the 3D volume. This maximized spatial coverage and the chance of identifying interior channel morphologies. However, this was only possible for the largest of paleochannels (Fig. 4.6). We used arbitrary lines perpendicular to the channel axis to get the best possible cross-sectional view of the channel. In these, the incision depth of the channel could be measured with roughly ±5 ms Two Way Travel Time (TWTT) vertical resolution. At certain points along their profile, the paleo-channel thalweg depths were measured relative to modern sea level and sea floor. Of the channels visible in the inlines and crosslines of MGL1510, most were within the uppermost ~20 ms below the sea floor and it was often difficult to differentiate the top of channels from sea floor. This made it impossible to determine if they extended up to the sea floor or not, potentially leading to overestimates of thalweg depth. Where possible, the channels were assessed at higher

resolutions where they intersected one of the EN370 sub-bottom profiles that pass through the MGL1510 grid with ~2.5-12 m vertical resolution beginning at the seafloor (based on a peak frequency range of ~30-150 Hz and a velocity of ~1500 m/s). This enabled us to get a better estimate of thalweg incision depth.

Smaller channels, less than ~10 ms (TWTT) deep and <250 m wide were often indistinguishable on in the 2D profiles from MGL1510 and had to be mapped in time slices (Fig. 4.6). The smaller channels were traced on a series of time slices at 1 ms (twtt) intervals to map out the drainage system. Because of interference in the seismic data under the channels (Fig. SF3.3B) and noise near the seafloor it was difficult to identify the true base of the channel so their absolute incision depths are estimated based on the deepest time slice that imaged the channel.

4.3.3 Age Control

Age control for this study is from correlation to IODP Expedition 313 sites M27 and M29 (Fig. 4.7; Miller et al., 2012). These cores were taken aboard the *L/B Kayd* in 2009 (Mountain et al., 2010). Biostratigraphy, amino acid racemization (AAR), and Carbon-14 data were generated to determine a chronostratigraphic framework (Miller et al., 2012) for the Pleistocene. Superposition was used to determine relative ages for units that were not present at sites M27 and M29, mainly channels and their fills.

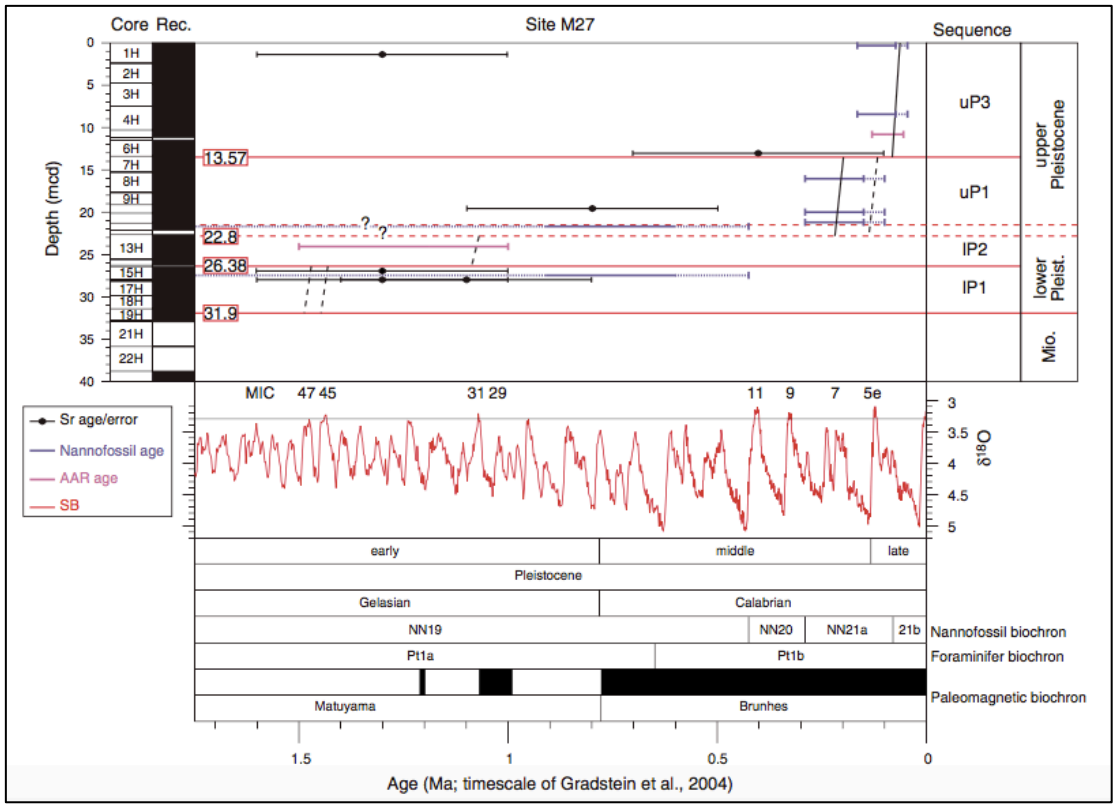

Figure 4.7: Pleistocene age control from IODP Exp 313 Site M27: Sr isotopes are plotted with error bars of ±0.3 m.y.. Rec. is recovery; black indicates recovered, white indicates gap. Time scale, paleomagnetic chrons (black—normal, white—reversed), and biochrons (time scale of Gradstein et al., 2004) are shown along with the benthic foraminiferal 18O stack of Lisiecki and Raymo (2005); major interglacial chrons (e.g., 5e, 7) are shown. MIS – Marine Isotope Stage; Pleist.—Pleistocene; Mio.—Miocene; AAR—amino acid racemization. Numbers in red boxes are the precise depth (in mcd) of stratal surfaces. Figure from Miller et al. (2012).

4.3.4 GIA During and Prior to the LGM

In order to assess the results of our channel interpretations and put them into a regional context it was necessary to evaluate them in relation to GIA conditions at the times they may have formed. GIA related deformation of the lithosphere is relatively well

known for the LGM (Peltier, 2004; Peltier et al., 2015). We use Peltier et al., (2015) and Corbett et al., (2017) to constrain the GIA field and ice sheet extents respectively during MIS 2. Aside from terminal moraines, that extended farther south than the terminal moraines of the LGM (e.g. the potential MIS 6 terminal moraine of Stanford (2010)), the glacial history of past, smaller ice sheets including MISs 4 and 5b have largely been eroded away by subsequent glaciations. To provide an estimate of what the GIA conditions may have been at MISs 4 and 5b, we use the model results of Kleman et al. (2013) to constrain the ice sheet limits as shown in Figure 4.4 panels B and C. Without GIA estimates from models for MISs 4 and 5b, we use the proximity of the forebulge peak and forebulge limit to the edge of the ice sheet during MIS 2 (Fig. 4.4A). Based on MIS 2 (Peltier et al., 2015), we place the forebulge peak ~300 km outboard of the ice sheet. The GIA forebulge signal appears to dissipate by ~1,000 km south of the terminal moraine (Peltier et al., 2015). Consequently, we suggest that 300 km and 1,000 km can be used as rough approximations of the distances to the forebulge peak and the limit of GIA forebulge effects. This is likely an overestimate of the distance, since the ice sheets during MISs 4 and 5b were thinner and less extensive than the ice sheet during MIS 2. Using these values we can place the approximate peak of the forebulge and GIA limits on our maps of estimated glacial extent for the MIS 4, 5b, and 5 averages.

4.4 Results

4.4.1 Pleistocene Seismic Stratigraphy of MGL1510

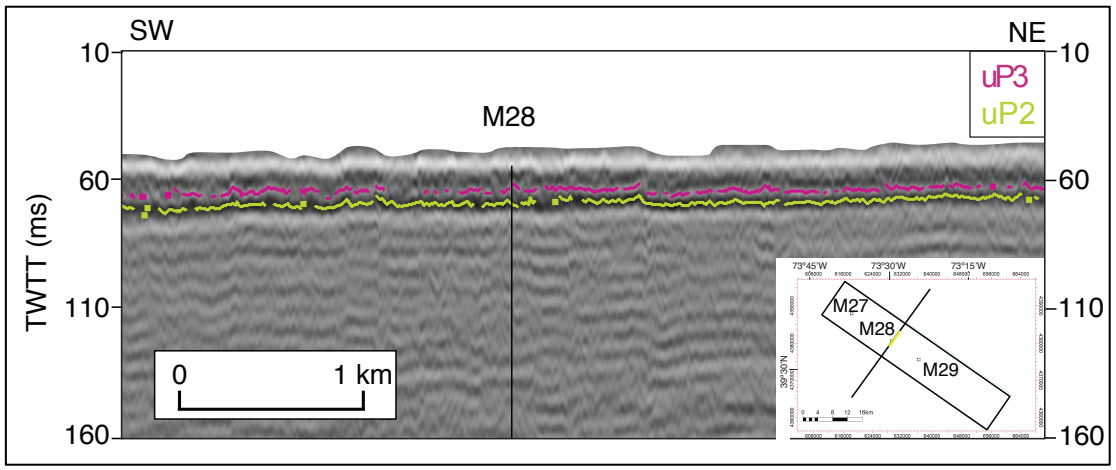

Figure 4.8: Major middle to late Pleistocene reflectors identified in the MGL1510 survey area. uP2 (yellow) is interpreted as the unconformity at the base of MIS 5. uP3 is interpreted to be an internal unconformity in MIS 5, likely associated with the lowstand at MIS 5d. Ages based on correlation to Miller et al. (2012).

We identify 2 Pleistocene reflectors in the MGL1510 survey area (Fig. 4.8). The lowest we correlate to the base of the uP2 sequence of Miller et al (2012). We designate this surface uP2 after Miller et al. (2012). It is an erosional surface correlatable across the MGL1510 survey area. It truncates a number of underlying units and marks a transition from moderately well imaged, continuous reflectors underneath to relatively poorly imaged, discontinuous to chaotic reflectors above. The surface displayed in map view shows no distinct topographic features (Fig. 4.9).

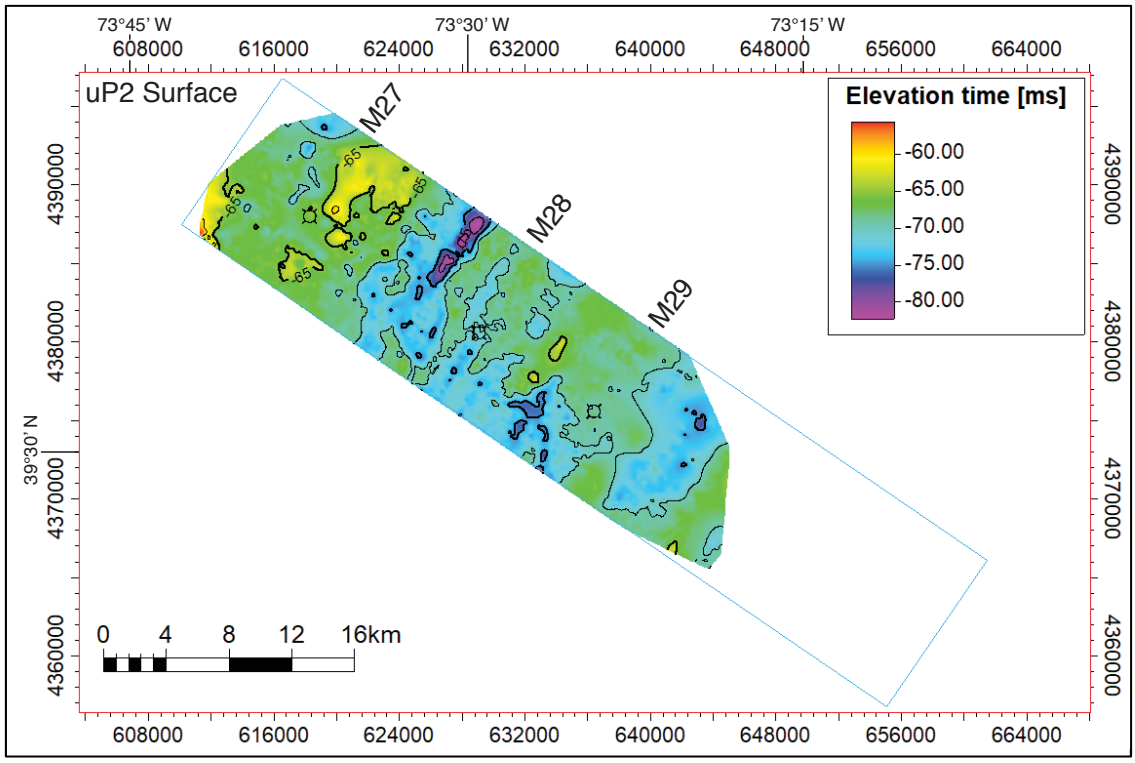

Figure 4.9: uP2, MIS 6 erosional surface.

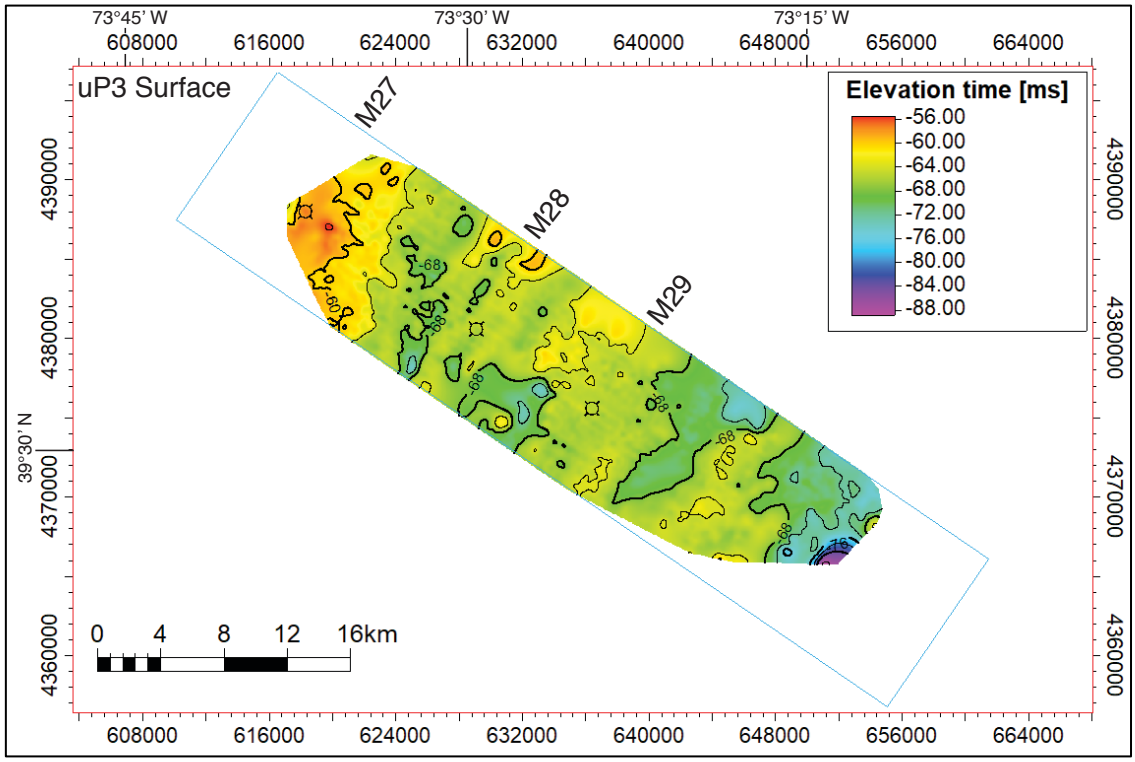

Figure 4.10: uP3, MIS 5D? erosional surface.

The second surface (Fig. 4.10) is located directly above the uP2 surface and we correlate it to the uP3 surface from Miller et al. (2012). It is less continuous than the top uP1 surface and due to imaging quality it cannot be traced to the northwest and southeast ends of the 3D grid.

Low quality imaging and data resolution make correlation difficult. The degraded image quality is a result of the relatively high density of shallow paleochannels, which distort the acoustic image of any underlying beds. There is also a significant amount of acoustic noise due to the relatively low (≤2) number of traces stacked in each 6.5x3.25 m bin. Also, a number of the channels incise through the picked horizons making them discontinuous. The noise, in conjunction with the discontinuous preservation of the strata, generates significant uncertainty in the picked surfaces. However, the relatively flat nature of the continental shelf sediments suggests that while there may be uncertainty in the picks, any error should be relatively small on a temporal scale.

4.4.2 Late Pleistocene to Holocene Channels in the MGL1510 Survey

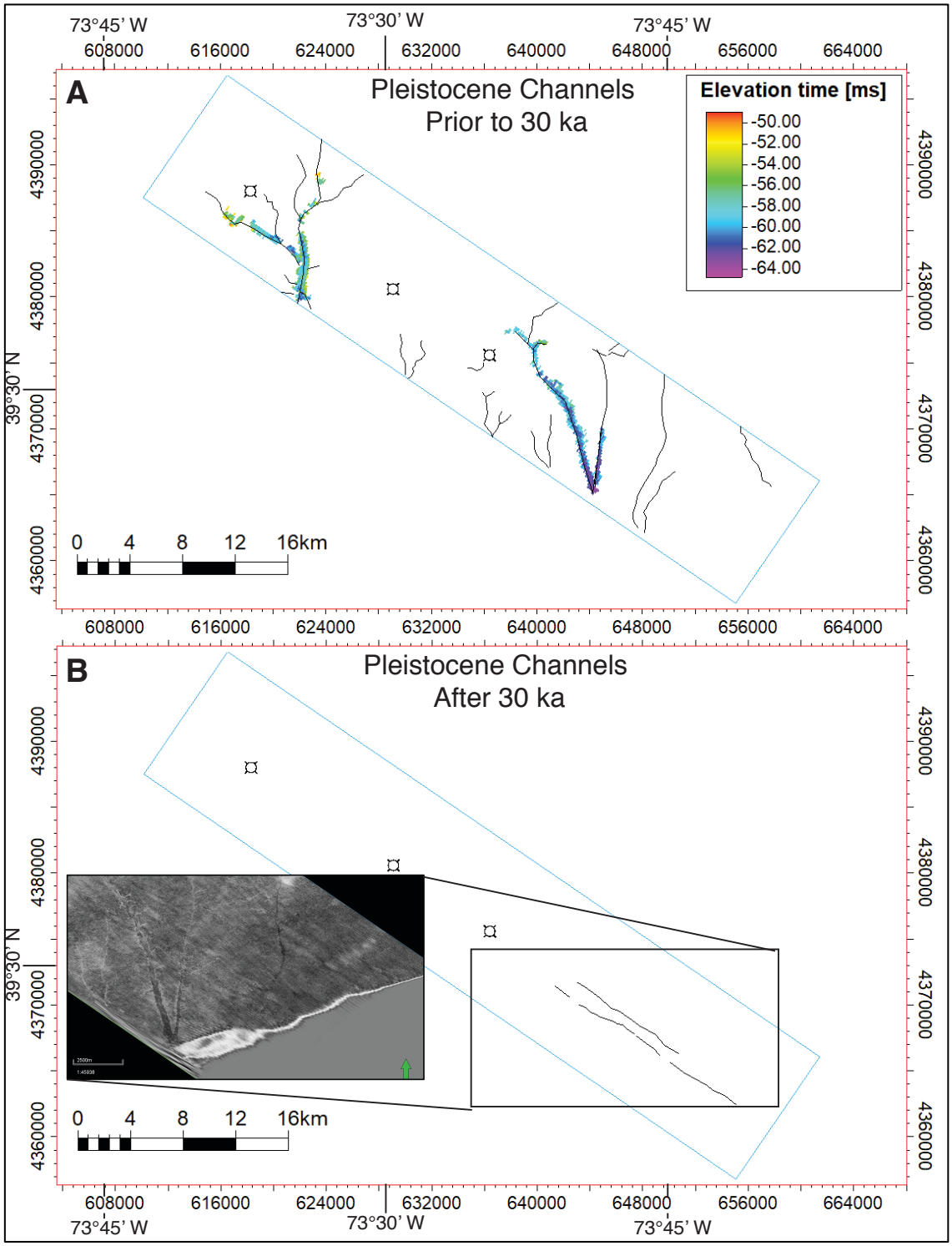

Figure 4.11: Mapped paleochannels from MGL1510. Panel A shows mapped paleochannels >30 ka. Panel B includes Paleochannels <30 ka that show a northwest-

southeast orientation. B includes a time slice at 66 ms. The color of the trace is the approximate depth in TWTT with blues indicating ~65 ms and yellow indicating ~50 ms of TWTT.

We identify two sets of Pleistocene channels in the MGL1510 survey area. The first set has a generally north-south orientation (Fig. 4.11a, SF3.2). These channels are above or incise the uP2 surface and consequently we interpret them to be younger than MIS 6 (<130 ka). Morphology of the channels ranges from relatively straight in the southeastern section of the survey area to meandering in the northwest. While the channels are well imaged in both the EN370 data sets and the time slices from the 3D volume, only the largest channels are well imaged in the inline and crossline profiles of the 3D volume. (Fig. 4.6). Incision depth of many of the channels is uncertain. This set of channels includes the uP4 channels of Miller et al. (2012), that are visible in EN370 Line 110, MGL1510 inlines and crosslines, and MGL1510 time slices (Fig. 4.6).

The second set of paleochannels (Fig. 4.11b) is only visible near the bathymetric scarp at the southeastern end of the seismic volume and even then only in time slices. These channels are poorly imaged due to their proximity to the sea floor. In inlines and crosslines they are often lost in the sea-floor noise. These channels are oriented northwest to southeast, sub parallel to the direction of seismic acquisition. They can be distinguished from collection artifacts in two ways. First, the channels are not perfectly linear, unlike the track lines through the area. Second, the channels are not exactly parallel to the tracklines and crosscut the scalloping artifacts (Fig. SF3.3A) generated during collection. While the channels are not visible anywhere in the 3D grid where they cross a EN370 sub-bottom line, they are sub parallel and relatively straight which makes

it possible to project them to EN370 lines 115, 27, and 19. In line 115, northwest of the visible traces in the 3D grid, there is a hint of the southwest channel (Fig. 4.12). Projecting the two channels farther offshore to where they would intersect the EN370 Lines 27 and 19, there are two visible channels (Fig. 4.12). In line 19 there is evidence of multiple incisions within the same paleochannel. The oldest channels system is indicated by the green in Figure 4.12, is marked by a relatively transparent seismic facies. Cutting that surface is a series of channels (magenta) with strong internal reflections. These may be correlatable to the magenta channel in line 27 which would indicate a ~north-south orientation. The magenta channels in line 19 are further incised by the cyan channels, which we interpret to be potential continuations of the MIS 2 channels observed in the MGL1510 survey area (Fig. 4.12). However, neither these channels, nor their fill have been imaged by high-resolution sub-bottom data or penetrated by vibracores where they are visible in the 3D grid. Also, there is no direct correlation of data in the MGL1510 3D survey area to EN370 Lines 19 or 27. The interpretations present are based solely on linear projections of the features from the 3D survey area and similar seismic facies identified in the EN370 data. Further studies may help to corroborate our interpretation.

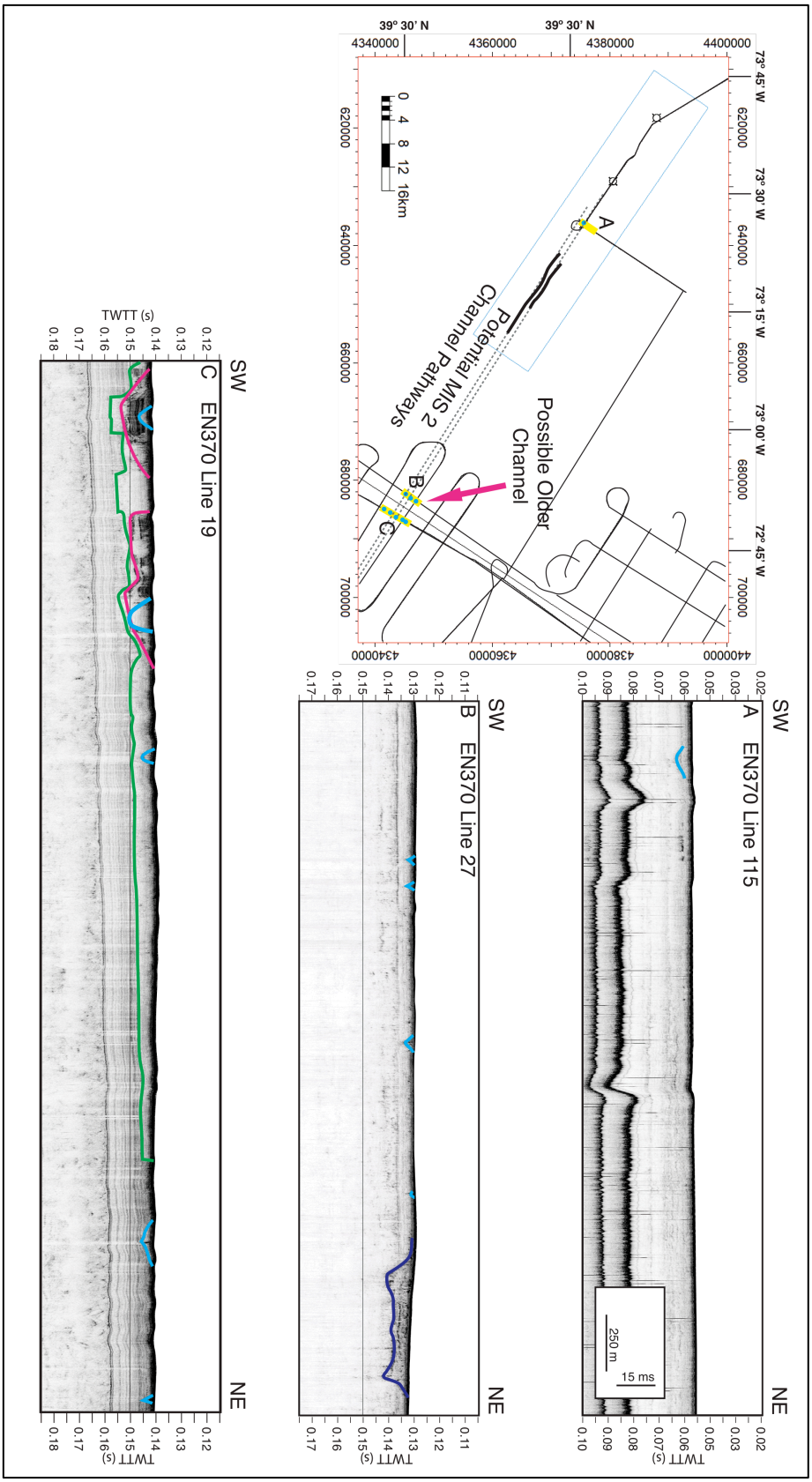
39° 30' N
39° 30' N
4340000
4360000
4380000
4400000
73° 45' W
73° 30' W
73° 15' W
73° 00' W
72° 45' W
620000
640000
660000
680000
700000
0 4 8 12 16km
A
B
C
Potential MIS 2 Channel Pathways
Possible Older Channel
SW
NE
A EN370 Line 115
B EN370 Line 27
C EN370 Line 19
250 m
15 ms
TWTT (s)

Figure 4.12: Subbottom imaging of potential uP5 channels. A series of three seismic profiles are displayed from northwest to southeast. In Line 115 the southwestern MIS 2 Channel may be visible. In Lines 27 and 19 there are several generations of channels with green being oldest with its distinctive transparent seismic facies, magenta is the next oldest with strong internal reflectors. In Line 19 magenta clearly cuts into green. Cyan is the youngest set of channels interpreted to be equivalent to, if not continuations of, the MIS 2 channels (<30 ka) identified in MGL1510 time slices.

4.4.3 Age Control

Primary age control for the seismic horizons is provided by correlation to sites M27 and M29 (see Fig. 4.5 for locations). Site M27 recovered 31.9 m of Pleistocene strata uncomfortably overlying Miocene sediments (Miller et al., 2012). Miller et al. (2012) followed the work of Carey et al. (2005) that identified 4 sequences between MIS 6/5e and MIS 2/1, but improved the chronology and updated the nomenclature based on the results of IODP expedition 313. Miller et al. (2012) subdivided the cored Pleistocene section into sequences lP1, lP2, uP1, uP2, and uP3. These were assigned ages based on strontium isotopes, nannofossil assemblages, and amino acid racemization (AAR) (Figs. 4.7 and 4.13). Based on strontium results from sequence lP1 and AAR data from lP2, lP2 is loosely dated to between 1.0 and 1.5 Ma. Based on Strontium results and superposition, lP1 is also between 1.0-1.5 Ma, but younger than lP2. Miller et al. (2012) correlated sequence uP1 to MIS 7 based on the assemblage of nanofossils; however, they could not completely rule out a correlation to MIS 5e. Results from this study do not conflict with the interpretation that uP1 is older than MIS 5. AAR results link uP2 to MIS 5c and uP3 is tied to MIS 5a based on biostratigraphy that indicates that it is older than 73 and 52 ka

at sites M27 and M29 respectively. Since uP4 was not drilled by IODP Expedition 313, nor has it been penetrated by any vibracores, Miller et al. (2012) hypothesized that the channel was formed during the MIS 2 and subsequently filled. However, this study identifies a second set of paleochannels that apparently crosscuts those identified by Miller et el. (2012). We suggest that the new channels termed here as uP5 are related to MIS 2 causing us to modify chronology of Miller et al. (2012) (Fig. 4.13). Based on our results we instead correlate uP4 as older than the LGM, though the exact age is uncertain and could be between 85 and 30 ka. We reinterpret the ages of Miller et al. (2012) to correlate uP3 with MIS 5c, and uP2 fill with MIS5e, which is reasonable given the error bars associated with their dates.

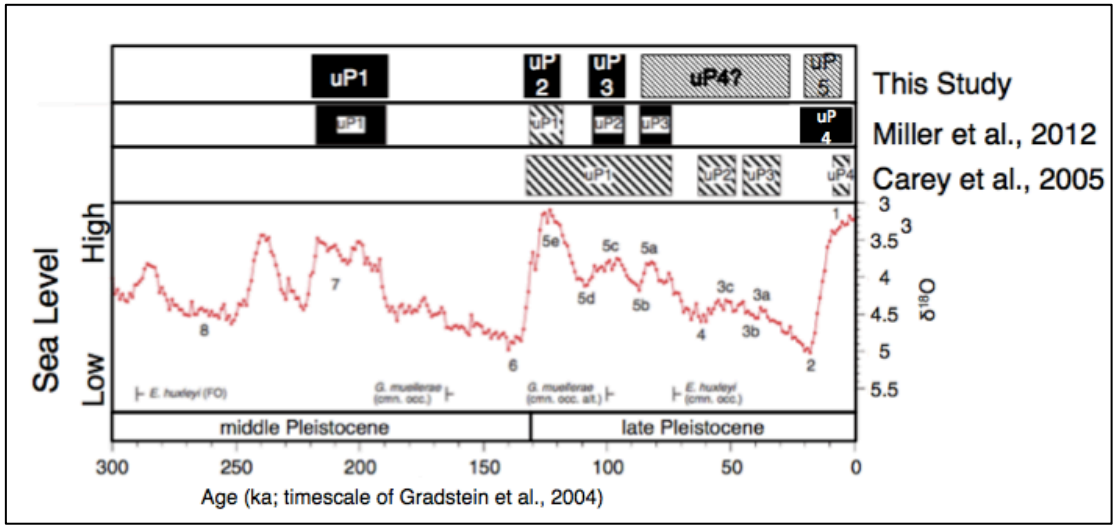

Figure 4.13: Middle to late Pleistocene chronology preserved in the MGL1510 survey area. The identification of a second set of paleochannels crosscutting those identified by Miller et al. (2012) prompted the movement of each Pleistocene Sequence (uP2-uP4) back one MIS. Figure modified after Miller et al. (2012), the $\delta^{18}O$ stack is from Lisiecki and Raymo (2005).

4.5 Discussion

4.5.1 Channel Incision Depth

Wickert et al. (2019) showed that the Mississippi River's incision into bedrock can be an indicator of the regional GIA signal at the time that the channel was incised. They identified a 300 km long section of the buried valley that is overdeepened. They attribute the overdeepened section to erosion through the uplifted forebulge between 2.5 and 0.8 Ma. The forebulge has subsequently collapsed, generating the over deepened section.

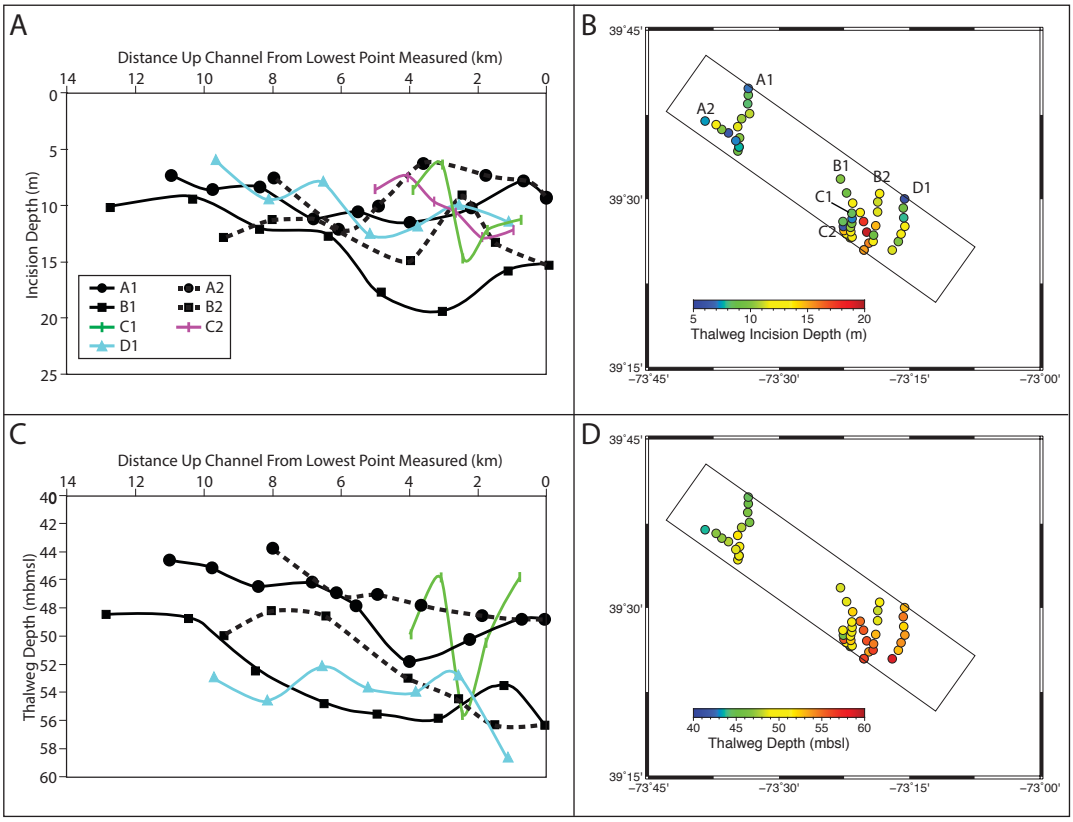

Figure 4.14: Thalweg measurements from major MGL1510 channels, older than 30 ka. A shows thalweg incision depth below sea floor. Note that many of the channels are near enough to sea floor that it is not possible to determine if they intersect with sea floor or

not. B is a map of incision depths. C and D show a graph and map of incision depths relative to modern sea level.

We assessed the channels within the 3D survey grid for similar overdeepening trends, looking for a MIS6 or younger signal (Fig. 4.14; Table 4.1). The thalweg depths were measured relative to sea floor and modern sea level. Figure 4.13 illustrates the results of this assessment and the data are available in Table 4.1. Only 4 channel systems were large enough to be measured and they were all interpreted to be between 120 and 30 ka. We identified incision depths of 5-22 meters below sea floor (mbsf) and 42-59 meters below modern sea level (mbmsl). Both the depth relative to sea floor and the depth relative to modern sea level increase with distance offshore. There is an average down channel slope of 0.4m/km. The incision depths are significantly above the MIS 4 or 5 levels of RSL in the survey area, especially when one accounts for likely GIA related uplift in the region at those times. Furthermore, the MIS 2 drainage system in the MGL1510 survey area and those documented by Nordfjord et al. (2009) are also at elevations significantly above their respective lowstand suggesting that they were relatively immature and did not incise to an equilibrium profile. As such, we interpret the channels to be incised into topography well above sea level. There is no significant trend over the survey area indicating incision through a forebulge or forebulge related topography. However, based on the likely distribution of GIA related uplift during these times (Fig. 4.4), none of the channels are imaged over a large enough region to record the GIA signal of differential uplift/subsidence. Based on the GIA model of Peltier et al. (2015) and the feature identified by Wickert et al. (2019) a study area of >200 km long would be necessary to see any such features.

Table 4.1: Thalweg incision measurements. The depths are in m converted from twtt using a seismic velocity of 1500 m/s.

Channel System	Segment	Point	Easting (m)	Northing (m)	Longitude	Latitude	Distance Up Stream Along Thalweg (m)	Incision Depth (m)	Width (m)	Thalweg Elevation Relative to Modern SL (m)
A	1	1	622072	4381146	-73.5788	39.5713	0	9.2	621	48.8
A	1	2	622251	4381819	-73.5766	39.5774	678	7.7	683	48.8
A	1	3	622313	4383313	-73.5756	39.5908	2196	10.1	571	50.2
A	1	4	621987	4385151	-73.579	39.6074	4008	11.5	270	51.8
A	1	5	622594	4386460	-73.5712	39.6191	5528	10.5	465	47.8
A	1	6	623889	4387324	-73.5565	39.6267	6814	11.0	896	46.2
A	1	7	623561	4388942	-73.56	39.6414	8377	8.2	583	46.4
A	2	1	623630	4390378	-73.5589	39.6543	9758	8.4	321	45.2
A	2	2	623622	4391480	-73.5588	39.6642	11026	7.1	378	44.6
A	1	2	622251	4381819	-73.5766	39.5774	678	7.7	683	48.8
A	3	1	621703	4382830	-73.5828	39.5866	1814	7.2	184	48.5
A	3	2	620463	4384109	-73.597	39.59744	3629	6.2	208	47.8
A	3	3	619359	4384652	-73.6097	39.6033	4896	10.1	448	47.0
A	3	4	618423	4385422	-73.6205	39.6104	6090	12.0	657	46.9
A	3	5	616591	4386008	-73.6417	39.6159	7986	7.4	286	43.7
B	1	1	643130	4365199	-73.3371	39.4244	0	15.2	590	56.3
B	2	1	643912	4366353	-73.3278	39.4347	1179	15.8	731	53.4
B	2	2	643517	4368152	-73.332	39.451	3098	19.4	609	55.9
B	2	3	642968	4369884	-73.338	39.4666	4877	17.6	612	55.5
B	2	4	642396	4371357	-73.3443	39.48	6431	12.6	569	54.8
B	2	5	641126	4372892	-73.3588	39.494	8461	11.9	433?	52.3
B	2	6	640080	4374541	-73.3706	39.5091	10392	9.2	339	48.6
B	2	7	639052	4376817	-73.3821	39.5298	12861	10.1	261	48.4

Channel System	Segment	Point	Easting (m)	Northing (m)	Longitude	Latitude	Distance Up Stream Along Thalweg (m)	Incision Depth (m)	Width (m)	Thalweg Elevation Relative to Modern SL (m)
B	3	1	644616	4366652	-73.3196	39.4373	1475	13.2	438	56.3
B	3	2	644661	4367681	-73.3188	39.4466	2483	9.0	232	54.5
B	3	3	655980	4369227	-73.3148	39.4604	3984	14.8	319	53.0
B	3	4	645255	4371522	-73.31106	39.48106	6377	11.4	385	48.6
B	3	5	645252	4373153	-73.31076	39.49576	8014	11.2	206	48.2
B	3	6	645542	4374559	-73.3071	39.50835	9424	12.7	354	50.0
C	1	1	640826	4367177	-73.36347	39.44266	729	11.2	212	45.8
C	1	2	640162	4367812	-73.37109	39.44846	1722	12.0	160	50.3
C	1	3	639776	4368358	-73.37543	39.45346	2414	14.6	214	55.5
C	1	4	639666	4369030	-73.37656	39.4593	3046	6.2	101	45.8
C	1	5	639572	4369821	-73.37749	39.46666	3883	8.4	95	49.7
C	2	1	641136	4367289	-73.3598	39.4436	954	12.0	240	49.5
C	2	2	640898	4368179	-73.36241	39.45165	1863	12.5	185	52.5
C	2	3	640824	4368897	-73.36314	39.45812	2620	10.5	184	49.5
C	2	4	641031	4369574	-73.36059	39.46419	3282	9.5	151	48.8
C	2	5	641064	4370346	-73.36004	39.47117	4046	7.2	123	48.8
C	2	6	641017	4371226	-73.3604	39.47910	5017	8.4	199?	50.3
D	1	1	647799	4365270	-73.282893	39.42433	1083	11.33775	285	58.725
D	1	2	648777	4366691	-73.27122	39.43693	2549	9.9	228	52.8
D	1	3	649203	4367964	-73.26599	39.44832	3789	11.775	210	54
D	1	4	649802	4369240	-73.25872	39.45872	5182	12.525	401	53.7
D	1	5	649570	4370631	-73.261127	39.47228	6528	7.875	202	52.2
D	1	6	649470	4372234	-73.261925	39.48673	8141	9.375	146	54.6
D	1	7	649656	4373752	-73.25943	39.5037	9698	5.85	144	52.95

4.5.2 Hudson Channel

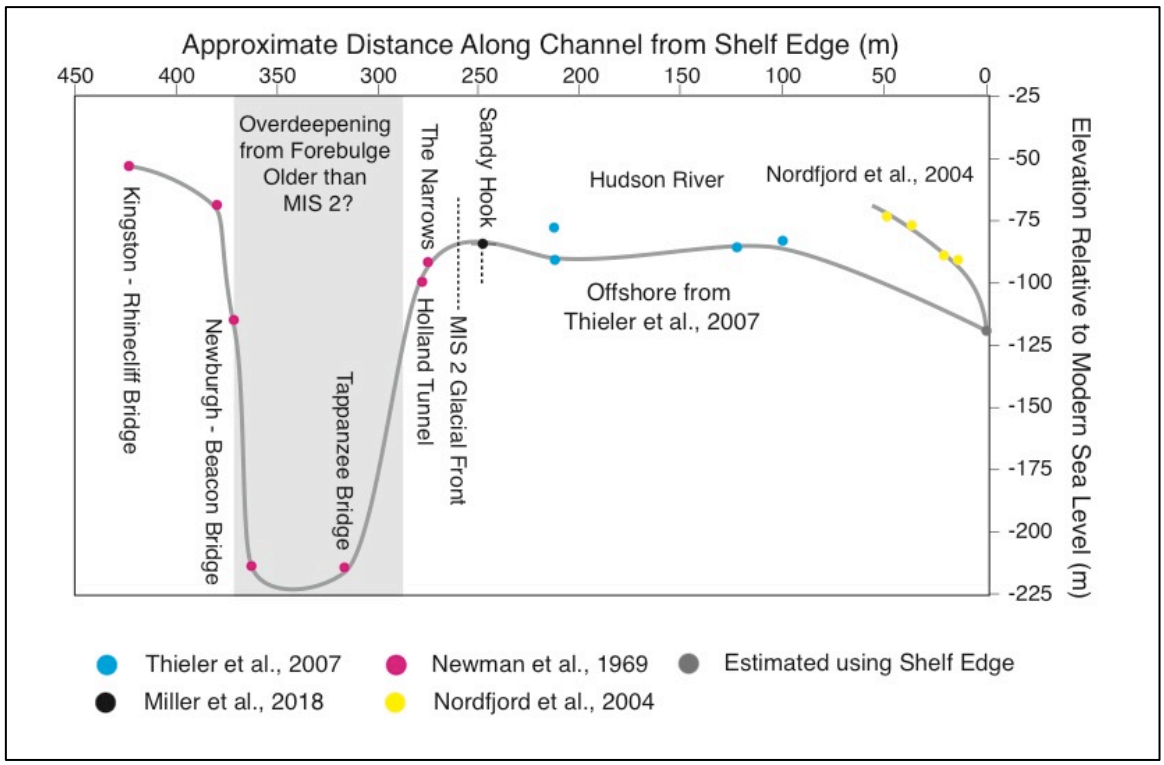

Figure 4.15: Elevations of buried paleochannel incisions relative to modern sea level. The data points are compiled from drilling results and high-resolution sub-bottom surveys. Yellow points indicate data from sub-bottom profiles mapping channels near the Toms River Canyon (Nordfjord et al., 2009). Blue points are based on sub-bottom data from Thieler et al. (2007), magenta and black are drill depths to basement reported by Newman et al. (1969) and Miller et al. (2018). Note, The point at Sandy Hook is west of the main Hudson Channel, but it is unlikely that the paleo-Raritan was more deeply incised than the Hudson so it provides a minimum incision depth.

We suggest that only the largest river systems may be able erode fast enough to keep pace with GIA and accurately reflect LGM GIA conditions. Today, the Hudson river is estuarine up to 250 km inland with the entire estuarine section incised to at or just

below base level (Traykovski et al., 2004). In such a large river, the rate of erosion is high enough to keep pace with the rate of uplift from GIA. Therefore the profile of past GIA uplifts may be recorded as overdeepening of the river incision. We present a profile of incision depths to bedrock for the Hudson River compiled from borings and sub-bottom profiles from literature, extending from onshore at Kingston, NY to near the edge of the continental shelf (Fig. 4.15, Newman et al., 1969; Johnson et al., 2018; Thieler et al., 2007).This profile shows a major overdeepening of the Hudson between the Tappan Zee Bridge and the Catskill Aqueduct (Newman et al., 1969) and a second potential minor overdeepening just offshore (Thieler et al., 2007). Newman et al., (1969) previously identified the larger overdeepening as part of the reversed bedrock surface profile of the Hudson. This was interpreted as an indicator that it was once a fjord. However, we reinterpret this to be an uplifted, eroded, and subsequently collapsed forebulge. Since the feature underlies the ice sheet during the last glacial maximum (Stanford, 2010), this leaves three options for the formation of the feature. First, the forebulge may have been formed during a pre-LGM glaciation. In this case, the basal fill would likely have a radiocarbon age of >~30 ka unless there was scouring during the LGM. Alternatively, the forebulge may have formed during a pause of glacial advance leading up to the last glacial maximum perhaps during MISs 3 and 4. The glaciation may have then advanced covering the site and creating a new GIA geometry with the forebulge migrating offshore. A third option, unrelated to any consideration of a forebulge, is the onshore overdeepened section may just be the result of glacial processes preferentially eroding the relatively weak arkosic Stockton Formation underlying part of the overdeepened region (Rickard et al., 1970). However, we think this is unlikely since

the overdeepened section was eroded to almost 100 m below what would have been LGM base level at ~120 m below present (Wright et al., 2009) and the Stockton Formation is not present under the entire overdeepened section.

The offshore evidence for an overdeepened section related to the LGM is less clear. There is a section roughly 30 km seaward of Sandy Hook that potentially exhibits ~10 m of overdeepening from the LGM (see fig. 4.14). If this feature is real, it is possible that it could be a normal fluvial scour, having nothing to do with GIA. Based on the location of maximum forebulge collapse on the eastern coast of North America between Atlantic City, NJ and Portsmouth, VA (Fig. 4.2) we would anticipate any such feature to be farther offshore. If it is another over deepened section offshore, the size discrepancy between the offshore and onshore Hudson over deepening could be an artifact of data availability; we do not have the coverage of data to identify the full over deepening offshore (either laterally or vertically). Thieler et al. (2007) only recorded down to ~140 ms and an over deepening as seen onshore would require a record twice that. Alternatively, the relatively small size (< 10 m of overdeepening) could be a function of ice sheet geometry, thicknesses, and duration. It could be a result of a thin ice sheet or a relatively short period of time where glaciation in the Hudson Valley extended far enough south for the forebulge to migrate offshore. The difference in lateral size between the overdeepening identified by Wickert et al. (2019) along the Mississippi (~300 km) and the possible overdeepenings of the Hudson (~100 km) could be a result of changing lithologies as suggested by S. Stanford (personal communication) or it could be a result of differences in mantle viscosity resulting in different spatial distributions of GIA related uplift as seen by Roy and Peltier (2015).

4.5.3 Regional Orientations of late Pleistocene to Holocene Channels and GIA

Knebel et al. (1979) first hypothesized that the pathways of offshore paleochannels on the New Jersey continental shelf, formed by terrestrial fluvial systems, which extended across the exposed continental shelf during sea-level lowstands, could be affected by tilting resulting from GIA. They observed a paleochannel associated with their "R" horizon that was oriented north-south that they hypothesized may have been an ancestral Hudson River. Its orientation is significantly different from the modern northwest-southeast orientation of the HSV (Fig. 4.14). They hypothesized that the change in channel orientation may have been a result of GIA related tilting of the landscape. Pico et al. (2018) modeled the response of hypothetical north-south oriented fluvial systems on the exposed continental shelf to the advance of the Laurentide ice sheet ~ 30 ka. In their model, the glacial advance resulted in an eastward migration of the north-south trending channels. To further test this hypothesis, it is necessary to see if the shift in channel orientations identified by Knebel et al. (1979) is systematic across the region, or stochastic. From this study we show two sets of channels: the first predates ~30 ka and is generally oriented north-south. These channels were likely formed during MISs 4 and 5b, or smaller fluctuations in sea level during MIS 3 or 5. The second set of channels, interpreted to have formed during the MIS 2 lowstand and filled during the subsequent sea-level rise, is oriented northwest-southeast.

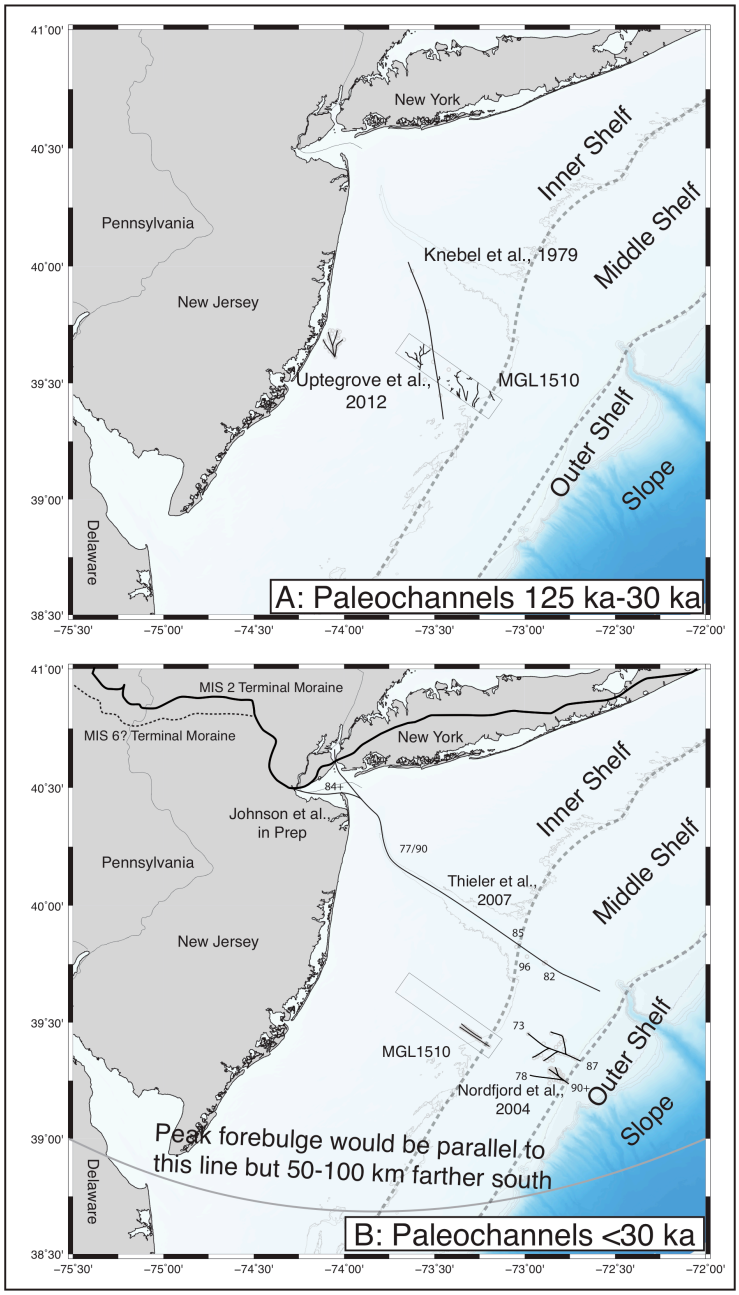

Figure 4.16: Regional maps of paleochannel drainage networks. Panel A shows Paleochannels prior to ~30 ka. These have a regional trend of north-south. Panel B shows paleochannels <30 ka that exhibit a northwest-southeast orientation. This shows good agreement between the mapped channels in MGL1510 with the limited data from other

studies in the region MIS 2 and 6 terminal moraines estimated from Stanford (2010) and Dyke (2003).

We compare the two sets of paleochannels from this study with others identified in the region (Fig. 4.16). Our results are consistent with other studies that have identified paleochannels in the region. Uptegrove et al. (2012) identified paleochannels that had a general north-south orientation offshore Barnegat Inlet, NJ (Fig. 4.16A). Based on vibracore data, these channels correlate to MIS 5. Nordfjord et al. (2009) mapped a series of paleochannels in the EN359 survey (Fig. 4.16B). These channel incisions are interpreted as MIS 2 and the fill as <12.5 ka. Buck et al. (1999) established these dates based on vibracore 27 (Fig. 4.5) that they interpret to have penetrated the edge of the buried channel and the underlying strata. They used foraminiferal assemblages to interpret sea-level variations in the sediments that correlate to the those radiometrically dated by Lagoe et al. (1997).

Thieler et al. (2007) did a high-resolution survey of the modern HSV. In the subbottom profiles, a deeper incision and subsequent fill is visible. Without core data it is not possible to be certain of the date of the fill, but it is interpreted that this incision is related to the MIS 2 lowstand.

Based on the new data from MGL1510 and the previous studies in the region, the shift in channel orientations appears to be a regional shift consistent with a regional process such as GIA. This requires further observations, but based on currently available observations, drainage system orientations in the Pleistocene may indicate an age where

other age control is sparse on the New Jersey continental shelf, with those >30 ka oriented ~north-south and those <30 ka oriented ~northwest-southeast.

Figure 4.4 shows estimates of the GIA field during MISs 2, 4, and 5b. Using the forebulge ranges from MIS 2 to estimate the GIA field during MISs 4 and 5b may be an overestimate of the distance from the glacial front to the forebulge peak as discussed previously. However, between 200 and 300 km there is little difference in the orientation of the forebulge in the study area, though a range of 200 km would put the forebulge north of the study area in several of the smaller glaciations. This would alter the magnitude of tilting but not the direction.

The channels prior to 30 ka flow north-south, outboard and perpendicular to the peripheral forebulges of MISs 4 and 5b (Fig. 4.4B and C), parallel to the orientation of maximum tilting. Pico et al. (2018), suggest that rapid growth of the eastern LIS during the build up to the LGM, particularly the Erie Lobe (Fig 4.2), could induce east-west tipping of the continental shelf between 32 and 26 ka (similar to the cartoon in 4.3A). As such, the orientation of drainage on the continental shelf would have had to shift to northwest-southeast in order to remain perpendicular to the forebulge as seen in the orientations of the <30 ka channels identified in this survey. Alternatively, rapid emplacement of the ice sheet and uplift of the forebulge south of the paleochannels could also cause them to divert to the east (Fig. 4.3B). Without better age control, it is not possible to rule out either scenario.

4.6 Conclusions

Based on new data from MGL1510, we provide a new interpretation for previously studied Pleistocene intervals from IODP Expedition 313 and EN370 sub-

bottom data. We identify two sets of paleochannels in the MGL1510 3D data set. The first set includes the paleochannels identified by Miller et al. (2012) as uP4 and those of Knebel et al., 1979 and is oriented north-south. This drainage system is crosscut by a second drainage system that is oriented northwest-southeast. This younger drainage system we interpret as uP5. Based on its crosscutting relationship with the channels of uP4 we reinterpret the chronology of Miller et al. (2012) such that uP5 is channel fill since the LGM (<30 ka), uP4 are channels between stages 5a and 3. This places uP3 during stage 5c, and uP2 as the fill during MIS 5e. We follow Miller et al. (2012) in placing uP1 in MIS 7. Better imaging and coring to recover datable materials from the proposed uP5 channels is necessary to further test this hypothesis.

While MGL1510 survey grid is likely not laterally extensive enough to record lateral differences in the amount of GIA related vertical land motion, an analysis of the Hudson River and HSV shows potential. We propose that the overdeepening of the paleo-Hudson Channel near the Tappan Zee Bridge identified by Newman et al. (1969) is a result of incision through a pre-LGM forebulge that has subsequently collapsed, similar to the feature identified by Wickert et al. (2019) under the Mississippi. Based on the size of the feature identified by Wickert et al. (2019) and the GIA model results of Peltier et al. (2015) a similar feature from the LGM would likely be >200 km across. There may be a LGM forebulge signal offshore, but more studies are necessary to confirm this.

The two sets of channels have different orientations. The first, dated to >30 ka, is oriented north-south, while the second set, interpreted to be <30 ka, is oriented northwest-southeast. This is consistent with other work done in the region that has mapped datable paleochannels and supports the hypothesis that lateral variability in the rates of GIA

related uplift likely resulted in the regional shift in drainage system as hypothesized by Knebel et al. (1979) and later modeled by Pico et al. (2018). The regional nature of this shift may point to a reliable way of dating shallow paleochannels on the New Jersey continental shelf based on their orientation.

4.7 References

Argus, D.F., Peltier, W., Drummond, R., and Moore, A.W., 2014. The Antarctica component of postglacial rebound model ICE-6G_C (VM5a) based on GPS positioning, exposure age dating of ice thicknesses, and relative sea level histories. Geophysical Journal International v. 198, n. 1, p. 537-563.

Ashley, G.M., Wellner, R.W., Esker, D., and Sheridan, R.E., 1991. Clastic sequences developed during late Quaternary glacio-eustatic sea-level fluctuations on a passive margin: Example from the inner continental shelf near Barnegat Inlet, New Jersey. Geological Society of America Bulletin v. 103, n. 12, p. 1607-1621.

Austin Jr., J.A., Christie-Blick, N., Malone, M.J., et al., 1998. Proceedings of the Ocean Drilling Program Initial Report 174A. College Station. doi: 10.2973/odp.proc.ir.174a.1998

Brain, M.J., Kemp, A.C., Horton, B.P., Culver, S.J., Parnell, A.C., and Cahill, N., 2015. Quantifying the contribution of sediment compaction to late Holocene salt-marsh sea-level reconstructions, North Carolina, USA. Quaternary Research v. 83, n. 1, p. 41-51.

Buck, K.F., Olson, H.C., and Austin Jr, J.A., 1999. Paleoenvironmental evidence for latest Pleistocene sea-level fluctuations on the New Jersey outer continental shelf: combining high-resolution sequence stratigraphy and foraminiferal analysis. Marine Geology v. 154, n. 1-4, p. 287-304.

Carey, J.S., Sheridan, R.E., Ashley, G.M., and Uptegrove, J., 2005. Glacially-influenced late Pleistocene stratigraphy of a passive margin: New Jersey's record of the North American ice sheet. Marine Geology v. 218, n. 1, p. 155-173.

Church, J.A., Godfrey, J.S., Jackett, D.R., and McDougall, T.J., 1991. A model of sea level rise caused by ocean thermal expansion. Journal of Climate v. 4, n. 4, p. 438-456.

Clark, J.A., Farrell, W.E., and Peltier, W.R., 1978. Global changes in postglacial sea level: a numerical calculation. Quaternary Research v. 9, n. 3, p. 265-287.

Corbett, L.B., Bierman, P.R., Stone, B.D., Caffee, M.W., and Larsen, P.L., 2017. Cosmogenic nuclide age estimate for Laurentide Ice Sheet recession from the terminal moraine, New Jersey, USA, and constrains on latest Pleistocene ice sheet history. Quaternary Research v. 87, n. 3, p. 482-498.

Davis, J.L., and Mitrovica, J.X., 1996. Glacial isostatic adjustment and the anomalous tide gauge record of eastern North America. Nature v. 379, p. 331-333.

Dillon, W.P., and Oldale, R.N., 1978. Late Quaternary sea-level curve: Reinterpretation based on glaciotectonic influence. Geology v. 6, n. 1, p. 56-60.

Duncan, C.S., Goff, J.A., Austin Jr., J.A., and Fulthorpe, C.S., 2000. Tracking the last sea-level cycle: seafloor morphology and shallow stratigraphy of the latest Quaternary New Jersey middle continental shelf. Marine Geology v. 170, p. 395-421.

Dyke, A., Andrews, J., Clark, P., England, J., Miller, G., Shaw, J., and Veillette, J., 2002. The Laurentide and Innuitian ice sheets during the last glacial maximum. Quaternary Science Reviews v. 21, n. 1-3, p. 9-31.

Dyke, A.S., Moore, A., and Robertson, L., 2003. Deglaciation of North America: Geological Survey of Canada, Open File 1574.

Emiliani, C., 1966, Isotopic paleotemperatures: Science v. 154, n. 3751, p. 851-857.

Engelhart, S.E., Peltier, W.R., and Horton, B.P., 2011. Holocene relative sea-level changes and glacial isostatic adjustment of the U.S. Atlantic coast. Geology. v. 39, p. 751-754. doi: 10.1130/G31857.1

Ewing, J.I. and Hollister, C.H., 1972. Regional aspects of deep sea drilling in the western North Atlantic. Initial Reports of the Deep Sea Drilling Project covering Leg 11 of the cruises of the drilling vessel "Glomar Challenger", Miami, Florida to Hoboken, New Jersey, April-June, 1970. doi: 10.2973/dsdp.proc.11.132.1972

Farrell, W.E. and Clark, J.A., 1976. On postglacial sea level. Geophysical Journal of the Royal Astronomical Society v. 46, p. 647-667. doi: 10.1111/j.1365-246X.1976.tb01252.x

Goff, J.A., Austin Jr, J.A., and Fulthorpe, C.S., 2013. Reinterpretation of the Franklin "Shore" in the Mid-Atlantic bight as a paleo-shelf edge. Continental Shelf Research v. 60, p. 64-69.

Gurnis, M., 1990. Bounds on global dynamic topography from Phanerozoic flooding of continental platforms. Nature v. 344, n. 6268, p. 754.

Gradstein, F. M., Ogg, J. G., and Smith, A. G., 2004. A geological time scale 2004. Cambridge University Press. Cambridge, U.K.. p. 1-589

Gregory, J.M., Griffies, S.M., Hughes, C.W., et al., 2019. Concepts and terminology for sea level: mean, variability and change, both local and global. Surveys in Geophysics. https://doi.org/10.1007/s10712-019-09525-z.

Johnson, C.S., Fan, Y., and Miller, K.G., in prep., Groundwater Extraction and Land Subsidence at Sandy Hook, NJ USA: A Groundwater Modeling Approach to Estimate Potential Contributions of Aquifer Compaction to Relative Sea-Level Rise.

Johnson, C.S., Miller, K.G., Browning, J.V., Kopp, R.E., Khan, N.S., Fan, Y., Stanford, S.D., and Horton, B.P., 2018. The role of sediment compaction and groundwater withdrawal in local sea-level rise, Sandy Hook, New Jersey, USA. Quaternary Science Reviews v. 181, p. 30-42.

Kleman, J., Fastook, J., Ebert, K., Nilsson, J., and Caballero, 2013. Pre-LGM Northern Hemisphere ice sheet topography. Climate of the Past v. 9, p. 2365-2378. doi: 10.5194/cp-9-2365-2013.

Knebel, H.J., Wood, S.A., and Spiker, E.C., 1979. Hudson River: evidence for extensive migration on the exposed continental shelf during Pleistocene time. Geology v. 7, n. 5, p. 254-258.

Kopp, R.E., 2013. Does the mid-Atlantic United States sea-level acceleration hot spot reflect ocean dynamic variability? Geophysical Research Letters v. 40, p. 3981-3985.

Kopp, R.E., Hay, C.C., Little, C.M., and Mitrovica, J.X., 2015. Geographic variability of sea-level change. Current Climate Change Reports v. 1, p. 192-204.

Lagoe, M.B., Davis, T.A., Austin Jr., J.A., and Olson, H.C., 1997. Foraminiferal constraints on very high-resolution seismic stratigraphy and Late Quaternary hustory, New Jersey continental shelf. Palaios v. 12, p. 249-266.

Leopold, L.B. and Bull, W.B., 1979. Base level, aggradation, and grade. Proceedings of the American Philosophical Society v. 123, n. 3, p. 168-202.

Lisiecki, L.E., and Raymo, M.E., 2005. A Pliocene-Pleistocene stack of 57 globally distributed benthic $\delta^{18}O$ records. Paleoceanography v. 20, p. PA1003. doi: 10.1029/2004PA001071.

Lugrin, L., 2016. Delta Progradation and Channel Drainage Systems from the Early Miocene to the Present Day Between Barnegat and Manasquan Inlets, New Jersey. M.S. Thesis, Rutgers University, New Brunswick, NJ. p. 1-176.

McHugh, C.M., Hartin, C.A., Mountain, G.S., and Gould, H.M., 2010. The role of glacio-eustasy in sequence formation: Mid-Atlantic Continental Margin, USA. Marine Geology v. 277, no. 1, p. 31-47.

McHugh, C.M. and Olson, H.C., 2002. Pleistocene chronology of continental margin sedimentation: New insights into traditional models, New Jersey. Marine Geology v. 186, p. 389-411.

Miller, K.G., Kopp, R.E., Horton, B.P., Browning, J.V., and Kemp, A.C., 2013. A geological perspective on sea-level rise and its impacts along the US mid-Atlantic coast. Earth's Future, v. 1, n. 1, p. 3-18.

Miller, K.G., Sugarman, P.J., Browning, J.V., Sheridan, R.E., Kulhanek, D.K., Monteverde, D.H., Wehmiller, J.F., Lombardi, C., and Feigenson, M.D., 2012. Pleistocene sequence stratigraphy of the shallow continental shelf, offshore New Jersey: Constraints from Integrated Ocean Drilling Program Leg 313 core holes. Geosphere v. 9, n. 1, p. 74-95.

Miller, K.G., Sugarman, P.J., Stanford, S., Browning, J.V., Baldwin, K., Buttari, B., Dunham, B., Farazaneh, M., Filo, R., Gagliano, M.P., Horton, B., Gallegos, G., Graham, S., Johnson, C., Khan, N., Kulhanek, D.K., Lombardi, C.J., McKoy, K., McLaughlin, P.P., Monteverde, Jr., D.H., Stanley, J.N., Woodard, S., and Malerba, N., 2018. Sandy Hook site report, in Miller, K.G., Sugarman, P.J., Browning, J.V., et al., eds., Proceedings of the Ocean Drilling Program, Initial reports, Volume 174AX (Suppl.): College Station, TX, Ocean Drilling Program.

Mitrovica, J.X., Tamisiea, M.E., Davis, J.L., and Milne, G.A., 2001. Recent mass balance of polar ice sheets inferred from patterns of global sea-level change. Nature v. 409, p. 1026-1029. doi: 10.1111/j.1365-246X.2011.05090.x.

Moucha, R., Forte, A.M., Mitrovica, J.X., Rowley, D.B., Quéré, S., Simmons, N.A., and Grand, S.P., 2008. Dynamic topography and long-term sea-level variations: There is no such thing as a stable continental platform. Earth and Planetary Science Letters v. 271, n. 1, p. 101-108.

Mountain, G.S., Nedimovic, M., Austin, J., Fulthorpe, C., Aali, M., Baldwin, K., Bhatnagar, T., Johnson, C., Kucuk, H.M., Newton, A., and Stanley, J.N., 2015,

Early results of an ultra-high resolution MCS survey across IODP Expedition 313 drillsites. American Geophysical Union. Fall Meeting, San Francisco, CA. Abstract: OS21A-1962

Mountain, G.S., Proust, J.-N., McInroy, D., and Cotterill, C., and the Expedition 313 Scientists, 2010. Proceedings of the Integrated Ocean Drilling Program, Expedition 313: Tokyo, Integrated Ocean Drilling Program Management International, Inc., doi:10.2204/iodp.proc .313.2010

Mountain, G.S., Burger, R.L., Delius, H., Fulthorpe, C.S., Austin, J.A., Goldberg, D.S., Steckler, M.S., McHugh, C.M., Miller, K.G., Monteverde, D.H., Orange, D.L., and Pratson, L.F., 2007. The long-term stratigraphic record on continental margins: Continental margin sedimentation: From sediment transport to sequence stratigraphy. International Association of Sedimentologists Special Publication, v. 37, p. 381-458.

Mountain, G.S., and Monteverde, D.H., 2000. Pleistocene deposition across the New Jersey shelfslope break. Eos (Transactions, American Geophysical Union), Fall Meeting Supplement no. 81, p. F654.

Mountain, G.S., Miller, K.G., Blum, P.,et al., 1994. Proceedings of the Ocean Drilling Program Initial Reports v. 150. College Station, TX (Ocean Drilling Program). doi:10.2973/odp.proc.ir.150.1994

Newman, W.S., Thurber, D.H., Zeiss, H.S., Allan, B.A., Rokach, A., and Musich, L., 1969. Late Quaternary geology of the Hudson River Estuary: a preliminary report. Transactions of the New York Academy of Sciences Series II v. 31, p548-570.

Nordfjord, S., Goff, J.A., Austin, J.A., and Duncan, L.S., 2009. Shallow stratigraphy and complex transgressive ravinement on the New Jersey middle and outer continental shelf. Marine Geology, v. 266, no. 1, p. 232-243.

Nordfjord, S., Goff, J.A., Austin Jr., J.A., and Sommerfield, C.K., 2004. Seismic geomorphology of buried channel systems on the New Jersey outer shelf: assessing past environmental conditions. Marine Geology v. 214, p. 339-364.

Oakley, B.A., and Boothroyd, J.C., 2012. Reconstructed topography of Southern New England prior to isostatic rebound with implications of total isostatic depression and relative sea level. Quaternary Research v. 78, n. 1, p. 110-118.

Piechuch, C.G., Huybers, P., Hay, C.C., Kemp, A.C., Little, C.M., Mitrovica, J.X., Ponte, R.M., and Tingley, M.P., 2018. Origin of spatial variation in US East Coast sea-level trends during 1900-2017. Nature v. 564, p. 401-408.

Peltier , W.R., Argus, D.F., and Drummond, R., 2015. Space geodesy constrains ice age terminal deglaciation. The global ICE-6G_C (VM5a) model. Journal of Geophysical Research. Solid Earth v. 120, p. 450-487. doi: 10.2003/3025JB011176.

Peltier, W., 2004. Global glacial isostasy and the surface of the ice-age Earth: the ICE-5G (VM2) model and GRACE. Annual Reviews of Planetary Science v. 32, p. 111-149.

Peltier, W.R., 1998. Postglacial variations in the level of the sea: Implications for climate dynamics and solid Earth geophysics. Reviews of Geophysics v. 36, n. 4, p. 603-689.

Peltier, W.R., and Andrews, J.T., 1976, Glacial-isostatic adjustment—I. The forward problem: Geophysical Journal International v. 46, n. 3, p. 605-646.

Pico, T., Mitrovica, J., Braun, J., and Ferrier, K., 2018. Glacial isostatic adjustment deflects the path of the ancestral Hudson River. Geology v. 46, n. 7, p. 591-594.

Pitman III, W.C. and Golovchenko, X., 1983. The effect of sea-level change on the shelfedge and slope of passive margins. Society of Economic Paleontologists and Mineralogists Special Publication v. 33, p. 41-58.

Poag, C.W., 1985. The New Jersey transect: stratigraphic framework and depositional history of a sediment-rich passive margin. In: Initial Reports of the Deep Sea Drilling Project. v. 95. Eds Poag, C.W., and Watts, A.B., and The Leg 95 Shipboard Party. US Government. Printing Office, Washington, DC. p. 763-817.

Rickard, L.V., Isachsen, Y.W., and Fisher, D.W., 1970. Geologic Map of New York. New York State Museum and Science Service. Map and Chart Series 15.

Roy, K., and Peltier, W., 2015. Glacial isostatic adjustment, relative sea level history and mantle viscosity: reconciling relative sea level model predictions for the US East coast with geological constraints. Geophysical Journal International v. 201, n. 2, p. 1156-1181.

Schwab, W.C., Denny, J.F., Foster, D.S., Lotto, L.L., Allison, M.A., Uchupi, E., Danforth, W.W., Swift, B.A., Thieler, E.R., and Butman, B., 2002. High-resolution Quaternary seismic stratigraphy of the New York Bight Continental Shelf. U.S. Geological Survey Open-File Report 02-152

Shackleton, N., 1987. Oxygen isotopes, ice volume and sea level. Quaternary Science Reviews v. 6, n. 3-4, p. 183-190.

Sheridan, R., Ashley, G., Miller, K., Waldner, J., Hall, D., and Uptegrove, J., 2000. Offshore-onshore correlation of upper Pleistocene strata, New Jersey Coastal Plain to continental shelf and slope. Sedimentary Geology v. 134, no. 1, p. 197-207.

Simms, A., Reynolds, L.C., Bentz, M., Roman, A., Rockwell, T., and Peters, R., 2016. Tectonic Subsidence of California Estuaries Increases Forecasts of Relative Sea-Level Rise. Estuaries and Coasts v. 39, p. 1571-1581.

Stanford, S.D., 2010. Onshore record of Hudson River drainage to the continental shelf from the late Miocene through the late Wisconsinan deglaciation, USA: synthesis and revision. Boreas v. 39, no. 1, p. 1-17.

Swift, D.J., 1974. Continental shelf sedimentation, The geology of continental margins. Springer, p. 117-135.

Thieler, E.R., Butman, B., Schwab, W.C., Allison, M.A., Driscoll, N.W., Donnelly, J.P., and Uchupi, E., 2007. A catastrophic meltwater flood event and the formation of the Hudson Shelf Valley. Palaeogeography, Palaeoclimatology, Palaeoecology v. 246, n. 1, p. 120-136.

Törnqvist, T.E., Wallace, D.J., Storms, J.E., Wallinga, J., Van Dam, R.L., Blaauw, M., Derksen, M.S., Klerks, C.J., Meijneken, C., and Snijders, E.M., 2008. Mississippi Delta subsidence primarily caused by compaction of Holocene strata. Nature Geoscience v. 1, p. 173-176.

Traykovski, P., Geyer, R., and Sommerfield, C., 2004. Rapid sediment deposition and fine‐scale strata formation in the Hudson estuary. Journal of Geophysical Research: Earth Surface v. 109, n. F02004, p. 1-20.

Uchupi, E., Driscoll, N., Ballard, R., and Bolmer, S., 2001. Drainage of late Wisconsin glacial lakes and the morphology and late quaternary stratigraphy of the New

Jersey–southern New England continental shelf and slope. Marine Geology v. 172, n. 1-2, p. 117-145.

Uptegrove, J., Monteverde, D.H., Whitesell, L.A., Stanford, S.D., and Waldner, J.S., 2015. High-resolution seismic tracing of the transgression across the coastal interface, Brigantine, New Jersey. Geophysics v. 80, n. 3, p. WB43-WB63.

Uptegrove, J., Waldner, J.S., Stanford, S.D., Monteverde, D.H., Sheridan, R.E., and Hall, D.W., 2012. Geology of the New Jersey Offshore in the Vicinity of Barnegat Inlet and Long Beach Island: New Jersey Geological and Water Survey Geologic Map Series (GMS) 12-3, p. 1-13.

van Hinte, J.A., Wise, S.W., and the Leg 93 Shipboard Party, 1987. Initial Reports of the Deep Sea Drilling Project v. 93. US Government. Printining Office, Washington, DC. p. 1-1423.

Wickert, A.D., Anderson, R.S., Mitrovica, J.X., Naylor, S., and Carson, E.C., 2019. The Mississippi River records glacial-isostatic deformation of North America. Science Advances v. 5, no. eaav2366, p. 1-7.

Wright, J.D., Sheridan, R.E., Miller, K.G., Uptegrove, J., Cramer, B.S., and Browning, J.V., 2009. Late Pleistocene sea level on the New Jersey Margin: Implications to eustasy and deep-sea temperature. Global and Planetary Change v. 66, p. 93-99.

Yin, J., Schlesinger, M.E., and Stouffer, R.J., 2009. Model projections of rapid sea-level rise on the northeast coast of the United States. Nature Geoscience, v. 2, p. 262-266.

CHAPTER 5: Conclusions

This dissertation integrated sedimentological studies, numerical modeling, groundwater models, cores, and seismic data to study processes that contribute to relative sea-level (RSL) change along the New Jersey margin. There are three primary goals of this study. The first is to identify and better understand the local processes that contribute to recent to modern RSL change, the second is to quantify their contributions at Sandy Hook. The third objective is to evaluate the effects of glacial isostatic adjustment (GIA) on the paleochannels of the New Jersey continental shelf and determine if they can be used as a record to aid in reconstructing past GIA effects to better understand the spatial distribution of GIA today.

5.1 Summary of Results

In Chapter 2, we performed sedimentological analyses on a transect of 3 cores that sampled the latest Pleistocene to Holocene section at Sandy Hook, NJ in order to evaluate the contributions from compaction of organic and inorganic sediments to the relatively high rate of RSL rise measured by the tide gauge at Sandy Hook. These analyses included percent organic matter, grain size, radiocarbon, and porosity measurements. The percent organic matter measurements were between 0.4 and 6.0%, too low and too dispersed in a siliciclastic matrix to compact on its own and significantly contribute to the rate of RSL rise at Sandy Hook. The porosity measurements, grains size analyses, and radiometric dates were used to develop a numerical model to simulate the autocompaction of the young (latest Pleistocene to Holocene), fine grained (<63μm) sediments underlying the tide gauge at Sandy Hook. The numerical model calculated porosity as a function of grain size, age, and burial depth. By removing one layer of

sediment at a time, the model was able to work backwards through time decompacting the sediment column based on the change in porosity with respect to changes in age, grain size, and burial depth. In this way we were able to determine that autocompaction of the young sediments underlying Sandy Hook was responsible for an average of 0.16 mm/yr (90% Confidence Interval; C.I. 0.06-0.32 mm/yr) for the 20th century leaving 0.7 mm/yr (90% C.I. 0.3-1.2 mm/yr) of excess sea-level rise at Sandy Hook due to local processes unaccounted for.

In Chapter 3, we built a 3 dimensional finite difference groundwater model to evaluate the potential for subsidence due to groundwater extraction at Sandy Hook and to assess the relative contributions of regional and local groundwater withdrawal. The model encompassed the northern half of the New Jersey coastal plain and the stratigraphy under Sandy Hook down to basement. It was a transient model that ran from 1885 to 2015 to simulate the temporal variability in the rate of groundwater related subsidence. We found that the 20th century average rate of groundwater related subsidence was 0.3 mm/yr with a maximum range of between 0.1 and 0.5 mm/yr. The modern rate is between 0.6 and 0.8 mm/yr. Regional and local sources of pumping are each responsible for roughly half of the total subsidence experienced at Sandy Hook since 1885. Up to 1965 the local pumping for Fort Hancock on Sandy Hook was the dominant source of subsidence. After 1965, regional groundwater pumping for surrounding Monmouth County, NJ became the dominant contributor to the rate of subsidence.

In Chapter 4, we used new 3D seismic data in combination with sub-bottom profiles to examine the response of paleochannels on the New Jersey inner continental shelf to GIA. Where possible, we measured incision depths of channel thalwegs along

their profiles in the 3D volume to try to identify differential uplift and/or subsidence related to GIA. Aside from a ~4m/km slope along the channel profiles there was no evidence of differential uplift from GIA in the 3D survey area. Poor data quality due to proximity to the sea-floor, collection/processing artifacts, and noise from numerous small scale channels limited the number of drainage systems that could be measured in this way. Further, the spatial coverage of the data set does not appear to be large enough to see regional variations in the amount of uplift. We also mapped the drainage systems and assigned relative ages to the channels in order to assess the whether differential GIA across the region could result in the rerouting of drainage systems across the exposed continental shelf. We found that ~30 ka the drainage systems across the shelf shifted from a north-south orientation visible in channels between 120 and 30 ka to a northwest-southeast trend in channels <30 ka. This is consistent with a mapped approximation of GIA fields prior to 30 ka that indicate a glacial forebulge trending east west resulting in a maximum tilting of the landscape in a north to south direction. During the last glacial maximum (~18-20 ka) the Laurentide Ice Sheet advanced far enough south for the peak of the forebulge to reach the New Jersey Continental Shelf and divert the drainage to the southeast. However, without better age control it is not possible to tell if this is because the southwest-northeast trending forebulge formed landward of the shelf causing a southeast tilt of the landscape or if the forebulge formed seaward of the paleochannels causing them to divert.

5.2 Implications and Contributions

The New Jersey margin is a hotspot for sea-level rise with tide gauges registering some of the highest rates of RSL rise along the east coast of North America. This is due

to a combination of local and regional processes including natural and anthropogenic compaction and GIA. The presence of a tide gauge and continually operating global positioning system stations at Sandy Hook, NJ provided an opportunity to test simulations that quantify the relative contributions of each of these processes to RSL rise. This study used sediment analyses of cores, well logs, and seismic data from Sandy Hook and the rest of the coastal plain to build a numerical model for autocompaction and a groundwater model to simulate the contributions of natural and anthropogenic compaction at Sandy Hook. This improves our understanding of the local processes that affect the rate of RSL rise and provides methods for estimating the contributions of autocompaction and groundwater related compaction at other locations. This could be particularly useful in locations where there are no tide gauges that need to estimate what the rate of RSL rise is for community planning.

Additionally this study added to our understanding of the Pleistocene record on the New Jersey inner continental shelf. We identified a potential new set of channels that made us reconsider and improve the chronology of the Pleistocene section of the inner continental shelf. We found evidence suggesting that there was a regional shift in channels trends that supports the hypothesis that GIA related tipping of the landscape redirected channel drainage on the shelf at 30 ka. This can lend support to some models of ice distribution during the LGM that would result in a southeast-northwest trending forebulge.

5.3 Limitations and Future Research

Chapters 2 and 3 of this study involved the development of models to simulate natural and anthropogenic compaction. They were applied to and tested at Sandy Hook,

NJ, a single location. Application of these methods of quantifying the contributions of coastal plain processes to RSL to other sites with similar tide gauge records would go a long way toward testing the robustness of the methods. If they prove applicable elsewhere, they could then be used with more confidence in places lacking sea-level records or GPS measurements of vertical land motion. While a combination of GIA, autocompaction, and groundwater extraction related subsidence likely closes the RSL the gap in rates of RSL rise between Sandy Hook, NJ and The Battery, NY, it is possible, given the error bars on the estimates, that there could be other local processes at work at one of the two sites causing the remaining ~0.4 mm/yr difference between the sites. Future work could try to identify any other processes affecting RSL at the two sites differently.

Our analysis of channels on the New Jersey continental shelf was limited by the resolution and spatial distribution of our data. Future studies will be necessary to test the results of this study. Sub-bottom profiles confirming the existence of the drainage system <30 ka and vibracores to recover channel fill materials from the MIS 2 and older channels is necessary to confirm the findings of this study.

APPENDIX 1: The Role of Sediment Compaction and Groundwater Withdrawal in Local Sea-Level Rise, Sandy Hook, New Jersey, USA: Supplementary Material

S1.1 Methods

S1.1.1 Sandy Hook Progradation Estimate

The rate of progradation for Sandy Hook was estimated based on the distance of the Sandy Hook Lighthouse from the northern tip of Sandy Hook at the time of its construction in 1764 (0.15 km; Moss, 1964) and its distance in 2016 as measured using Google Earth (2.24 km). Based on the 2.09 km of progradation over this 252 year interval, the estimated rate is 8.3 m/yr.

S1.1.2 Sample Retrieval

Between April and May 2014, a north-south transect of three coreholes were drilled at Sandy Hook. The cores, designated North Maintenance Yard (NMY), Salt Shed (SS), and South Maintenance Yard A (SMY-A), span approximately 4 km of the spit (Figure 4.1). The cores recovered Quaternary and Cretaceous sediments penetrating to 86.9 m at the NMY, 77.7 m at the SS, and 53.3 m at the SMY. Overall recovery was ~80%, with greater recovery in the finer sediments (Miller et al., in prep.). Particularly challenging to drill were the upper Quaternary sands, which tended to jam the barrel or fall out of the shoe during extraction. The samples were described and imaged in the field immediately after recovery and then wrapped in plastic before being transported to the Rutgers Core Repository for refrigerated storage, where they were further examined and sampled (Miller et al., in prep.). Samples were taken at 3.0 m (5 ft) intervals for the sand rich portions of the cores and at 1.5 m (2.5 ft) intervals for the mud rich portions of

the cores. Care was taken to get representative samples and avoid anomalous sections or areas of rapid change in the core.

	Number of Samples from Each Core		
Analysis	NMY	SS	SMY-A
Percent Organic Matter	33	33	23
Grain Size	34	34	25
Porosity	37	30	23
Radiocarbon Ages	16	6	4

Table ST1.1: Number of samples taken for each analysis.

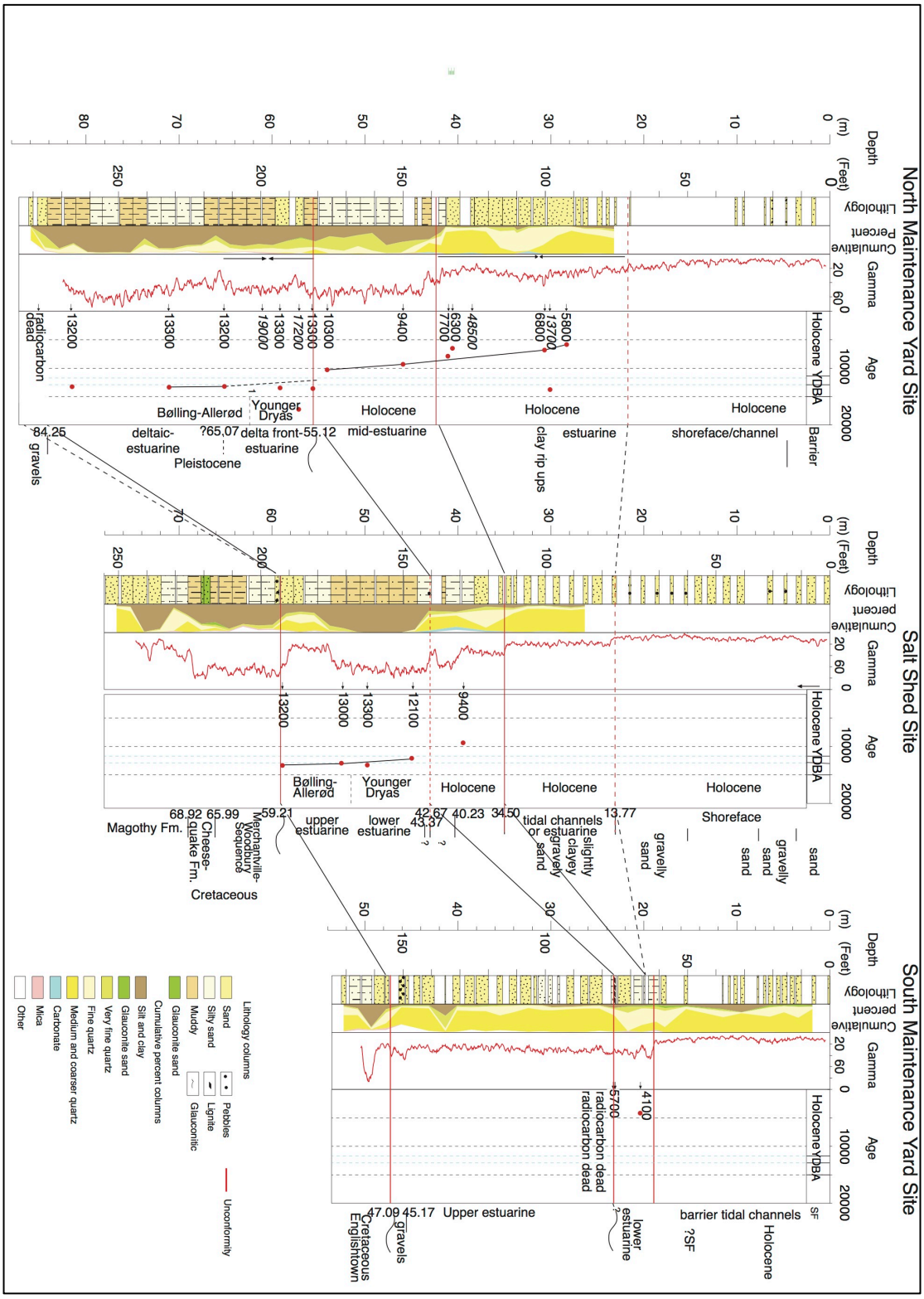
North Maintenance Yard Site
Salt Shed Site
South Maintenance Yard Site
Depth
(m)
(Feet)
Lithology
Cumulative percent
Gamma
Age
Holocene
YDBA
Barrier
Bølling-Allerød
Younger Dryas
Holocene
deltaic-estuarine
delta front-estuarine
mid-estuarine
estuarine
shoreface/channel
clay rip ups
Pleistocene
gravels
Magothy Fm.
Cheesequake Fm.
Merchantville-Woodbury Sequence
Cretaceous
upper estuarine
lower estuarine
tidal channels or estuarine
Shoreface
sand
gravelly sand
slightly clayey gravelly sand
radiocarbon dead
barrier tidal channels
?SF
SF
Upper estuarine
Cretaceous Englishtown
Lithology columns
Sand
Silty sand
Muddy
Glauconite sand
Glauconite sand
Slit and clay
Cumulative percent columns
Fine quartz
Very fine quartz
Medium and coarser quartz
Carbonate
Mica
Other
Pebbles
Lignite
Glauconitic
Unconformity

Figure SF1.1: Correlation of Sandy Hook Sediment Cores. For each core the first column is lithology, the second is cumulative percent, the third is the gamma log, and the fourth is calibrated radiocarbon ages.

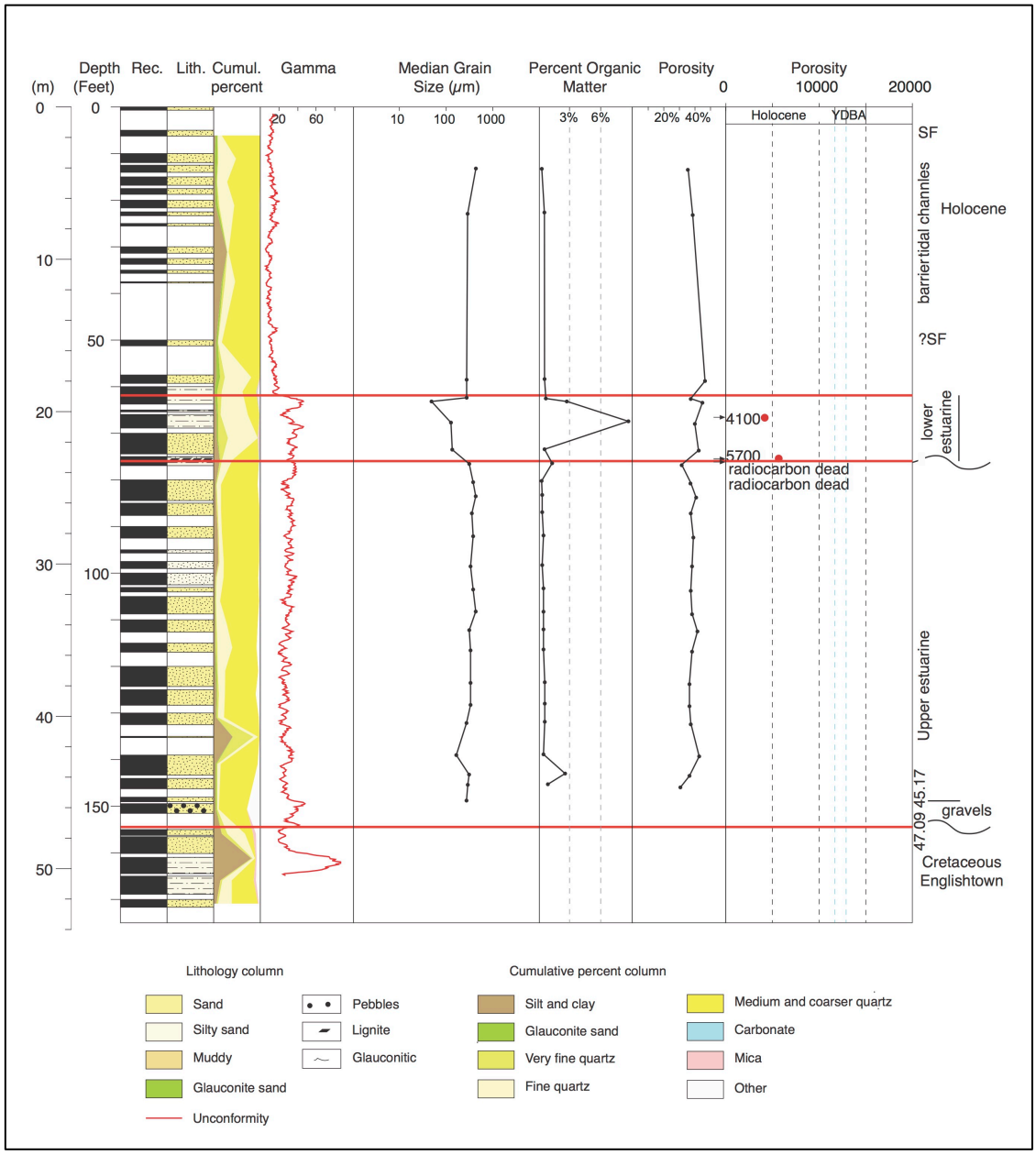

Figure SF1.2: SH-SMY-A. See Fig. 2.4 for description.

S1.1.3 Cumulative Percent

Cumulative percent plots for the sediments of each core were produced using washed samples. Each sample was dried and weighed (W_d) before being washed through a 63 μm sieve. The residual (coarser than 63 μm) was then dried and weighed (W_{63}) to calculate the percent sand (P_s). The remainder was the percent mud (P_m).

$$P_s = \left(\frac{W_d - W_{63}}{W_d}\right) \times 100\% \qquad \text{(SE1.1)}$$

$$P_m = 100\% - P_s \qquad \text{(SE1.2)}$$

The process was then repeated using successively coarser sieves for each sand size fraction (very fine, fine, medium, and coarse). The sand fractions were then examined visually to estimate the percentage quartz, glauconite, carbonate (including foraminifers, shells, etc.), mica, and other materials.

S1.1.4 Percent Organic Matter

The percent organic matter was found using the loss on ignition method following the work of Heiri et al. (2001). The measurements were taken in the Benthic Ecology Lab at Rutgers Department of Marine and Coastal Sciences. 1 cc samples were taken at the above-mentioned sampling intervals. More closely spaced samples were taken in areas of rapid lithologic variation to make sure that all lithologies were represented. The 1 cc samples were each placed in a premeasured tinfoil boat (M_b). The wet samples and boats (M_{w+b}) were weighed to get a wet sample weight (M_w).

$$M_w = M_{w+b} - M_b \qquad \text{(SE1.3)}$$

The samples were then placed in marked crucibles to be placed in a drying oven. The samples spent more than 48 hours in the drying oven at ~55° C to ensure that the samples were completely dried. The samples were then taken out of the oven and allowed to cool

in a desiccator for ~15 minutes before taking the mass of the dry sample and tinfoil boat (M_{d+b}). The mass dry (M_d) is then calculated by removing the mass of the boat (Equation SE4)

$$M_d = M_{d+b} - M_b \quad \text{(SE1.4)}$$

This step could only be done with four samples at a time to ensure as little humidity as possible contaminated the samples. When exposed to the open air, the samples gained ~2 μg of mass per minute, which translates to as much as 0.07% of the sample's mass every five minutes of exposure. The measurement was also repeated several times after repeated dryings in order to prevent any significant error humidity might generate in the results.

Once this step was completed the percentage water could be calculated to compare with the percent water (P_w) found while measuring porosity.

$$P_w = \left(\frac{M_w - M_d}{M_d}\right) \times 100\% \quad \text{(SE1.5)}$$

After the dry mass was measured, the sample was placed in a muffle furnace at 550° C for 4 hours as recommended by Heiri et al. (2001). The samples then cooled in the furnace overnight before being placed in the drying oven for ~48 hours to remove any moisture absorbed during cooling. Once dry, the post-ashing mass $M_{(a+b)}$ was measured. Once again, only four samples were taken out of the drying oven at a time and allowed to cool in a desiccator for 15 minutes before measuring the mass.

$$\text{Inorganic Mass } (M_{550}) = M_{a+b} - M_b \quad \text{(SE1.6)}$$

Percent organic matter (OM) was then calculated using the following equation.

$$\%\, OM = \frac{M_d - M_{550}}{M_d} \times 100\% \quad \text{(SE1.7)}$$

While we did not run duplicates of any of the samples, Heiri et al. (2001) showed that across laboratories there is typically less than a ±2% error to measurements of mixed sediment with <~30% OM. Duplicate measurements of mass showed <0.05 % error caused by issues with humidity. As such, we apply an error of ±3% (2σ) to all of our samples

S1.1.5 Grain Size Analysis

Grain size analysis was done using a Malvern Mastersizer 3000 in the Sea Level Research Lab at Rutgers Department of Marine and Coastal Sciences. 1 cc samples were collected at ~1.5 m (5 ft) intervals in muds and ~3.0 m (10 ft) intervals in sands as near as possible to porosity samples. Samples were prepared for the Malvern by placing each 1 cc of sediment in a falcon tube. The tubes were then filled with 20-30 ml of 30% hydrogen peroxide in order to burn off any organic material. The samples were allowed to sit for ~24 hours before being placed in a warm water bath at 50-60 °C. The samples were left in the bath until the hydrogen peroxide finished reacting with the organic material (2-4 weeks). More hydrogen peroxide was added as necessary. The falcon tubes were then filled to 40 ml with deionized water and placed in a centrifuge for a minimum of 3 minutes at 3600 rpm. Some samples required significantly more time for the fine material to fall out of suspension. Once complete, the water and hydrogen peroxide was poured off the top. The process of adding deionized water and running the samples through the centrifuge was repeated twice more for each sample to ensure that all of the hydrogen peroxide and any organic residue was removed from the sample. At this point the samples were ready to be placed in the Malvern. 10 ml of deionized water containing calgon was placed in the test tube with the sample. The samples were then allowed to

soak for 24 hours and then placed in a sonicator for 30 minutes. Once the sample was ready to be run, the sample was stirred up. Immediately upon finishing stirring a pipette was used to take a sample, which was then placed in the Malvern, which then measured the distribution of grain sizes volumetrically. This process was repeated at least twice for all samples to ensure a good representative sample was taken with the pipette.

S1.1.6 Age Model Error

We used BACON, a Bayesian tool for age-depth modeling (Blaauw and Christen, 2013), to create an alternative age model to the linear models used in the main text of this article and to constrain potential error for our initial age model. However, the BACON model had difficulty modeling the rapid deposition at the base of the Pleistocene Section at both the NMY and SS sites. In particular, the BACON models consistently required the sediments to be older than the material sampled and dated from those sediments in the lower portion of the age model. This would require significant (>10 m) reworking of material down section that is unlikely. Because of this we chose to use our linear age models as shown in the main text.

37.42944 #d.min	1 #cc
58.61304 #d.max	0 #postbomb
1 #d.by	IntCal13 #cc1
0 #depths.file	Marine13 #cc2
NA #slump	SHCal13 #cc3
400 #acc.mean	ConstCal #cc4
1.5 #acc.shape	m #unit
0.7 #mem.mean	0 #normal
4 #mem.strength	3 #t.a
48 #hiatus.depths	4 #t.b
1000 #hiatus.mean	0 #d.R
8 #hiatus.shape	0 #d.STD
0 #BCAD	0.95 #prob

Table ST1.2: Bacon Age Model Priors

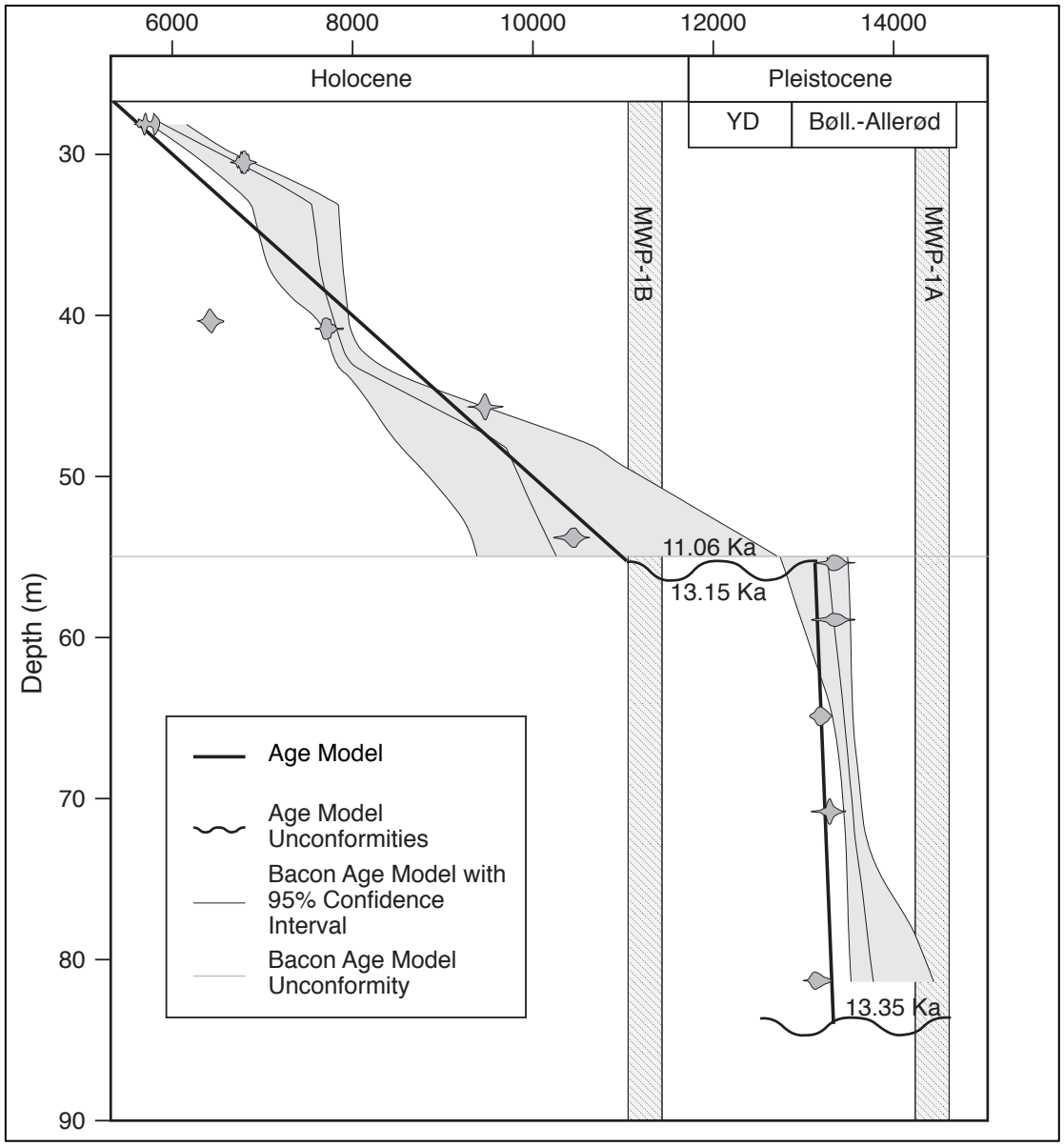

Figure SF1.3: NMY Age Model with Bacon Error. The thin black line indicates the mean and the thin gray lines indicate the 90% confidence interval.

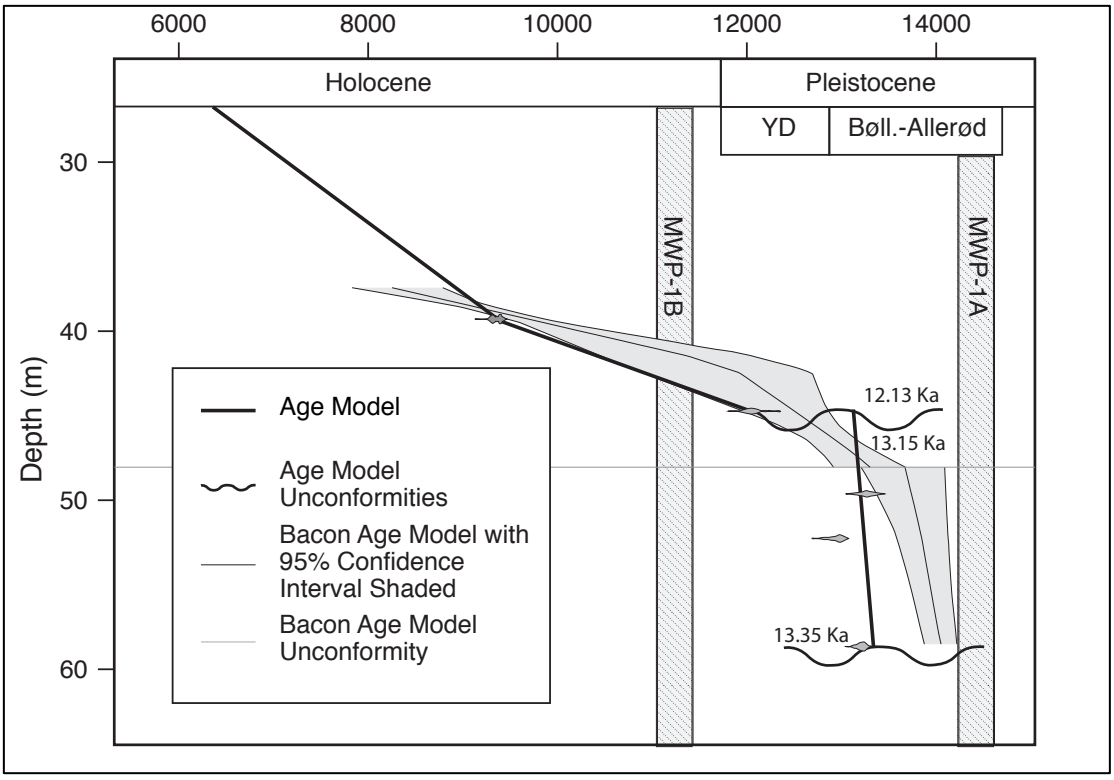

Figure SF1.4: SS age model with Bacon Error. See Figure SF1.3 for explanation.

S1.1.7 Porosity

Porosity was measured down core using the above-mentioned sampling scheme. Porosity (*Por*) was measured gravimetrically and calculated using equation SE8 where V_p is the pore volume and V_g is the grain volume.

$$\boldsymbol{Por} = \frac{\boldsymbol{V_p}}{\boldsymbol{V_g}} \qquad \textbf{(SE1.8)}$$

Samples were collected using pre-weighed (M_p) 20 cubic centimeter plugs in order to know the approximate sample volume. The samples were then immediately taken to the lab for processing. A 50 ml beaker was marked for each sample and had its mass measured (M_b). The plug and wet sample were then placed in the beaker and the mass of

the wet sample, beaker, and plug (M_{spbw}) was then measured. The beaker and plug masses were then subtracted to find the wet mass (M_w) of the sample.

$$M_w = M_{spbw} - M_p - M_b \quad \text{(SE1.9)}$$

The samples were then placed in an oven at ~55° C for 48 hours in order to dry the sample. The mass of each sample including the plug and beaker (M_{spbd}) was then measured to get the dry mass (M_d).

$$M_d = M_{spbd} - M_p - M_b \quad \text{(SE1.10)}$$

The pore volume (V_p) was then estimated using the amount of water lost during drying (V_{wl}), which assumes that little or no water was lost during drilling or the subsequent storage before the samples were taken and that the mass of water lost (M_{wl}) is the pore volume. This seems to be accurate for the finer grained sections of the core. However, coarser sections including shoreface and outwash deposits tended to dewater faster making this method less effective for those intervals.

$$V_p = V_{wl} = \ M_{wl} = M_w - M_d \quad \text{(SE1.11)}$$

The grain volume was then measured by displacing a known volume of water in a graduated cylinder. The dry samples were removed from the beaker and plugs and placed into graduated cylinders with a known volume of water. The cylinders were then sealed and allowed to soak for a minimum of 48 hours before the samples were stirred to remove any air bubbles trapped in the sediment. A known volume of water was then used to rinse the stirring rod and the inside of the graduated cylinder. The samples were then allowed to soak for an additional 48 hours before a final volume measurement was taken. The difference between the final volume of water and sediments (V_{w+s}) and the total

volume of water (including initial and the water used to rinse) (V_w) allowed for the calculation of the grain volume (V_g) of each sediment sample.

$$V_g = V_{w+s} - V_w \quad \text{(SE1.12)}$$

The grain volume and pore volume were then put into Equation SE8 to calculate porosity.

A second measurement of porosity, independent of the pore volume and the amount of water retained in the core, was made in order to verify the results. Porosity was calculated using the volume of the plug (20 cc) as the total volume of the sample assuming that any space not taken up by grains was pore volume. This value would include both air and water space in the core.

In the second method, Supplementary Equation SE8 was modified to remove the pore volume variable (Equation SE13). Total Volume (V_{tot}) was always the volume of the plug (20 cc) and grain volume was the same grain volume measured and calculated previously.

$$Por = \frac{V_{tot} - V_g}{V_{tot}} \quad \text{(SE1.13)}$$

While this volume allowed for the isolation and removal of issues with dewatering of the core samples before processing it did have some significant drawbacks. The second porosity value can only be an estimate for several reasons. Large grains along the outside of the sample can be caught on the edge of the plug during sampling thereby blocking sediment from entering and fully filling the plug. In other cases, friction along the inner wall of the plug caused the sediment to drag leaving large gaps in the sample once again preventing the sample from filling the entire 20 cc plug. Even with the difficulties, this method showed that the initial method (Equation SE8) was accurate to within an average

of 3.8% for sediments with a coarse fraction <50% while it underestimated the porosity of samples with a coarse fraction >50% by an average of 5.1%.

A third method of measuring the porosity involved using the pore volume (Equation SE11) and the plug volume (20 cc, V_{tot}). This method (Equation SE1.14) avoided using the total combined volume of the grains and pore space, both of which were measured.

$$Por = \frac{V_p}{V_{tot}} \quad \text{(SE1.14)}$$

This method tended to underestimate the porosity relative to Equation SE8. However, by calculating porosity using 3 separate methods we were able to calculate the standard deviation between the 3 methods and provide an error estimate for our results. We report our results using Equation SE8.

S1.1.8 Numerical Modeling

S1.1.8.1 Observed Trends

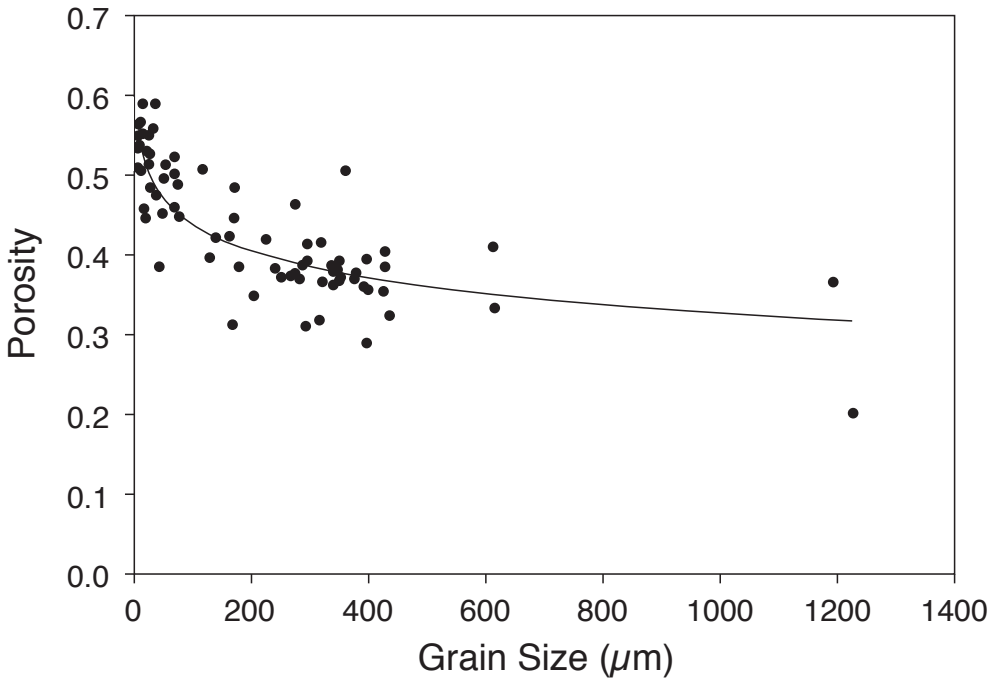

Figure SF1.5: Porosity vs. Grain Size for all Quaternary Sediments at Sandy Hook

$$\boldsymbol{por = -0.048 \times \ln(ø) + 0.659} \qquad \mathbf{r^2 = 0.709} \qquad \mathbf{(SE1.15)}$$

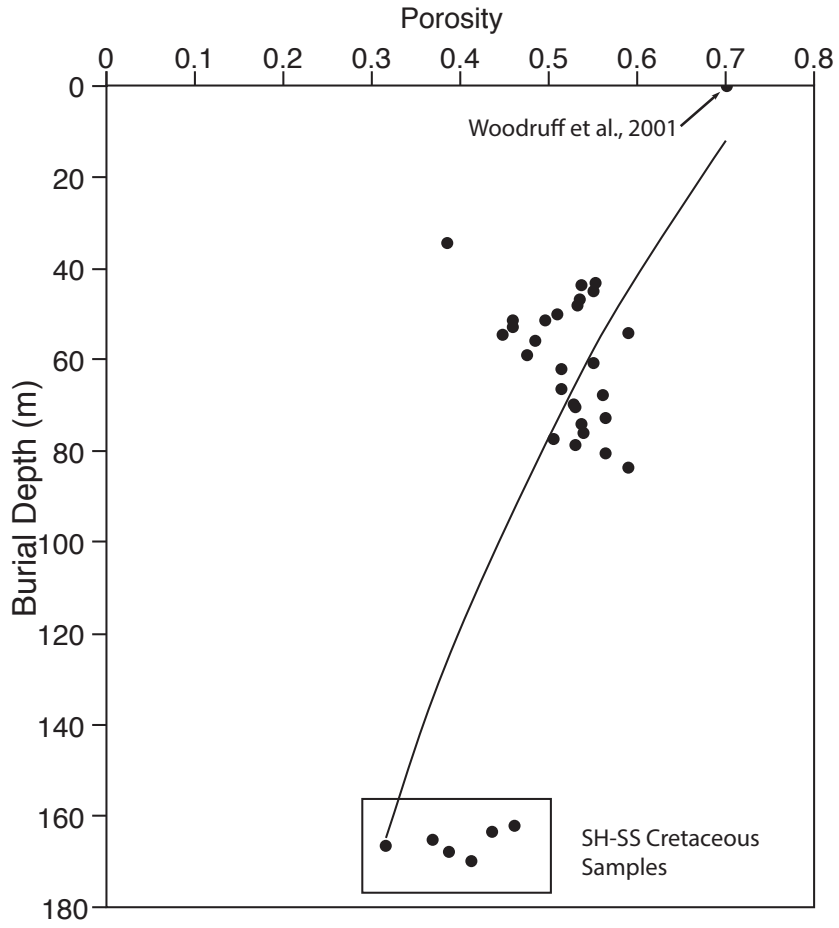

Figure SF1.6: Porosity vs. Modified Depth for Silts

$$\mathbf{z = -191.3 \times \ln(por) - 56.20} \qquad \mathbf{r^2 = 0.45} \qquad \mathbf{(SE1.16)}$$

S1.1.8.2 Inputs for Deriving Porosity Functions

Porosity	Grain Size (μm)	Depth (m)	Age (yrs)	Data Source
0.537	37.7	42.23	10850	SH-SS
0.551	7.1	45.27	13160	SH-SS
0.535	6.8	46.79	13180	SH-SS
0.533	8.4	48.31	13200	SH-SS
0.510	8.1	49.84	13220	SH-SS
0.459	17.4	51.37	13240	SH-SS
0.459	18.5	52.89	13260	SH-SS
0.590	14.5	54.04	13280	SH-SS
0.506	10.7	54.24	13280	SH-SS
0.461	37.6	92.51	83910000	SH-SS*
0.436	24.8	94.03	84220000	SH-SS*
0.369	22.9	95.56	84520000	SH-SS*
0.315	36.3	97.08	84830000	SH-SS*
0.387	15.0	98.30	85100000	SH-SS*
0.414	26.1	100.05	85550000	SH-SS*
0.453	48.5	19.30	3941	SH-SMY
0.553	14.8	43.34	8653	SH-NMY
0.496	51.4	51.36	10260	SH-NMY
0.446	19.8	54.41	10870	SH-NMY
0.485	24.7	55.92	13150	SH-NMY
0.475	38.0	59.01	13180	SH-NMY
0.551	26.2	60.54	13190	SH-NMY
0.513	54.0	62.03	13200	SH-NMY
0.514	26.8	66.60	13230	SH-NMY
0.560	34.3	68.11	13240	SH-NMY
0.528	28.1	69.64	13250	SH-NMY
0.530	22.3	70.76	13260	SH-NMY
0.563	8.1	72.70	13270	SH-NMY
0.537	8.7	74.18	13280	SH-NMY
0.539	10.6	75.74	13290	SH-NMY
0.506	14.1	77.27	13300	SH-NMY
0.529	24.3	78.79	13310	SH-NMY
0.565	10.6	80.30	13320	SH-NMY
0.589	35.8	83.37	13350	SH-NMY
0.7	33.5	0.1	0.5	Hudson River Estuary (Woodruff et al., 2001)

Table ST1.3: Inputs for derivation of porosity equations. Porosity as a f(grain size, burial depth and age) use the first four columns of data while porosity as a f(grain size and burial depth) only uses the first 3. * indicates data from Cretaceous sediments where the age and depth data were estimated. Ages were estimated from correlation to SMY-B (Miller et al., in prep.). Depths were estimated by adding 100 m to the current depth to approximate the maximum burial depth.

S1.1.8.3 Monte Carlo Simulation to Estimate Error in Decompaction Model

To estimate the time history of decompaction and its uncertainty, we employed the following algorithm.

First, sample the radiocarbon ages based on their measured values and associated errors:

$$\boldsymbol{a_{ik}^{'} = \hat{a}_i + \varepsilon_{aik}} \qquad \textbf{(SE1.17)}$$

where *i* indexes the age observations, *k* indexes the samples, $\hat{a}_i$ is the mean observation of the age *i*, and ε_{aik} is normally distributed based on the error of the measured radiocarbon data.

Second, sample the depth of the radiocarbon measurements:

$$\boldsymbol{d_{ik}^{'} = \hat{d}_i + \varepsilon_{dik}} \qquad \textbf{(SE1.18)}$$

where $\hat{d}_i$ is the mean observation of the depth *i*, and ε_{dik} is normally distributed based on the error of the depth. To avoid depth inversions (where $d_{(i+1)k}^{'} < d_{ik}^{'}$), $\varepsilon_{d(i+1)k}$ is sampled from a truncated normal distribution with a lower bound given by $\hat{d}_{(i+1)k} - \hat{d}_{ik}$.

Third, use the sampled ages and depths to regress multi-segmented linear age models for the NMY and SS. Age inversions are eliminated in this step by forcing any age profile to have the age monotonically increase with depth. This is done in the cases of the lowermost Quaternary sections of the NMY and SS where the ages are nearly indistinguishable by assigning the youngest age to the minimum depth and the maximum

age to the maximum depth of the section. This is step is performed differently from step two since the mean observed ages are inverted in the basal sections of the NMY and SS.

For NMY

$$\boldsymbol{a_{ik}^{'} = \beta_{1k} d_{ik}^{'} + \gamma_{1k} \quad if\ d_i^{'} \leq 55.11\ \mathrm{m}} \qquad \textbf{(SE1.19)}$$

$$a_{ik}^{'} = \beta_{2k} d_{ik}^{'} + \gamma_{2k} \quad if\ d_i^{'} > 55.11\ \mathrm{m}$$

For SS

$$\boldsymbol{a_{ik}^{'} = \beta_{3k} d_{ik}^{'} + \gamma_{3k} \qquad if d_{ik}^{'} \leq 39.25\ m} \qquad \textbf{(SE1.20)}$$

$$a_{ik}^{'} = \beta_{4k} d_{ik}^{'} + \gamma_{4k} \qquad \text{if } d_{ik}^{'} \leq 44.63\ m$$

$$a_{ik}^{'} = \beta_{5k} d_{ik}^{'} + \gamma_{5k} \qquad if\ d_{ik}^{'} > 44.63\ m$$

Fourth, sample the uncertainty in depth (z), porosity (ρ), and grain size (φ) of all sediments and ages of Cretaceous sediments (a). Ages of Cretaceous sediments are estimated based on their stratigraphic position within the Cretaceous stratigraphy of New Jersey and pollen data (Miller et al., in prep.). The Cretaceous sediments are used to constrain older/deeper portion the porosity equation (6).

$$\boldsymbol{z_{ik}^{'} = \hat{z}_i + \varepsilon_{zik}} \qquad \textbf{(SE1.21)}$$

$$\boldsymbol{\rho_{ik}^{'} = \hat{\rho}_i + \varepsilon_{\rho ik}} \qquad \textbf{(SE1.22)}$$

$$\boldsymbol{\phi_{ik}^{'} = \hat{\phi}_i + \varepsilon_{\phi ik}} \qquad \textbf{(SE1.23)}$$

$$a_{ik}^{'} = \hat{a}_i + \varepsilon_{aik} \qquad \text{(SE1.24)}$$

Fifth, using those samples with $\phi_{ik}^{'} < 63$ μm, estimate the coefficients of the linear equation relating porosity to grain size, depth and age as well as their covariance:

$$\boldsymbol{\rho'_{ik} = m_{1k} \ln(\phi'_{ik}) + m_{2k} \ln(d'_{ik}) + m_{3k} \ln(a'_{ik}) + m_0 + \varepsilon_{ik}} \quad \textbf{(SE1.25)}$$

Sixth, linearly interpolate between data points for grain size (ϕ'_{ik}) such that each discrete layer in the sediment column is assigned a grain size.

Seventh, use the piecewise linear age models from three to assign ages to each layer of the model.

For NMY

$$\boldsymbol{t_{ik} = \beta_{1k} z'_{ik} + \gamma_{1k} \quad if\ z'_{ik} \leq 55.11\ \text{m}} \quad \textbf{(SE1.26)}$$

$$t_{ik} = \beta_{2k} z'_{ik} + \gamma_{2k} \quad if\ z'_{ik} > 55.11\ \text{m}$$

Eighth, for use in decompaction, generate 100 samples of the m_{jk} using the coefficient covariance matrix estimated in step five. The sampled coefficients are denoted $m_{jkl.}$

Ninth, decompact the sediment column, following the method in the main text, using each set of sampled coefficients m_{jk} to estimate a modern decompaction rate $\hat{r}_{il}$ based on the change in thickness resulting from the change in porosity during each time step.

$$\rho_{ik} = m_{1k} \ln(\phi'_{ik}) + m_{2k} \ln(d'_{ik}) + m_{3k} \ln(t'_{ik}) + m_0 + \varepsilon_{ik} \quad \text{(SE1.27)}$$

Repeat steps one through nine thirty times. Denote the median of decompaction rate estimates $\hat{r}_{il}$ over all $i = 1 \ldots m$ and all $l = 1 \ldots 100$ as $\overline{\hat{r}_m}$. Terminate after N repetitions if $|\bar{r}_N - \bar{r}_{N-30}| < 0.0001$.

The distribution over all $\widehat{r_{il}}$ is the estimate of decompaction rates.

S1.1.9 Matlab Script for Decompaction with Porosity as a Function of Grain Size and Depth

```
%Sandy Hook Decompaction Model with Uncertainty and Porosity as a Function of Grain Size
%and Depth
%October 19, 2017
%By: Christopher S. Johnson
%SH_Decompaction_Model_F_gs_depth.m
%Iteratively decompacts the SH-NMY column. For each iteration it generates
%a random set of values for grain size, age, and depth before recomputing
%the equation for porosity and then decompacting the sediment column



%Grain Size is in µm
%All depths and distances are in m
%Ages are in years
%Compaction Rate is in mm/yr
clear;


%a is a counter for generating random values of the NMY_rc data
%b is a counter for generating the NMY_rc_er_upper data set above the
%unconformity at 55.11 m
b=1;
%c is a counter for generating the NMY_rc_er_lower data set below the
%unconformity at 55.11 m
c=1;
%d is a counter for generating random values for the SS_rc data set
```

```
%e is a counter for generating the SS_rc_er_lower data set
e=1;
%f
%g = counter used to assign ages to all of the SS Quaternary Data based on
%the established age models.
%h
%i = iteration counter
%j = counter for assigning random values to all NMY data
%k = counter for assigning random values to all SS quaternary data
%l = counter for assigning random values to all SS cretaceous data
%m = counter for withdrawling all data for points with gs<63 µm
%n=500; number of iterations of model
%o = counter for adding all data points with gs?63 µm to a single matrix
%for regression
%p = counter for finding residuals
%q = counter for assigning depths to all layers (first variable assigned to
%decompaction)
%r = counter for assigning sedimentation rates to all NMY layers
%s
%t
%u
%v
%w = Used
%x
%y
%z
%aa
%bb
```

```
%cc counter for the repetitions within each iteration with different
%coefficients
dd=1; %counter for recording outputs
nn=0;
count=0;

%compaction model pre-sets
n=50; %number of iterations
i=0;
thickness=0.01; %sets the original layer thickness (m)
max_depth=84; %sets the maximum depth in the NMY (m)
bot_sand=43; %sets the depth of the bottom of the sand in the NMY (m)
layers=max_depth/thickness; %sets the number of layers
modern_compaction_rates=zeros(n,1); %initializes variable to store all modern compaction rates.
compaction_rates=zeros(layers,n); %initializes variable to store all compaction data (curves).
prev_twentiethcentury_percentile=zeros(1,3);

%Errors
%Age Error is included in input
depth_er=0.3048/2; %Maximum depth error is ±.3048 m (±1 ft) ~2 Sigma, so
                %~1/2 is 1 Sigma
gs_er=.13;      %gs_er in percent of value (1 sigma)
por_er=.1;     %Porosity error in percent (not percent of value). (1 sigma)
%age error for radiocarbon ages is based on maxiumum and minimum values
%(set in input data list)
%age error for SS Cretaceous data is 1,000,000 years (1 sigma)
```

```
load ('NMY_rc_age'); %Loads Raw NMY Radio Carbon Dates in the format[Depth, Median Age, Lower Age Limit, Upper Age Limit].
load ('SS_rc_age');  %Loads Raw SS Radio Carbon Dates in the format[Depth, Median Age, Lower Age Limit, Upper Age Limit].
load ('NMY_input'); %Loads the raw NMY data in the format depth, gs, gs error (1 sigma μm), porosity, and porosity error (1 sigma in percent).
load ('SS_input_quaternary'); %Loads the raw SS Quaternary data in the format depth, gs, gs error (1 sigma μm), porosity, and porosity error (1 sigma in percent).
load ('SS_input_cretaceous'); %Loads the raw SS Cretaceous data in the format depth, gs, gs error (1 sigma μm), porosity, and porosity error (1 sigma in percent), age, age error (assumes 1 million years (1 sigma)).


porosity_v_depth=zeros(layers,n);
twentiethCenturyAverage=zeros(n,1);
variables=zeros(4,n);
noiselist=zeros(n,1);
NMY_ages=zeros(size(NMY_rc_age,1),n+1);%Stores all of the ages from each iteration at the NMY
Tracker_age=zeros(layers,n);
Tracker_gs=zeros(layers,n);
%turns off rank deficient warning
warning('off','stats:LinearModel:RankDefDesignMat');
prev_avg_twentiethcentury=0;


while nn==0;
    i=i+1;
    %creates working copies of the NMY and SS data
    NMY_data=NMY_input;
```

```
SS_data_quaternary=SS_input_quaternary;
SS_data_cretaceous=SS_input_cretaceous;

%Begins to initialize matricies
NMY_data_er=zeros(size(NMY_input,1),4);
SS_data_er_quaternary=zeros(size(SS_input_quaternary,1),4);
SS_data_er_cretaceous=zeros(size(SS_input_cretaceous,1),4);
NMY_rc_er=zeros(size(NMY_rc_age,1),2); %The randomly created ages and depths for the NMY radiocarbon data
NMY_er=zeros(size(NMY_input,1),3);
SS_rc_er=zeros(size(SS_rc_age,1),2); %The randomly created ages and depths for the SS radiocarbon data
SS_rc_er_upper=zeros(2,2);
NMY_input(:,6)=0; %sets a sixth column for NMY input that is held open for dates to be assigned later.
SS_input_quaternary(:,6)=0; %sets a sixth column for SS input quaternary that is held open for dates to be assigned later.
NMY_agemodel_age_lower=ones(2,1);

%Assigns random age values to the NMY Radiocarbon Data Set
for a=1:size(NMY_rc_age,1);

    NMY_rc_er(a,1)=normrnd(NMY_rc_age(a,1),depth_er);

    %Removes the Possibility of depth inversions caused by error (we
    %know what the relative position of each of the samples are.
    if a>1;
        if NMY_rc_er(a,1)<=NMY_rc_er(a-1,1);
            NMY_rc_er(a,1)=NMY_rc_er(a-1,1)+(NMY_rc_age(a,1)-NMY_rc_age(a-1,1));
```

```
        end
    end
    NMY_rc_er(a,2)= normrnd(NMY_rc_age(a,2),(NMY_rc_age(a,3)/2));


    %Assigns the RC dates from the NMY to a separate matrix, one for
    %the upper portion of the NMY and one for the lower.
    NMY_rc_er_upper(1,1)=0;
    NMY_rc_er_upper(1,2)=0;
    if NMY_rc_er(a,1) <= 55.11
        NMY_rc_er_upper(b+1,1)=NMY_rc_er(a,1);
        NMY_rc_er_upper(b+1,2)=NMY_rc_er(a,2);
        b=b+1;
    else
        NMY_rc_er_lower(c,1)=NMY_rc_er(a,1);
        NMY_rc_er_lower(c,2)=NMY_rc_er(a,2);
        c=c+1;
    end
end
NMY_rc_er_lower(c,1)=84;
NMY_rc_er_lower(c,2)=13350;
%Resets b and c variabls for the next iteration
b=1;
c=1;
e=1;

for d=1:size(SS_rc_age,1);
    SS_rc_er(d,1)=normrnd(SS_rc_age(d,1),depth_er);
```

```
    %Removes the Possibility of depth inversions caused by error (we
    %know what the relative position of each of the samples are.
    if d>1;
       if SS_rc_er(d,1)<=SS_rc_er(d-1,1);
          SS_rc_er(d,1)=SS_rc_er(d-1,1)+(SS_rc_age(d,1)-SS_rc_age(d-1,1));
       end
    end

     SS_rc_er(d,2)= normrnd(SS_rc_age(d,2),(SS_rc_age(d,3)/2));

     if SS_rc_er(d,1)>=45.25
        SS_rc_er_lower(e,1)=SS_rc_er(d,1);
        SS_rc_er_lower(e,2)=SS_rc_er(d,2);
        e=e+1;
     end
end

SS_rc_er_upper(2,1)=SS_rc_er(1,1);
SS_rc_er_upper(2,2)=SS_rc_er(1,2);

SS_rc_er_middle(1,1)=SS_rc_er(1,1);
SS_rc_er_middle(1,2)=SS_rc_er(1,2);
SS_rc_er_middle(2,1)=SS_rc_er(2,1);
SS_rc_er_middle(2,2)=SS_rc_er(2,2);

SS_rc_er_lower(5,1)=59.21;
SS_rc_er_lower(5,2)=13350;
```

```
%Creates the upper age model for the NMY (yr/m)
NMY_rc_er_upper_depth=NMY_rc_er_upper(:,1);
NMY_rc_er_upper_age=NMY_rc_er_upper(:,2);
NMY_agemodel_upper=regress(NMY_rc_er_upper_age,NMY_rc_er_upper_depth);

%Creates the lower age model for the NMY (yr/m)
NMY_rc_er_lower_depth=NMY_rc_er_lower(:,1);
NMY_rc_er_lower_age=NMY_rc_er_lower(:,2);
NMY_rc_er_lower_depth(:,2)=1;
[NMY_agemodel_age_lower(2,1),index_max]=max(NMY_rc_er_lower_age);
[NMY_agemodel_age_lower(1,1),index_min]=min(NMY_rc_er_lower_age);
NMY_agemodel_depth_lower=[55.1 1; 84 1];

NMY_agemodel_lower=regress(NMY_agemodel_age_lower,NMY_agemodel_depth_lower);

%if NMY_agemodel_lower(1,1)>=0;
%Creates the upper age model for the SS upper section (yr/m)
SS_rc_er_upper_depth=SS_rc_er_upper(:,1);
SS_rc_er_upper_age=SS_rc_er_upper(:,2);
SS_agemodel_upper=regress(SS_rc_er_upper_age,SS_rc_er_upper_depth);

%Creates the middle age model for the SS middle section (yr/m)
SS_rc_er_middle_depth=SS_rc_er_middle(:,1);
SS_rc_er_middle_age=SS_rc_er_middle(:,2);
SS_rc_er_middle_depth(:,2)=1;
```

```
SS_agemodel_middle=regress(SS_rc_er_middle_age,SS_rc_er_middle_depth);

%Creates the lower age model for the SS lower section (yr/m)
SS_rc_er_lower_depth=SS_rc_er_lower(:,1);
SS_rc_er_lower_age=SS_rc_er_lower(:,2);
SS_rc_er_lower_depth(:,2)=1;
SS_agemodel_lower=regress(SS_rc_er_lower_age,SS_rc_er_lower_depth);

%Assigns random values for depth, gs, and porosity of the NMY data
for j=1:size(NMY_data_er,1)
   NMY_data_er(j,1)=normrnd(NMY_data(j,1),depth_er);
   if j>1
      if NMY_data_er(j,1)<=NMY_data_er(j-1,1)
         NMY_data_er(j,1)=NMY_data_er(j-1,1)+(NMY_data(j,1)-NMY_data(j-1,1));
      end
   end
   NMY_data_er(j,2)=normrnd(NMY_data(j,2),gs_er*NMY_data(j,2));
   NMY_data_er(j,3)=normrnd(NMY_data(j,4),por_er);
end

%Assigns random values for depth, gs, and porosity of the Quaternary SS data
for k=1:size(SS_data_er_quaternary,1)
   SS_data_er_quaternary(k,1)=normrnd(SS_data_quaternary(k,1),depth_er);
   if k>1
      if SS_data_er_quaternary(k,1)<=SS_data_er_quaternary(k-1,1)
         SS_data_er_quaternary(k,1)=SS_data_er_quaternary(k-1,1)+(SS_data_quaternary(k,1)-
SS_data_quaternary(k-1,1));
      end
```

```
    end
    SS_data_er_quaternary(k,2)=normrnd(SS_data_quaternary(k,2),gs_er*SS_data_quaternary(k,2));
    SS_data_er_quaternary(k,3)=normrnd(SS_data_quaternary(k,4),por_er);
  end

    %Assigns random values for depth, gs, and porosity of the Cretaceous SS data
  for l=1:size(SS_data_er_cretaceous,1)
    SS_data_er_cretaceous(l,1)=normrnd(SS_data_cretaceous(l,1),depth_er);
    if l>1
      if SS_data_er_cretaceous(l,1)<=SS_data_er_cretaceous(l-1,1)
        SS_data_er_cretaceous(l,1)=SS_data_er_cretaceous(l-1,1)+(SS_data_cretaceous(l,1)-
SS_data_cretaceous(l-1,1));
      end
    end
    SS_data_er_cretaceous(l,2)=normrnd(SS_data_cretaceous(l,2),gs_er*SS_data_cretaceous(l,2));
    SS_data_er_cretaceous(l,3)=normrnd(SS_data_cretaceous(l,4),por_er);
  end


   %Assigns ages to all of the NMY data using age model from above
  for f=1:size(NMY_data,1)
    if NMY_data_er(f,1)<=55.11
      NMY_data_er(f,4)=NMY_data_er(f,1)*NMY_agemodel_upper;
    else
      NMY_data_er(f,4)=NMY_data_er(f,1)*NMY_agemodel_lower(1,1)+NMY_agemodel_lower(2,1);
    end
  end
```

```
%Assigns ages to all fo the SS Quaternary Data
for g=1:size(SS_data_quaternary,1)
    if SS_data_er_quaternary(g,1)<=SS_rc_er(1,1);
        SS_data_er_quaternary(g,4)=SS_data_er_quaternary(g,1)*SS_agemodel_upper;
    elseif SS_data_er_quaternary(g,1)<=SS_rc_er(2,1);

SS_data_er_quaternary(g,4)=SS_data_er_quaternary(g,1)*SS_agemodel_middle(1,1)+SS_agemodel_middl
e(2,1);
    else

SS_data_er_quaternary(g,4)=SS_data_er_quaternary(g,1)*SS_agemodel_lower(1,1)+SS_agemodel_lower(
2,1);
    end
end

%Assigns random ages to Cretaceous data from SS
for h=1:size(SS_data_cretaceous,1)
    SS_data_er_cretaceous(h,4)=normrnd(SS_data_cretaceous(h,6),SS_data_cretaceous(h,7));
end




%Concatenates all data into a working group for regressing the porosity
%equation
clear all_data_er reg_data_er reg_porosity_data_er;
all_data_er=vertcat(NMY_data_er,SS_data_er_quaternary,SS_data_er_cretaceous);

o=1;
```

```
for m=1:size(all_data_er,1)
   if all_data_er(m,2)<=63
      reg_porosity_data_er(o,1)=all_data_er(m,3);
      reg_data_er(o,1)=log(all_data_er(m,2)); %gs
      reg_data_er(o,2)=log(all_data_er(m,1));  %depth
      %reg_data_er(o,3)=log(all_data_er(m,4));   %age
      o=o+1;
   end
end

%Inputs the data from the modern hudson of Woodruff et al., 2001.
reg_data_er(o,1)=log(normrnd(33.5,gs_er*33.5)); %GS
reg_data_er(o,2)=log(normrnd(.1,.01)); %Depth
%reg_data_er(o,3)=log(.5); %assumes errors in age are so small as to be trivial
reg_data_er(:,3)=1;
reg_porosity_data_er(o,1)=normrnd(.7,por_er);

Regresses the porosity function
porosity_function=regress(reg_porosity_data_er,reg_data_er);

%Stores Variables
variables(1,i)=porosity_function(1,1);
variables(2,i)=porosity_function(2,1);
variables(3,i)=porosity_function(3,1);

%Commented out to remove age variable from equation
%variables(4,i)=porosity_function(4,1);
model=LinearModel.fit(reg_data_er,reg_porosity_data_er);
```

```
mu=model.Coefficients.Estimate;
mu=mu(1:3);

cv=model.CoefficientCovariance(1:3,1:3);

coefficients=mvnrnd(mu,cv,100);



%Begins decompaction
for cc=1:1

%Initialization of all matricies for decompaction model
%intializes all matricies for decompation model
P=zeros(layers,1); %Sets variable for porosity
Po=zeros(layers,1); %Sets initial porosity values
H=zeros(layers,1); %sets up a variable for each layer thickness
Ho=ones(layers,1); %Sets up a variable for each layer's initial thickness
                %before each itteration.
Ho=Ho*thickness; %Sets the initial layer thicknesses to what you set as your layer
          %thickness
DeltaHlayer=zeros(layers,1); %Creates a variable to track the change in
                    %layer thickness from one itteration to the
                    %next
DeltaHtotbylayer=zeros(layers,1); %Calulates the total compaction of each layer.
DeltaHperLayer=zeros(layers,1);
```

```
sedrate=zeros(layers,1);


AgePerm=zeros(layers,1);
Age=zeros(layers,1); %Sets an age variable to track changes in age after
                %each layer removal.


Agenot=zeros(layers,1); %Sets a variable to track the previous age of a layer.
Depth=zeros(layers,1);
CompactionRate=zeros(layers,1);
twentiethCenturyCompactionRate=zeros(50,1);



%assigns inital depths to all layers
for q=1:layers
   Depth(q,1)=q*thickness;
end


%Sets grain sizes for all layers (by interpolating from NMY data with
%errors included)
grainsize=interp1(NMY_data_er(:,1),NMY_data_er(:,2),Depth);


%creates tracker for grain size data across iterations
for bb=1:layers
   Tracker_gs(bb,i)=grainsize(bb,1);
end


%Sets a sed rate for each layer in meters per year
for r=1:layers
```

```
    depthcheck=r*thickness;
    if depthcheck<55.401
        sedrate(r,1)=1/NMY_agemodel_upper;
    else
        sedrate(r,1)=1/NMY_agemodel_lower(1,1);
    end
end

%Sets an age for each layer
for s=1:layers
    if Depth(s,1)<55.401
        AgePerm(s,1)=s*thickness*NMY_agemodel_upper;
    else
        AgePerm(s,1)=NMY_agemodel_lower(2,1)+(s*thickness*NMY_agemodel_lower(1,1));
    end
    Tracker_age(s,i)=AgePerm(s,1);
end
Agenot=AgePerm;
Age=AgePerm;

%Sets initial porosity values
for t=1:layers
    if grainsize(t,1)<=63
        Po(t,1)=coefficients(cc,2)*log(grainsize(t,1))+coefficients(cc,3)*log(Depth(t,1))+coefficients(cc,1);
    else
        Po(t,1)=0;
    end
    P(t,1)=Po(t,1);
```

```
    %porosity_v_depth(t,i+1)=P(t,1);
end

for u=1:layers %u is the layer removed
    for v=u+1:layers %calculates the corresponding change to each layer (v) below u after u is removed.
   Age(v,1)=Age(v,1)-Age(u,1);
   Depth(v,1)=Depth(v,1)-Depth(u,1);



  if grainsize(v,1)<=63
      P(v,1)=coefficients(cc,2)*log(grainsize(v,1))+coefficients(cc,3)*log(Depth(v,1))+coefficients(cc,1);
      H(v,1)=(P(v,1)/Po(v,1))*Ho(v,1);
      DeltaHlayer(v,1)=H(v,1)-Ho(v,1);
  else
      DeltaHlayer(v,1)=0;
  end
  DeltaHtotbylayer(v,1)=DeltaHtotbylayer(v,1)+DeltaHlayer(v,1);
    end
  Po=P;
  Ho=H;
  DeltaHperLayer(u,1)=sum(DeltaHlayer);
  DeltaHlayer=DeltaHlayer*0;
  CompactionRate(u,1)=DeltaHperLayer(u,1)/Age(u,1)*1000;
  %multiplying by 1000 converts from m/yr to mm/yr
end
totcompaction=sum(DeltaHtotbylayer);
for x=1:layers
compaction_rates(x,dd)=CompactionRate(x,1);
```

```
end

 minimum=min(compaction_rates(:,dd));

%for y=1:100
   twentiethCenturyCompactionRate=CompactionRate(1:50);
%end
twentiethCenturyAverage(dd,1)=mean(twentiethCenturyCompactionRate);
modern_compaction_rates(dd,1)=CompactionRate(1,1);
twentiethcentury_percentile=prctile(twentiethCenturyAverage,[10,50,90]);
modern_percentile=prctile(modern_compaction_rates,[5,10,50,90,95]);
clear CompactionRate



disp(dd);

   %Discards any iteration with a compaction rate that is negative at any point
   %during the modeled time period since it is not plausible that the sediment
   %column is expanding.
   if minimum<0
       dd=dd-1;
   end
   dd=dd+1;
end

  if mod(dd,300)==0
```

```
        diff=abs(twentiethcentury_percentile(1,2)-prev_twentiethcentury_percentile(1,2));
        if diff<0.0001
           nn=1;
        else
           nn=0;
           disp('the previous twentieth century percentiles were');
           disp(prev_twentiethcentury_percentile);
           disp('the current twentieth century percentiles are');
           disp(twentiethcentury_percentile);
           disp('the difference is...');
           disp(diff);
           prev_twentiethcentury_percentile=twentiethcentury_percentile;
        end

     end

      count=count+1;
      disp('The outer iteration is');
      disp(i);

end
for w=1:layers
   porosity_v_depth(w,1)=thickness*w;
end

stdev_twentiethcentury=std(twentiethCenturyAverage);
avg_twentiethcentury=sum(twentiethCenturyAverage)/dd;
stdev_Mod_Comp=std(modern_compaction_rates);
```

```
avg_modern_rate=sum(modern_compaction_rates)/dd;
percentilestwentiethcenturyaverage=prctile(twentiethCenturyAverage,[5,10,50,90,95]);
percentiles_modern_compaction_rates=prctile(modern_compaction_rates,[5,10,50,90,95]);

%Displays the model output
disp('average modern compaction rate is ');
disp(avg_modern_rate);
disp(' after ');
disp(dd);
disp('iterations.');
disp('The standard deviation is ');
disp(stdev_Mod_Comp);
disp('The 5th, 10th, 50th, 90th, and 95th percentiles for the 20th century average are');
disp(percentilestwentiethcenturyaverage);
disp('END.');

warning('on','stats:LinearModel:RankDefDesignMat'); %Turns rank deficient warning back on.
```

S1.1.10: Matlab Script for Decompaction with Porosity as a function of Grain Size, Burial Depth, and Age

```
%Sandy Hook Decompaction Model with Uncertainty and Porosity as a Function of Grain Size,
%Depth, and Age.
%October 19, 2017
%By: Christopher S. Johnson
%SH_Decompaction_Model_F_gs_depth_age.m
%Iteratively decompacts the SH-NMY column. For each iteration it generates
%a random set of values for grain size, age, and depth before recomputing
```

```
%the equation for porosity and then decompacting the sediment column



%Grain Size is in µm
%All depths and distances are in m
%Ages are in years
%Compaction Rate is in mm/yr
clear;
%a is a counter for generating random values of the NMY_rc data
%b is a counter for generating the NMY_rc_er_upper data set above the
%unconformity at 55.11 m
b=1;
%c is a counter for generating the NMY_rc_er_lower data set below the
%unconformity at 55.11 m
c=1;
%d is a counter for generating random values for the SS_rc data set
%e is a counter for generating the SS_rc_er_lower data set
e=1;
%f
%g = counter used to assign ages to all of the SS Quaternary Data based on
%the established age models.
%h
%i = iteration counter
%j = counter for assigning random values to all NMY data
%k = counter for assigning random values to all SS quaternary data
%l = counter for assigning random values to all SS cretaceous data
%m = counter for withdrawling all data for points with gs<63 µm
%n=500; number of iterations of model
```

```
%o = counter for adding all data points with gs?63 μm to a single matrix
%for regression
%p = counter for finding residuals
%q = counter for assigning depths to all layers (first variable assigned to
%decompaction)
%r = counter for assigning sedimentation rates to all NMY layers
%s
%t
%u
%v
%w = Used
%x
%y
%z
%aa
%bb
%cc counter for the repetitions within each iteration with different
%coefficients
dd=1; %counter for recording outputs
nn=0;
count=0;


%compaction model pre-sets
n=50; %number of iterations
i=0;
thickness=0.01; %sets the original layer thickness (m)
max_depth=84; %sets the maximum depth in the NMY (m)
bot_sand=43; %sets the depth of the bottom of the sand in the NMY (m)
```

```
layers=max_depth/thickness; %sets the number of layers
modern_compaction_rates=zeros(n,1); %initializes variable to store all modern compaction rates.
compaction_rates=zeros(layers,n); %initializes variable to store all compaction data (curves).
prev_twentiethcentury_percentile=zeros(1,3);

%Errors
%Age Error is included in input
depth_er=0.3048/2; %Maximum depth error is ±.3048 m (±1 ft) ~2 Sigma, so
                %~1/2 is 1 Sigma
gs_er=.13;      %gs_er in percent of value (1 sigma)
por_er=.1;    %Porosity error in percent (not percent of value). (1 sigma)
%age error for radiocarbon ages is based on maxiumum and minimum values
%(set in input data list)
%age error for SS Cretaceous data is 1,000,000 years (1 sigma)



load ('NMY_rc_age'); %Loads Raw NMY Radio Carbon Dates in the format[Depth, Median Age, Lower
Age Limit, Upper Age Limit].
load ('SS_rc_age');  %Loads Raw SS Radio Carbon Dates in the format[Depth, Median Age, Lower Age
Limit, Upper Age Limit].
load ('NMY_input'); %Loads the raw NMY data in the format depth, gs, gs error (1 sigma μm), porosity,
and porosity error (1 sigma in percent).
load ('SS_input_quaternary'); %Loads the raw SS Quaternary data in the format depth, gs, gs error (1 sigma
μm), porosity, and porosity error (1 sigma in percent).
load ('SS_input_cretaceous'); %Loads the raw SS Cretaceous data in the format depth, gs, gs error (1 sigma
μm), porosity, and porosity error (1 sigma in percent), age, age error (assumes 1 million years (1 sigma)).
```

```
porosity_v_depth=zeros(layers,n);
twentiethCenturyAverage=zeros(n,1);
variables=zeros(4,n);
noiselist=zeros(n,1);
NMY_ages=zeros(size(NMY_rc_age,1),n+1);%Stores all of the ages from each iteration at the NMY
Tracker_age=zeros(layers,n);
Tracker_gs=zeros(layers,n);
%turns off rank deficient warning
warning('off','stats:LinearModel:RankDefDesignMat');
prev_avg_twentiethcentury=0;

while nn==0;
   i=i+1;
   %creates working copies of the NMY and SS data
   NMY_data=NMY_input;
   SS_data_quaternary=SS_input_quaternary;
   SS_data_cretaceous=SS_input_cretaceous;

   %Begins to initialize matricies
   NMY_data_er=zeros(size(NMY_input,1),4);
   SS_data_er_quaternary=zeros(size(SS_input_quaternary,1),4);
   SS_data_er_cretaceous=zeros(size(SS_input_cretaceous,1),4);
   NMY_rc_er=zeros(size(NMY_rc_age,1),2); %The randomly created ages and depths for the NMY
radiocarbon data
   NMY_er=zeros(size(NMY_input,1),3);
   SS_rc_er=zeros(size(SS_rc_age,1),2); %The randomly created ages and depths for the SS radiocarbon
data
```

```
SS_rc_er_upper=zeros(2,2);
NMY_input(:,6)=0; %sets a sixth column for NMY input that is held open for dates to be assigned later.
SS_input_quaternary(:,6)=0; %sets a sixth column for SS input quaternary that is held open for dates to be assigned later.
NMY_agemodel_age_lower=ones(2,1);

%Assigns random age values to the NMY Radiocarbon Data Set
for a=1:size(NMY_rc_age,1);

  NMY_rc_er(a,1)=normrnd(NMY_rc_age(a,1),depth_er);

  %Removes the Possibility of depth inversions caused by error (we
  %know what the relative position of each of the samples are.
  if a>1;
    if NMY_rc_er(a,1)<=NMY_rc_er(a-1,1);
      NMY_rc_er(a,1)=NMY_rc_er(a-1,1)+(NMY_rc_age(a,1)-NMY_rc_age(a-1,1));
    end
  end
  NMY_rc_er(a,2)= normrnd(NMY_rc_age(a,2),(NMY_rc_age(a,3)/2));

  %Assigns the RC dates from the NMY to a separate matrix, one for
  %the upper portion of the NMY and one for the lower.
  NMY_rc_er_upper(1,1)=0;
  NMY_rc_er_upper(1,2)=0;
  if NMY_rc_er(a,1) <= 55.11
    NMY_rc_er_upper(b+1,1)=NMY_rc_er(a,1);
    NMY_rc_er_upper(b+1,2)=NMY_rc_er(a,2);
```

```
        b=b+1;
    else
        NMY_rc_er_lower(c,1)=NMY_rc_er(a,1);
        NMY_rc_er_lower(c,2)=NMY_rc_er(a,2);
        c=c+1;
    end
end
NMY_rc_er_lower(c,1)=84;
NMY_rc_er_lower(c,2)=13350;
%Resets b and c variabls for the next iteration
b=1;
c=1;
e=1;

for d=1:size(SS_rc_age,1);
   SS_rc_er(d,1)=normrnd(SS_rc_age(d,1),depth_er);

   %Removes the Possibility of depth inversions caused by error (we
   %know what the relative position of each of the samples are.
   if d>1;
      if SS_rc_er(d,1)<=SS_rc_er(d-1,1);
         SS_rc_er(d,1)=SS_rc_er(d-1,1)+(SS_rc_age(d,1)-SS_rc_age(d-1,1));
      end
   end

    SS_rc_er(d,2)= normrnd(SS_rc_age(d,2),(SS_rc_age(d,3)/2));

    if SS_rc_er(d,1)>=45.25
```

```
        SS_rc_er_lower(e,1)=SS_rc_er(d,1);
        SS_rc_er_lower(e,2)=SS_rc_er(d,2);
        e=e+1;
    end
end

SS_rc_er_upper(2,1)=SS_rc_er(1,1);
SS_rc_er_upper(2,2)=SS_rc_er(1,2);

SS_rc_er_middle(1,1)=SS_rc_er(1,1);
SS_rc_er_middle(1,2)=SS_rc_er(1,2);
SS_rc_er_middle(2,1)=SS_rc_er(2,1);
SS_rc_er_middle(2,2)=SS_rc_er(2,2);

SS_rc_er_lower(5,1)=59.21;
SS_rc_er_lower(5,2)=13350;

%Creates the upper age model for the NMY (yr/m)
NMY_rc_er_upper_depth=NMY_rc_er_upper(:,1);
NMY_rc_er_upper_age=NMY_rc_er_upper(:,2);
NMY_agemodel_upper=regress(NMY_rc_er_upper_age,NMY_rc_er_upper_depth);

%Creates the lower age model for the NMY (yr/m)
NMY_rc_er_lower_depth=NMY_rc_er_lower(:,1);
NMY_rc_er_lower_age=NMY_rc_er_lower(:,2);
NMY_rc_er_lower_depth(:,2)=1;
[NMY_agemodel_age_lower(2,1),index_max]=max(NMY_rc_er_lower_age);
[NMY_agemodel_age_lower(1,1),index_min]=min(NMY_rc_er_lower_age);
```

```
NMY_agemodel_depth_lower=[55.1 1; 84 1];


NMY_agemodel_lower=regress(NMY_agemodel_age_lower,NMY_agemodel_depth_lower);


%if NMY_agemodel_lower(1,1)>=0;
%Creates the upper age model for the SS upper section (yr/m)
SS_rc_er_upper_depth=SS_rc_er_upper(:,1);
SS_rc_er_upper_age=SS_rc_er_upper(:,2);
SS_agemodel_upper=regress(SS_rc_er_upper_age,SS_rc_er_upper_depth);

%Creates the middle age model for the SS middle section (yr/m)
SS_rc_er_middle_depth=SS_rc_er_middle(:,1);
SS_rc_er_middle_age=SS_rc_er_middle(:,2);
SS_rc_er_middle_depth(:,2)=1;
SS_agemodel_middle=regress(SS_rc_er_middle_age,SS_rc_er_middle_depth);

%Creates the lower age model for the SS lower section (yr/m)
SS_rc_er_lower_depth=SS_rc_er_lower(:,1);
SS_rc_er_lower_age=SS_rc_er_lower(:,2);
SS_rc_er_lower_depth(:,2)=1;
SS_agemodel_lower=regress(SS_rc_er_lower_age,SS_rc_er_lower_depth);

%Assigns random values for depth, gs, and porosity of the NMY data
for j=1:size(NMY_data_er,1)
   NMY_data_er(j,1)=normrnd(NMY_data(j,1),depth_er);
   if j>1
```

```
        if NMY_data_er(j,1)<=NMY_data_er(j-1,1)
            NMY_data_er(j,1)=NMY_data_er(j-1,1)+(NMY_data(j,1)-NMY_data(j-1,1));
        end
    end
    NMY_data_er(j,2)=normrnd(NMY_data(j,2),gs_er*NMY_data(j,2));
    NMY_data_er(j,3)=normrnd(NMY_data(j,4),por_er);
end

%Assigns random values for depth, gs, and porosity of the Quaternary SS data
for k=1:size(SS_data_er_quaternary,1)
    SS_data_er_quaternary(k,1)=normrnd(SS_data_quaternary(k,1),depth_er);
    if k>1
        if SS_data_er_quaternary(k,1)<=SS_data_er_quaternary(k-1,1)
            SS_data_er_quaternary(k,1)=SS_data_er_quaternary(k-1,1)+(SS_data_quaternary(k,1)-
SS_data_quaternary(k-1,1));
        end
    end
    SS_data_er_quaternary(k,2)=normrnd(SS_data_quaternary(k,2),gs_er*SS_data_quaternary(k,2));
    SS_data_er_quaternary(k,3)=normrnd(SS_data_quaternary(k,4),por_er);
end

    %Assigns random values for depth, gs, and porosity of the Cretaceous SS data
for l=1:size(SS_data_er_cretaceous,1)
    SS_data_er_cretaceous(l,1)=normrnd(SS_data_cretaceous(l,1),depth_er);
    if l>1
        if SS_data_er_cretaceous(l,1)<=SS_data_er_cretaceous(l-1,1)
            SS_data_er_cretaceous(l,1)=SS_data_er_cretaceous(l-1,1)+(SS_data_cretaceous(l,1)-
SS_data_cretaceous(l-1,1));
```

```
        end
    end
    SS_data_er_cretaceous(l,2)=normrnd(SS_data_cretaceous(l,2),gs_er*SS_data_cretaceous(l,2));
    SS_data_er_cretaceous(l,3)=normrnd(SS_data_cretaceous(l,4),por_er);
end


 %Assigns ages to all of the NMY data
for f=1:size(NMY_data,1)
    if NMY_data_er(f,1)<=55.11
        NMY_data_er(f,4)=NMY_data_er(f,1)*NMY_agemodel_upper;
    else
        NMY_data_er(f,4)=NMY_data_er(f,1)*NMY_agemodel_lower(1,1)+NMY_agemodel_lower(2,1);
    end
end

%Assigns ages to all fo the SS Quaternary Data
for g=1:size(SS_data_quaternary,1)
    if SS_data_er_quaternary(g,1)<=SS_rc_er(1,1);
        SS_data_er_quaternary(g,4)=SS_data_er_quaternary(g,1)*SS_agemodel_upper;
    elseif SS_data_er_quaternary(g,1)<=SS_rc_er(2,1);

SS_data_er_quaternary(g,4)=SS_data_er_quaternary(g,1)*SS_agemodel_middle(1,1)+SS_agemodel_middl
e(2,1);
    else

SS_data_er_quaternary(g,4)=SS_data_er_quaternary(g,1)*SS_agemodel_lower(1,1)+SS_agemodel_lower(
2,1);
```

```
   end
end

%Assigns random ages to Cretaceous data from SS
for h=1:size(SS_data_cretaceous,1)
   SS_data_er_cretaceous(h,4)=normrnd(SS_data_cretaceous(h,6),SS_data_cretaceous(h,7));
end




%cats all data into a working group for regressing the porosity
%equation
clear all_data_er reg_data_er reg_porosity_data_er;
all_data_er=vertcat(NMY_data_er,SS_data_er_quaternary,SS_data_er_cretaceous);


o=1;
for m=1:size(all_data_er,1)
   if all_data_er(m,2)<=63
      reg_porosity_data_er(o,1)=all_data_er(m,3);
      reg_data_er(o,1)=log(all_data_er(m,2)); %gs
      reg_data_er(o,2)=log(all_data_er(m,1));  %depth
      reg_data_er(o,3)=log(all_data_er(m,4));   %age
      o=o+1;
   end
end
%Inputs the data from the modern hudson of Woodruff et al., 2001.
reg_data_er(o,1)=log(normrnd(33.5,gs_er*33.5)); %GS
reg_data_er(o,2)=log(normrnd(.1,.01)); %Depth
```

```
reg_data_er(o,3)=log(.5); %assumes errors in age are so small as to be trivial
reg_data_er(:,4)=1;
reg_porosity_data_er(o,1)=normrnd(.7,por_er);



porosity_function=regress(reg_porosity_data_er,reg_data_er);
%Stores Variables
variables(1,i)=porosity_function(1,1);
variables(2,i)=porosity_function(2,1);
variables(3,i)=porosity_function(3,1);
variables(4,i)=porosity_function(4,1);
model=LinearModel.fit(reg_data_er,reg_porosity_data_er);

% modelres=table2array(model.Residuals);
%residuals=zeros(size(reg_porosity_data_er,1),1);
%for p=1:size(reg_porosity_data_er,1);
%    residuals(p,1)=modelres(p,1);
%end
%stdev_res=std(residuals);
%noise=normrnd(0,stdev_res);
%noiselist(i,1)=noise;

mu=model.Coefficients.Estimate;
mu=mu(1:4);

cv=model.CoefficientCovariance(1:4,1:4);

coefficients=mvnrnd(mu,cv,100);
```

```
%Begins decompaction
for cc=1:1

%Initialization of all matricies for decompaction model
%intializes all matricies for decompation model
P=zeros(layers,1); %Sets variable for porosity
Po=zeros(layers,1); %Sets initial porosity values
H=zeros(layers,1); %sets up a variable for each layer thickness
Ho=ones(layers,1); %Sets up a variable for each layer's initial thickness
                %before each itteration.
Ho=Ho*thickness; %Sets the initial layer thicknesses to what you set as your layer
          %thickness
DeltaHlayer=zeros(layers,1); %Creates a variable to track the change in
                    %layer thickness from one itteration to the
                    %next
DeltaHtotbylayer=zeros(layers,1); %Calulates the total compaction of each layer.
DeltaHperLayer=zeros(layers,1);
sedrate=zeros(layers,1);

AgePerm=zeros(layers,1);
Age=zeros(layers,1); %Sets an age variable to track changes in age after
               %each layer removal.

Agenot=zeros(layers,1); %Sets a variable to track the previous age of a layer.
Depth=zeros(layers,1);
CompactionRate=zeros(layers,1);
```

```
twentiethCenturyCompactionRate=zeros(50,1);



%assigns inital depths to all layers
for q=1:layers
   Depth(q,1)=q*thickness;
end

%Sets grain sizes for all layers (by interpolating from NMY data with
%errors included)
grainsize=interp1(NMY_data_er(:,1),NMY_data_er(:,2),Depth);

%creates tracker for grain size data across iterations
for bb=1:layers
   Tracker_gs(bb,i)=grainsize(bb,1);
end

%Sets a sed rate for each layer in meters per year
for r=1:layers
   depthcheck=r*thickness;
   if depthcheck<55.401
      sedrate(r,1)=1/NMY_agemodel_upper;
   else
      sedrate(r,1)=1/NMY_agemodel_lower(1,1);
   end
end

%sets an age for each layer
```

```
    for s=1:layers
        if Depth(s,1)<55.401
            AgePerm(s,1)=s*thickness*NMY_agemodel_upper;
        else
            AgePerm(s,1)=NMY_agemodel_lower(2,1)+(s*thickness*NMY_agemodel_lower(1,1));
        end
        Tracker_age(s,i)=AgePerm(s,1);
    end
    Agenot=AgePerm;
    Age=AgePerm;

    %Sets initial porosity values
    for t=1:layers
        if grainsize(t,1)<=63

Po(t,1)=coefficients(cc,2)*log(grainsize(t,1))+coefficients(cc,3)*log(Depth(t,1))+coefficients(cc,4)*log(Ag
e(t,1))+coefficients(cc,1);
        else
            Po(t,1)=0;
        end
        P(t,1)=Po(t,1);
        %porosity_v_depth(t,i+1)=P(t,1);
    end

    for u=1:layers %u is the layer removed
        for v=u+1:layers %calculates the corresponding change to each layer (v) below u after u is removed.
       Age(v,1)=Age(v,1)-Age(u,1);
       Depth(v,1)=Depth(v,1)-Depth(u,1);
```

```
    if grainsize(v,1)<=63

P(v,1)=coefficients(cc,2)*log(grainsize(v,1))+coefficients(cc,3)*log(Depth(v,1))+coefficients(cc,4)*log(Ag
e(v,1))+coefficients(cc,1);
        H(v,1)=(P(v,1)/Po(v,1))*Ho(v,1);
        DeltaHlayer(v,1)=H(v,1)-Ho(v,1);
    else
        DeltaHlayer(v,1)=0;
    end
    DeltaHtotbylayer(v,1)=DeltaHtotbylayer(v,1)+DeltaHlayer(v,1);
     end
    Po=P;
    Ho=H;
    DeltaHperLayer(u,1)=sum(DeltaHlayer);
    DeltaHlayer=DeltaHlayer*0;
    CompactionRate(u,1)=DeltaHperLayer(u,1)/Age(u,1)*1000;
    %multiplying by 1000 converts from m/yr to mm/yr
  end
  totcompaction=sum(DeltaHtotbylayer);
  for x=1:layers
  compaction_rates(x,dd)=CompactionRate(x,1);
  end
  minimum=min(compaction_rates(:,dd));

  twentiethCenturyCompactionRate=CompactionRate(1:50);
```

```
twentiethCenturyAverage(dd,1)=mean(twentiethCenturyCompactionRate);
modern_compaction_rates(dd,1)=CompactionRate(1,1);
twentiethcentury_percentile=prctile(twentiethCenturyAverage,[10,50,90]);
modern_percentile=prctile(modern_compaction_rates,[5,10,50,90,95]);
clear CompactionRate



disp(dd);

   %Discards any iteration that has a negative compaction rate at any point during
   %modeled time period since it is not plausible that the sediment column is
   %expanding.
   if minimum<0
       dd=dd-1;
   end
   dd=dd+1;
end

  if mod(i,450)==0

      diff=abs(twentiethcentury_pe
      rcentile(1,2)-prev_twentiethcentury_percentile(1,2));
      if diff<0.0001
         nn=1;
      else
         nn=0;
         disp('the previous twentieth century percentiles were');
```

```
            disp(prev_twentiethcentury_percentile);
            disp('the current twentieth century percentiles are');
            disp(twentiethcentury_percentile);
            disp('the difference is...');
            disp(diff);
            prev_twentiethcentury_percentile=twentiethcentury_percentile;
          end

      end

       count=count+1;
       disp('The outer iteration is');
       disp(i);

end
for w=1:layers
   porosity_v_depth(w,1)=thickness*w;
end

stdev_twentiethcentury=std(twentiethCenturyAverage);
avg_twentiethcentury=sum(twentiethCenturyAverage)/dd;
stdev_Mod_Comp=std(modern_compaction_rates);
avg_modern_rate=sum(modern_compaction_rates)/dd;
percentilestwentiethcenturyaverage=prctile(twentiethCenturyAverage,[5,10,50,90,95]);
percentiles_modern_compaction_rates=prctile(modern_compaction_rates,[5,10,50,90,95]);

%Displays model outputs
disp('average modern compaction rate is ');
```

```
disp(avg_modern_rate);
disp(' after ');
disp(dd);
disp('iterations.');
disp('The standard deviation is ');
disp(stdev_Mod_Comp);
disp('The 5th, 10th, 50th, 90th, and 95th percentiles for the 20th century average are');
disp(percentilestwentiethcenturyaverage);
disp('END.');

warning('on','stats:LinearModel:RankDefDesignMat'); %Turns rank deficient warning back on.
```

S1.1.11 Modeled Sea-Level Rise Sandy Hook Relative to The Battery

Tide-gauge data (from the Permanent Service for Mean Sea-Level, Holgate et al., 2013; PSMSL, 2016) and geological proxies (from the database of Kopp et al., 2016) from eastern North America between Florida and Nova Scotia were fit using a spatio-temporal empirical hierarchical model, following the method described in Kopp et al (2015b). This model separates the spatio-temporal sea-level process into high-, medium- and low-frequency terms. The optimized time scales of the high-, medium- and low-frequency processes are respectively τ_h = 13 years, τ_m = 230 years and τ_l = 9.3 kyr; other hyperparameters are shown in Table ST1.4.

Optimized Hyperparameters			
Low frequency			
amplitude	σ_l	8.9	m
time scale	τ_l	9.3	kyr
length scale	Υ_l	12.1	degrees
Medium frequency			
amplitude	σ_m	76	Mm
time scale	τ_m	226	yr
length scale	Υ_m	1.6	degrees
High frequency			
amplitude	σ_h	13.4	Mm
time scale	τ_h	6.1	yr
length scale	Υ_h	2.3	degrees
White Noise	σ_w	2.4	mm
Datum Offset	σ_O	41	mm

Table ST1.4: Optimized Parameters

S1.2 Results

S1.2.1 Grain Size

NMY			SS			SMY-A		
Sample Depth (m)	Median Grain Size (μm)	1 StDev Error User & Instrument	Sample Depth (m)	Median Grain Size (μm)	1 StDev Error User & Instrument	Sample Depth (m)	Median Grain Size (μm)	1 StDev Error User & Instrument
1.73	1226.38	**280.0**	1.98	400.9	**4.6**	4.05	432.31	**5.8**
23.92	338.14	8.0	6.24	397.5	**4.3**	4.07	426.27	**10.1**
26.97	437.61	188.1	11.12	350.8	**2.0**	6.99	296.01	14.2
30.02	241.93	**0.6**	13.85	393.0	**0.9**	17.82	274.91	**2.2**
33.07	170.77	29.7	16.91	1193.4	**65.8**	19.04	276.64	**2.4**
36.11	178.01	29.0	25.14	613.0	**31.8**	19.29	48.47	7.9
40.73	252.91	31.3	32.48	617.4	**108.4**	20.63	128.88	11.7
42.74	204.38	35.4	34.56	249.0	89.27	22.40	141.58	3.9
43.33	14.77	2.5	37.65	268.2	**1.3**	23.34	317.04	33.3
46.78	74.74	3.1	40.70	37.7	7.9	24.53	377.44	4.5
48.31	71.09	2.0	43.75	11.5	0.1	25.44	429.44	2.0
49.83	71.05	2.3	45.26	7.1	0.02	26.57	354.26	8.8
51.35	51.40	2.4	46.78	6.8	0.04	28.10	398.03	9.5
52.88	76.70	1.6	48.31	8.4	0.03	30.02	339.28	1.7
54.40	19.79	0.2	49.83	8.1	0.2	31.54	380.21	17.6
55.93	24.67	1.6	51.37	17.4	0.7	33.03	427.89	20.7
55.90	28.26	1.6	52.89	18.5	0.2	34.22	319.54	4.2
59.00	38.01	13.0	54.04	14.5	0.2	35.53	347.92	1.8
60.53	26.23	8.5	54.05	10.7	0.6	37.64	339.25	15.2
62.02	54.05	2.8	54.40	360.6	21.3	39.07	351.00	29.4
63.55	70.60	1.6	56.02	275.5	3.1	40.30	284.51	12.4
66.59	26.78	1.6	57.22	289.3	18.7	42.42	163.90	6.5
68.10	34.35	21.7	58.12	295.8	5.2	43.66	321.47	7.9
69.63	28.12	2.2	58.73	225.1	10.1	44.39	293.18	34.9
70.75	22.33	5.4	60.50	123.1	10.7	45.38	284.44	**4.9**
72.69	8.11	0.2	61.11	46.9	0.6			
74.17	8.70	0.2	61.11	47.9	0.6			
75.73	10.59	0.5	62.02	37.6	4.6			
77.26	14.07	0.4	63.54	24.8	0.2			
78.79	24.29	2.4	65.07	22.9	0.5			
80.29	10.55	0.6	66.59	36.3	1.3			
81.79	172.31	1.5	67.81	15.0	0.1			
83.36	35.82	4.3	69.56	26.1	30.05*			
84.78	168.15	68.4	69.62	14.5	7.6			

Table ST1.5: Median Grain Size Results. Instrument errors are as follows: for the >63 μm fraction ±8.0 μm, for 10-63 μm ±1.0 μm, and for the <10 μm fraction ±0.3 μm. Errors in bold indicate only 1 sample was run with only 3 measurements to estimate error.

S1.2.2 Percent Organic Matter

NMY		SS		SMY-A	
Sample Depth (m)	%OM	Sample Depth (m)	%OM	Sample Depth (m)	%OM
1.73	0.2%	1.98	0.3%	4.05	0.3%
23.92	0.4%	6.24	0.3%	6.99	0.5%
26.97	0.4%	11.12	2.2%	17.82	0.5%
30.02	0.6%	13.83	0.3%	19.04	0.6%
33.07	0.9%	16.91	0.2%	19.29	2.7%
36.11	0.7%	25.14	0.3%	20.63	8.7%
40.73	0.9%	32.46	0.5%	22.40	0.5%
42.74	0.9%	34.56	1.3%	23.34	1.2%
43.32	3.7%	37.64	0.5%	24.53	0.2%
46.78	1.2%	40.69	3.0%	25.44	0.3%
48.31	1.2%	43.73	4.8%	26.57	0.3%
49.83	1.5%	45.26	4.5%	28.10	0.5%
51.35	1.9%	46.78	4.2%	30.02	0.3%
52.88	1.3%	48.31	4.9%	31.54	0.5%
54.40	3.2%	49.83	4.7%	33.03	0.4%
55.90	5.4%	51.35	4.3%	34.22	0.4%
59.00	2.7%	52.88	3.3%	35.53	0.4%
60.53	3.8%	54.04	2.2%	37.64	0.5%
62.02	3.6%	54.05	3.8%	39.07	0.5%
63.55	4.3%	54.40	0.6%	40.30	0.5%
66.59	5.7%	56.02	1.1%	42.42	0.4%
68.10	2.9%	57.22	1.1%	43.66	2.6%
69.63	3.9%	58.12	1.7%	44.39	0.8%
70.75	3.7%	58.77	1.0%		
72.69	4.9%	60.50	1.2%		
74.17	5.1%	61.11	6.1%		
75.73	4.8%	62.02	8.9%		
77.26	4.2%	63.54	6.3%		
78.79	5.3%	65.07	9.6%		
80.29	4.7%	66.59	10.9%		
81.79	3.1%	67.81	8.1%		
83.36	4.4%	69.56	3.6%		
84.78	0.7%	69.62	4.1%		

Table ST1.6: Percent Organic Matter Results, error is likely no more than ±2% (Heiri et al., 2001).

S1.2.3 Porosity

NMY			SS			SMY-A		
Depth (m)	Porosity	1 StDev Error	Depth (m)	Porosity	1 StDev Error	Depth (m)	Porosity	1 StDev Error
1.75	20.2%	7%	1.99	35.6%	3%	4.07	35.6%	3%
23.94	38.7%	**4%**	6.26	29.0%	8%	7.01	39.3%	3%
26.99	32.5%	**4%**	11.14	39.4%	1%	17.84	46.4%	3%
28.51	38.1%	**4%**	13.85	36.1%	4%	19.06	37.6%	2%
30.04	38.3%	**4%**	16.93	36.6%	7%	19.31	45.3%	3%
31.57	40.7%	**4%**	25.16	41.1%	3%	20.65	39.8%	0%
33.09	44.6%	**4%**	32.47	33.4%	5%	22.41	42.2%	4%
34.61	38.6%	**4%**	34.58	38.6%	5%	23.36	31.8%	5%
36.13	38.5%	**4%**	37.65	37.5%	6%	24.55	37.1%	5%
37.66	34.9%	**4%**	43.75	53.7%	0%	25.46	40.5%	4%
40.75	37.3%	**4%**	45.27	55.1%	0%	26.59	37.2%	6%
42.76	35.0%	**4%**	46.80	53.5%	1%	28.11	39.4%	3%
43.34	55.3%	**4%**	48.32	53.3%	1%	30.03	38.0%	2%
46.80	48.9%	**1%**	49.85	51.0%	1%	31.56	37.8%	4%
48.33	50.1%	**1%**	51.37	45.9%	1%	33.05	38.5%	2%
49.85	46.0%	**4%**	52.89	45.9%	1%	34.24	41.6%	1%
51.37	49.6%	**1%**	54.05	59.0%	1%	35.55	38.2%	1%
52.90	44.8%	**4%**	54.42	50.6%	12%	37.65	36.3%	3%
54.42	44.6%	**1%**	56.02	37.8%	2%	39.09	36.9%	3%
55.92	48.5%	**1%**	57.22	38.8%	5%	40.32	37.1%	4%
59.02	47.5%	1%	58.14	41.5%	3%	42.44	42.5%	2%
60.55	55.1%	0%	58.79	41.9%	3%	43.67	36.7%	5%
62.04	51.3%	0%	60.51	42.2%	2%	44.41	31.1%	6%
63.57	52.3%	3%	62.04	46.1%	1%			
66.61	51.4%	1%	63.56	43.6%	1%			
68.12	56.0%	2%	65.09	36.9%	**1%**			
69.64	52.8%	2%	66.61	31.5%	**1%**			
70.77	53.0%	3%	67.83	38.7%	**1%**			
72.71	56.3%	2%	69.58	41.4%	0%			
74.19	53.7%	1%						
75.75	53.9%	2%						
77.28	50.6%	1%						
78.80	52.9%	2%						
80.31	56.5%	2%						
81.81	48.5%	1%						
83.37	58.9%	2%						
84.80	31.2%	8%						

Table ST1: Porosity Results. Average errors are as follows: for the >63 μm fraction ±1σ = ±4%, for <63 μm ±1σ = ±1%. Bold error values indicate that error was estimated based on the average for that grain size category.

S1.3 Discussion

S1.3.1 Results of Porosity as a function of Grain Size and Burial Depth

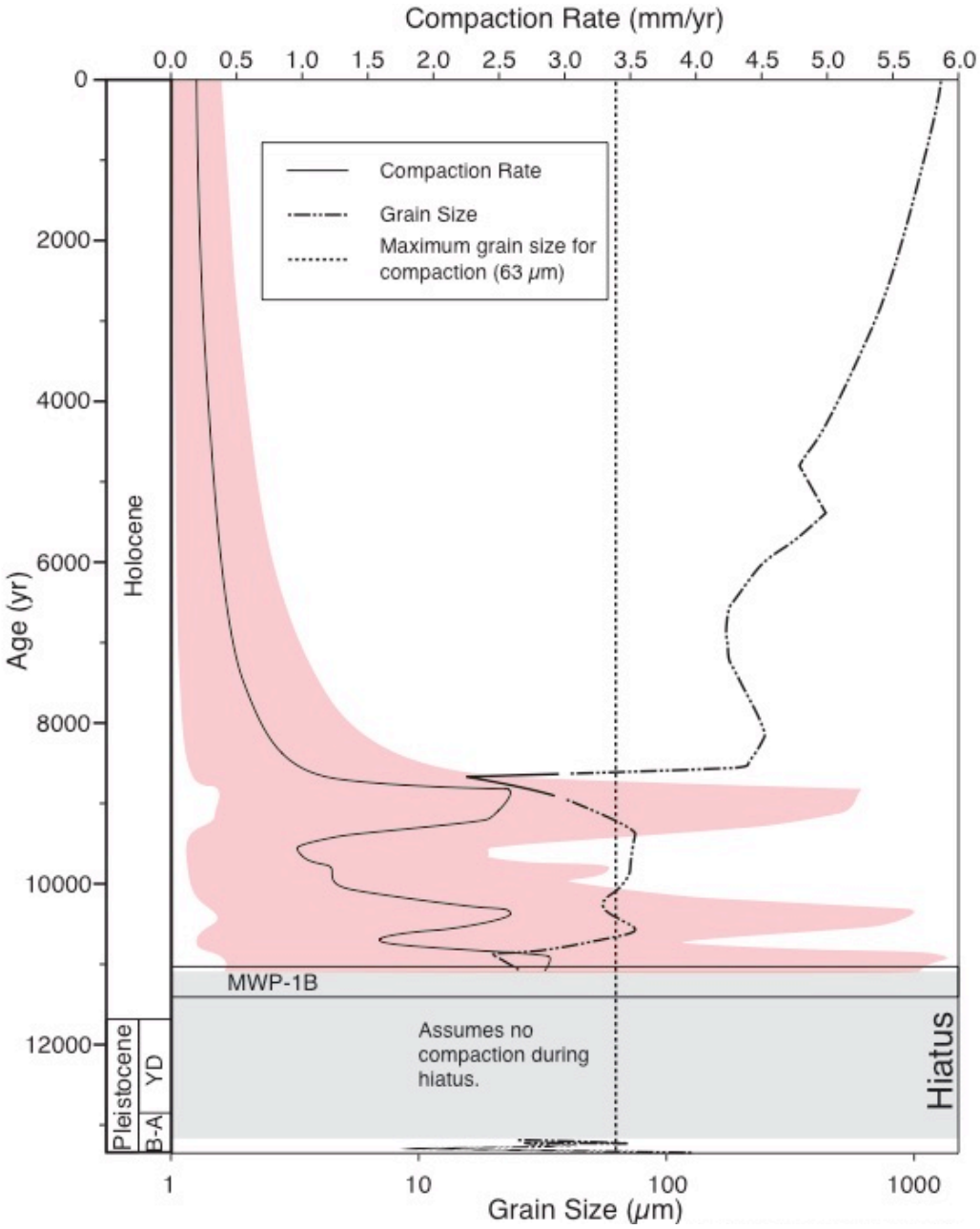

Figure SF1.7: Compaction rate when modeled with porosity as a function of only grain size and burial depth (Equation 2). The red indicates a 90% C.I.. It is also important to note that this model does not account for compaction during the hiatus.

S1.4 References

Blaauw, M., Christen, J.A., 2013. Bacon Manual V2.2. http://www.chrono.qub.ac.uk/blaauw/manualBacon_2.2.pdf [28 November, 2016].

dePaul, V.T., Rice, D.E., and Zapecza, O.S., 2008. Water-level changes in aquifers of the Atlantic Coastal Plain, predevelopment to 2000. U.S. Geological Survey Scientific Investigations Report 2007-5247, p 1-88.

Heiri, O., Lotter A.F., and Lemcke, G., 2001. Loss on ignition as a method for estimating organic and carbonate content in sediments: reproducibility and comparability of results. Journal of Paleolimnology v. 25, p. 101-110.

Holgate, S.J., Matthes, A., Woodworth, P.L., Rickards, L.J., Tamisiea, M.E., Bradshaw, E., Foden, P.R., Gordon, K.M., Juvrejeva, S., Pugh, J., 2013. New data systems and products at the permanent service for mean sea level. Journal of Coastal Research v. 29, n. 3, p. 493-504.

Kopp, R.E., Horton, B.P., Kemp, A.C., and Tebaldi, C., 2015b. Past and future sea-level rise along the coast of North Carolina, USA. Climate Change v. 132, n. 4, p. 693-707.

Kopp R.E., Kemp, A.C., Bittermann, K., Horton, B.P., Donnelly, J.P., Gehrels, W.R., Hay, C.C., Mitrovica, J.X., Morrow, E.D., and Rahmstorf, 2016. Temperature-driven global sea-level variability in the common era. Proceedings of the National Academy of Sciences v. 113, n. 11, E1434-E1441.

Moss, G.H., 1964. Navoo to the Hook. Jersey Close Press, Locust, New Jersey.

Miller, K.G., Stanford, S., Browning, J.V., et al., in prep. Sandy Hook site, in Miller, K.G., Sugarman, P.J., Browning, J.V., et al., eds., Proceedings of the Ocean Drilling Program Initial reports, Volume 174AX (Suppl.): College Station, TX, Ocean Drilling Program.

Permanent Service for Mean Sea Level (PSMSL), 2016. Tide Gauge Data. http://www.psmsl.org/obtaining/ [17 July, 2016]

Woodruff, J.D., Rockwell Geyer, W., Sommerfield, C.K., and Driscoll, N.W., 2001. Seasonal variation of sediment deposition in the Hudson River estuary. Marine Geology v. 179, p. 105-119.

APPENDIX 2: Groundwater Extraction and Land Subsidence at Sandy Hook, NJ USA: A Groundwater Modeling Approach to Estimate Potential Contributions of Aquifer Compaction to Relative Sea-Level Rise

S2.1 Supplemental Methods

S2.1.1 Gridding Observation Wells

```
%Well_Gridder.m
%Created by Christopher S. Johnson
%Nov. 19, 2018


%Uptade Jan 29, 2019
%V1_1
%Accounts for the number of observations in each well over the desired time
%period, so not only does the stat number include the number of wells, but
%all the number of observations in each well.

%Update Feb 19, 2019
%V2_2 Creates a second output matrix indicating the hydro zone that the
%gridded pump wells are in.

%Regrids all observation wells
clear

%List of used variables
```

```
%a

%b

%c

%d

%e

%f

%g

%h

%i

%j

%k

%l

%m

ee=1;%Counter for FinalOutput


%Insert text file name of model grid here. Model grid should be exported

%from ModelMuse and in the format X Y Z Column Row Layer

%a=dlmread('Model_Grid_SHGWM_V2.11.0.txt');

GridInput=dlmread('SHGWM_V2.13.15_Grid.txt');

%GridInput=dlmread('ModelGridwHydroZones_2_13_8.txt');

%Isolates the Cols Rows and Layers

Col=GridInput(:,4);

Row=GridInput(:,5);

Layer=GridInput(:,6);


%Determines the Number of Cols, Rows, and Layers

NumCols=max(Col);

NumRows=max(Row);
```

```
NumLayers=max(Layer);

%Multiplies the number of columns and the number of layers to determine the
%total number of rows necessary in the output matrix
Col_Row=NumCols*NumRows;

%Creates a blank matrix for the col number row number, x coord, y coord,
%and the elevation at the center point of each layer 1-XX.
%In the form... Col Row X Y ZLay1 ZLay2...
Initial_Grid_Reorg=zeros(Col_Row,NumLayers+4);

f=1;

%Sets the Col# and Row# for matrix c.
for d=1:NumRows
   for e=1:NumCols

      Initial_Grid_Reorg(f,2)=d;
      Initial_Grid_Reorg(f,1)=e;



      f=f+1;
   end

end

%Works through the input matrix (a) layer by layer assigning the X Coord,
%Y Coord, and the elevations for the centerpoints of each layer.
```

```
for g=1:size(GridInput,1)

    Initial_Grid_Reorg((((GridInput(g,5)-1)*NumCols)+(GridInput(g,4))),3)=GridInput(g,1);
    Initial_Grid_Reorg((((GridInput(g,5)-1)*NumCols)+(GridInput(g,4))),4)=GridInput(g,2);
    Initial_Grid_Reorg((((GridInput(g,5)-
1)*NumCols)+(GridInput(g,4))),GridInput(g,6)+4)=GridInput(g,3);

end



%Creates Matrix Grid_ReOrg which will transform the centerpoint elevations of each
%layer in matrix Inital_Grid_Reorg to the layer basal elevations in matrix h.
   Grid_ReOrg=zeros(Col_Row,NumLayers+4);
   Grid_ReOrg(:,1)=Initial_Grid_Reorg(:,1);
   Grid_ReOrg(:,2)=Initial_Grid_Reorg(:,2);
   Grid_ReOrg(:,3)=Initial_Grid_Reorg(:,3);
   Grid_ReOrg(:,4)=Initial_Grid_Reorg(:,4);

% Calculates the basal elevations for each layer
for i=1:size(Initial_Grid_Reorg,1)
   HalfThick=0.5*(Initial_Grid_Reorg(i,5)-Initial_Grid_Reorg(i,6));
   Grid_ReOrg(i,5)=Initial_Grid_Reorg(i,5)-HalfThick;

   HalfThick=(Initial_Grid_Reorg(i,5)-HalfThick)-Initial_Grid_Reorg(i,6);
   Grid_ReOrg(i,6)=Initial_Grid_Reorg(i,6)-HalfThick;

   for j=7:NumLayers+4
      HalfThick=(Initial_Grid_Reorg(i,j-1)-HalfThick)-Initial_Grid_Reorg(i,j);
```

```
      Grid_ReOrg(i,j)=Initial_Grid_Reorg(i,j)-HalfThick;
   end
end



%%%%%%%%%%%%%%%%%%%%%%%%%%%%%%%%%%%%%%%%%%%%%%%%%%%%%%%%%%%%%%%%%%%%%%%
%Begins the portion of the script that organizes the observation wells into grid cells
%%%%%%%%%%%%%%%%%%%%%%%%%%%%%%%%%%%%%%%%%%%%%%%%%%%%%%%%%%%%%%%%%%%%%%%

%Imports the text file list of observation wells. Should be in the
%format X Y Z WellID Time(year) Head(m) Stat StatID
AllHeadInput=dlmread('AnnualObsData_UTM.txt');

%Indicate the angle of grid rotation here
%In the SHGWM the grid is rotated 42 degrees counterclockwise.
GridRotation=42; %Grid roation here in degrees
GridAngle=GridRotation*pi()/180;
InvGridAngle=pi()/2-GridRotation;
%Indicate the size of the grid cells here (m)
Gridspacing=1000;
halfspacing=Gridspacing/2;

%Calculates the slope for the columns (remember for the SHGWM the columns
%are NW-SE)
%ColumnSlope=-sin(InvGridAngle)/cos(InvGridAngle);
%ColumnSlope=((sin(pi()/2)+GridAngle))/(cos((pi()/2)-GridAngle));
```

```
%Calculates the slope for the rows (remember for the SH_GWM the rowsare
%NE-SW)
RowSlope=(sin(GridAngle))/(cos(GridAngle));


ColumnSlope=-1/RowSlope;



%Creates a new matrix (k) that has all of the attributes of matrix h (col#,
%row#, X, Y, and Base elevation of all layers, plus 2 rows for the y
%intercepts of the layer and row equations.
Grid_ReOrg_wInts=zeros(size(Grid_ReOrg,1),size(Grid_ReOrg,2)+2);
for l=1:size(Grid_ReOrg,2)
   Grid_ReOrg_wInts(:,l)=Grid_ReOrg(:,l);
end

%Calculates intercepts for columns and rows
for m=1:size(Grid_ReOrg_wInts,1)
   Grid_ReOrg_wInts(m,size(Grid_ReOrg_wInts,2)-1)=Grid_ReOrg_wInts(m,4)-
ColumnSlope*Grid_ReOrg_wInts(m,3);
   Grid_ReOrg_wInts(m,size(Grid_ReOrg_wInts,2))=Grid_ReOrg_wInts(m,4)-
RowSlope*Grid_ReOrg_wInts(m,3);
end

%Column Intercept Correction
ColIntCor=(Grid_ReOrg_wInts(1,size(Grid_ReOrg,2)+1)-Grid_ReOrg_wInts(2,size(Grid_ReOrg,2)+1))/2;
%Row Intercept Correction
RowIntCor=(Grid_ReOrg_wInts(1,size(Grid_ReOrg,2)+2)-
Grid_ReOrg_wInts(2,size(Grid_ReOrg,2)+2))/2;
```

```
for aa=1890:2015
   clear HeadInput
   cc=1;
   for bb=1:size(AllHeadInput,1)
      if AllHeadInput(bb,5)==aa
         HeadInput(cc,1)=AllHeadInput(bb,1);
         HeadInput(cc,2)=AllHeadInput(bb,2);
         HeadInput(cc,3)=AllHeadInput(bb,3);
         HeadInput(cc,4)=AllHeadInput(bb,4);
         HeadInput(cc,5)=AllHeadInput(bb,5);
         HeadInput(cc,6)=AllHeadInput(bb,6);
         HeadInput(cc,7)=AllHeadInput(bb,7);
         HeadInput(cc,8)=AllHeadInput(bb,8);
         cc=cc+1;
      end
   end



   if cc==1
      HeadInput=zeros(1,8);
   end

%Creates a matrix of the head observations, coordinates, and the associated
%grid cells
%Matrix takes the form x, y, z,  well ID,  time (d),head, column#, row#, layer#
Head_GridLocs=zeros(size(HeadInput,1),10);
```

```
 for n=1:size(HeadInput,1)
    o=1;

    %Tests to see if the observation well is outside the model grid (below
    %col 1 or above row 1)
    %Tests for outside the grid below the first column
    if HeadInput(n,2) < ColumnSlope * HeadInput(n,1) + Grid_ReOrg_wInts(o,(size(Grid_ReOrg_wInts,2)-
1)) + ColIntCor
        Head_GridLocs(n,1)=9999;
        Head_GridLocs(n,2)=NaN;
        Head_GridLocs(n,3)=NaN;
        Head_GridLocs(n,4)=HeadInput(n,4);
        Head_GridLocs(n,5)=NaN;
        Head_GridLocs(n,5)=NaN;
        Head_GridLocs(n,6)=NaN;
        Head_GridLocs(n,7)=NaN;
        Head_GridLocs(n,8)=NaN;
        Head_GridLocs(n,9)=99999;
        test=1;

    %Tests for outside the grid above the first row
    elseif HeadInput(n,2) > RowSlope * HeadInput(n,1) +
Grid_ReOrg_wInts(o,(size(Grid_ReOrg_wInts,2))) + RowIntCor
        Head_GridLocs(n,1)=NaN;
        Head_GridLocs(n,2)=9999;
        Head_GridLocs(n,3)=NaN;
```

```
        Head_GridLocs(n,4)=HeadInput(n,4);
        Head_GridLocs(n,5)=NaN;
        Head_GridLocs(n,5)=NaN;
        Head_GridLocs(n,6)=NaN;
        Head_GridLocs(n,7)=NaN;
        Head_GridLocs(n,8)=NaN;
        Head_GridLocs(n,9)=99999;
        test=1;
    else
        test=0;
    end

    while test < 1
        %Tests the columns
        if HeadInput(n,2) < ColumnSlope * HeadInput(n,1) +
Grid_ReOrg_wInts(o,(size(Grid_ReOrg_wInts,2)-1)) - ColIntCor

            %Tests the rows
            if HeadInput(n,2) > RowSlope * HeadInput(n,1) +
Grid_ReOrg_wInts(o,(size(Grid_ReOrg_wInts,2))) - RowIntCor

                %Tests Layers
                p=1;
                while test < 1
                    if HeadInput(n,3) > Grid_ReOrg_wInts(o,p+4)
                        Head_GridLocs(n,1)=Grid_ReOrg_wInts(o,3); %Sets X Coordinate
                        Head_GridLocs(n,2)=Grid_ReOrg_wInts(o,4); %Sets Y Coordinate
                        Head_GridLocs(n,3)=Grid_ReOrg_wInts(o,p+4); %Sets Z Coordinate
```

```
  Head_GridLocs(n,4)=HeadInput(n,4); %Sets the Well ID
  Head_GridLocs(n,5)=HeadInput(n,5); %Sets the Time (d)
  Head_GridLocs(n,6)=HeadInput(n,6); %Sets the Head (m)
  Head_GridLocs(n,7)=Grid_ReOrg_wInts(o,1); %Sets the Column Number
  Head_GridLocs(n,8)=Grid_ReOrg_wInts(o,2); %Sets the Row #
  Head_GridLocs(n,9)=p; %Sets the Layer #
  Head_GridLocs(n,10)=HeadInput(n,7); %Sets the number of observations
  test=1;
else
  test=0;
end
p=p+1;
if p > NumLayers %Tests to see if the observation well is below the grid
   Head_GridLocs(n,1)=NaN;
   Head_GridLocs(n,2)=NaN;
   Head_GridLocs(n,3)=9999;
   Head_GridLocs(n,4)=HeadInput(n,4);
   Head_GridLocs(n,5)=NaN;
   Head_GridLocs(n,5)=NaN;
   Head_GridLocs(n,6)=NaN;
   Head_GridLocs(n,7)=NaN;
   Head_GridLocs(n,8)=NaN;
   Head_GridLocs(n,9)=99999;
   test=1;

end
```

```
            end %End While Loop


        end %End Row Test


    end %End Column Test
    o=o+1;

    %Tests if the observed well is outside of the model grid (below the
    %last row and above the last column)
    if o > size(Grid_ReOrg_wInts,1)-1

        Head_GridLocs(n,1)=9999;
        Head_GridLocs(n,2)=9999;
        Head_GridLocs(n,3)=NaN;
        Head_GridLocs(n,4)=HeadInput(n,4);
        Head_GridLocs(n,5)=NaN;
        Head_GridLocs(n,5)=NaN;
        Head_GridLocs(n,6)=NaN;
        Head_GridLocs(n,7)=NaN;
        Head_GridLocs(n,8)=NaN;
        Head_GridLocs(n,9)=99999;
        test=1;
    end


  end
end
```

```
%%%%%%%%%%%%%%%%%%%%%%%%%%%%%%%%%%%%%%%%%%%%%%%%%%%%%%%%%%%
%Begins to resort and organize the observation wells by grid cell
%averages all values within the same grid cell to one value.
%Then adds weight to each cell based on the number of wells in that cell
%%%%%%%%%%%%%%%%%%%%%%%%%%%%%%%%%%%%%%%%%%%%%%%%%%%%%%%%%%%

%GridedObsWells is a matrix containing Col Row Layer x y z WellCount SumOfHeads Time(day)
GridedObsWells=zeros(size(GridInput,1),10);

GridedObsWells(:,1)=GridInput(:,4); %Col
GridedObsWells(:,2)=GridInput(:,5); %Row
GridedObsWells(:,3)=GridInput(:,6); %Layer
GridedObsWells(:,4)=GridInput(:,1); %X
GridedObsWells(:,5)=GridInput(:,2); %Y
GridedObsWells(:,6)=GridInput(:,3); %Z



for q=1:size(Head_GridLocs,1)

  if Head_GridLocs(q,9) == 99999



  else
```

```
    RowNumber=((Head_GridLocs(q,9)-1) * NumCols * NumRows) + ((Head_GridLocs(q,8)-1) *
NumCols) + Head_GridLocs(q,7);
    GridedObsWells(RowNumber,7) = GridedObsWells(RowNumber,7)+1; %Counts the number of
observation wells in the grid cell
    GridedObsWells(RowNumber,8) = GridedObsWells(RowNumber,8) + Head_GridLocs(q,6);
    GridedObsWells(RowNumber,9) = Head_GridLocs(q,5);
    GridedObsWells(RowNumber,10)= GridedObsWells(RowNumber,10)+Head_GridLocs(q,10);
%Counts the total number of observations from that cell

    end

 end


 %Cleans the grid to only the cells with observation wells in them.
 DistilledGriddedObsWells=zeros(1,10);
 s=1;
 for r=1:size(GridedObsWells,1)
   if GridedObsWells(r,7)>0
      DistilledGriddedObsWells(s,1)=GridedObsWells(r,1);
      DistilledGriddedObsWells(s,2)=GridedObsWells(r,2);
      DistilledGriddedObsWells(s,3)=GridedObsWells(r,3);
      DistilledGriddedObsWells(s,4)=GridedObsWells(r,4);
      DistilledGriddedObsWells(s,5)=GridedObsWells(r,5);
      DistilledGriddedObsWells(s,6)=GridedObsWells(r,6);
      DistilledGriddedObsWells(s,7)=GridedObsWells(r,7);
      DistilledGriddedObsWells(s,8)=GridedObsWells(r,8);
      DistilledGriddedObsWells(s,9)=GridedObsWells(r,9);
```

```
    DistilledGriddedObsWells(s,10)=GridedObsWells(r,10);
    s=s+1;
  end
end

% Divides the sum of the observed heads by the number of the observed heads to get the average.
for t=1:size(DistilledGriddedObsWells,1)
  DistilledGriddedObsWells(t,8)=DistilledGriddedObsWells(t,8)/DistilledGriddedObsWells(t,7);
end



%format X Y Z WellID Time(day) Head(m) Stat StatID
Output=zeros(size(DistilledGriddedObsWells,1),8);
Output(:,1)=DistilledGriddedObsWells(:,4);
Output(:,2)=DistilledGriddedObsWells(:,5);
Output(:,3)=DistilledGriddedObsWells(:,6);
for u=1:size(DistilledGriddedObsWells,1)
   Output(u,4)=u;
end
Output(:,5)=aa;
Output(:,6)=DistilledGriddedObsWells(:,8);
Output(:,7)=DistilledGriddedObsWells(:,10);
Output(:,8)=1;
```

```
%HydroZoneOutput=zeros(size(Output,1),2);
%HydroZoneOutput(:,1)=Output(:,4);
for t=1:size(Output,1)
   for u=1:size(GridInput,1)
      if DistilledGriddedObsWells(t,1)==GridInput(u,4)
         if DistilledGriddedObsWells(t,2)==GridInput(u,5)
            if DistilledGriddedObsWells(t,3)==GridInput(u,6)
               Output(t,4)=Output(t,4)+(100000000*GridInput(u,7));
            end
         end
      end
   end
end

   for dd=1:size(Output,1)
      FinalOutput(ee,1)=Output(dd,1);
      FinalOutput(ee,2)=Output(dd,2);
      FinalOutput(ee,3)=Output(dd,3);
      FinalOutput(ee,4)=Output(dd,4)+1000*(Output(dd,5));
      FinalOutput(ee,5)=(Output(dd,5)-1885)*365.25;
      FinalOutput(ee,6)=Output(dd,6);
      FinalOutput(ee,7)=Output(dd,7);
      FinalOutput(ee,8)=Output(dd,8);
      ee=ee+1;
   end

% clear Output
```

```
% clear DistilledGriddedObsWells
% clear GridedObsWells
% clear HeadInput
% clear Head_GridLocs
end



% HydroZoneOutput=zeros(size(Output,1),2);
% HydroZoneOutput(:,1)=Output(:,4);
% for t=1:size(Output,1)
%     for u=1:size(GridInput,1)
%         if DistilledGriddedObsWells(t,1)==GridInput(u,4)
%             if DistilledGriddedObsWells(t,2)==GridInput(u,5)
%                 if DistilledGriddedObsWells(t,3)==GridInput(u,6)
%                     HydroZoneOutput(t,2)=GridInput(u,7);
%                 end
%             end
%         end
%     end
% end
% %
% %
```

S2.2 Supplementary Results

S2.2.1 Sensitivity of model to confining unit storage parameters at Sandy Hook, NJ

Table ST2.1 Model sensitivity to storage parameters of confining units. S_s=S_{skv}.

	Compaction (mm)							Compaction Rate (mm/yr)						
Year	Ss= 6.4e-3 Sske= 6.4E-5*b	Ss= 0.02 Sske= 2E-4*b	Ss= 0.01 Sske= 1E-4*b	Ss= 0.005 Sske= 5E-5*b	Ss= 2.5E-3 Sske= 2.5E-5*b	Ss= 1.25E-3 Sske= 1.25E-5*b	Ss= 6.25E-4 Sske= 6.25E-6*b	Ss= 6.4e-3 Sske= 6.4E-5*b	Ss= 0.02 Sske= 2E-4*b	Ss= 0.01 Sske= 1E-4*b	Ss= 0.005 Sske= 5E-5*b	Ss= 2.5E-3 Sske= 2.5E-5*b	Ss= 1.25E-3 Sske= 1.25E-5*b	Ss= 6.25E-4 Sske= 6.25E-6*b
1885	0	0	0	0	0	0	0	0	0	0	0	0	0	0
1886	0	0	0	0	0	0	0	0	0	0	0	0	0	0
1887	0.000679	0.00060	0.00106	0.00068	0.00053	0.00039	0.00031	0.00067	0.00060	0.00106	0.00068	0.00053	0.00039	0.00031
1888	0.00122	0.00069	0.0013	0.00102	0.00075	0.00064	0.00054	0.00054	9.5E-05	0.00024	0.00033	0.00022	0.00025	0.00023
1889	0.00171	0.00058	0.00148	0.00126	0.00095	0.00088	0.00074	0.00049	-0.00011	0.00018	0.00024	0.00019	0.00024	0.00020
1890	0.00215	0.00054	0.00164	0.00161	0.00116	0.00112	0.00092	0.00044	-0.00003	0.00016	0.00035	0.00020	0.00023	0.00017
1891	0.00243	0.00062	0.00186	0.00181	0.00144	0.00133	0.00107	0.00028	8E-05	0.00022	0.0002	0.00028	0.00021	0.00014
1892	0.0027	0.00063	0.00206	0.00198	0.00174	0.00154	0.00122	0.00027	0.00001	0.0002	0.00017	0.0003	0.00021	0.00015
1893	0.00297	0.00075	0.00207	0.00228	0.00197	0.00171	0.00134	0.00027	0.00011	0.00001	0.0003	0.00023	0.00017	0.00012
1894	0.00341	0.00066	0.0021	0.00269	0.00225	0.00192	0.00145	0.00044	-9.2E-05	3E-05	0.00041	0.00028	0.00021	0.00011
1895	0.0037	0.00057	0.00214	0.00294	0.00241	0.00209	0.00154	0.00029	-9E-05	4E-05	0.00025	0.00016	0.00017	0.00009
1896	0.0377	0.0307	0.0343	0.0361	0.0374	0.0403	0.0441	0.034	0.03012	0.03216	0.03316	0.03499	0.03821	0.04256
1897	0.0725	0.0644	0.0677	0.0711	0.0761	0.0823	0.0889	0.0348	0.0337	0.0334	0.035	0.0387	0.042	0.0448
1898	0.109	0.0978	0.101	0.108	0.116	0.127	0.135	0.0365	0.0334	0.0333	0.0369	0.0399	0.0447	0.0461
1899	0.145	0.131	0.136	0.149	0.159	0.176	0.183	0.036	0.0332	0.035	0.041	0.043	0.049	0.048
1900	0.217	0.196	0.204	0.222	0.239	0.264	0.269	0.072	0.065	0.068	0.073	0.08	0.088	0.086
1901	0.292	0.266	0.274	0.302	0.32	0.356	0.356	0.075	0.07	0.07	0.08	0.081	0.092	0.087
1902	0.369	0.336	0.345	0.383	0.41	0.447	0.442	0.077	0.07	0.071	0.081	0.09	0.091	0.086

	Compaction (mm)							Compaction Rate (mm/yr)						
Year	Ss= 6.4e-3 Sske= 6.4E-5*b	Ss= 0.02 Sske= 2E-4*b	Ss= 0.01 Sske= 1E-4*b	Ss= 0.005 Sske= 5E-5*b	Ss= 2.5E-3 Sske= 2.5E-5*b	Ss= 1.25E-3 Sske= 1.25E-5*b	Ss= 6.25E-4 Sske= 6.25E-6*b	Ss= 6.4e-3 Sske= 6.4E-5*b	Ss= 0.02 Sske= 2E-4*b	Ss= 0.01 Sske= 1E-4*b	Ss= 0.005 Sske= 5E-5*b	Ss= 2.5E-3 Sske= 2.5E-5*b	Ss= 1.25E-3 Sske= 1.25E-5*b	Ss= 6.25E-4 Sske= 6.25E-6*b
1903	0.449	0.409	0.42	0.467	0.503	0.543	0.526	0.08	0.073	0.075	0.084	0.093	0.096	0.084
1904	0.528	0.478	0.497	0.55	0.598	0.635	0.606	0.079	0.069	0.077	0.083	0.095	0.092	0.08
1905	0.611	0.547	0.575	0.636	0.692	0.731	0.678	0.083	0.069	0.078	0.086	0.094	0.096	0.072
1906	0.698	0.624	0.652	0.723	0.791	0.819	0.747	0.087	0.077	0.077	0.087	0.099	0.088	0.069
1907	0.752	0.633	0.674	0.778	0.86	0.877	0.779	0.054	0.009	0.022	0.055	0.069	0.058	0.032
1908	0.822	0.652	0.718	0.849	0.93	0.928	0.812	0.07	0.019	0.044	0.071	0.07	0.051	0.033
1909	0.883	0.692	0.772	0.913	0.992	0.969	0.844	0.061	0.04	0.054	0.064	0.062	0.041	0.032
1910	0.944	0.738	0.822	0.974	1.05	1	0.874	0.061	0.046	0.05	0.061	0.058	0.031	0.03
1911	1.02	0.799	0.892	1.06	1.12	1.06	0.925	0.076	0.061	0.07	0.086	0.07	0.06	0.051
1912	1.1	0.867	0.965	1.13	1.18	1.11	0.974	0.08	0.068	0.073	0.07	0.06	0.05	0.049
1913	1.17	0.93	1.04	1.21	1.24	1.16	1.02	0.07	0.063	0.075	0.08	0.06	0.05	0.046
1914	1.25	0.997	1.11	1.28	1.3	1.21	1.07	0.08	0.067	0.07	0.07	0.06	0.05	0.05
1915	1.32	1.07	1.18	1.34	1.36	1.26	1.11	0.07	0.073	0.07	0.06	0.06	0.05	0.04
1916	1.39	1.13	1.25	1.41	1.41	1.31	1.15	0.07	0.06	0.07	0.07	0.05	0.05	0.04
1917	1.53	1.27	1.38	1.55	1.53	1.43	1.27	0.14	0.14	0.13	0.14	0.12	0.12	0.12
1918	1.86	1.58	1.69	1.87	1.84	1.74	1.56	0.33	0.31	0.31	0.32	0.31	0.31	0.29
1919	1.9	1.61	1.74	1.91	1.87	1.76	1.57	0.04	0.03	0.05	0.04	0.03	0.02	0.01
1920	1.98	1.68	1.81	1.98	1.93	1.81	1.6	0.08	0.07	0.07	0.07	0.06	0.05	0.03
1921	2.05	1.75	1.89	2.04	1.99	1.86	1.62	0.07	0.07	0.08	0.06	0.06	0.05	0.02
1922	2.12	1.83	1.97	2.11	2.04	1.91	1.65	0.07	0.08	0.08	0.07	0.05	0.05	0.03
1923	2.18	1.9	2.04	2.17	2.1	1.95	1.67	0.06	0.07	0.07	0.06	0.06	0.04	0.02
1924	2.25	1.97	2.11	2.23	2.15	2	1.69	0.07	0.07	0.07	0.06	0.05	0.05	0.02
1925	2.31	2.04	2.18	2.29	2.2	2.04	1.71	0.06	0.07	0.07	0.06	0.05	0.04	0.02
1926	2.37	2.11	2.25	2.35	2.26	2.08	1.72	0.06	0.07	0.07	0.06	0.06	0.04	0.01
1927	2.44	2.18	2.31	2.41	2.31	2.12	1.74	0.07	0.07	0.06	0.06	0.05	0.04	0.02

	Compaction (mm)							Compaction Rate (mm/yr)						
Year	Ss= 6.4e-3 Sske= 6.4E-5*b	Ss= 0.02 Sske= 2E-4*b	Ss= 0.01 Sske= 1E-4*b	Ss= 0.005 Sske= 5E-5*b	Ss= 2.5E-3 Sske= 2.5E-5*b	Ss= 1.25E-3 Sske= 1.25E-5*b	Ss= 6.25E-4 Sske= 6.25E-6*b	Ss= 6.4e-3 Sske= 6.4E-5*b	Ss= 0.02 Sske= 2E-4*b	Ss= 0.01 Sske= 1E-4*b	Ss= 0.005 Sske= 5E-5*b	Ss= 2.5E-3 Sske= 2.5E-5*b	Ss= 1.25E-3 Sske= 1.25E-5*b	Ss= 6.25E-4 Sske= 6.25E-6*b
1928	2.5	2.26	2.38	2.47	2.36	2.15	1.76	0.06	0.08	0.07	0.06	0.05	0.03	0.02
1929	2.56	2.33	2.45	2.54	2.42	2.2	1.78	0.06	0.07	0.07	0.07	0.06	0.05	0.02
1930	2.57	2.33	2.46	2.55	2.42	2.19	1.78	0.01	0	0.01	0.01	0	-0.01	0
1931	2.59	2.34	2.48	2.56	2.43	2.19	1.78	0.02	0.01	0.02	0.01	0.01	0	0
1932	2.6	2.35	2.49	2.57	2.43	2.19	1.78	0.01	0.01	0.01	0.01	0	0	0
1933	2.61	2.36	2.51	2.58	2.44	2.19	1.78	0.01	0.01	0.02	0.01	0.01	0	0
1934	2.63	2.38	2.53	2.59	2.45	2.19	1.78	0.02	0.02	0.02	0.01	0.01	0	0
1935	2.71	2.46	2.62	2.67	2.53	2.25	1.79	0.08	0.08	0.09	0.08	0.08	0.06	0.01
1936	2.79	2.54	2.69	2.75	2.61	2.32	1.83	0.08	0.08	0.07	0.08	0.08	0.07	0.04
1937	2.87	2.63	2.77	2.83	2.68	2.39	1.89	0.08	0.09	0.08	0.08	0.07	0.07	0.06
1938	2.95	2.71	2.85	2.91	2.76	2.46	1.95	0.08	0.08	0.08	0.08	0.08	0.07	0.06
1939	3.03	2.79	2.93	2.98	2.84	2.53	2.01	0.08	0.08	0.08	0.07	0.08	0.07	0.06
1940	3.2	2.97	3.1	3.16	3.01	2.7	2.16	0.17	0.18	0.17	0.18	0.17	0.17	0.15
1941	3.44	3.31	3.4	3.4	3.27	2.95	2.49	0.24	0.34	0.3	0.24	0.26	0.25	0.33
1942	4.42	4.24	4.34	4.35	4.24	4.02	3.66	0.98	0.93	0.94	0.95	0.97	1.07	1.17
1943	5.81	5.52	5.67	5.77	5.77	5.65	5.34	1.39	1.28	1.33	1.42	1.53	1.63	1.68
1944	7.27	6.85	7.06	7.27	7.43	7.41	7.03	1.46	1.33	1.39	1.5	1.66	1.76	1.69
1945	8.8	8.2	8.5	8.86	9.18	9.19	8.61	1.53	1.35	1.44	1.59	1.75	1.78	1.58
1946	9.2	8.28	8.75	9.35	9.9	9.88	8.85	0.4	0.08	0.25	0.49	0.72	0.69	0.24
1947	9.72	8.52	9.15	9.94	10.6	10.3	9	0.52	0.24	0.4	0.59	0.7	0.42	0.15
1948	10.2	8.76	9.53	10.5	11.1	10.5	9.1	0.48	0.24	0.38	0.56	0.5	0.2	0.1
1949	10.6	8.98	9.88	10.9	11.5	10.7	9.19	0.4	0.22	0.35	0.4	0.4	0.2	0.09
1950	11	9.2	10.2	11.3	11.7	10.8	9.24	0.4	0.22	0.32	0.4	0.2	0.1	0.05
1951	11.3	9.41	10.5	11.6	11.9	10.8	9.28	0.3	0.21	0.3	0.3	0.2	0	0.04
1952	11.7	9.62	10.8	11.9	12	10.9	9.31	0.4	0.21	0.3	0.3	0.1	0.1	0.03

	Compaction (mm)							Compaction Rate (mm/yr)						
Year	Ss= 6.4e-3 Sske= 6.4E-5*b	Ss= 0.02 Sske= 2E-4*b	Ss= 0.01 Sske= 1E-4*b	Ss= 0.005 Sske= 5E-5*b	Ss= 2.5E-3 Sske= 2.5E-5*b	Ss= 1.25E-3 Sske= 1.25E-5*b	Ss= 6.25E-4 Sske= 6.25E-6*b	Ss= 6.4e-3 Sske= 6.4E-5*b	Ss= 0.02 Sske= 2E-4*b	Ss= 0.01 Sske= 1E-4*b	Ss= 0.005 Sske= 5E-5*b	Ss= 2.5E-3 Sske= 2.5E-5*b	Ss= 1.25E-3 Sske= 1.25E-5*b	Ss= 6.25E-4 Sske= 6.25E-6*b
1953	11.9	9.82	11.1	12.2	12.2	10.9	9.32	0.2	0.2	0.3	0.3	0.2	0	0.01
1954	12.2	10	11.3	12.4	12.2	11	9.32	0.3	0.18	0.2	0.2	0	0.1	0
1955	12.4	10.2	11.6	12.6	12.3	11	9.32	0.2	0.2	0.3	0.2	0.1	0	0
1956	12.6	10.4	11.8	12.8	12.4	11	9.31	0.2	0.2	0.2	0.2	0.1	0	-0.01
1957	12.8	10.6	12	12.9	12.4	11.1	9.31	0.2	0.2	0.2	0.1	0	0.1	0
1958	13	10.8	12.2	13.1	12.5	11.1	9.3	0.2	0.2	0.2	0.2	0.1	0	-0.01
1959	13.2	10.9	12.5	13.2	12.5	11.1	9.3	0.2	0.1	0.3	0.1	0	0	0
1960	13.3	11.1	12.6	13.3	12.6	11.2	9.3	0.1	0.2	0.1	0.1	0.1	0.1	0
1961	13.5	11.3	12.8	13.4	12.6	11.2	9.3	0.2	0.2	0.2	0.1	0	0	0
1962	13.6	11.5	13	13.4	12.6	11.2	9.29	0.1	0.2	0.2	0	0	0	-0.01
1963	13.7	11.6	13.2	13.5	12.7	11.3	9.29	0.1	0.1	0.2	0.1	0.1	0.1	0
1964	13.8	11.8	13.3	13.6	12.7	11.3	9.29	0.1	0.2	0.1	0.1	0	0	0
1965	13.9	12	13.5	13.7	12.8	11.3	9.28	0.1	0.2	0.2	0.1	0.1	0	-0.01
1966	14	12.1	13.6	13.7	12.8	11.3	9.28	0.1	0.1	0.1	0	0	0	0
1967	14.1	12.3	13.8	13.8	12.9	11.4	9.28	0.1	0.2	0.2	0.1	0.1	0.1	0
1968	14.2	12.5	13.9	13.9	12.9	11.4	9.28	0.1	0.2	0.1	0.1	0	0	0
1969	14.2	12.6	14	14	13	11.5	9.29	0	0.1	0.1	0.1	0.1	0.1	0.01
1970	14.3	12.8	14.2	14	13.1	11.6	9.3	0.1	0.2	0.2	0	0.1	0.1	0.01
1971	14.5	13	14.4	14.2	13.2	11.7	9.37	0.2	0.2	0.2	0.2	0.1	0.1	0.07
1972	14.6	13.2	14.5	14.3	13.3	11.8	9.47	0.1	0.2	0.1	0.1	0.1	0.1	0.1
1973	14.7	13.4	14.7	14.4	13.5	11.9	9.58	0.1	0.2	0.2	0.1	0.2	0.1	0.11
1974	15.1	13.8	15.1	14.7	13.8	12.2	9.87	0.4	0.4	0.4	0.3	0.3	0.3	0.29
1975	15.5	14.3	15.5	15.2	14.3	12.7	10.3	0.4	0.5	0.4	0.5	0.5	0.5	0.43
1976	16.1	15	16.1	15.7	14.8	13.2	10.8	0.6	0.7	0.6	0.5	0.5	0.5	0.5
1977	16.6	15.6	16.7	16.2	15.4	13.8	11.4	0.5	0.6	0.6	0.5	0.6	0.6	0.6

	Compaction (mm)							Compaction Rate (mm/yr)						
Year	Ss= 6.4e-3 Sske= 6.4E-5*b	Ss= 0.02 Sske= 2E-4*b	Ss= 0.01 Sske= 1E-4*b	Ss= 0.005 Sske= 5E-5*b	Ss= 2.5E-3 Sske= 2.5E-5*b	Ss= 1.25E-3 Sske= 1.25E-5*b	Ss= 6.25E-4 Sske= 6.25E-6*b	Ss= 6.4e-3 Sske= 6.4E-5*b	Ss= 0.02 Sske= 2E-4*b	Ss= 0.01 Sske= 1E-4*b	Ss= 0.005 Sske= 5E-5*b	Ss= 2.5E-3 Sske= 2.5E-5*b	Ss= 1.25E-3 Sske= 1.25E-5*b	Ss= 6.25E-4 Sske= 6.25E-6*b
1978	17.1	16.1	17.2	16.8	15.9	14.3	11.9	0.5	0.5	0.5	0.6	0.5	0.5	0.5
1979	17.6	16.8	17.8	17.3	16.4	14.8	12.3	0.5	0.7	0.6	0.5	0.5	0.5	0.4
1980	18.3	17.4	18.4	17.9	17.1	15.4	12.9	0.7	0.6	0.6	0.6	0.7	0.6	0.6
1981	18.9	18.1	19.1	18.5	17.7	16.1	13.5	0.6	0.7	0.7	0.6	0.6	0.7	0.6
1982	19.5	18.8	19.8	19.1	18.3	16.7	14.1	0.6	0.7	0.7	0.6	0.6	0.6	0.6
1983	20.2	19.6	20.5	19.8	19	17.3	14.6	0.7	0.8	0.7	0.7	0.7	0.6	0.5
1984	20.7	20.2	21.2	20.4	19.6	17.9	15.1	0.5	0.6	0.7	0.6	0.6	0.6	0.5
1985	21.5	21	21.9	21	20.2	18.5	15.7	0.8	0.8	0.7	0.6	0.6	0.6	0.6
1986	22.3	21.7	22.6	21.7	20.9	19.2	16.2	0.8	0.7	0.7	0.7	0.7	0.7	0.5
1987	23.1	22.5	23.4	22.4	21.6	19.8	16.8	0.8	0.8	0.8	0.7	0.7	0.6	0.6
1988	23.8	23.2	24.1	23.1	22.1	20.3	17.2	0.7	0.7	0.7	0.7	0.5	0.5	0.4
1989	24.5	23.8	24.8	23.8	22.7	20.9	17.7	0.7	0.6	0.7	0.7	0.6	0.6	0.5
1990	24.9	24.3	25.2	24.3	23.1	21.2	17.8	0.4	0.5	0.4	0.5	0.4	0.3	0.1
1991	25.6	24.9	25.9	25	23.6	21.7	18.2	0.7	0.6	0.7	0.7	0.5	0.5	0.4
1992	26.2	25.5	26.4	25.6	24.1	22	18.5	0.6	0.6	0.5	0.6	0.5	0.3	0.3
1993	26.8	26.1	27	26.2	24.6	22.4	18.7	0.6	0.6	0.6	0.6	0.5	0.4	0.2
1994	27.3	26.6	27.5	26.7	25	22.8	18.9	0.5	0.5	0.5	0.5	0.4	0.4	0.2
1995	27.9	27.2	28.1	27.3	25.5	23.2	19.2	0.6	0.6	0.6	0.6	0.5	0.4	0.3
1996	28.4	27.7	28.7	27.8	25.9	23.5	19.4	0.5	0.5	0.6	0.5	0.4	0.3	0.2
1997	29	28.3	29.3	28.4	26.5	24	19.7	0.6	0.6	0.6	0.6	0.6	0.5	0.3
1998	29.6	29	29.9	29	27	24.4	20	0.6	0.7	0.6	0.6	0.5	0.4	0.3
1999	30.3	29.6	30.6	29.6	27.5	24.9	20.3	0.7	0.6	0.7	0.6	0.5	0.5	0.3
2000	30.9	30.3	31.2	30.2	28.1	25.3	20.7	0.6	0.7	0.6	0.6	0.6	0.4	0.4
2001	31.6	31.1	32	31	28.7	25.9	21.1	0.7	0.8	0.8	0.8	0.6	0.6	0.4
2002	32.4	31.8	32.7	31.7	29.4	26.4	21.5	0.8	0.7	0.7	0.7	0.7	0.5	0.4

	Compaction (mm)							Compaction Rate (mm/yr)						
Year	Ss= 6.4e-3 Sske= 6.4E-5*b	Ss= 0.02 Sske= 2E-4*b	Ss= 0.01 Sske= 1E-4*b	Ss= 0.005 Sske= 5E-5*b	Ss= 2.5E-3 Sske= 2.5E-5*b	Ss= 1.25E-3 Sske= 1.25E-5*b	Ss= 6.25E-4 Sske= 6.25E-6*b	Ss= 6.4e-3 Sske= 6.4E-5*b	Ss= 0.02 Sske= 2E-4*b	Ss= 0.01 Sske= 1E-4*b	Ss= 0.005 Sske= 5E-5*b	Ss= 2.5E-3 Sske= 2.5E-5*b	Ss= 1.25E-3 Sske= 1.25E-5*b	Ss= 6.25E-4 Sske= 6.25E-6*b
2003	33.1	32.5	33.4	32.4	30	26.9	21.8	0.7	0.7	0.7	0.7	0.6	0.5	0.3
2004	33.8	33.3	34.2	33.1	30.6	27.5	22.2	0.7	0.8	0.8	0.7	0.6	0.6	0.4
2005	34.6	34.1	34.9	33.9	31.3	28	22.6	0.8	0.8	0.7	0.8	0.7	0.5	0.4
2006	35.4	34.8	35.7	34.7	32	28.6	23	0.8	0.7	0.8	0.8	0.7	0.6	0.4
2007	36.2	35.7	36.5	35.5	32.8	29.1	23.4	0.8	0.9	0.8	0.8	0.8	0.5	0.4
2008	37	36.6	37.3	36.3	33.6	29.7	23.8	0.8	0.9	0.8	0.8	0.8	0.6	0.4
2009	37.8	37.4	38.1	37.1	34.4	30.2	24.1	0.8	0.8	0.8	0.8	0.8	0.5	0.3
2010	38.7	38.3	39	38	35.2	30.8	24.5	0.9	0.9	0.9	0.9	0.8	0.6	0.4
2011	39.5	39.2	39.7	38.8	35.9	31.3	24.8	0.8	0.9	0.7	0.8	0.7	0.5	0.3
2012	40.1	39.9	40.4	39.4	36.5	31.6	25	0.6	0.7	0.7	0.6	0.6	0.3	0.2
2013	40.9	40.7	41.1	40.2	37.2	32.1	25.3	0.8	0.8	0.7	0.8	0.7	0.5	0.3
2014	41.6	41.5	41.8	40.9	37.9	32.5	25.5	0.7	0.8	0.7	0.7	0.7	0.4	0.2
2015	42.4	42.3	42.6	41.7	38.6	33	25.8	0.8	0.8	0.8	0.8	0.7	0.5	0.3

S2.2.2 Sensitivity of model to aquifer unit storage parameters at Sandy Hook, NJ

Table ST2.2: Model sensitivity to storage parameters of aquifers. Sskv =0 for aquifers.

	Compaction (mm)							Compaction Rate (mm/yr)						
Year	Ss=1E-6, Sske=1E -6*b	Ss=1E-8, Sske=1E -8*b	s=1E-7, Sske=1E -7*b	Ss=5E-7, Sske=5E -7*b	Ss-5E-6, Sske=5E -6*b	Ss=1E-5, Sske=1E -5*b	Ss=1E-4, Sske=1E -4*b	Ss=1E-6, Sske=1E -6*b	Ss=1E-8, Sske=1E -8*b	s=1E-7, Sske=1E -7*b	Ss=5E-7, Sske=5E -7*b	Ss-5E-6, Sske=5E -6*b	Ss=1E-5, Sske=1E -5*b	Ss=1E-4, Sske=1E -4*b
1885	0	0	0	0	0	0	0	0	0	0	0	0	0	0
1886	0	0	0	0	0	0	0	0	0	0	0	0	0	0
1887	0.000679	0.00104	0.00105	0.00072	0.000512	0.000521	0.00056	0.000679	0.00104	0.00105	0.00072	0.000512	0.000521	0.00056
1888	0.00122	0.00178	0.00179	0.00137	0.00108	0.000909	0.000775	0.000541	0.00074	0.00074	0.00065	0.000568	0.000388	0.000215
1889	0.00171	0.00244	0.00238	0.00197	0.00149	0.00125	0.00102	0.00049	0.00066	0.00059	0.0006	0.00041	0.000341	0.000245
1890	0.00215	0.00295	0.0029	0.00241	0.00192	0.00166	0.00115	0.00044	0.00051	0.00052	0.00044	0.00043	0.00041	0.00013
1891	0.00243	0.00324	0.00313	0.00266	0.00222	0.00207	0.00133	0.00028	0.00029	0.00023	0.00025	0.0003	0.00041	0.00018
1892	0.0027	0.00352	0.0034	0.00306	0.00239	0.00235	0.00151	0.00027	0.00028	0.00027	0.0004	0.00017	0.00028	0.00018
1893	0.00297	0.0038	0.00369	0.00356	0.00275	0.00263	0.00174	0.00027	0.00028	0.00029	0.0005	0.00036	0.00028	0.00023
1894	0.00341	0.00427	0.00409	0.00375	0.00301	0.00288	0.00197	0.00044	0.00047	0.0004	0.00019	0.00026	0.00025	0.00023
1895	0.0037	0.0044	0.00437	0.00417	0.00323	0.00319	0.00221	0.00029	0.00013	0.00028	0.00042	0.00022	0.00031	0.00024
1896	0.0377	0.0374	0.0375	0.0374	0.0362	0.0364	0.0333	0.034	0.033	0.03313	0.03323	0.03297	0.03321	0.03109
1897	0.0725	0.0711	0.0714	0.0717	0.0647	0.0693	0.059	0.0348	0.0337	0.0339	0.0343	0.0285	0.0329	0.0257
1898	0.109	0.107	0.108	0.108	0.0945	0.103	0.0852	0.0365	0.0359	0.0366	0.0363	0.0298	0.0337	0.0262
1899	0.145	0.146	0.145	0.145	0.13	0.138	0.111	0.036	0.039	0.037	0.037	0.0355	0.035	0.0258
1900	0.217	0.217	0.217	0.216	0.202	0.208	0.175	0.072	0.071	0.072	0.071	0.072	0.07	0.064
1901	0.292	0.29	0.291	0.291	0.276	0.277	0.188	0.075	0.073	0.074	0.075	0.074	0.069	0.013
1902	0.369	0.364	0.365	0.369	0.352	0.349	0.248	0.077	0.074	0.074	0.078	0.076	0.072	0.06
1903	0.449	0.442	0.443	0.447	0.432	0.424	0.307	0.08	0.078	0.078	0.078	0.08	0.075	0.059
1904	0.528	0.522	0.522	0.526	0.499	0.501	0.367	0.079	0.08	0.079	0.079	0.067	0.077	0.06
1905	0.611	0.607	0.603	0.612	0.571	0.583	0.43	0.083	0.085	0.081	0.086	0.072	0.082	0.063

	Compaction (mm)							Compaction Rate (mm/yr)						
Year	Ss=1E-6, Sske=1E -6*b	Ss=1E-8, Sske=1E -8*b	s=1E-7, Sske=1E -7*b	Ss=5E-7, Sske=5E -7*b	Ss-5E-6, Sske=5E -6*b	Ss=1E-5, Sske=1E -5*b	Ss=1E-4, Sske=1E -4*b	Ss=1E-6, Sske=1E -6*b	Ss=1E-8, Sske=1E -8*b	s=1E-7, Sske=1E -7*b	Ss=5E-7, Sske=5E -7*b	Ss-5E-6, Sske=5E -6*b	Ss=1E-5, Sske=1E -5*b	Ss=1E-4, Sske=1E -4*b
1906	0.698	0.691	0.685	0.703	0.653	0.667	0.453	0.087	0.084	0.082	0.091	0.082	0.084	0.023
1907	0.752	0.759	0.749	0.766	0.667	0.633	-0.21	0.054	0.068	0.064	0.063	0.014	-0.034	-0.663
1908	0.822	0.824	0.814	0.833	0.729	0.69	-0.323	0.07	0.065	0.065	0.067	0.062	0.057	-0.113
1909	0.883	0.885	0.874	0.894	0.786	0.75	-0.342	0.061	0.061	0.06	0.061	0.057	0.06	-0.019
1910	0.944	0.943	0.936	0.957	0.844	0.807	-0.332	0.061	0.058	0.062	0.063	0.058	0.057	0.01
1911	1.02	1.02	1.01	1.04	0.918	0.875	-0.362	0.076	0.077	0.074	0.083	0.074	0.068	-0.03
1912	1.1	1.1	1.09	1.11	0.993	0.944	-0.332	0.08	0.08	0.08	0.07	0.075	0.069	0.03
1913	1.17	1.17	1.17	1.19	1.06	1.02	-0.296	0.07	0.07	0.08	0.08	0.067	0.076	0.036
1914	1.25	1.24	1.24	1.26	1.12	1.09	-0.249	0.08	0.07	0.07	0.07	0.06	0.07	0.047
1915	1.32	1.31	1.31	1.33	1.19	1.16	-0.23	0.07	0.07	0.07	0.07	0.07	0.07	0.019
1916	1.39	1.38	1.38	1.4	1.25	1.22	-0.179	0.07	0.07	0.07	0.07	0.06	0.06	0.051
1917	1.53	1.52	1.52	1.54	1.39	1.36	-0.0441	0.14	0.14	0.14	0.14	0.14	0.14	0.1349
1918	1.86	1.84	1.83	1.87	1.72	1.68	0.25	0.33	0.32	0.31	0.33	0.33	0.32	0.2941
1919	1.9	1.92	1.9	1.93	1.65	1.46	-1.98	0.04	0.08	0.07	0.06	-0.07	-0.22	-2.23
1920	1.98	1.99	1.98	2	1.72	1.53	-2.26	0.08	0.07	0.08	0.07	0.07	0.07	-0.28
1921	2.05	2.06	2.05	2.07	1.79	1.6	-2.28	0.07	0.07	0.07	0.07	0.07	0.07	-0.02
1922	2.12	2.13	2.12	2.14	1.86	1.67	-2.24	0.07	0.07	0.07	0.07	0.07	0.07	0.04
1923	2.18	2.2	2.18	2.21	1.93	1.74	-2.18	0.06	0.07	0.06	0.07	0.07	0.07	0.06
1924	2.25	2.26	2.25	2.27	1.99	1.8	-2.12	0.07	0.06	0.07	0.06	0.06	0.06	0.06
1925	2.31	2.33	2.31	2.34	2.06	1.87	-2.06	0.06	0.07	0.06	0.07	0.07	0.07	0.06
1926	2.37	2.39	2.37	2.4	2.12	1.93	-1.99	0.06	0.06	0.06	0.06	0.06	0.06	0.07
1927	2.44	2.45	2.43	2.46	2.18	2	-1.93	0.07	0.06	0.06	0.06	0.06	0.07	0.06
1928	2.5	2.51	2.5	2.52	2.24	2.06	-1.87	0.06	0.06	0.07	0.06	0.06	0.06	0.06
1929	2.56	2.57	2.56	2.58	2.31	2.13	-1.79	0.06	0.06	0.06	0.06	0.07	0.07	0.08
1930	2.57	2.59	2.58	2.59	2.29	2.08	-2.28	0.01	0.02	0.02	0.01	-0.02	-0.05	-0.49
1931	2.59	2.6	2.59	2.61	2.31	2.09	-2.33	0.02	0.01	0.01	0.02	0.02	0.01	-0.05
1932	2.6	2.62	2.6	2.62	2.32	2.11	-2.33	0.01	0.02	0.01	0.01	0.01	0.02	0

	Compaction (mm)							Compaction Rate (mm/yr)						
Year	Ss=1E-6, Sske=1E -6*b	Ss=1E-8, Sske=1E -8*b	s=1E-7, Sske=1E -7*b	Ss=5E-7, Sske=5E -7*b	Ss-5E-6, Sske=5E -6*b	Ss=1E-5, Sske=1E -5*b	Ss=1E-4, Sske=1E -4*b	Ss=1E-6, Sske=1E -6*b	Ss=1E-8, Sske=1E -8*b	s=1E-7, Sske=1E -7*b	Ss=5E-7, Sske=5E -7*b	Ss-5E-6, Sske=5E -6*b	Ss=1E-5, Sske=1E -5*b	Ss=1E-4, Sske=1E -4*b
1933	2.61	2.63	2.62	2.64	2.34	2.12	-2.33	0.01	0.01	0.02	0.02	0.02	0.01	0
1934	2.63	2.65	2.63	2.65	2.36	2.14	-2.31	0.02	0.02	0.01	0.01	0.02	0.02	0.02
1935	2.71	2.72	2.71	2.73	2.47	2.29	-1.63	0.08	0.07	0.08	0.08	0.11	0.15	0.68
1936	2.79	2.8	2.79	2.81	2.55	2.37	-1.43	0.08	0.08	0.08	0.08	0.08	0.08	0.2
1937	2.87	2.88	2.87	2.89	2.63	2.45	-1.3	0.08	0.08	0.08	0.08	0.08	0.08	0.13
1938	2.95	2.96	2.95	2.97	2.71	2.53	-1.2	0.08	0.08	0.08	0.08	0.08	0.08	0.1
1939	3.03	3.04	3.02	3.04	2.79	2.61	-1.11	0.08	0.08	0.07	0.07	0.08	0.08	0.09
1940	3.2	3.2	3.19	3.21	3	2.88	-0.082	0.17	0.16	0.17	0.17	0.21	0.27	1.028
1941	3.44	3.46	3.44	3.46	3.24	3.07	-0.0095	0.24	0.26	0.25	0.25	0.24	0.19	0.0725
1942	4.42	4.43	4.42	4.43	4.21	4.02	0.628	0.98	0.97	0.98	0.97	0.97	0.95	0.6375
1943	5.81	5.82	5.81	5.82	5.59	5.4	1.83	1.39	1.39	1.39	1.39	1.38	1.38	1.202
1944	7.27	7.29	7.26	7.27	7.05	6.86	3.21	1.46	1.47	1.45	1.45	1.46	1.46	1.38
1945	8.8	8.82	8.79	8.8	8.58	8.38	4.7	1.53	1.53	1.53	1.53	1.53	1.52	1.49
1946	9.2	9.39	9.35	9.28	8.3	7.27	-6.93	0.4	0.57	0.56	0.48	-0.28	-1.11	-11.63
1947	9.72	9.91	9.87	9.8	8.82	7.77	-9.27	0.52	0.52	0.52	0.52	0.52	0.5	-2.34
1948	10.2	10.4	10.3	10.3	9.29	8.25	-9.8	0.48	0.49	0.43	0.5	0.47	0.48	-0.53
1949	10.6	10.8	10.8	10.7	9.72	8.67	-9.78	0.4	0.4	0.5	0.4	0.43	0.42	0.02
1950	11	11.2	11.2	11.1	10.1	9.06	-9.58	0.4	0.4	0.4	0.4	0.38	0.39	0.2
1951	11.3	11.5	11.5	11.4	10.4	9.4	-9.32	0.3	0.3	0.3	0.3	0.3	0.34	0.26
1952	11.7	11.8	11.8	11.7	10.8	9.72	-9.05	0.4	0.3	0.3	0.3	0.4	0.32	0.27
1953	11.9	12.1	12.1	12	11	10	-8.8	0.2	0.3	0.3	0.3	0.2	0.28	0.25
1954	12.2	12.4	12.4	12.3	11.3	10.3	-8.55	0.3	0.3	0.3	0.3	0.3	0.3	0.25
1955	12.4	12.6	12.6	12.5	11.5	10.5	-8.32	0.2	0.2	0.2	0.2	0.2	0.2	0.23
1956	12.6	12.8	12.8	12.7	11.8	10.7	-8.09	0.2	0.2	0.2	0.2	0.3	0.2	0.23
1957	12.8	13	13	12.9	11.9	10.9	-7.86	0.2	0.2	0.2	0.2	0.1	0.2	0.23
1958	13	13.2	13.2	13.1	12.1	11.1	-7.64	0.2	0.2	0.2	0.2	0.2	0.2	0.22

	Compaction (mm)							Compaction Rate (mm/yr)						
Year	Ss=1E-6, Sske=1E -6*b	Ss=1E-8, Sske=1E -8*b	s=1E-7, Sske=1E -7*b	Ss=5E-7, Sske=5E -7*b	Ss-5E-6, Sske=5E -6*b	Ss=1E-5, Sske=1E -5*b	Ss=1E-4, Sske=1E -4*b	Ss=1E-6, Sske=1E -6*b	Ss=1E-8, Sske=1E -8*b	s=1E-7, Sske=1E -7*b	Ss=5E-7, Sske=5E -7*b	Ss-5E-6, Sske=5E -6*b	Ss=1E-5, Sske=1E -5*b	Ss=1E-4, Sske=1E -4*b
1959	13.2	13.4	13.3	13.3	12.3	11.3	-7.44	0.2	0.2	0.1	0.2	0.2	0.2	0.2
1960	13.3	13.5	13.5	13.4	12.4	11.4	-7.25	0.1	0.1	0.2	0.1	0.1	0.1	0.19
1961	13.5	13.6	13.6	13.5	12.6	11.6	-7.08	0.2	0.1	0.1	0.1	0.2	0.2	0.17
1962	13.6	13.8	13.8	13.7	12.7	11.7	-6.92	0.1	0.2	0.2	0.2	0.1	0.1	0.16
1963	13.7	13.9	13.9	13.8	12.8	11.8	-6.79	0.1	0.1	0.1	0.1	0.1	0.1	0.13
1964	13.8	14	14	13.9	12.9	11.9	-6.92	0.1	0.1	0.1	0.1	0.1	0.1	-0.13
1965	13.9	14.1	14.1	14	13	12	-6.86	0.1	0.1	0.1	0.1	0.1	0.1	0.06
1966	14	14.2	14.2	14.1	13.1	12.1	-6.75	0.1	0.1	0.1	0.1	0.1	0.1	0.11
1967	14.1	14.3	14.2	14.1	13.2	12.1	-6.62	0.1	0.1	0	0	0.1	0	0.13
1968	14.2	14.3	14.3	14.2	13.3	12.2	-6.47	0.1	0	0.1	0.1	0.1	0.1	0.15
1969	14.2	14.4	14.4	14.3	13.4	12.3	-6.28	0	0.1	0.1	0.1	0.1	0.1	0.19
1970	14.3	14.5	14.5	14.4	13.5	12.4	-6.07	0.1	0.1	0.1	0.1	0.1	0.1	0.21
1971	14.5	14.6	14.6	14.5	13.6	12.6	-5.81	0.2	0.1	0.1	0.1	0.1	0.2	0.26
1972	14.6	14.8	14.8	14.7	13.7	12.7	-5.5	0.1	0.2	0.2	0.2	0.1	0.1	0.31
1973	14.7	14.9	14.9	14.8	13.9	12.9	-5.18	0.1	0.1	0.1	0.1	0.2	0.2	0.32
1974	15.1	15.2	15.2	15.1	14.3	13.4	-3.16	0.4	0.3	0.3	0.3	0.4	0.5	2.02
1975	15.5	15.7	15.7	15.6	14.8	13.9	-2.12	0.4	0.5	0.5	0.5	0.5	0.5	1.04
1976	16.1	16.2	16.2	16.1	15.3	14.5	-1.52	0.6	0.5	0.5	0.5	0.5	0.6	0.6
1977	16.6	16.7	16.7	16.7	15.9	15	-0.764	0.5	0.5	0.5	0.6	0.6	0.5	0.756
1978	17.1	17.3	17.2	17.2	16.4	15.5	-0.0466	0.5	0.6	0.5	0.5	0.5	0.5	0.7174
1979	17.6	17.8	17.8	17.7	16.9	16.1	0.612	0.5	0.5	0.6	0.5	0.5	0.6	0.6586
1980	18.3	18.4	18.4	18.3	17.6	16.8	1.79	0.7	0.6	0.6	0.6	0.7	0.7	1.178
1981	18.9	19	19	18.9	18.2	17.4	2.97	0.6	0.6	0.6	0.6	0.6	0.6	1.18
1982	19.5	19.6	19.6	19.6	18.9	18.1	3.96	0.6	0.6	0.6	0.7	0.7	0.7	0.99
1983	20.2	20.3	20.3	20.2	19.5	18.8	4.85	0.7	0.7	0.7	0.6	0.6	0.7	0.89
1984	20.7	20.9	20.9	20.8	20.1	19.3	4.93	0.5	0.6	0.6	0.6	0.6	0.5	0.08

	Compaction (mm)							Compaction Rate (mm/yr)						
Year	Ss=1E-6, Sske=1E -6*b	Ss=1E-8, Sske=1E -8*b	s=1E-7, Sske=1E -7*b	Ss=5E-7, Sske=5E -7*b	Ss-5E-6, Sske=5E -6*b	Ss=1E-5, Sske=1E -5*b	Ss=1E-4, Sske=1E -4*b	Ss=1E-6, Sske=1E -6*b	Ss=1E-8, Sske=1E -8*b	s=1E-7, Sske=1E -7*b	Ss=5E-7, Sske=5E -7*b	Ss-5E-6, Sske=5E -6*b	Ss=1E-5, Sske=1E -5*b	Ss=1E-4, Sske=1E -4*b
1985	21.5	21.6	21.6	21.5	20.8	20	6.04	0.8	0.7	0.7	0.7	0.7	0.7	1.11
1986	22.3	22.4	22.4	22.3	21.6	20.9	7.22	0.8	0.8	0.8	0.8	0.8	0.9	1.18
1987	23.1	23.2	23.2	23.1	22.4	21.7	8.2	0.8	0.8	0.8	0.8	0.8	0.8	0.98
1988	23.8	23.9	23.9	23.8	23.1	22.2	7.76	0.7	0.7	0.7	0.7	0.7	0.5	-0.44
1989	24.5	24.6	24.6	24.5	23.7	22.9	8.42	0.7	0.7	0.7	0.7	0.6	0.7	0.66
1990	24.9	25.1	25.1	25	24.1	23.1	7.31	0.4	0.5	0.5	0.5	0.4	0.2	-1.11
1991	25.6	25.8	25.7	25.7	24.9	24	8.03	0.7	0.7	0.6	0.7	0.8	0.9	0.72
1992	26.2	26.3	26.3	26.2	25.3	24.4	7.93	0.6	0.5	0.6	0.5	0.4	0.4	-0.1
1993	26.8	26.9	26.9	26.8	26	25.1	8.49	0.6	0.6	0.6	0.6	0.7	0.7	0.56
1994	27.3	27.4	27.4	27.3	26.5	25.5	8.56	0.5	0.5	0.5	0.5	0.5	0.4	0.07
1995	27.9	28	28	27.9	27.1	26.2	9.88	0.6	0.6	0.6	0.6	0.6	0.7	1.32
1996	28.4	28.6	28.6	28.5	27.6	26.7	10.2	0.5	0.6	0.6	0.6	0.5	0.5	0.32
1997	29	29.2	29.2	29.1	28.2	27.3	10.6	0.6	0.6	0.6	0.6	0.6	0.6	0.4
1998	29.6	29.8	29.8	29.7	28.9	28	11.4	0.6	0.6	0.6	0.6	0.7	0.7	0.8
1999	30.3	30.4	30.4	30.3	29.5	28.6	12.2	0.7	0.6	0.6	0.6	0.6	0.6	0.8
2000	30.9	N/A	N/A	31	30.2	29.3	13.3	0.6	N/A	N/A	0.7	0.7	0.7	1.1
2001	31.6	N/A	N/A	31.7	31	30.2	14.8	0.7	N/A	N/A	0.7	0.8	0.9	1.5
2002	32.4	N/A	N/A	32.4	31.7	30.9	15.9	0.8	N/A	N/A	0.7	0.7	0.7	1.1
2003	33.1	N/A	N/A	33.1	32.4	31.6	16.8	0.7	N/A	N/A	0.7	0.7	0.7	0.9
2004	33.8	N/A	N/A	33.9	33.2	32.4	17.9	0.7	N/A	N/A	0.8	0.8	0.8	1.1
2005	34.6	N/A	N/A	34.6	34	33.2	19.1	0.8	N/A	N/A	0.7	0.8	0.8	1.2
2006	35.4	N/A	N/A	35.4	34.7	34	20.2	0.8	N/A	N/A	0.8	0.7	0.8	1.1
2007	36.2	N/A	N/A	36.2	35.6	34.8	21.2	0.8	N/A	N/A	0.8	0.9	0.8	1
2008	37	N/A	N/A	37.1	36.4	35.7	22.1	0.8	N/A	N/A	0.9	0.8	0.9	0.9
2009	37.8	N/A	N/A	37.9	37.2	36.4	22.7	0.8	N/A	N/A	0.8	0.8	0.7	0.6
2010	38.7	N/A	N/A	38.7	38.1	37.3	23.5	0.9	N/A	N/A	0.8	0.9	0.9	0.8

	Compaction (mm)							Compaction Rate (mm/yr)						
Year	Ss=1E-6, Sske=1E -6*b	Ss=1E-8, Sske=1E -8*b	s=1E-7, Sske=1E -7*b	Ss=5E-7, Sske=5E -7*b	Ss-5E-6, Sske=5E -6*b	Ss=1E-5, Sske=1E -5*b	Ss=1E-4, Sske=1E -4*b	Ss=1E-6, Sske=1E -6*b	Ss=1E-8, Sske=1E -8*b	s=1E-7, Sske=1E -7*b	Ss=5E-7, Sske=5E -7*b	Ss-5E-6, Sske=5E -6*b	Ss=1E-5, Sske=1E -5*b	Ss=1E-4, Sske=1E -4*b
2011	39.5	N/A	N/A	39.5	38.8	38	23.8	0.8	N/A	N/A	0.8	0.7	0.7	0.3
2012	40.1	N/A	N/A	40.2	39.4	38.5	23.3	0.6	N/A	N/A	0.7	0.6	0.5	-0.5
2013	40.9	N/A	N/A	40.9	40.2	39.3	24.4	0.8	N/A	N/A	0.7	0.8	0.8	1.1
2014	41.6	N/A	N/A	41.7	40.9	40.1	25.2	0.7	N/A	N/A	0.8	0.7	0.8	0.8
2015	42.4	N/A	N/A	42.5	41.8	41	26.3	0.8	N/A	N/A	0.8	0.9	0.9	1.1

S2.2.3 Sensitivity of Model to the Magnitude of Local Pumping at Sandy Hook

Table ST2.3: Model sensitivity at the Sandy Hook tide gauge to the local rate of pumping at Sandy Hook. Pumping rates for civilian and military use are in m^3/d per person.

Total Subsidence (mm)					Subsidence Rate (mm/yr)				
Mil=0.946 Civ=0.189	Mil=0.095 Civ=0.019	Mil=0.473 Civ=0.095	Mil=1.420 Civ=0.284	Mil=1.703 Civ=0.341	Mil=0.946 Civ=0.189	Mil=0.095 Civ=0.019	Mil=0.473 Civ=0.095	Mil=1.420 Civ=0.284	Mil=1.703 Civ=0.341
0	0	0	0	0	0	0	0	0	0
0	0	0	0	0	0	0	0	0	0
0.000679	0.000679	0.000679	0.0000736	0.000679	0.000679	0.000679	0.000679	0.0000736	0.000679
0.00122	0.00122	0.00122	0.000234	0.00122	0.000541	0.000541	0.000541	0.0001604	0.000541
0.00171	0.00171	0.00171	0.000321	0.00171	0.00049	0.00049	0.00049	0.000087	0.00049
0.00215	0.00215	0.00215	0.000529	0.00215	0.00044	0.00044	0.00044	0.000208	0.00044
0.00243	0.00243	0.00243	0.000657	0.00243	0.00028	0.00028	0.00028	0.000128	0.00028
0.0027	0.0027	0.0027	0.000771	0.0027	0.00027	0.00027	0.00027	0.000114	0.00027
0.00297	0.00297	0.00297	0.000851	0.00297	0.00027	0.00027	0.00027	0.00008	0.00027
0.00341	0.00341	0.00341	0.000871	0.00341	0.00044	0.00044	0.00044	2E-05	0.00044
0.0037	0.0037	0.0037	0.000876	0.0037	0.00029	0.00029	0.00029	5E-06	0.00029
0.0377	0.00778	0.0208	0.0337	0.0647	0.034	0.00408	0.0171	0.032824	0.061

Total Subsidence (mm)					Subsidence Rate (mm/yr)				
Mil=0.946 Civ=0.189	Mil=0.095 Civ=0.019	Mil=0.473 Civ=0.095	Mil=1.420 Civ=0.284	Mil=1.703 Civ=0.341	Mil=0.946 Civ=0.189	Mil=0.095 Civ=0.019	Mil=0.473 Civ=0.095	Mil=1.420 Civ=0.284	Mil=1.703 Civ=0.341
0.0725	0.0114	0.0382	0.0678	0.126	0.0348	0.00362	0.0174	0.0341	0.0613
0.109	0.0153	0.0566	0.112	0.19	0.0365	0.0039	0.0184	0.0442	0.064
0.145	0.0194	0.0752	0.161	0.258	0.036	0.0041	0.0186	0.049	0.068
0.217	0.0271	0.111	0.228	0.386	0.072	0.0077	0.0358	0.067	0.128
0.292	0.035	0.148	0.319	0.522	0.075	0.0079	0.037	0.091	0.136
0.369	0.0426	0.187	0.393	0.661	0.077	0.0076	0.039	0.074	0.139
0.449	0.0508	0.227	0.47	0.802	0.08	0.0082	0.04	0.077	0.141
0.528	0.0591	0.267	0.55	0.955	0.079	0.0083	0.04	0.08	0.153
0.611	0.0677	0.31	0.627	1.11	0.083	0.0086	0.043	0.077	0.155
0.698	0.0764	0.353	0.736	1.26	0.087	0.0087	0.043	0.109	0.15
0.752	0.0815	0.38	0.783	1.36	0.054	0.0051	0.027	0.047	0.1
0.822	0.0891	0.415	0.853	1.48	0.07	0.0076	0.035	0.07	0.12
0.883	0.0965	0.448	0.924	1.6	0.061	0.0074	0.033	0.071	0.12
0.944	0.103	0.477	0.986	1.7	0.061	0.0065	0.029	0.062	0.1
1.02	0.113	0.516	1.06	1.84	0.076	0.01	0.039	0.074	0.14
1.1	0.12	0.554	1.14	1.99	0.08	0.007	0.038	0.08	0.15
1.17	0.129	0.592	1.24	2.13	0.07	0.009	0.038	0.1	0.14
1.25	0.139	0.63	1.33	2.25	0.08	0.01	0.038	0.09	0.12
1.32	0.145	0.667	1.42	2.38	0.07	0.006	0.037	0.09	0.13
1.39	0.153	0.702	1.49	2.5	0.07	0.008	0.035	0.07	0.12
1.53	0.17	0.769	1.63	2.73	0.14	0.017	0.067	0.14	0.23
1.86	0.201	0.931	2.13	3.32	0.33	0.031	0.162	0.5	0.59
1.9	0.206	0.959	2.2	3.4	0.04	0.005	0.028	0.07	0.08
1.98	0.213	0.998	2.31	3.53	0.08	0.007	0.039	0.11	0.13
2.05	0.223	1.03	2.43	3.66	0.07	0.01	0.032	0.12	0.13
2.12	0.231	1.07	2.54	3.78	0.07	0.008	0.04	0.11	0.12
2.18	0.239	1.1	2.64	3.9	0.06	0.008	0.03	0.1	0.12

Total Subsidence (mm)					Subsidence Rate (mm/yr)				
Mil=0.946 Civ=0.189	Mil=0.095 Civ=0.019	Mil=0.473 Civ=0.095	Mil=1.420 Civ=0.284	Mil=1.703 Civ=0.341	Mil=0.946 Civ=0.189	Mil=0.095 Civ=0.019	Mil=0.473 Civ=0.095	Mil=1.420 Civ=0.284	Mil=1.703 Civ=0.341
2.25	0.245	1.14	2.74	4.01	0.07	0.006	0.04	0.1	0.11
2.31	0.251	1.17	2.84	4.13	0.06	0.006	0.03	0.1	0.12
2.37	0.26	1.2	2.94	4.24	0.06	0.009	0.03	0.1	0.11
2.44	0.265	1.23	3.03	4.35	0.07	0.005	0.03	0.09	0.11
2.5	0.269	1.26	3.12	4.46	0.06	0.004	0.03	0.09	0.11
2.56	0.282	1.3	3.23	4.58	0.06	0.013	0.04	0.11	0.12
2.57	0.287	1.31	3.24	4.59	0.01	0.005	0.01	0.01	0.01
2.59	0.295	1.32	3.26	4.61	0.02	0.008	0.01	0.02	0.02
2.6	0.304	1.33	3.28	4.63	0.01	0.009	0.01	0.02	0.02
2.61	0.314	1.34	3.3	4.64	0.01	0.01	0.01	0.02	0.01
2.63	0.324	1.36	3.33	4.66	0.02	0.01	0.02	0.03	0.02
2.71	0.345	1.4	3.45	4.81	0.08	0.021	0.04	0.12	0.15
2.79	0.366	1.45	3.56	4.94	0.08	0.021	0.05	0.11	0.13
2.87	0.387	1.5	3.68	5.06	0.08	0.021	0.05	0.12	0.12
2.95	0.409	1.54	3.79	5.19	0.08	0.022	0.04	0.11	0.13
3.03	0.428	1.59	3.9	5.32	0.08	0.019	0.05	0.11	0.13
3.2	0.459	1.68	4.16	5.62	0.17	0.031	0.09	0.26	0.3
3.44	0.497	1.82	4.66	6.05	0.24	0.038	0.14	0.5	0.43
4.42	0.607	2.31	6.11	7.79	0.98	0.11	0.49	1.45	1.74
5.81	0.759	3.01	8.19	10.3	1.39	0.152	0.7	2.08	2.51
7.27	0.918	3.74	10.4	12.9	1.46	0.159	0.73	2.21	2.6
8.8	1.08	4.52	12.6	15.6	1.53	0.162	0.78	2.2	2.7
9.2	1.14	4.73	13.2	16.3	0.4	0.06	0.21	0.6	0.7
9.72	1.21	5	14	17.2	0.52	0.07	0.27	0.8	0.9
10.2	1.27	5.25	14.7	18.1	0.48	0.06	0.25	0.7	0.9
10.6	1.33	5.47	15.4	18.8	0.4	0.06	0.22	0.7	0.7
11	1.38	5.67	15.9	19.5	0.4	0.05	0.2	0.5	0.7

Total Subsidence (mm)					Subsidence Rate (mm/yr)				
Mil=0.946 Civ=0.189	Mil=0.095 Civ=0.019	Mil=0.473 Civ=0.095	Mil=1.420 Civ=0.284	Mil=1.703 Civ=0.341	Mil=0.946 Civ=0.189	Mil=0.095 Civ=0.019	Mil=0.473 Civ=0.095	Mil=1.420 Civ=0.284	Mil=1.703 Civ=0.341
11.3	1.43	5.84	16.5	20.1	0.3	0.05	0.17	0.6	0.6
11.7	1.47	6.01	16.9	20.7	0.4	0.04	0.17	0.4	0.6
11.9	1.51	6.15	17.4	21.2	0.2	0.04	0.14	0.5	0.5
12.2	1.54	6.29	17.7	21.6	0.3	0.03	0.14	0.3	0.4
12.4	1.57	6.41	18.1	22	0.2	0.03	0.12	0.4	0.4
12.6	1.61	6.52	18.4	22.4	0.2	0.04	0.11	0.3	0.4
12.8	1.65	6.63	18.7	22.7	0.2	0.04	0.11	0.3	0.3
13	1.68	6.73	19	23	0.2	0.03	0.1	0.3	0.3
13.2	1.72	6.83	19.2	23.3	0.2	0.04	0.1	0.2	0.3
13.3	1.76	6.91	19.5	23.6	0.1	0.04	0.08	0.3	0.3
13.5	1.79	7	19.7	23.8	0.2	0.03	0.09	0.2	0.2
13.6	1.83	7.07	19.8	24	0.1	0.04	0.07	0.1	0.2
13.7	1.87	7.15	20	24.2	0.1	0.04	0.08	0.2	0.2
13.8	1.91	7.21	20.2	24.3	0.1	0.04	0.06	0.2	0.1
13.9	1.96	7.28	20.3	24.5	0.1	0.05	0.07	0.1	0.2
14	2	7.34	20.4	24.6	0.1	0.04	0.06	0.1	0.1
14.1	2.06	7.41	20.5	24.7	0.1	0.06	0.07	0.1	0.1
14.2	2.11	7.48	20.6	24.8	0.1	0.05	0.07	0.1	0.1
14.2	2.18	7.56	20.7	25	0	0.07	0.08	0.1	0.2
14.3	2.26	7.64	20.9	25.1	0.1	0.08	0.08	0.2	0.1
14.5	2.36	7.73	21	25.2	0.2	0.1	0.09	0.1	0.1
14.6	2.47	7.85	21.2	25.4	0.1	0.11	0.12	0.2	0.2
14.7	2.59	7.97	21.3	25.6	0.1	0.12	0.12	0.1	0.2
15.1	2.75	8.19	21.8	26	0.4	0.16	0.22	0.5	0.4
15.5	2.92	8.48	22.4	26.8	0.4	0.17	0.29	0.6	0.8
16.1	3.14	8.83	23.2	27.6	0.6	0.22	0.35	0.8	0.8
16.6	3.37	9.19	23.9	28.5	0.5	0.23	0.36	0.7	0.9

Total Subsidence (mm)					Subsidence Rate (mm/yr)				
Mil=0.946 Civ=0.189	Mil=0.095 Civ=0.019	Mil=0.473 Civ=0.095	Mil=1.420 Civ=0.284	Mil=1.703 Civ=0.341	Mil=0.946 Civ=0.189	Mil=0.095 Civ=0.019	Mil=0.473 Civ=0.095	Mil=1.420 Civ=0.284	Mil=1.703 Civ=0.341
17.1	3.6	9.53	24.6	29.3	0.5	0.23	0.34	0.7	0.8
17.6	3.88	9.9	25.4	30.1	0.5	0.28	0.37	0.8	0.8
18.3	4.29	10.3	26.2	31	0.7	0.41	0.4	0.8	0.9
18.9	4.73	10.8	27	31.9	0.6	0.44	0.5	0.8	0.9
19.5	5.21	11.3	27.9	32.9	0.6	0.48	0.5	0.9	1
20.2	5.7	11.9	28.8	33.9	0.7	0.49	0.6	0.9	1
20.7	6.25	12.4	29.5	34.7	0.5	0.55	0.5	0.7	0.8
21.5	6.81	13	30.4	35.7	0.8	0.56	0.6	0.9	1
22.3	7.4	13.6	31.3	36.6	0.8	0.59	0.6	0.9	0.9
23.1	8	14.2	32.2	37.6	0.8	0.6	0.6	0.9	1
23.8	8.61	14.8	32.9	38.4	0.7	0.61	0.6	0.7	0.8
24.5	9.17	15.4	33.8	39.2	0.7	0.56	0.6	0.9	0.8
24.9	9.49	15.8	34.4	39.7	0.4	0.32	0.4	0.6	0.5
25.6	9.97	16.4	35.2	40.5	0.7	0.48	0.6	0.8	0.8
26.2	10.4	16.8	35.8	41.1	0.6	0.43	0.4	0.6	0.6
26.8	10.8	17.4	36.6	41.8	0.6	0.4	0.6	0.8	0.7
27.3	11.2	17.8	37.2	42.4	0.5	0.4	0.4	0.6	0.6
27.9	11.7	18.4	37.9	43.2	0.6	0.5	0.6	0.7	0.8
28.4	12	18.8	38.6	43.9	0.5	0.3	0.4	0.7	0.7
29	12.4	19.3	39.3	44.6	0.6	0.4	0.5	0.7	0.7
29.6	12.9	19.8	40	45.4	0.6	0.5	0.5	0.7	0.8
30.3	13.3	20.3	40.8	46.2	0.7	0.4	0.5	0.8	0.8
30.9	13.7	20.8	41.6	47	0.6	0.4	0.5	0.8	0.8
31.6	14.2	21.4	42.5	48	0.7	0.5	0.6	0.9	1
32.4	14.7	22	43.4	49	0.8	0.5	0.6	0.9	1
33.1	15.1	22.6	44.3	49.9	0.7	0.4	0.6	0.9	0.9
33.8	15.7	23.2	45.2	50.8	0.7	0.6	0.6	0.9	0.9

Total Subsidence (mm)					Subsidence Rate (mm/yr)				
Mil=0.946 Civ=0.189	Mil=0.095 Civ=0.019	Mil=0.473 Civ=0.095	Mil=1.420 Civ=0.284	Mil=1.703 Civ=0.341	Mil=0.946 Civ=0.189	Mil=0.095 Civ=0.019	Mil=0.473 Civ=0.095	Mil=1.420 Civ=0.284	Mil=1.703 Civ=0.341
34.6	16.3	23.8	46.1	51.8	0.8	0.6	0.6	0.9	1
35.4	16.9	24.5	47.1	52.8	0.8	0.6	0.7	1	1
36.2	17.6	25.3	48	53.9	0.8	0.7	0.8	0.9	1.1
37	18.2	26.1	49.1	54.9	0.8	0.6	0.8	1.1	1
37.8	18.8	26.8	50.1	56	0.8	0.6	0.7	1	1.1
38.7	19.4	27.5	51.1	57.1	0.9	0.6	0.7	1	1.1
39.5	20	28.2	52	58	0.8	0.6	0.7	0.9	0.9
40.1	20.6	28.8	52.8	58.8	0.6	0.6	0.6	0.8	0.8
40.9	21.3	29.5	53.6	59.7	0.8	0.7	0.7	0.8	0.9
41.6	21.9	30.2	54.5	60.5	0.7	0.6	0.7	0.9	0.8
42.4	22.6	31	55.4	61.5	0.8	0.7	0.8	0.9	1

S2.2.4 Effects of Regional vs. Local Pumping at Sandy Hook, NJ

Table ST2.4: Model results of regional vs. local pumping tests at Sandy Hook

	Compaction (mm)			Compaction Rate (mm/yr)		
Year	Local Wells Only	Regional Wells Only	All Wells	Local Wells Only	Regional Wells Only	All Wells
1885	0	0	0	0	0	0
1886	0	0	0	0	0	0
1887	0.000679	0.0000736	0.0000736	0.000679	0.0000736	0.0000736
1888	0.00122	0.000234	0.000234	0.000541	0.0001604	0.0001604
1889	0.00171	0.000321	0.000321	0.00049	0.000087	0.000087
1890	0.00215	0.000529	0.000529	0.00044	0.000208	0.000208
1891	0.00243	0.000657	0.000657	0.00028	0.000128	0.000128
1892	0.0027	0.000771	0.000771	0.00027	0.000114	0.000114
1893	0.00297	0.000851	0.000851	0.00027	0.00008	0.00008
1894	0.00341	0.000871	0.000871	0.00044	2E-05	2E-05
1895	0.0037	0.000876	0.000876	0.00029	5E-06	5E-06
1896	0.0377	0.000882	0.0216	0.034	6E-06	0.020724
1897	0.0725	0.000882	0.0516	0.0348	0	0.03
1898	0.109	0.000882	0.0753	0.0365	0	0.0237
1899	0.145	0.000882	0.107	0.036	0	0.0317
1900	0.217	0.000882	0.153	0.072	0	0.046
1901	0.292	0.000882	0.214	0.075	0	0.061
1902	0.369	0.000882	0.277	0.077	0	0.063
1903	0.449	0.000882	0.346	0.08	0	0.069
1904	0.528	0.000882	0.415	0.079	0	0.069
1905	0.611	0.000882	0.484	0.083	0	0.069
1906	0.698	0.000882	0.556	0.087	0	0.072
1907	0.752	0.000882	0.587	0.054	0	0.031
1908	0.822	0.000882	0.641	0.07	0	0.054
1909	0.883	0.000882	0.69	0.061	0	0.049
1910	0.944	0.000882	0.738	0.061	0	0.048
1911	1.02	0.000882	0.786	0.076	0	0.048
1912	1.1	0.000882	0.854	0.08	0	0.068
1913	1.17	0.000882	0.923	0.07	0	0.069
1914	1.25	0.000882	0.992	0.08	0	0.069
1915	1.32	0.000882	1.06	0.07	0	0.068
1916	1.39	0.000882	1.12	0.07	0	0.06
1917	1.53	0.000882	1.21	0.14	0	0.09
1918	1.86	0.00123	1.41	0.33	0.000348	0.2
1919	1.9	0.00134	1.42	0.04	0.00011	0.01
1920	1.98	0.0014	1.48	0.08	6E-05	0.06
1921	2.05	0.00142	1.52	0.07	2E-05	0.04
1922	2.12	0.00142	1.56	0.07	0	0.04
1923	2.18	0.00142	1.61	0.06	0	0.05
1924	2.25	0.00142	1.66	0.07	0	0.05
1925	2.31	0.00142	1.71	0.06	0	0.05
1926	2.37	0.00143	1.76	0.06	0.00001	0.05
1927	2.44	0.00143	1.8	0.07	0	0.04
1928	2.5	0.00143	1.84	0.06	0	0.04
1929	2.56	0.00825	1.87	0.06	0.00682	0.03
1930	2.57	0.0159	1.87	0.01	0.00765	0
1931	2.59	0.0211	1.88	0.02	0.0052	0.01
1932	2.6	0.029	1.89	0.01	0.0079	0.01
1933	2.61	0.0378	1.9	0.01	0.0088	0.01
1934	2.63	0.0477	1.9	0.02	0.0099	0
1935	2.71	0.0614	1.94	0.08	0.0137	0.04
1936	2.79	0.0789	1.99	0.08	0.0175	0.05
1937	2.87	0.0954	2.03	0.08	0.0165	0.04
1938	2.95	0.111	2.07	0.08	0.0156	0.04
1939	3.03	0.127	2.11	0.08	0.016	0.04
1940	3.2	0.142	2.2	0.17	0.015	0.09

	Compaction (mm)			Compaction Rate (mm/yr)		
Year	Local Wells Only	Regional Wells Only	All Wells	Local Wells Only	Regional Wells Only	All Wells
1941	3.44	0.157	2.38	0.24	0.015	0.18
1942	4.42	0.172	3.12	0.98	0.015	0.74
1943	5.81	0.187	4.23	1.39	0.015	1.11
1944	7.27	0.202	5.4	1.46	0.015	1.17
1945	8.8	0.218	6.62	1.53	0.016	1.22
1946	9.2	0.236	6.77	0.4	0.018	0.15
1947	9.72	0.257	7.07	0.52	0.021	0.3
1948	10.2	0.279	7.35	0.48	0.022	0.28
1949	10.6	0.295	7.61	0.4	0.016	0.26
1950	11	0.307	7.83	0.4	0.012	0.22
1951	11.3	0.321	8.07	0.3	0.014	0.24
1952	11.7	0.333	8.25	0.4	0.012	0.18
1953	11.9	0.344	8.42	0.2	0.011	0.17
1954	12.2	0.356	8.61	0.3	0.012	0.19
1955	12.4	0.365	8.76	0.2	0.009	0.15
1956	12.6	0.39	8.9	0.2	0.025	0.14
1957	12.8	0.418	9.05	0.2	0.028	0.15
1958	13	0.444	9.19	0.2	0.026	0.14
1959	13.2	0.473	9.34	0.2	0.029	0.15
1960	13.3	0.504	9.5	0.1	0.031	0.16
1961	13.5	0.538	9.59	0.2	0.034	0.09
1962	13.6	0.574	9.73	0.1	0.036	0.14
1963	13.7	0.612	9.85	0.1	0.038	0.12
1964	13.8	0.655	9.94	0.1	0.043	0.09
1965	13.9	0.698	10	0.1	0.043	0.06
1966	14	0.75	10.1	0.1	0.052	0.1
1967	14.1	0.809	10.2	0.1	0.059	0.1
1968	14.2	0.877	10.3	0.1	0.068	0.1
1969	14.2	0.96	10.4	0	0.083	0.1
1970	14.3	1.05	10.4	0.1	0.09	0
1971	14.5	1.16	10.5	0.2	0.11	0.1
1972	14.6	1.28	10.5	0.1	0.12	0
1973	14.7	1.42	10.6	0.1	0.14	0.1
1974	15.1	1.57	10.8	0.4	0.15	0.2
1975	15.5	1.73	11	0.4	0.16	0.2
1976	16.1	1.95	11.3	0.6	0.22	0.3
1977	16.6	2.21	11.6	0.5	0.26	0.3
1978	17.1	2.44	11.9	0.5	0.23	0.3
1979	17.6	2.7	12.1	0.5	0.26	0.2
1980	18.3	3.09	12.4	0.7	0.39	0.3
1981	18.9	3.5	12.6	0.6	0.41	0.2
1982	19.5	3.97	12.9	0.6	0.47	0.3
1983	20.2	4.43	13.2	0.7	0.46	0.3
1984	20.7	4.97	13.4	0.5	0.54	0.2
1985	21.5	5.52	13.6	0.8	0.55	0.2
1986	22.3	6.1	13.9	0.8	0.58	0.3
1987	23.1	6.69	14.2	0.8	0.59	0.3
1988	23.8	7.3	14.3	0.7	0.61	0.1
1989	24.5	7.86	14.5	0.7	0.56	0.2
1990	24.9	8.18	14.6	0.4	0.32	0.1
1991	25.6	8.66	14.8	0.7	0.48	0.2
1992	26.2	9.04	14.9	0.6	0.38	0.1
1993	26.8	9.49	15.1	0.6	0.45	0.2
1994	27.3	9.93	15.2	0.5	0.44	0.1
1995	27.9	10.4	15.4	0.6	0.47	0.2
1996	28.4	10.7	15.5	0.5	0.3	0.1
1997	29	11.1	15.7	0.6	0.4	0.2
1998	29.6	11.6	15.8	0.6	0.5	0.1
1999	30.3	12	16	0.7	0.4	0.2
2000	30.9	12.4	16.2	0.6	0.4	0.2
2001	31.6	12.9	16.4	0.7	0.5	0.2
2002	32.4	13.3	16.7	0.8	0.4	0.3
2003	33.1	13.8	16.9	0.7	0.5	0.2
2004	33.8	14.4	17.1	0.7	0.6	0.2

	Compaction (mm)			Compaction Rate (mm/yr)		
Year	Local Wells Only	Regional Wells Only	All Wells	Local Wells Only	Regional Wells Only	All Wells
2005	34.6	15	17.3	0.8	0.6	0.2
2006	35.4	15.6	17.5	0.8	0.6	0.2
2007	36.2	16.2	17.7	0.8	0.6	0.2
2008	37	16.9	17.9	0.8	0.7	0.2
2009	37.8	17.5	18.2	0.8	0.6	0.3
2010	38.7	18.1	18.4	0.9	0.6	0.2
2011	39.5	18.7	18.5	0.8	0.6	0.1
2012	40.1	19.3	18.7	0.6	0.6	0.2
2013	40.9	19.9	18.8	0.8	0.6	0.1
2014	41.6	20.6	19	0.7	0.7	0.2
2015	42.4	21.3	19.1	0.8	0.7	0.1

APPENDIX 3: Impacts of Late Pleistocene to Holocene Glacial Isostatic Adjustment on Paleochannels of the New Jersey Margin

Christopher S. Johnson
Gregory S. Mountain
Kenneth G. Miller

S3.1 EN370 Sub-bottom Profiles

S.3.1.1 Sub-bottom profile processing script

#Chrip Processing V1

#Chirp_Proc_V1.sh

#Created by Christopher S. Johnson

#Version Date: August 20, 2018

#Summary - Converts from jsf to segy and applies a depth correction to adjust for

the variable depth of the sled.

#This Version updates the script to multiply the dt by 10 and the TSTAT by 10 to

make account for the program not being able to handle any decimals for #miliseconds

rm binary depthcor header *.su *.sgy

```
a=$1

source ~/.profile

#-------------------------------------------------
#Converts all .jsf line segments to .sgy and then to su and corrects the header values
#-------------------------------------------------------------------------------------

for a2 in *.jsf

do

#removes the last 4 charcters from string variable (removes file extension)

a=${a2%????}



#Reads the jsf file for headers and outputs it to a text file to later use to fill field #record
number.
lstjsf -b $a.jsf > $a"_jsf_header".txt
sed '1d;$d'  $a"_jsf_header".txt | sed '0d;$d' > tmp1.txt
awk '{ print $1 }' tmp1.txt > tmp2.txt
a2b < tmp2.txt n1=1 > fldr
```

```
#converts jsf2segy NOTE: must have jsf2segy compiled and in your .profile.
jsf2segy -a -o $a.sgy $a.jsf  #-a converts analytic (must check jsf header with lstjsf -b to
ensure it is analytic) to envelope.


segyread tape=$a.sgy | segyclean > $a.su


#retrieves the tracl, swdep, and scalel headers.
#swdep - water depth at source
#scalel - scaler to be applied to all coordinates inbytes 73-88 to give a real value
#(positive multiplier, negative divisor)
sugethw < $a.su key=tracl,swdep,scalel output=geom > tmp3.txt


awk '{ printf "%.0f %.0f %.0f %.0f\n", $1, $2, $3, $2 / $3 / 1500 * 1000 * 10 * 2  }'
tmp3.txt > $a"_depth_cor".txt


#Creates a temporary text file containing the tracl and the tstat (delay)
awk '{ print $4 }' $a"_depth_cor".txt > tmp4.txt


#converts tmp2.txt to a binary file that can be input into the header for the su file
a2b < tmp4.txt n1=1 > depthcor
```

```
#Creates a binary file to insert a new dt in ns
sugethw < $a.su key=dt output=geom > tmp5.txt
awk '{ printf "%.0f\n", $1 * 10 }' tmp5.txt > tmp6.txt
a2b < tmp6.txt n1=1 > dtnanosec


#Inserts depth correction to delrt and the ping number into fldr (for later sorting), finally
corrects scalco value to -10000
sushw < $a.su infile=depthcor key=tstat  | sushw infile=fldr key=fldr | sushw
infile=dtnanosec key=dt| sushw a=-10000 key=scalco > $a"_raw".su

rm $a.su
rm tmp*
rm depthcor
rm fldr

done

#Concatinates all su files
echo "concatenating files"
cat *_raw.su > $1"_raw".su
```

```
echo "sorting traces"

susort < $1"_raw".su fldr tracl > $1"_sorted".su


echo "checking depth correction"

#Creates a text file of the headers tracl, swdep, scalel, and tstat (ms)

sugethw < $1"_sorted".su key=tracl,swdep,scalel,tstat output=geom > tmp5.txt

awk '{ printf "%.0f %.0f %.0f %.0f\n", $1, $2, $3,$4, $2 / $3 / 1500 * 1000 * 1000 * -2

}' tmp5.txt > $1"_depth_cor".txt




echo "Running Static Correction"

suchw <$1"_sorted".su >$1"_ns5000".su key1=ns a=7500


sustatic <$1"_ns5000".su hdrs=1 sign=1 > $1"_depthcor".su


#converts back to µs from 10ths of µs

sugethw < $1"_depthcor".su key=dt output=geom > tmp7.txt

awk '{ printf "%.0f\n", $1 / 10

 }' tmp7.txt > tmp8.txt

a2b < tmp8.txt n1=1 > dtmicrosec


sushw < $1"_sorted".su > $1"_nodepthcor".su key=dt infile=dtmicrosec
```

```
sushw < $1"_depthcor".su > $1"_milisec".su key=dt infile=dtmicrosec



sustack < $1"_nodepthcor".su key=fldr > $1"_nodepthcor_stacked".su
sustack < $1"_milisec".su key=fldr > $1"_stacked_final".su
echo "displaying stacked non-depth corrected line"
suximage <  $1"_nodepthcor_stacked".su perc=95 &
echo " prop displaying stacked depth corrected line"
suximage <  $1"_stacked_final".su perc=95 &

echo "creating segy file"
segyhdrs < $1"_stacked_final".su

segywrite < $1"_stacked_final".su tape=$1.sgy

#Extracts the Navigation Data
echo "extracting navigation data"
sugethw < $1"_stacked_final".su key=sx,sy,scalco,tracl output=geom > tmpnav.txt
awk '{ printf "%.6f %.6f %.0f\n", $1 / $3 / 60 , $2 / $3 / 60 * -1, $4}' tmpnav.txt >
$1"_nav".txt
```

```
echo "Moving outputs to output folder"
cp $1"_nav".txt ../Output/$1"_nav".txt
cp $1.sgy ../Output/$1.sgy

rm $1"_sorted".su
rm $1"_milisec".su
rm $1"_nodepthcor".su
rm $1"_raw".su
rm $1"_nodepthcor".su
rm $1"_ns5000".su
rm $1"_depthcor".su
rm *raw.su
rm *0*.sgy
rm tmp*
rm *jsf_head*
rm *depth_cor*
#------------------------------------------------------------------------
#End of Script
#------------------------------------------------------------------------
```

S3.2 Supplementary Methods

S3.2.1 MGL1510 3D Seismic

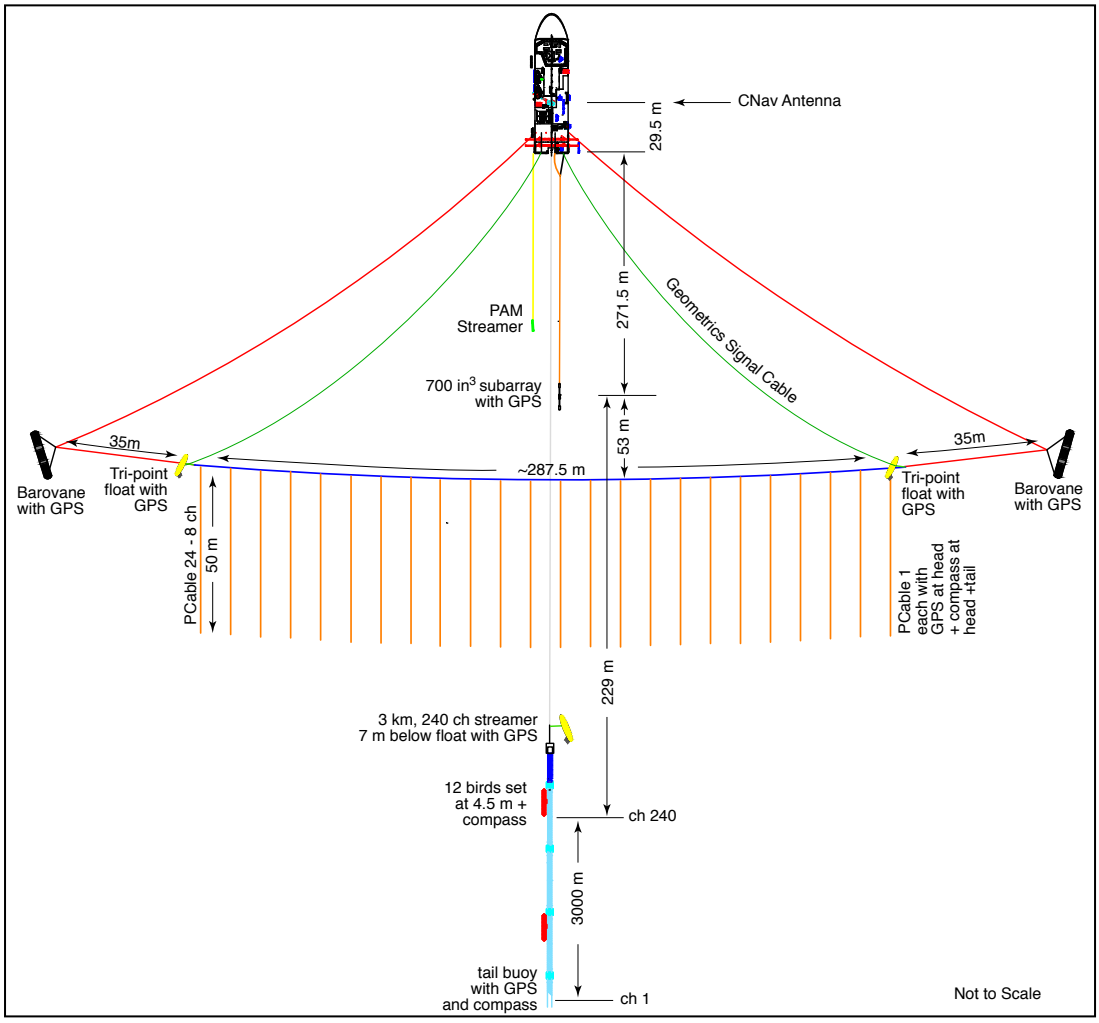

Figure SF3.1: Diagram of MGL1510 seismic array.

S3.2.2 GIA Prior to LGM

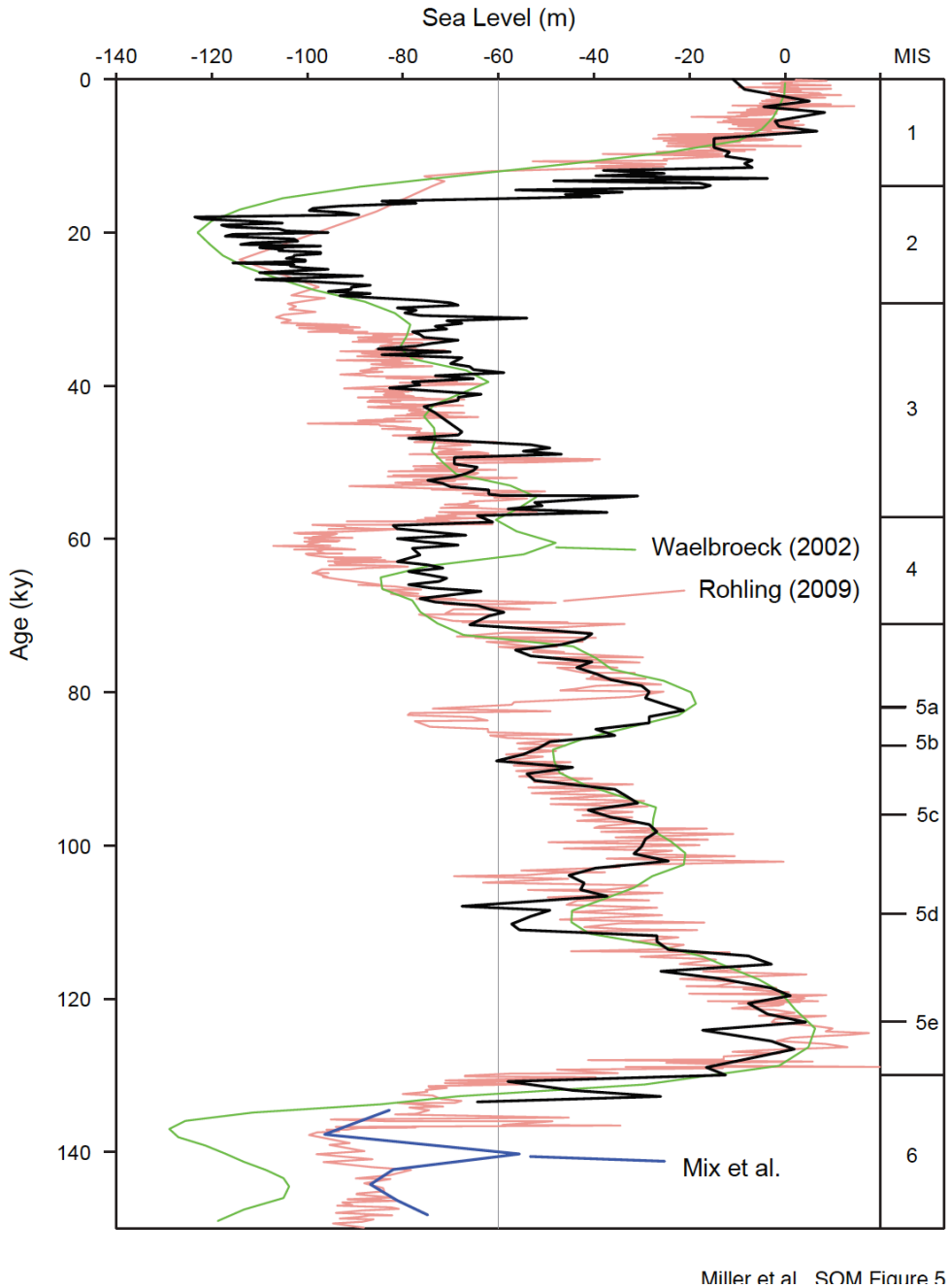

Figure SF3.2 Sea Level curve from Miller et al. (Personal Communication).

S3.3 Supplementary Results

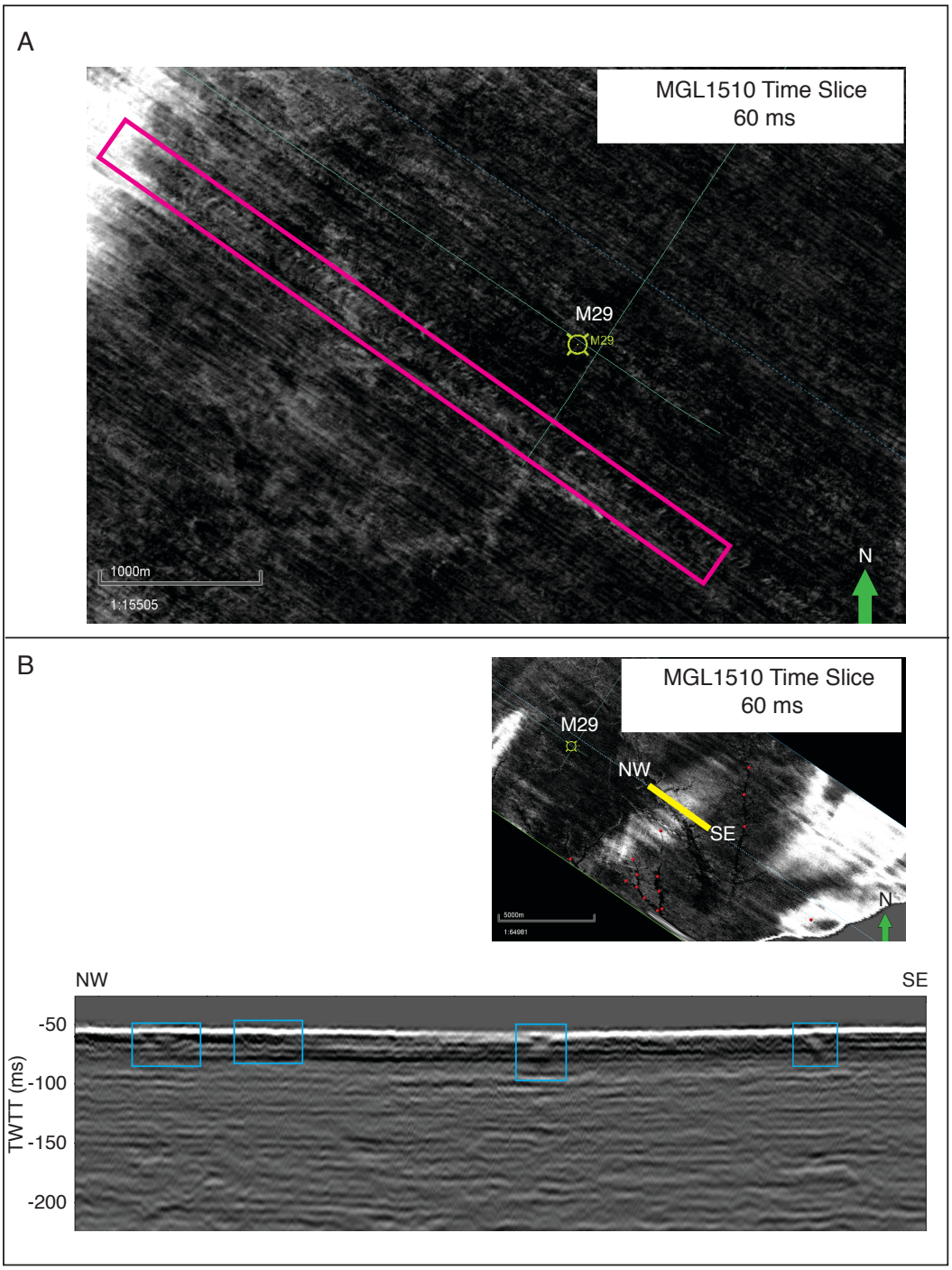

Figure SF3.3 Imaging artifacts in the MGL1510 3D seismic volume. A: The magenta box outlines severe scalloping along a trackline. While obvious in that line, it is still present,

though subtler, in most. B: The cyan boxes outline channels imaged in the 2D inline and the noise they generate below them.

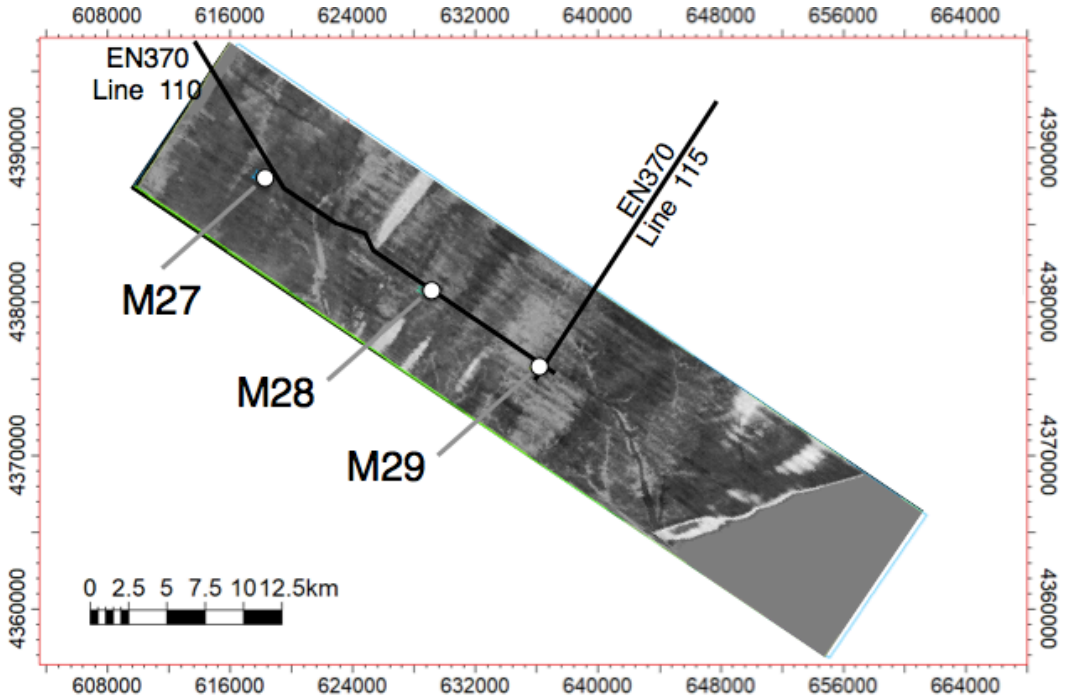

Figure SF3.4: Time slice at 66 ms TWTT. It shows some of the >30 ka.

S3.4 References

Mix, A.C., Le, J., and Shackleton, N.J., 1995. Benthic foraminiferal stable isotope stratigraphy of Site 846: 0-1.8 Ma. *In* Pisias, N.G., Mayer, L.A., Janecek, T.R., Palmer-Julson, A., and van Andel, T.H. (Eds.), Proceedings of the Ocean Drilling Program, Scientific Results 138. College Station, Tx (Ocean Drilling Program), p. 839-854. doi:10.2973/odp.proc.sr.138.160.1995

Rohling, E. J., Grant, K, Bolshaw, M., Roberts, A. P., Siddall, M., Hemleben, C., and Kucera, M., 2009. Antarctic temperature and global sea level closely coupled over the past five glacial cycles. Nature Geosciences v. 2, p. 500-504.

Waelbroeck, C., Labeyrie, L., Michel, E., Duplessy, J. C., McManus, J. F., Lambeck, K., Balbon, E., and Labracherie, M., 2002. Sea-Level and deep water temperature changes derived from benthic foraminifera isotopic records. Quaternary Science Reviews v. 21, i. 1-3, p. 295-305.